Mechanistic Insights into Curvature Perception: A Systematic Study on Cellular Responses to Curved Surface Topographies

Dissertation

der Mathematisch-Naturwissenschaftlichen Fakultät

der Eberhard Karls Universität Tübingen

zur Erlangung des Grades eines

Doktors der Naturwissenschaften

(Dr. rer. nat.)

vorgelegt von

Kerstin Frey

aus Reutlingen

Tübingen

2025

Gedruckt mit Genehmigung der Mathematisch-Naturwissenschaftlichen Fakultät der Eberhard Karls Universität Tübingen.

Tag der mündlichen Qualifikation:	04.06.2025
Dekan:	Prof. Dr. Thilo Stehle
1. Berichterstatter:	Prof. Dr. Günter Gauglitz
2. Berichterstatter:	Prof. Dr. Ralf Kemkemer

"*Life is not easy for any of us. But what of that? We must have perseverance and above all confidence in ourselves. We must believe that we are gifted for something and that this thing must be attained.*"

Marie Curie

Index

Abbreviations and Symbols

Abbreviations

A	Area
a or $a_{0.5}$	Arc length or half arc length
AFM	Atomic force microscopy
AR	Aspect ratio
ASC	Adipose-derived stem cells (here: human adipose-derived stem cells unless stated differently)
A431	Human epidermoid carcinoma cell line
btw	Short for between, meaning the transition zone between the cylinders of the CurvChip
BSA	Bovine serum albumin
CO_2	Carbondioxide
cf.	confer/conferatur (latin), meaning compare
cm or cm^2	Centimeter or square centimeter
CN03	Rho Activator II by Cytoskeleton, Inc.
curv	Short for curvature, meaning the curved region of the CurvChip topographies
CurvChip	Chip platform with curved topographies developed in the present work
d	distance between the cell/nucleus (center of mass) to cylinder axis
diH_2O	Deionized water
DMEM	Dulbecco's modified eagle medium
DMSO	Dimethyl sulfoxide
DNA	Deoxyribonucleic acid
DRR	Dose-response-relationship
ECM	Extracellular matrix
ED50	half maximal response, here used as a measure of curvature sensitivity/avoidance
EdU	5-ethynyl-2'-deoxyuridine; nucleoside used in a proliferation assay
EDTA	Ethylenediaminetetraacetic acid
e.g.	exempli gratia (latin), meaning for example
EGF	Epidermal growth factor
FA	Focal adhesions
f-actin	Filamentous actin
FCS	Fetal calf serum
FN	Fibronectin
GEF-H1	one of the Rho guanine nucleotide exchange factors
GTPase	Other name of G-Proteins, a family of hydrolase enzymes, transduceing signals by binding to Guanosin triphosphate (GTP) and hydrolyze it to GDP (Guanosin diphosphate).
HD	High density

h	Topography height
hdF	Human dermal fibroblasts, numbers indicate different donors (cf. Table 5, p.43)
HMDS	Hexamethyldisilazane
hVSMC	Human vascular smooth muscle cells
i.e.	id est (latin), meaning that is
IF	Intermediate filaments
IQR	Interquartile range
KASH	Klarsicht, ANC-1 and Syne homology
k	Cell perceived curvature [μm^{-1}]
kDa	Kilodaltons
kV	Kilovolts
LED	Light emitting diode
LINC	Linker of the Nucleoskeleton and Cytoskeleton
m	Meter
MDCK	Mardin-Darby Canine Kidney cell line; healthy renal epithelial cells form cockel spaniel
Med	Median
MEF	Mouse embryonic fibroblasts
min	Minute
mJ	Microjoule
mm or mm²	Millimeter or square millimeter
mM	Millimolar
MSC	Mesenchymal stem cells or mesenchymal stroma cells
NA	Numerical aperture
NIH-3T3 cells	Fibroblast cell line isolated from a mouse embryo
nm	Nanometer [10^{-9} m]
N_2	Nitrogen
NPC	Nuclear pore complex
NUC	Nucleus
O_2	Oxygen
p.	Page
pp.	Pages
p>0.05 or ns	p-value larger 0.05, difference is not statistically significant
p< 0.05 or *	p-value smaller than 0.05, difference is statistically significant
p< 0.01 or **	p-value smaller than 0.01, difference is statistically highly significant
p< 0.001 or ***	p-value smaller than 0.001, difference is statistically most significant
PBS	Phosphate buffered saline
PDMS	Polydimethylsiloxane
PFA	Paraformaldehyde
PRK1	Protein kinase N1 PKN or protein kinase c-related kinases PKR

PS	Polystyrene
P/S	Penicillin/Streptomycin
PV	Peak to valley (roughness)
PVC	Polyvinylchloride
R	Radius of curvature
r	Radius of base circle of spherical topographies of the CurvChip
Rho	Sub-family of RhoGTPases (see GTP ases)
RMS	Root mean square
ROCK	Rho-associated coiled-coil forming kinase, also Rho associated kinase also ROK
ROI	Region of interest
rps	Rounds per second
s	Second
SE	Standard error of the mean
SEM	Scanning electron microscopy
SOP	Standard operation procedure
StDev	Standard deviation
SUN	(short for Sad1 and UNC-84)
TPU	Thermoplastic polyurethane elastomer
US-FDA	United States Food and Drug Administration
UV	ultraviolet
VN	vitronectin
v/v (% v/v)	Volume in volume; Percent by volume
w/o	Without, here mainly meaning without pharmacological manipulation
w/v (% w/v)	weight per volume
YAP	yes-associate protein
2-D	Two dimensional
2.5-D	Two-point-5 dimensional also pseudo 3-D
3-D	Three dimensional

Symbols

∆Ψ	difference of the angle of orientation of nucleus and cell
κ	Surface curvature (1/R)
µg	Microgram
µL	Microliter
µM	Micromolar [10^{-6} mol L^{-1}]
µm or µm²	Micrometer [10^{-6} m] or square micrometer [10^{-12} m²]
φ	the measured angle between the cylinder axis and the cell/nucleus axis of elongation
Ψ	angle of orientation

Abstract

"In vivo cells are surrounded by a highly complex and tissue-specific microenvironment, which is known to influence cell behavior, like cell morphology or migration, as well as cell function to generate and maintain healthy tissue. Not only (bio-) chemical factors […], but also physical cues such as geometrical cues are important signals provided by the environment."[1]

In vitro, geometric cues include three dimensional physical cues like curvatures and other spatial topographies like angular grooves and pillars. While in the past the majority of studies deployed sharp edged topographies, investigating the influence of surface parameters like ridge width and groove depth on cell behavior, studies deploying in vivo-like, curved, topographical features, only emerged in the last decade.

Results of these "studies show that geometrical features on a wide-ranging size scale can affect cell behavior […], such as cell spreading, migration or cytoskeletal organization"[1]. Moreover, in the last decade there is "growing evidence that cells can also sense and respond to curvatures, larger than themselves and that these geometrical cues can even overrule nanoscale guidance cues." [1] However, "the mechanism by which cells perceive geometrical curvature of one to several cell sizes remains unclear and systematic studies to reveal the contact guidance response to quantitatively changing curvature are rare." [1]

Addressing these gaps, the present work comprises two main parts: the material science part, with the development of the CurvChip, a highly defined platform with various curved topographies ranging from tens of micrometer to the mesoscale, and the second, biological part, which uses this CurvChip platform to systematically study the cell response to these highly defined surfaces.

Using uniaxial, cylindrically shaped convex topographies, a systematic study with mesenchymal cells with and without pharmacological manipulation of the cytoskeleton reveals that cell behavior, morphology as well as cell function are affected by the curved substrate. Results furthermore indicate that cells possess a highly sensitive and robust mechanism of curvature perception, further suggesting that cells can perceive curvatures smaller than 1/1500 μm^{-1} and that the nucleus might be the central organelle in curvature perception.

Investigation of healthy as well as cancerous epithelial cells on micro-spherical segments indicates that cellular changes associated with cancer might affect a cells response to curvature, i.e. cancerous cells seem to be more sensitive in regard to convex substrate curvature and other substrate metrics such as structure height.

[1] Exact quote from Frey et al. (*1*).

In summary, in a first step this work provides a model system with highly defined surfaces and a systematic variation of surface parameters, the CurvChip. In a second step this CurvChip was used to generate new insights in cell behavior on curved topographies of various sizes, including the curvature perception mechanism of cells.

Zusammenfassung

In vivo sind Zellen umgeben von einer hoch komplexen, gewebsspezifischen Mikroumgebung, die dafür bekannt ist, Zellverhalten, wie die Morphologie oder Migration, aber auch die Zellfunktion zu beeinflussen und dazu dient, gesundes Gewebe zu ermöglichen und aufrecht zu erhalten. Dabei sind nicht nur (bio-) chemische, sondern auch biophysikalische Faktoren, wie geometrische Merkmale, wichtig.

In vitro, geometrische Signale beinhalten dreidimensionale physikalische Merkmale, wie Krümmungen und andere räumliche Topografien, wie Rillen- und Säulen-Strukturen. Während in der Vergangenheit die meisten Studien scharfkantige Topografien verwendeten und den Einfluss von Oberflächenparametern wie Gratbreite und Rillentiefe auf das Zellverhalten untersuchten, kamen Studien mit *in vivo*-ähnlichen, gekrümmten topografischen Merkmalen erst im letzten Jahrzehnt auf.

Die Ergebnisse dieser Studien zeigen, dass geometrische Merkmale auf einer breiten Größenskala das Zellverhalten, wie die Zellmigration und die Organisation des Zytoskeletts, beeinflussen können. Darüber hinaus gibt es in den letzten zehn Jahren vermehrt Hinweise darauf, dass Zellen auch Krümmungen wahrnehmen und darauf reagieren können, die größer sind als sie selbst, und dass diese geometrischen Merkmale sogar Orientierungssignale im Nanomaßstab überlagern können. Die Mechanismen, die hinter der Wahrnehmung dieser Krümmungen steckt, bleibt jedoch unklar und es gibt kaum systematische Studien, die das Zellverhalten in Abhängigkeit von Krümmungsveränderungen quantifizieren.

Diese Lücken adressierend, umfasst die vorliegende Arbeit zwei Teile: einen materialwissenschaftlichen Teil, mit der Entwicklung des CurvChips, einer Plattform mit verschiedenen, hochgradig definierten, gekrümmten Topografien, die von mehreren zehn Mikrometern bis zur Mesoskala reichen, sowie dem zweiten, biologischen Teil, der diese CurvChip Plattform für systematische Studien des Zellverhaltens verwendet.

Ergebnisse einer dieser systematischen Untersuchungen, mit mesenchymalen Zellen auf uniaxialen, zylindrisch geformten, konvexen Oberflächenstrukturen, mit und ohne pharmakologische Manipulation des Zytoskeletts, zeigen, das sowohl das Zellverhalten als auch die Morphologie und Zellfunktionen vom gekrümmten Substrat beeinflusst werden. Ergebnisse deuten zudem darauf hin, dass Zellen einen hoch sensitiven, aber auch hoch robusten Mechanismus besitzen müssen, und diese mesenchymalen Zellen, damit Krümmungen wahrnehmen können die kleiner als 1/1500 μm^{-1} sind. Darüber hinaus scheint der Zellkern für die Krümmungswahrnehmung von zentraler Bedeutung zu sein.

Durch die Kultivierung von gesunden und Epithelzellen aus Krebsgewebe auf mikro-sphärischen Segmenten konnte zudem gezeigt werden, dass kanzeröse Veränderung der Zellen die Wahrnehmung von Krümmungen beeinflussen könnte, genauer scheinen

Krebszellen empfindlicher auf konvexe Substratkrümmungen und andere Substratparameter wie die Strukturhöhe zu reagieren.

Zusammenfassend bietet die vorliegende Arbeit in einem ersten Schritt ein Modelsystem mit höchst definierten Oberflächenstrukturen, die eine systematische Variation von verschiedenen Oberflächenparametern erlaubt, den CurvChip. Dieser CurvChip wurde dann, in einem zweiten Schritt verwendet um neue Einblicke in das Zellverhalten auf gekrümmten Topographien verschiedener Größen, einschließlich des Mechanismus der Krümmungswahrnehmung, zu generieren.

Preface

The ***first chapter*** gives a short overview of the theoretical background of the general relevant biological topics covering basic information on the complexity of the biological system, factors known to influence cell behavior and cell signaling.
The ***second chapter*** provides an overview of the most relevant literature in the field, as well as the motivation and specific objectives of the present work.
Chapters three to six cover the experimental work and results while ***chapter seven*** will complete the work with a conclusion and outlook.

Parts of the present work (i.e. *Chapter IV The CurvChip – A Model System* and corresponding parts of *Chapter III Experimental Part*) have been published in

> *Current Directions in Biomedical Engineering 4 (1), pp. 453 – 456; 2018; DOI: 10.1515/cdbme-2018-0108* [Reference (*2*)]

and

> *Current Directions in Biomedical Engineering 7 (2), pp. 550-553; 2021; DOI: 10.1515/cdbme-2021-2140* [Reference (*3*)]

Moreover, parts of the present work (i.e. parts of the *Abstract* and *Chapters I Theoretical Background, IV The CurvChip – A Model System,* and *V Mesenchymal Cells on Uniaxial, Cylindrical Curvatures,* and corresponding parts of *Chapter III Experimental Part*) have been published in

> *Advanced healthcare materials 14, 2402865, 2025; DOI: 10.1002/adhm.202402865* [Reference (*1*)]

I. Theoretical Background

The Extracellular Environment – a Complex System

The cell (micro-) environment is a highly complex milieu surrounding a cell in vivo. This environment includes all factors affecting cell behavior and function. Like visualized in Figure 1, these factors comprise biochemical cues, including the extracellular matrix (ECM) composition, the interaction with adjacent cells, and the presence and composition of soluble factors like cytokines, hormones and growth factors. Additionally, biophysical cues, including geometrical factors (two- and three-dimensional), as well as mechanical forces are of importance, amongst other things. The relative impact of the different factors is known to be at least partially tissue and cell type dependent, further increasing the complexity.

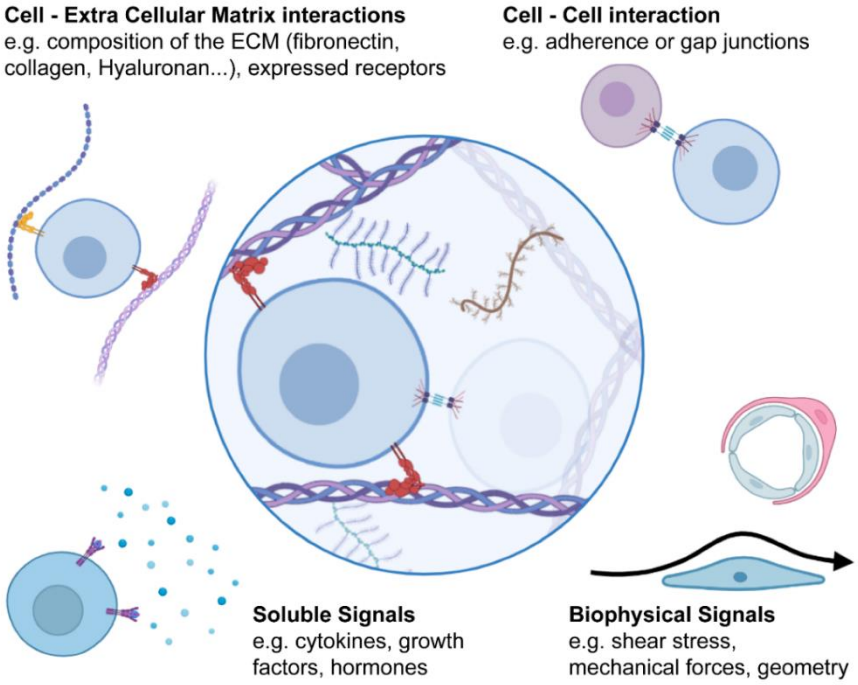

Figure 1 **Illustration of different environmental cues influencing cell behavior and function.** Created in BioRender.com

The various factors influence fundamental processes like cell differentiation, migration, proliferation and survival and, therefore, also tissue structure and function in events like tissue morphogenesis, regeneration and homeostasis. (*4–6*) This involvement in fundamental processes emphasizes the importance of gaining a detailed understanding of these processes on a cell and tissue level. Consequently, understanding the processes would also result in the situation that these processes can be influenced, and this knowledge can then, ultimately, be

deployed in fields like tissue engineering (*4, 5*), implant design (*7, 8*), as well as organ-on-a-chip and other in vitro platforms that are aiming to reproduce different in vivo situations (*9, 10*).

The probably most apparent constituent providing these influencing factors is the extracellular matrix (ECM). Generally, it is defined as tissue specific, organized, insoluble macromolecular three-dimensional network surrounding the cell in vivo. In accordance to the respective tissue and its function, the ECM, can be opaque and mineralized forming rigid structures like bones and teeth but also transparent and gel-like as in the vitreous body of the eye and even highly resistant to tensile stresses as needed for tendons. (*11* (p. 1057)) Besides previously indicated chemical cues, also geometrical features in the cell vicinity are presented by the ECM and adjacent cells, ranging from nanometer structures like fibronectin fibrils to micrometer structures like capillaries (approx. 2 µm radius), collagen fibril bundles (1 to 20 µm radius) and osteons up to mesoscale structures like the vena cava with a radius of about 1 500 µm. (*12–16*)

Together, this underlines the complexity and interdependency of different biochemical and biophysical factors resulting from the extracellular environment. The following paragraphs, therefore, aim to give a condensed overview of different biochemical and biophysical cues and their interaction with the cell.

Biochemical Factors

Depending on the *in situ* existing ECM molecules, different biochemical signals are presented to the cells. Amongst others, fibronectin, vitronectin, laminin, as well as collagen I exhibit different functional domains with specific bioactivities, as indicated in Figure 2. These domains include cell receptor binding sites, i.e. integrin-binding domains, like the well described fibronectin type III domain 9 and 10 (FN III 9-10). The latter contains the well-known amino acid sequence RGD (single letter amino acid abbreviation for: arginine-glycine-aspartic acid), as well as the less familiar LDV (leucine-aspartic acid-valin) in the variable region of fibronectin. (*17, 18*) Beyond that, these functional domains also include sites for interaction with other ECM molecules in order to form an organized network, on one side, and to allow the formation of local depots of soluble molecules, like growth factors, on the other side. The probably best-described example of a biding side for soluble molecules is the FN III 12-14 of fibronectin (*19*) which was shown to bind more than 25 different growth factors without inhibiting their activity.

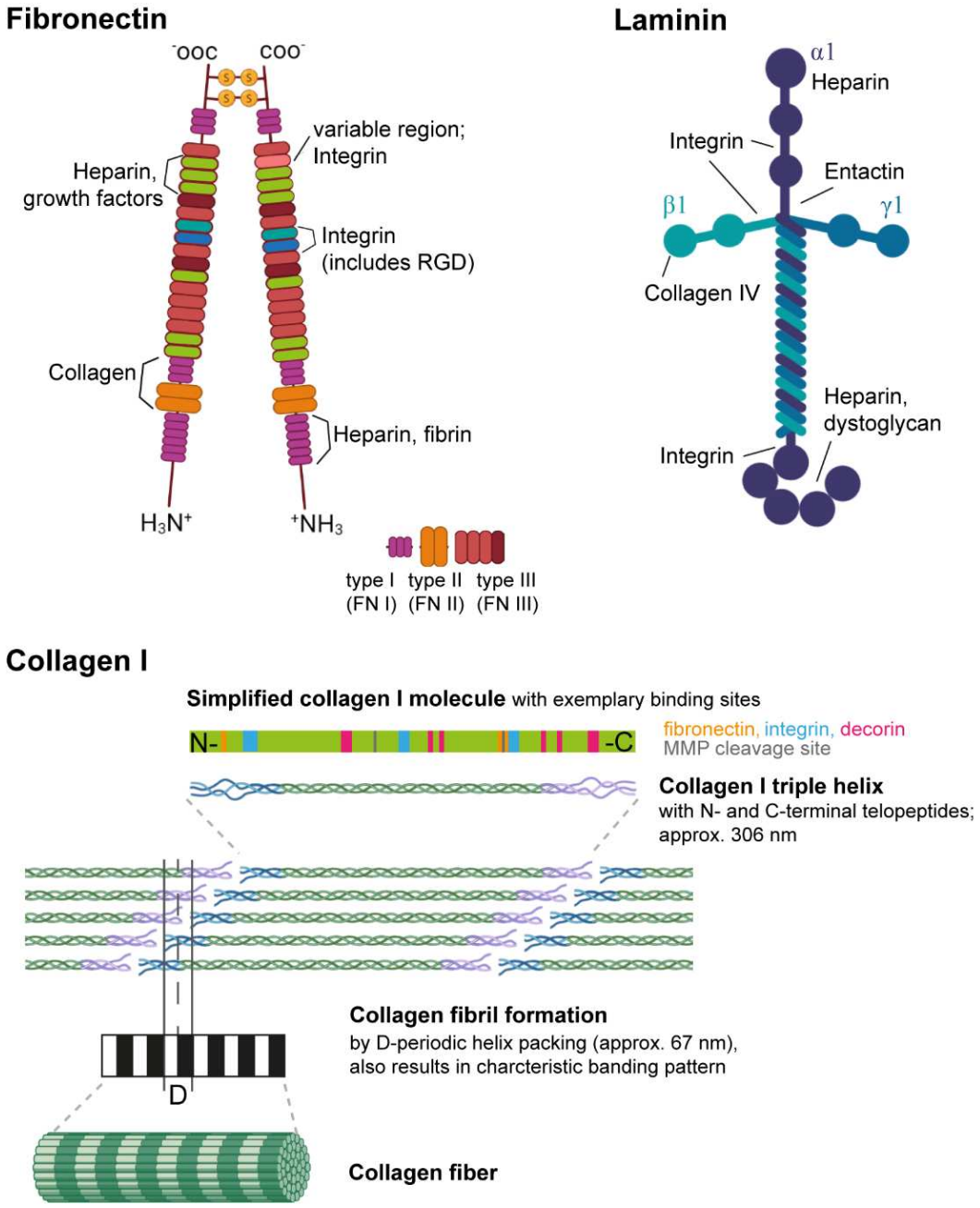

Figure 2 **Different bioactive domains in an exemplary fibronectin dimer, laminin heterotrimer and collagen I triple helix.** ***Fibronectin*** Based on splicing and post translational modification of only one encoding gene up to 20 variants of human fibronectin exist. Dimerization based on two disulfide-bonds takes place at the C-terminus. The monomers consist of different domains FN I, FN II and FN III as indicated. Cell binding takes place at FN III 9-10 via RGD and FN III variable region via LDV amino acid sequences. ***Laminin*** Encoded by multiple genes, three heterologous chains are linked together at the so called coiled-coil region, assembling in different combinations of laminin variants. Cell-binding takes place via RGD, YIGSR/PDGSR, IKVAV amino acid sequences (indicated from top to bottom). ***Collagen I*** Triple-helical molecules are formed by two α1 and one α2 chain. These left-handed triple helices have a multitude of bioactive domains, exemplary domains are visualized in the simplified collagen molecule (adapted from Madhurapantula et al. (*20* (p. 150))). After secretion the triple-helical molecules assemble into highly ordered structures, the collagen fibrils. When these collagen fibrils are

crosslinked higher-order collagen fibers and collagen fiber bundles can result. Created in BioRender.com. (*11* (pp. 1066), *17, 18, 21*)

Cell-ECM Interaction

In general, cell-matrix interaction includes the direct interaction between cell receptors and the insoluble macromolecules as well as the interplay between receptors and soluble molecules, both in their bound and dispersed forms. This interaction is mediated by several types of cell surface receptors, including immunoglobulin-like receptors, glycoproteins, and proteoglycans (i.e. syndecans) (*22*). However, the probably most studied cell surface receptors mediating cell-matrix adhesion is the glycoprotein superfamily of integrins.

Integrins are noncovalently associated heterodimeric transmembrane glycoproteins consisting of at least eighteen different α and eight β subunits, forming 24 types of heterodimers in humans (*23*). Both subunits contain an extracellular domain, a membrane spanning part as well as a short cytoplasmic tail. The extracellular domains can bind to specific amino acid sequences (e.g. RGD, LDV) of the above-mentioned cell adhesion domains. The intracellular tails bind to a cluster of proteins mediating the linkage of the ECM to the cytoskeleton of the cell and as well as the interaction with different signaling pathways (e.g. through proteins of the Rho family (*24*)). When the cytoskeletal element is f-actin, these protein plaques are also known as focal adhesions (FA).

Based on this structure, focal adhesions allow bi-directional chemical signaling as well as force transmission across the plasma membrane. This provides the cell with information about their biochemical but also biophysical environment (*25*).

This also results in different compositions of the adhesion plaques, or integrin adhesomes, depending on the different types of integrins and extracellular components they are interacting with. However, like previously stated by Guasch et al. (*26*), a complete understanding of the "spatiotemporal dynamic interaction" of integrins with specific signaling pathways is mostly still lacking, as integrins are known to interact with various proteins (*27*). As described above, fibronectin (cf. Figure 2), for instance, has more than one integrin binding site and is interacting with αvβ3 and α5β1 integrins, while vitronectin also binds αvβ3 integrin, but also αvβ5 and αIIbβ3. Furthermore, it is also known that not only the chemical composition of the environment but also biophysical factors like ligand density have an impact on the resulting cell response (*26, 28, 29*).

Cell-Cell Interaction

Adjacent cells also directly interact with each other via different kinds of proteinous junctions and are, therefore, also providing biochemical signals. Regarding these direct cell-cell

contacts, it is important to consider that in vivo different kinds of tissues exist. As described by Alberts et al. (*11* (pp. 1035)), the connective tissue, which has its origin in the mesenchyme, is consisting mostly of extracellular matrix with sparsely distributed cells, whereas epithelial tissues are composed of tightly connected cell sheets, that can be semi-permeable. In the latter tissues the extracellular matrix is mainly present as a thin mat, known as *basal lamina* or basement membrane, which is giving the cell a kind of basal-apical polarity. Analogue to this, cells are also distinguished as either mesenchymal or epithelial cells, depending on their tissue origin.

In general, there are three major cellular junction families allowing intercellular interactions: The first two families are tight or occluding junctions, responsible for sealing the space between the cells, and channel forming or gap/communicating junctions, allowing direct communication between neighboring cells.

The third major junction family are the cell-cell anchoring junctions or adhesion junctions, that are connecting the cytoskeleton (actin or intermediate filaments) of adjacent cells with each other using special transmembrane adhesion proteins known as cadherins (*30*). Here different subgroups are defined, depending on the cell and tissue type: Belt like adherens junctions, or zonula adherens, are spanning the complete cell in basal/apical polarized epithelial cell sheets. The second kind of adherens junctions are more spot-like junctions, also known as *punctum* or *punctate* adherens junctions, which are formed between mesenchymal cells as well as during early stages of epithelial polarization and wound closure. The third type of anchoring junctions is found in epithelial sheets at the point where several cells meet, e.g. tricellular adherens junction, and can be described as an in-between junction of the above. (*31, 32*)

Cell-Cell junctions are known to impact many different cell functions in healthy and diseased tissues like cancer, including cell migration, proliferation (e.g. contact inhibition), cell death, as well as synthesis of matrix molecules. (*33–36*)

Comparable to cell-matrix junctions, cell-cell junctions do not only allow biochemical signaling, but they also facilitate the exchange of biophysical cues. This does not only happen via ion-/molecule-exchange through gap junctions but also due to the coupling of junctional components to the cytoskeleton. Based on this coupling to the cytoskeleton, they also contribute to the exchange of stresses between cells. (*30*) Moreover, there is strong evidence that these forces are needed to form functioning cell-cell as well as cell-matrix junctions, i.e. adherens junctions and cell-matrix anchoring junctions, and, therefore, also to form functioning tissues. (*37–39*)

Generally, in vivo and in vitro, (chemical) signals originate from cells in the same organism (in vivo) or culture plate (in vitro) or even the same cell. Therefore, one can differentiate between three modes of action: autocrine, from the same cell, paracrine, form a cell in close vicinity, or endocrine, from a more distant cell in the same organism. The latteris only possible in vivo, while in vitr*o* an additional source of signals is the cell culture medium being used. For instance, it was observed that fibroblasts cultivated on collagen gels are only highly contractile in the presence of fibronectin in the serum (*40–43*). Moreover, there are indications, that contractility is primarily mediated by fibronectin, which in this case is only present in the medium and was shown to bind to cells as well as to collagen itself (*40–42*).

This interdependency between released and received signals results in a feedback loop, where changes in the environment affect biochemical and biophysical processes in the cell for instance regarding contractility (*43*), migration (*44*), proliferation (*45*) or protein expression (*35*), including cytokine or ECM molecule generation, which then in turn alter the composition of the extracellular environment.

Biophysical Factors

As stated previously, dependent on its composition, the ECM can form rigid, gel-like, textures as well as structures that are highly resistant to tensile stresses. (*11* (p. 1057)) This difference in rigidity exemplifies that the extracellular environment also provides (various) biophysical cues that are found to be perceived by the cells growing in or on these different extracellular matrices.

Besides ECM rigidity, which has been shown to influence fundamental processes like cell spreading, migration (durotaxis or mechanotaxis), and differentiation (*46, 47*), there are other biophysical factors, that can be perceived by cells. These cues include other mechanical forces resulting from movement of the organism or body fluids like blood, small electrical fields, temperature, or concentration gradients of soluble factors, ligand density, as well as geometrical cues (*48, 49*).

Regarding cell migration behavior, for instance, different phenomena are described, comparable to durotaxis, where cells were observed to migrate towards stiffer areas (*50*). Cells were also observed to migrate towards areas with more dense ligands (haptotaxis) (*51*), or along different directed topographical cues like grooves and ridges (*52*) as well as cylindrical (*53, 54*) or uniaxial wavy surface structures (*55*) (contact guidance). However, also the intensity of light (phototaxis), electrostatic potential (galvanotaxis) and gravitational potential (geotaxis) as well as combination of several cues on cell migration were described in literature, like listed by Cortese et al. (*49*).

However, the understanding of how a specific cue is perceived by the cell and elicits a response like orientation or migration remains elusive for most of the environmental factors. The following sections will give an overview of for the present work relevant biophysical cues and corresponding cell responses, including mechanical cues, ligand density and geometrical cues.

Mechanical Cues

In general, the umbrella term “mechanical cues” comprises extrinsic cues, such as fluid flow, shear stress, and compressive forces, as well as intrinsic cues of the direct cell surrounding (e.g., ECM, cell culture substrate), including stiffness/elasticity and topographies in different sizes (*56*). The cell perception process enabling cells to perceive these mechanical cues is known as mechanotransduction. Like mentioned previously, the mechanisms of cellular mechanosensitivity remain fairly elusive. However, a range of key elements have been identified to be involved in cellular perception and reaction to biophysical parameter of their surroundings.

Mechanotransduction and Cell-ECM Adhesions

The first, key element of mechanotransduction, and probably the most fundamental, is the integrin-mediated cell adhesion, which enables cells to probe their surroundings using pulling forces.

As indicated previously, cells are attached to their environment, via different surface receptors spanning the cell membrane, the most prominent example being integrins. Integrins are receptors for special motifs in the extracellular matrix and connected to the cytoskeleton via a multitude of proteins (integrin adhesome forming focal adhesions; FA) on their cytosolic side, like mentioned previously. (*57*) Via the activation of different signaling pathways (e.g. Rho/ROCK), this connection to the cytoskeleton, more precise the actomyosin fiber system, generates tension at the adhesion site, as the contractile acto-myosin network, is pulling the junctions and, therefore, the ECM inward. (*58*)

This force application triggers mechanosensitive adhesion strengthening, by catch-bond formation as well as integrin clustering, by recruiting of more integrins to the site of adhesion to enforce the adhesion (increased avidity). (*11* (p. 1080), *59*)). To some extent the scope of the recruitment is dependent on the rigidity of the substrate/environment/ECM, as it counterbalances the applied force by the cell.

These traction forces enable the cell to actively (inside-out signaling) and passively (outside-in signaling) sense and respond to the mechanical properties of its surrounding.

Externally applied force (e.g. fluid shear stress or substrate stretching) to a prestressed system, like the adhering cell, for instance, can cause mechanical distortion that leads to

structural change of the cell adhesion apparatus, i.e. mechanosensors in the adhesion apparatus, like talin (*11* (p. 1081)). This change can include protein unfolding, exposing otherwise hidden domains and allowing additional catalytic activity (e.g. phosphorylation) or protein binding. Furthermore, this mechanical distortion can modulate mechanosensitive ion channels, as well as the assembly and stability of receptor-ligand complexes. (*58, 60*)

Altogether, these changes lead to the propagation of signals via different pathways (e.g. Rho/ROCK) and, therefore, structural and morphological cell adaption to varying mechanical properties of the cell's environment, including changes of the forces exerted by integrin-based cell adhesions. (*58, 58*) This resulting feedback loop again leads to cell responses including cell spreading and reorientation (*39, 61, 62*), as well as migration (durotaxis) (*47*) but also cell differentiation (*46*) and tissue formation, both in healthy and diseased models (*63, 64*).
However, a complete understanding of the interaction of integrins with specific signaling pathways is mostly still lacking (*26*). Recent studies, however, showed that the extent and type of cell reaction also including mechanotransduction is also dependent on the involved type of integrin molecules: While α5β1 (fibronectin) was shown to be linked to RhoA/ROCK/myosin II pathway and, therefore, force generation, αvβ3 (fibronectin and vitronectin) was identified to be linked to GEF-H1/RhoA/mDia1 but not myosin II and, therefore, FA-cytoskeleton reinforcement and consequently to enabling mechanotransduction but not force generation (*26, 65, 66*).

The Nucleus as a Mechanosensor

A closely related, second, mechanosensitive element was identified more recently: the nucleus. (*67*) The nucleus is the largest and stiffest cell organelle of eukaryotic cells and due to the fact that it contains most of the cells' DNA it plays a central role in almost all cell functions and responses.
In general, the nuclear lumen, which is harboring the DNA, is enclosed by the so-called nuclear envelope (schematically depicted in Figure 3). This envelope comprises two phospholipid bilayers, also known as inner and outer nuclear membranes, as well as the underlying lamina, a proteinous meshwork mostly consisting of lamins. The two membranes enclose the perinuclear space and are connected at the nuclear pore complexes (NPC).
NPCs form a direct gateway for molecules from the cytoplasm into the nuclear lumen. While small molecules and ions can easily diffuse through the channels, controlled import and export mechanisms exist for larger molecules (approx. > 40 kDa) often involving the binding to receptors for specific transporter proteins (*68*). Apart from that, there are also reports that the transport through the NPCs is mechanosensitive, as active transport is affected by forces

acting on the nucleus, e.g. by affecting the pore size and allowing larger molecules to pass, like it was described for the transcription factor YAP (yes-associate protein) (*69*).

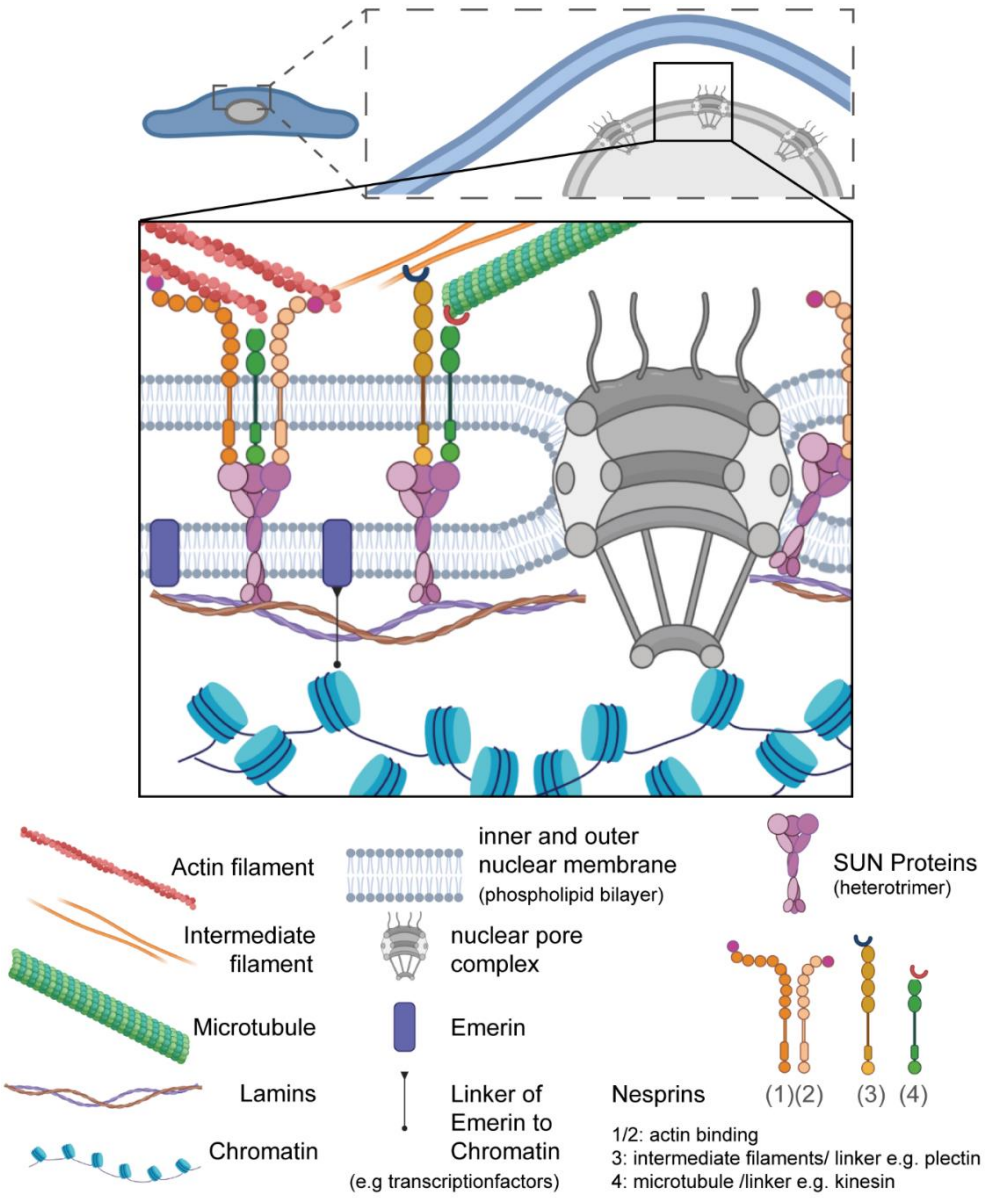

Figure 3 **Illustration of the nuclear envelope, pore complex (NPC), and LINC complex (Linker of the Nucleoskeleton and Cytoskeleton).** The LINC Complex is formed by nesprins, whose KASH domains interact with SUN Proteins in the perinuclear space and with the cytoskeleton with their cytoplasmic domains. This interaction can be direct or via linker proteins, like plectin in case of intermediate filaments or kinesin in case of microtubule. The nucleoplasmic domains of the SUN proteins interact with varying nuclear structures, including the lamina, chromatin and the NPC. (*68*) Created in BioRender.com.

Moreover, force transmission to the nucleus is not solely an indirect process caused by the general deformation of the cell, the nucleus is also directly linked to the cytoskeleton creating a physical continuum between the nucleus, cytoskeleton as well as the extracellular matrix.

The protein complex mediating this interaction is known as the LINC (Linker of the Nucleoskeleton and Cytoskeleton) complex and is also visualized in Figure 3. The main components of these complexes are the SUN- and KASH-domain proteins:
SUN (short for Sad1 and UNC-84) proteins form multimers and span the inner nuclear membrane with their SUN-domain localized in the perinuclear space and their nucleoplasmic domains interacting with the nucleoskeleton (i.e. lamina), the NPC, chromatin and other proteins like emerin. (*68, 70*)
The KASH (Klarsicht, ANC-1 and Syne homology[2]) proteins (i.e. nesprins[2]), on the contrary, are located in the outer nuclear membrane with the KASH-domain facing the perinuclear space, where it interacts with the SUN-domain of the respective proteins. The cytoplasmic domains of the nesprins interact with the cytoskeleton, including actin filaments, microtubule as well as intermediate filaments. (*71*)

The LINC complex has been shown to be important in many cellular functions including those involving nuclear positioning like cell polarity, division, differentiation and motility (*72* (p. 5)).
Versaevel et al. (*72*), for instance, showed that the apical stress fibers in elongated cells form a sort of cage (the perinuclear actin cap), that is directly connected to both the nucleus (via the LINC complex) and the basal ECM (via FA). This cage helps to secure the nucleus location by applying a normal compressive force, that is even deforming and indenting the nucleus. Furthermore, the LINC complex also couples the nucleus to other cytoskeletal components such as the microtubules, which are connected to nesprins via the motorprotein kinesin-1. The motion of the kinesin towards the plus end of the microtubule has been shown to generate a pulling force resulting in nuclear reorientation, as well as possible deformation of the nucleus (*73, 74*).

Moreover, other mechanical stresses generated by the cell or applied at the cell surface, have been shown to be transferred to the nucleus. (*67, 75, 76*) However, the extent to which the LINC complex is (significantly) involved in the transmission of different forces to the nucleus is not yet fully understood, as some studies also point out potential LINC-independent mechanisms, like also listed by Jahed et al. (*77*).
Nuclear morphology, for instance, has been shown to change depending on different factors which represent various forces acting on the nucleus. During cell spreading or by increased cell contractility, the normal compressive force by the stress fibers of the perinuclear actin cap is increased, resulting in nuclear flattening and, therefore, increase in the nuclear projected area.

[2] In mammalian syne proteins that are anchoring nuclei are also referred to as nesprins, for nuclear envelope spectrin repeat proteins. However not all KASH-proteins contain spectrin repeats. (*71*).

On the contrary, lateral compression exerted by central stress fibers (commonly not associated with LINC) during cell elongation (e.g. by shear stress or contact guidance cues) can induce a more elongated, smaller nucleus in terms of projected area. (*78*).

And finally, changes in stress exposure of the nucleus can also lead to nuclear remodeling, including lamina restructuring (*79*) and chromatin condensation (*78, 80*), consequently causing in a change in nuclear area (*79*) as well as altered nuclear mechanics (*81*) and even gene expression was shown to be affected. Cells with more condensed nuclei for instance show a decreased proliferation (*78, 82*). And the change in nuclear mechanics was shown to be related to a change in Lamin expression (*79*) but also chromatin condensation, both also processes associated with stem cell differentiation. (*83–85*)

Implications of Cell-Cell Interactions

Another factor influencing cell perception and processing of biophysical cues is the contact to other cells or cell collectives. As mentioned previously, the cytoskeletons of neighboring cells are mechanically coupled by cell-cell (adherence) junctions transmitting tensions between neighboring cells (*38*). Among other things, this coupling generates some kind of resistance against (extrinsic and intrinsic) forces but also enables fast and far-reaching communication between cells (*86*). Comparable to focal adhesions, adherence junctions are composed of E-cadherins which are associated with various, different molecules, including mechanosensors and different protein kinases. And like for FA, adhesion junctions have been shown to activate different pathways including Rho/ROCK/myosin II pathway. (*38, 87*)

A cell function often studied in the context of force coupling is collective movement of cellular monolayers, where long ranging motion over 10 to 15 cells can be observed, depending on the cell type and tissue dimension (*86, 88*). Like described by Chen et al. (*89*) studies furthermore showed, a dependence of coordinated monolayer movement on the amount and strength of cell-cell junctions: Disturbed cell-cell junctions were shown to affect the directed collective migration leading to movements comparable to single cell migration described for mesenchymal cells, while cells with passive cell-cell junctions sustained the collective migration (*88*).

Moreover, force coupling was also shown to be involved in ordering mechanisms of (confined) cell monolayers, including the occurrence of coordinated swirling patterns (*89, 90*), as well as other nematic orders like the perfect alignment of spindle-shaped NIH-3T3 cells in micropatterned stripes with a width smaller than the cells correlation length (*91*).

Additionally, cell density has also been shown to be involved in affecting different cell functions, including cell proliferation (contact inhibition) as well as stem cell differentiation. As collected by Petzold and Gentlemen in their review (*56*), initial seeding density of stem cells cultures in

vitro has been shown to drive lineage commitment, independent of the later culture density. Lower cell density, and, therefore, less coupling to other cells, was associated to the expression of osteogenic markers comparable to cultures on rigid substrates like described by Engler et al. (*46*). Suggesting a possible involvement of mechanotransduction and stress coupling in cell density associated differentiation.

Ligand Density

However, cell density and substrate stiffness are not the only factors shown to affect cell processes associated with mechanotransduction, like cell spreading, differentiation or YAP translocation to the nucleus.

Stanton et al. (*25, 92*) show that, besides substrate stiffness modulation, also variations in ligand density influence mechanotransduction processes such as mechanically induced YAP translocation to the nucleus. They even showed that ligand density induced YAP localization was independent of substrate stiffness: at low densities cytoplasmic YAP location was predominant, while high ligand density always resulted in translocation of YAP to the nucleus (*92* (p. 3)). Additionally, they show that the ligand density leading to YAP depends on αvβ3 integrin mediated cell adhesion. As mentioned previously, studies have shown that αvβ3 seems to be responsible for reinforcing the link between the focal adhesions and the cytoskeleton and enabling mechanotransduction but not force generation.

Moreover, Kilian and Mrksich (*29*) found that despite the density of ligands, also their affinity is involved in directing mechanotransduction related stem cell fate. Using defined gold surfaces (self-assembled monolayers alkanethiolates on gold) with two different RGD containing peptides, one with high and the other with low affinity to αvβ3, they showed a stiffness but also density and affinity dependent stem cell differentiation. Substrates “presenting high affinity peptides promote osteogenesis, those presenting a low affinity peptide at high density promote myogenesis and those that present a low affinity peptide at low density promote neurogenesis.” (*29* (p. 4))

Additionally, the distance between ligands on a nanometer level have also been shown to have an influence on focal adhesion assembly and surfaces with ligand distance larger than 73 nm have been shown to fail the induction of focal adhesion formation. (*28, 93, 94*)

Geometrical Cues

Generally, geometrical cues can comprise both, anisotropically distributed, two-dimensional chemical signals like 2-D patterns of adhesive molecules, as well as three-dimensional physical cues like curvatures and other spatial topographies like grooves and pillars. Like mentioned previously, geometrical cues presented by the native microenvironment, are ranging from nanometer structures like fibronectin fibrils to micrometer structures like

capillaries (approx. 2 µm radius), collagen fibril bundles (1 to 20 µm radius) and osteons up to mesoscale structures like the vena cava with a radius of about 1 500 µm. (*12–16*).

In vitro-studies have shown that both two- and three-dimensional geometrical cues influence (fundamental) cell functions, including proliferation, differentiation, orientation and (oriented) migration of single cells as well as cell collectives. (*95–100*)

For instance, Chen et al. (*98*) have shown that the size of 2-D cell adhesion areas cell survival and proliferation, while other (*95, 96*) studies have demonstrated that the size and geometry of these 2-D cell adhesion areas affects cell differentiation. Moreover Kilian et al. (*96*) have found an interdependency between the curvature of the perimeter of the micropattern and stem cell differentiation, while topographical 3-D surface curvature was also associated with stem cell differentiation (*97*).

Another phenomenon, known as contact guidance, was observed for many different directed, topographical cues as well as cell types. It describes the capability of cells to react to substratum micro- and nanotopographies with an oriented response such as reorientation or directed migration.

The first studies starting in the 1900s describing the phenomenon of contact guidance, in terms of cellular alignment and shape adaptions to topographies, were using glass cylinders.(*53, 101, 102*) However, to link the observed cell behavior to the substrate shape, micro-fabricated surface topographies have been used with defined sizes, and often angular shape, such as nano- and micrometer grooves and ridges.(*103–105*) Investigations have shown that contact guidance cell response to ridges and grooves in nano- to micrometer scale is strongly dependent on feature size parameters including distance, pitch and depth.(*52*) Investigations regarding relevant, in vivo-like features, however, are only emerging in the last decade and are, therefore, still rare. Moreover, they often lack a systemic approach of an independent variation of single parameter.

Cell Signaling

As mentioned previously signals, both chemical and biophysical, that are perceived by cells can originate from cells in the same organism (in vivo) or culture plate (in vitro) or even the same cell.

This interdependency between released and received signals results in the propagation of signals via different pathways (e.g. Rho/ROCK) and, therefore, structural and morphological cell adaption for instance regarding cell contractility (*43*), changes in the forces exerted by integrin-based cell adhesions (*58, 58*), protein expression (*35*), which then, in turn, alter the composition of the extracellular environment but also cell spreading and reorientation (*39, 61, 62*), migration (*44*), proliferation (*45*).

However, cell signaling and mechanisms of underlying cell responses are highly complex and not well understood. Some cell responses like reorientation or directional movement are affected by various factors, like previously described for migration (chemotaxis, haptotaxis, durotaxis, contact guidance, galvanotaxis, etc., cf. p. 6 Biophysical Factors). In order to be able to respond in a directed way, cells need to perceive the direction of the guiding signal, respond to it, and be able to control their behavior by means of a feedback loop; a regulation mechanism that was previously described as an automatic controller, by Kemkemer et al. (*106*) (cf. Curvature Detection: Orientation, Positioning and Migration on Substrates with Curvature p. 25).
On the molecular basis, signal detection, transduction, processing, and response are mediated by signaling cascades also known as pathways.

RhoGTPases

The family of small RhoGTPases, including 5 sub-families (Rho, Rac, Cdc42, Rnd, RhoBTB) are central molecules in these signaling pathways as they act as molecular switches involved in many important cell processes, including morphogenesis, motility and proliferation (*107*). They transduce signals between different receptors, by switching between an inactive (GDP[3]-bound) and an active (GTP-bound[4]) conformation. The activity is mediated by guanine nucleotide exchange factors (GEFs), that exchange GDP for GTP, and GTPase-activating proteins (GAPs), hydrolyzing GTP to GDP and guanin nucleotide dissociation inhibitor (GDI), suggested to block spontaneous activation (*11* (p. 821), *107*).

RhoGTPases are shown to be involved in regulation of cytoskeletal elements, like exemplarily shown for intermediate filaments and actin networks in Figure 4 (*107–111*). The probably best-investigated families of the Rho family are RhoA, Rac1, and CdC42. Moreover, all three of them are associated with the actin cytoskeleton: While Rac and Cdc42 activation, respectively, lead to protrusive rich lamellipodia and filopodia formation, Rho activation is associated with the formation of contractile actomyosin stress fibers and mature focal adhesions (cf. Figure 4). (*107, 110, 112*) Activation leads to the transduction of the signal to different downstream target proteins or effectors, resulting in different signaling cascades or pathways. However, although RhoA, Rac1, and CdC42 have distinct roles in actin regulation and various effectors, they still share some downstream effectors for instance Arp2/3, an actin polymerization factor (*107*) illustrating the complexity of signal transduction pathways.

[3] **G**uanosin **di****p**hosphate (GDP)
[4] **G**uanosin **t**ri**p**hosphate (GTP)

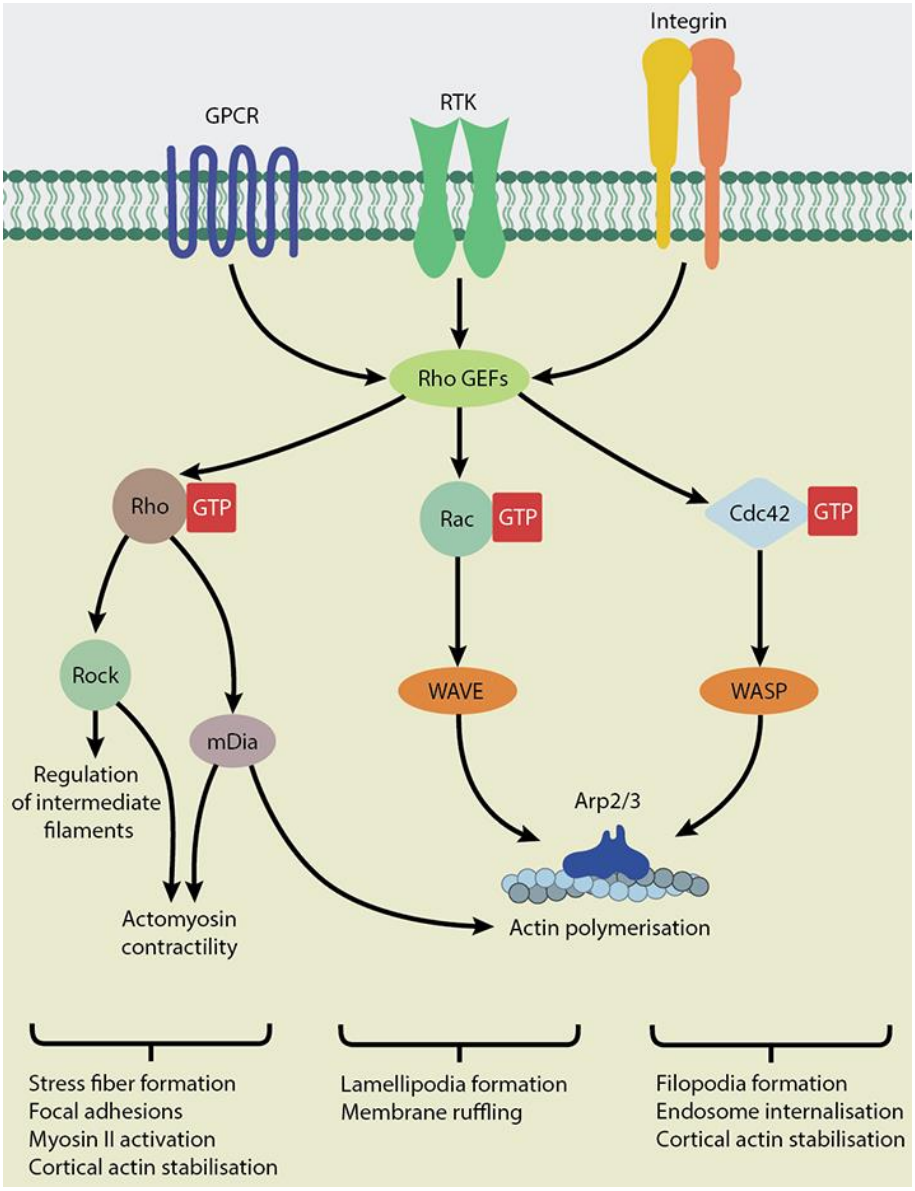

Figure 4 **Rho family members are key regulators of the cytoskeleton**. GPCR: G-protein coupled receptors, RTK: receptor tyrosine kinase, GEFs: Guanine nucleotide exchange factors [copied from www.mechanobio.info (*111*)][5]

RhoA Pathways

As stated above, the RhoA signaling pathways belong to the relatively well known pathways and have been shown to be central to the cell's response to biophysical and chemical signals from the cell's environment including the mechanotransduction process (*38, 113, 114*). For the assembly of a contractile actomyosin network two RhoA downstream effectors are required: mDia1 (mammalian homolog of Drosophila diaphanous also, mammalian diaphanous 1) and

[5] Image copied from www.mechanobio.info (*111*) and used under a Creative Commons Attribution – NonCormercial – ShareAlike 4.0 International license. (https://creativecommons.org/licenses/by-nc/4.0/)) Copyright MBInfo, 2018 National University of Singapore

ROCK (Rho-associated coiled-coil forming kinase, also Rho associated kinase/ROK) (*115*). Like mentioned previously, different integrins have been shown to be associated with distinct RhoA pathways: α5β1 integrin (fibronectin) is linked to RhoA/ROCK/myosin II pathway and, therefore, force generation, while αvβ3 integrin (fibronectin and vitronectin) was identified to be linked to GEF-H1/RhoA/mDia1 but not myosin II and, therefore, FA-cytoskeleton reinforcement and consequently to enabling mechanotransduction but not force generation (*26, 65, 66*).

The mDia1 protein is a formin molecule, promoting actin nucleation and polymerization, resulting in long, straight actin filaments, while ROCK is a serine/theonin kinase that is able to phosphorylate various substrates, as indicated by Narumiya et al. in their review (*116*). By inactivating the myosin-binding subunit of myosin phosphatase and phosphorylation of myosin light chain, ROCK increases myosin light chain phosphorylation and hence actin-myosin-cross-linking as well as actomyosin contractility. Furthermore, ROCK also activates LIM-kinase, which inactivates coflin, an actin-depolymerizing factor, further stabilizing and increasing the amount of actin filaments. (*116*)

Interaction with Other Cellular Structures and Functions

GEF-H1, one of the Rho guanine nucleotide exchange factors (GEF), nicely illustrates the interplay of different cellular structures and functions. GEF-H1 is known to bind and be regulated by their binding to microtubule. Therefore, it couples the dynamics of the microtubule to Rho GTPase activation in both normal cell functions as well as pathophysiological situations, like reviewed by Birkenfeld et al. (*108*). For instance, in cell migration, microtubule depolymerization (and GEF-H1 release) at the rear is connected to increased myosin contractility leading to tail retraction and microtubule growth at the front (bound GEF-H1) results in increased Rac1 activity and lamelipodia formation. (*108, 117, 118*)

II. Objectives, Motivation and State of the Art

Objectives and Motivation

Like stated in chapter I section on Geometrical Cues, studies deploying in vivo-like, curved, topographical features instead of sharp-edged surface features, only emerged in the last decade and are, therefore, rare and often lack a systemic approach of an independent variation of single parameter. Furthermore, over the last decade there is growing evidence that cells can also sense and respond do three-dimensional geometrical cues, in particular curvatures, larger than themselves and that these geometrical cues can even overrule nanoscale guidance cues (*54, 100, 119–125*). However, the mechanism by which cells are able to respond to geometrical curvature of one to several cell sizes remains unclear and systematic studies to reveal the contact guidance response to changing curvature in a quantitative manner are rare.

Addressing these gaps, the first objective of this work was to develop a model system with defined, curved surface topographies ranging from radii of curvature in the range of tens of microns to the mesoscale. The assembly of this platform should enable specific variation of parameters and, therefore, a systematic study of cell response to those changes (*Chapter IV The CurvChip – A Model System*).

The second objective was to conduct systematic cell studies using the developed model system, the CurvChip platform.

Using uniaxially curved model surfaces in the mesoscale, the response of mesenchymal cells to varying surface parameters was investigated. In following steps, the cellular behavior upon systematic manipulation of the cell's cytoskeleton and variation of the protein coating of the topographies was investigated (C*hapter V Mesenchymal Cells on Uniaxial,* Cylindrical Curvatures), in order to address the following key questions:

- Is there a correlation between substrate curvature and structural cellular adaption?
- What is the minimal curvature (maximal radius of curvature) a cell can perceive?
- Is the adaption to substrate curvature dependent on the cell type or origin?
- Is there a difference between collective cell behavior (high cell density) and single cell behavior (low cell density) on curved substrates?
- What is the role of different structural molecules and organelles (e.g. actomyosin stress fibers, microtubules and nucleus) in cell adaption to substrate curvature?
- Do the proteins presented to the cell i.e. via surface coating affect cellular adaption to substrate curvature?

Using spherically curved model surfaces in the meso scale, the cell response of cells with strong intercellular contacts (i.e. epithelial cells) was investigated. Using healthy epithelial cells and cancerous cells, the key question was if there is a difference in cell behavior between healthy and diseased cells (chapter *VI. Epithelial Cells on Spherical Curvatures*).

Gaining an understanding in how cells respond to and perceive these physiologically more realistic surface topographies will not only help to better understand fundamental cell processes in healthy and diseased cells and enable scientists to study these cells in more complex and physiologically relevant surroundings (i.e. organ on a chip (*126–128*) or disease models (*10, 129*)). The knowledge can also be applied in fields like tissue engineering or implant design (*100, 130–133*).

State of the Art

Model Systems – Systematic Variations for Profound Analysis

As described previously, the native cell surrounding is highly complex, with a multitude of different interdependent parameters, and many mechanisms and synergies in influencing cells are not yet fully understood.

Generally, this multitude of signals include both biochemical parameters, like composition of proteins and their cell adhesion ligands, as well as different biophysical cues. The latter ranges from density and affinity of the ligands (*29, 51*), to stiffness of the environment (*46, 50*) as well as other guidance cues such as chemical and physical gradients (*49*) and geometrical patterns (*52–55, 134*).

To systematically unravel these interdependencies and elucidate possible mechanisms, model systems have been developed. These platforms decrease the complexity of the cell surrounding while allowing a systematic variation of different parameter, including surface coating and roughness as well as topographical dimensions, to investigate their influence on cell behavior and function and hence to clarify possible synergies in order to gain an understanding of fundamental mechanisms.

When it comes to investigating the influence of geometrical parameters on cell behavior and function, there are different approaches. One way of differentiating these approaches is regarding the dimensionality of the geometrical cues: The probably most deployed approach uses two-dimensional (2-D), chemical surface patterns, with cell adhesive geometrical features (*98, 135*). Another approach applies three-dimensional topographical surface patterns, creating a pseudo-3-D or 2.5-D surrounding for the cells. (*52, 136–139*). Moreover, there are efforts to combine the two types of cues, like most recently by van der Putten et al. (*134*),

generating a platform with multidimensional cues: curved, uniaxial topographical cues which were selectively patterned with ECM proteins using UV photopatterning.

Li and Kilian (*140*) give a comprehensive overview of different systems used in research, ranging from 2-D patterned surfaces and 2.5-D environments to 3-D hydrogels, while the following sections only aim to give a short overview.

2-D Patterned Surfaces

Using methods like microcontact printing and atomic force dip pen lithography for localized deposition of different proteins or using self-assembling monolayers (SAM), the spacial distribution as well as biochemical composition of the 2-D surface patterns can be regulated precisely. The resulting patterns can be used to study the relationships between cell shape and intercellular function, including cytoskeletal organization (*98, 135, 141*) as well as proliferation or differentiation (*95, 98, 128*) on a single cell as well as a multicellular basis, depending on the dimensions of the pattern. Moreover, it is also possible to unravel the interaction and interdependency of different environmental cues, such as adhesion geometry and substrate stiffness, by combining hydrogel systems with defined viscoelastic properties and micropatterning.

Lee et al. (*142, 143*), for instance, could show, that both, cell shape and matrix stiffness, influence differentiation of mesenchymal stem cells and maintenance of multipotency by influencing actomyosin contractility on a single cellular level and that there is a synergy between cell pattern induced shape and substratum stiffness.

Cultivating multiple cells on one micropattern (*143*), however, they could also show the influence of cell density as well as position in a cell layer to have influence on multipotency and differentiation.

Nevertheless, in these 2-D approaches the cell microenvironments is highly artificial, which is not only due to the common use of man-made patterns such as rectangles, stars and others for restricting cell spreading, but also on account of the planarity, inducing an apical-basal polarity in the cells, caused by the missing third dimension. The transfer of the results to in vivo situations is, therefore, not always feasible.

2.5-D Environments

Some limitations of 2-D surface patterns, can be overcome by adding a third dimension to the substrate surface, creating pseudo-3-D or 2.5-D environment, which is more realistic in mimicking the natural cell environment, by maintaining a simpler way of monitoring and cultivation of cells compared to 3-D culture.

Regarding 2.5-D approaches, however, a distinction between different types of topographies is still necessary. While first studies describing the phenomenon of contact guidance were

using glass cylinders (*53, 101, 102*), the interest in linking the observed cell behavior to the substrate shape, and other specific surface parameter, lead to the use of highly defined, micro-fabricated, sharp-edged topographies. This shift in used topographies was further enabled by the development of microfabrication techniques in the late 20th century as also described by Dunn (*103*). Microfabrication allows the fabrication of topographies with defined sizes, such as nano- and micrometer grooves and ridges (*104, 105*). Investigations have shown that contact guidance cell response to ridges and grooves in nano- to micrometer scale is strongly dependent on feature size parameters including distance, pitch and depth. (*52*)
Certainly, these sharp-edged topographies are also highly artificial and do not reflect the native biological situation. More recently, however, increasing numbers of studies were published investigating cell responses to all kinds of 2.5-D curved surfaces, displaying more in vivo-like surface parameters compared to the sharp-edged ones. Although there is a multitude of different curved model surfaces, an attempt to give an overview is made in the following section.

Generally, 2.5-D substrates with curved topographies can be divided based on the axiality of their curvature, resulting gaussian curvature as well as cross-section of the topography. Among the simplest surface features are certainly uniaxial curvatures ranging from being a horizontal (circular) cylinder (*54, 119, 121*), to an horizontal, elliptic cylinder or cylindroid (*123, 136*), followed by sinusoidal wavy topographies (*144–146*) and anything in between cylindroidal and sinusoidal topographies (*147*), to undefined wavy surface structures (*148*), like illustrated in Figure 5.

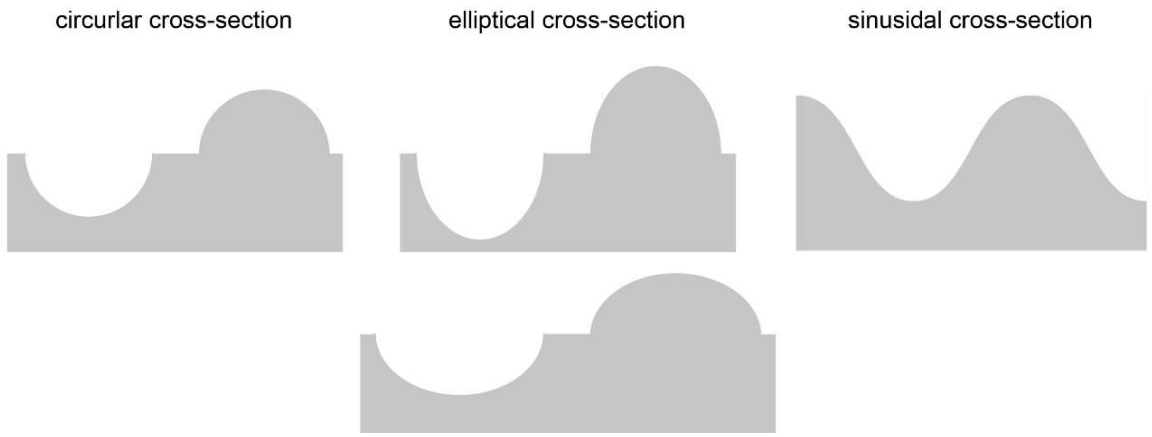

Figure 5 **Different types of cross-sections in uniaxial model systems with 2.5-D curved features.** The least complex surface feature is the topography with a circular cross-section, as its curvature κ is constant over the whole topography, followed by topographies with an elliptical cross-section. For elliptical cross sections, depending on the orientation of the ellipse different resulting curvature presentations for the same base structure are possible. In both cases, circular cross section and elliptical

cross section, the resulting topography is usually only concave or convex, while for sinusoidal cross-sectioned topographies there is a direct transition between convex and concave areas.

Due to their uniaxiality (one surface vector is zero), these surface topographies all have a gaussian curvature of zero. When the second surface vector, which is zero for uniaxial curvatures, increases or decreases, the gaussian curvature also either increases (curvature>0), when both principal curvatures have the same sign (positive gaussian curvature) or decreases (curvature<0) when the principal curvature of both surface vectors is different (negative gaussian curvature). These possibilities are leading to elliptic (both convex) and hyperbolic surfaces (one convex and one concave).
The simples elliptic surface features are (partial) spheres (*97, 122, 149–151*), followed by the other curved features of the CurvChip (*2*), with square and rectangular basic shapes (cf. Figure 13 B, p. 58). Whereas hyperbolic surface features cannot exist alone resulting in surfaces with both feature types in proximity. Examples are the “hills-and-valleys landscape” used by Pieuchot et al. (*120*), which has sinusoidal curvature progression for both surface vectors, the “sphere-with-skirt” surface features deployed by Bade et al. (*152*) and the different topographies mimicking the epidermal-dermal interface by Viswanathan et al. (*127*).

All of the above-mentioned surfaces have advantages/disadvantages when it comes to using them as model systems for studying cell responses: While some of the surfaces features are more artificial than others, the more artificial model surfaces, like deployed in the CurvChip, (cf. chapter IV The CurvChip – A Model System) might enable a more direct correlation of a certain observation to specific surface parameters than compared with more realistic/ in vivo-like surfaces and vice versa. For instance, on cylindrical surfaces, the cell perceived curvature, can be calculated for every position of the cell on the cylinder, when knowing the angle of orientation of the cell and the radius of the cylinder (cf. Calculation of the Cell and Nucleus Perceived Curvature of Cells on Cylindrical Topographies, p. 55). Allowing cell studies to directly correlate the perceived curvature with the cell function/behavior or change thereof, which is much more difficult for sinusoidal surface topographies or cylindroids.
Generally, some of the advantages/disadvantages clearly relate to the specific scientific question in focus, while there are others more related to technical challenges, including the fabrication of the model systems as well as cell related issues including cultivation and monitoring/imaging of the cells.
Moreover, the scientific world challenges model systems and related findings to be updated continuously by further increasing complexity and allowing a step-by-step investigation of the updates on cell behavior and function and hence to clarify possible synergies in order to gain and improve the understanding of fundamental mechanisms.

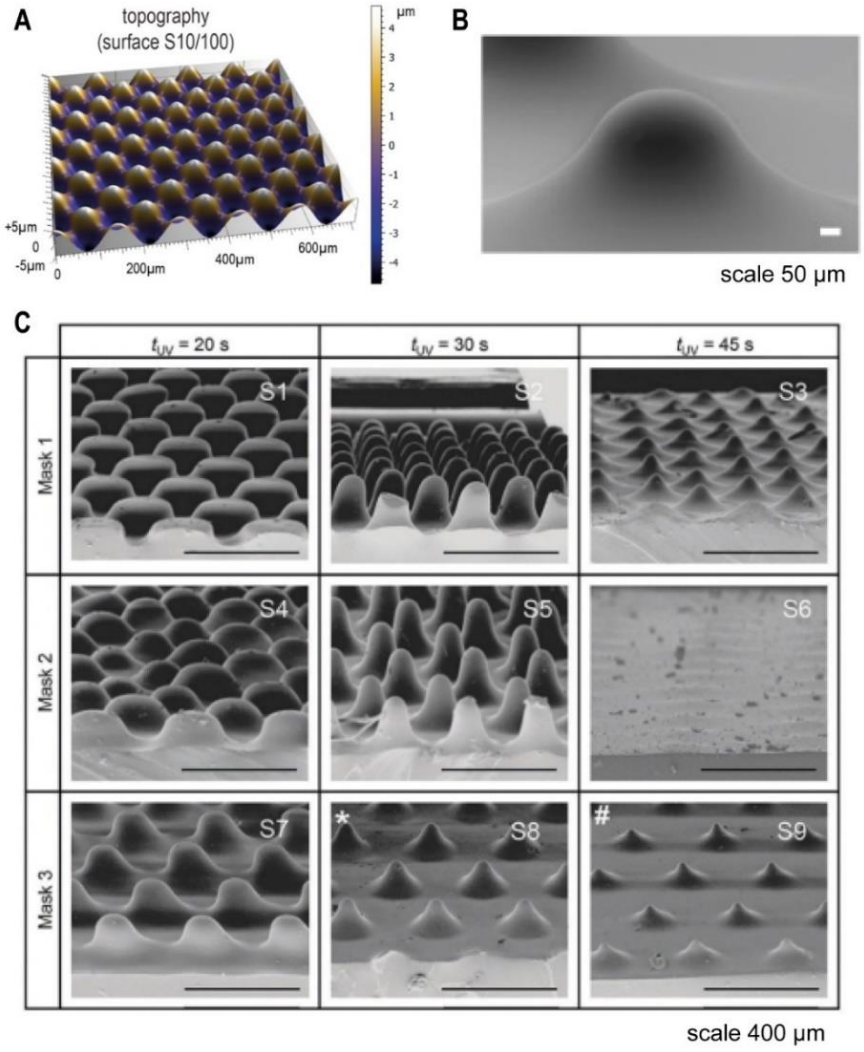

Figure 6 **Exemplary images of topographies with both hyperbolic and elliptic elements**. ***A*** Scheme of "hills-and valleys landscape" used by Pieuchot et al. (*120*)[6], ***B*** SEM image of "sphere-with-skirt" surface features deployed by Bade et al. (*152*)[7] and ***C*** SEM images of the different topographies mimicking the epidermal-dermal interface by Viswanathan et al. (*127*)[8].

Cell Studies Curvature

Like described in the previous section, recent studies investigated cell responses to all kinds of 2.5-D, curved surfaces, reaching from spherically curved (*97, 122, 151, 153*), and cylindrical curvatures with circular cross-section (*54, 119, 121, 154*), and cylindrical curvatures with

[6] Image copied from Pieuchot et al. (*120*) supplementary figure 1 and used under a Creative Commons Attribution 4.0 International license (https://creativecommons.org/licenses/by/4.0/)
[7] This image reprinted under permission of Elsevier. It was originally published in Biophysical Journal, Volume 114, Issue 6, Bade, Nathan D.; Xu, Tina; Kamien, Randall D.; Assoian, Richard K.; Stebe, Kathleen J., *Gaussian Curvature Directs Stress Fiber Orientation and Cell Migration*, 1467-1476, Copyright Biophysical Society (2018)
[8] Image copied from Viswanathan et al. (*127*) figure 2 B and used under a Creative Commons Attribution 3.0 Unported license (https://creativecommons.org/licenses/by/3.0/)

elliptical cross-section (*123*) to Gaussian curvatures (*121, 152*) and sinusoidal curvatures in one and multiple axes (*120, 146, 155*). They show that multiple cell functions, like morphology and cytoskeletal organization, as well as migratory behavior and even stem cell differentiation are affected by variations in cell scale curvature. (*156*)

Effect of Substrate Curvature on Differentiation and Gene Expression

The investigation of cell differentiation and respectively dedifferentiation is an important field of research, as understanding is decisive for the field of tissue engineering and regenerative medicine (*157*).

Both biochemical as well as biophysical cues are known to influence (stem) cell differentiation, most well-known of these are probably growth factors, like TGF-β (*158*), as well as surface stiffness (*46*), respectively. But also geometrical cues influence the gene expression of cells, including 2-D surface patterns (*95, 96, 159*), edged nano- and micro-topographies (*160, 161*) as well as different kinds of 2.5-D curved surface topographies (*97, 120, 122, 123, 150*).

Using their sinusoidal “hills-and-valleys landscape”, Pieuchot et al. (*120*), for instance, showed that a total of 637 genes were differently regulated in cells cultivated on the topographies compared to the transcriptome of cells on flat control surfaces. Of these genes, 361 were described to be “characterized with biologically described functions, including 181 highly expressed genes”, underlining the possible impact of curvature on the gene expression and function of cells.

Other studies showed that, using “more native-like” cell environments, in terms of geometry, can also help maintaining the phenotype and viability of cells whose culture capacity is limited using conventional cell culture conditions. Two examples for this positive effect of a “more native-like” geometrical cell environment were described by Poon et al. (*150*) and Gouveia et al. (*153*). Poon et al. (*150*) used primary alveolar epithelial cells and “substrates containing hemispherical cavities mimicking the architecture and size of mouse and human alveoli” and Gouveia et al. (*153*) were cultivating human corneal epithelial cells on convexly curved substrates showing they support “growth, stratification, and differentiation […] in vitro, while maintaining their structural integrity and shape without any supporting carriers, scaffolds or crosslinking agents”. Moreover, López-Fagundo et al. (*162*) used a biomimetic, synthetic feeder layer, “presenting the stiffness and topography of live MEFs” (mouse embryonic fibroblasts) to allow the cultivation of embryonic stem cells (ESCs) without losing their pluripotency and ability to self-renewal comparable to the cultivation on MEFs but without the need of a “co-culture of live xenogenic feeder cells”.

Moreover, Cannon and Gouveia (*154*) showed that milliscale, concave substrate curvature leads to “myoblast alignment over large-scale areas” and “also promote cell differentiation and

formation of denser, more compact tissues comprising highly oriented multinucleated myotubes", further stressing the importance of larger-scale curvatures for tissue organization.

Besides, cultivation of human mesenchymal stem cells on (convex) spherical topographies in a curvature κ range of 1/2000 µm to 1/125 µm, showed that curvature alone has an influence on stem cell differentiation even in the absence of soluble differentiation factors (*97, 122*). Interestingly, substrates with curvatures κ from 1/2000 µm to 1/250 µm seem to induce adipogenic differentiation (*122*), while κ from 1/750 µm to 1/125 µm (*97*) seem to induce osteogenic differentiation. However, an influence of the cell origin (adipose derived vs. bone marrow derived stem cells) on differentiation outcome, as indicated in literature (*163*), cannot be fully excluded, as in the study investigating adipogenic differentiation adipose derived mesenchymal stem cells were used (*122*), while the study looking for osteogenic differentiation used bone marrow derived mesenchymal stem cells (*97*).

Still, the findings of Lee et al. (*122*) and Werner et al. (*97*) are in line with the previously described (*159*) phenomenon that nuclear morphology affects gene expression. Especially since Werner et al. (*97*) did not only investigate convex, spherical topographies, they also included their concave equivalences, showing no (significant) increase in osteogenic differentiation compared to the flat control surface. Furthermore, by investigation of the f-actin expression, and nuclear morphology, they showed that on convex surface topographies the nuclei were flattened and stretched over the surface and individual fibers of the perinuclear actin cap even caused indention of the nuclear membrane, while nuclei of cells on flat surfaces were flattened but showed no indentions. Moreover, nuclei of cells growing in concave structures showed no pronounced deformation resulting in almost elliptical nuclei.

Lin et al. (*123*) investigated (adipose derived) stem cell migration and osteogenic differentiation on uniaxial, "elliptical supra-cellular topographies" (cf. Figure 5 "elliptical cross section"), where the cells have more freedom to avoid curvature compared to spherical curvatures. They observed a significant increase in osteogenic differentiation (i.e. osteocalcin expression) on all types of cylindroids compared to the flat control surface, even in the absence of soluble differentiation factors in the medium. The highest osteocalcin expression, in the absence of soluble differentiation factors, was observed for the cylindroid with the medium aspect ratio (AR; equaling the medium apex-curvature) followed by the cylindroid with low and then high AR (low apex-curvature and high apex-curvature respectively). This finding, however, did not correlate with the differences observed for the nucleus shape of cells cultivated on curvatures and flat surfaces. However, differences could be observed depending on where the cell was located on the cylindroids i.e., for cells growing on the high curvature apex compared to the mid basal regions with lower curvatures. These differences include a higher f-actin expression

and collagen I expression for cells in high curved regions, both of which are related to osteogenic differentiation (*95*).

Although the deployed topographies might be more “physiological relevant”, the curvature varies on the structures which makes it difficult to directly correlate the observed local cellular responses to the surface curvature, and even more difficult to correlate it to the curvature the cell perceives. This highlights one of the disadvantages of this more complex curvatures compared to the cylindrical topographies like they are deployed in the CurvChip, for instance, and further stresses the importance of systematic studies and platforms enabling these studies.

Curvature Detection: Orientation, Positioning and Migration on Substrates with Curvature

Cells adhering on surfaces with uniaxial curvatures as well as surfaces with more complex topographies, having hyperbolic and elliptic surface features (cf. 2.5-D Environments, p. 19), the cell perceived curvature depends on the position and orientation on the substrate, as they can reorient to a position with lower surface curvature.

Automated Controller

As mentioned previously, cell-responses like reorientation or directional movement are affected by various factors, for migration the responses to different factors are known as chemotaxis, haptotaxis, durotaxis, contact guidance, galvanotaxis, etc.; (cf. Biophysical Factors, p. 6). To be able to respond in such a directed way, cells need to perceive the direction of the guiding signal, respond to it, and be able to control their behavior by means of a feedback loop; a regulation mechanism that was previously described as an automatic controller, by Kemkemer et al. (*106*).

On a macroscopic level the main features of an automatic controller are firstly an element that is able to measure the cellular current status (here: angle of orientation Ψ), compare it with the setpoint (Ψ_0) (at the summation point Σ) resulting in an angle- and field-dependent (unknown) function g(Ψ, signal). The second element is some kind of reaction unit with a motor, enabling the response (with a strength k_2), while the third part is some kind of feedback loop, feeding back the output ($\Psi(t)$) into the input in a way that allows the minimization of the deviation of the output from the desired level (setpoint).

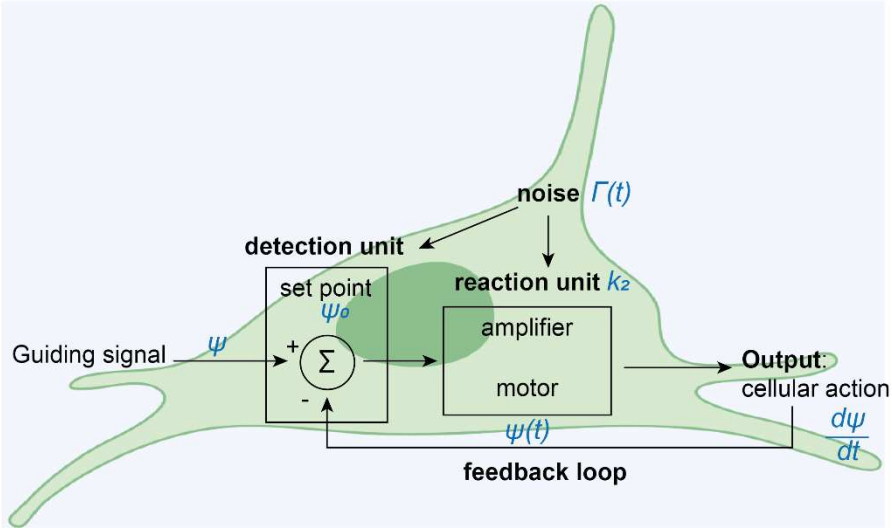

Figure 7 **Schematic representation of an automatic controller, with a predicted machine equation described in Equation 1.** The main features are first the detection unit, which is responsible for measuring the current state of the cell and comparing it with setpoint, secondly the reaction unit with a motor that enables the cell response or output and thirdly some kind of feedback loop feeding back the output to the detection unit allowing a to minimalize the deviation between the output and the setpoint. Adapted from (*106, 164*) and created in BioRender.com.

Together this results in the following predicted machine equation for one cell:

$$\frac{d\Psi}{dt} = -k_2 \times g(\Psi, \text{signal}) + \Gamma(t) \qquad \textbf{Equation 1}$$

(Predicted) machine equation for one cell, describing the cellular response to an eternal guiding signal with -k2×g(Ψ,signal) describing the extracellular guiding signal and Γ(t) the stochastic signal or "noise".

This stochastic differential equation comprises the deterministic signal, describing the cellular response to an extracellular guiding signal ($-k_2 \times g(\Psi,\text{signal})$) and the stochastic signal Γ(t), which has to be introduced since random orientation is observed in case of no guidance signal (e.g. flat surface). This stochastic "noise" is described by Kemkemer et al (*165*) as "an unavoidable component of real-world systems" originating from external factors as well as intrinsic properties of the controller components. And albeit engineers try to avoid noise in their technical signal transductions, in biological systems Kemkemer et al. (*165*) describe that this noise might also impose an advantage as it is able to optimize the function of the system, as described for the search mode of white blood cells.

Migration and (Re-) Orientation

On a phenomenological basis, an increasing number of researchers investigated the cellular response to different curved surface topographies, including undefined wavy surface structures (*148*), sinusoidal wavy topographies (*144–146*) and horizontal (circular) cylinders

(*54, 119, 121, 154*), horizontal, elliptic cylinders or cylindroids (*123, 136*) as well as spherical topographies (*97, 122, 149–151*) and more complex topographies (*120, 127, 152*).
In 1976, Dunn and Heath (*166*), were the first to observe that fibroblasts align in the direction of minimal curvature, when cultivated on curved glass fibers with a radius up to 100 µm, and that the orientation response is lost for smaller curvatures. Subsequent studies (*167–169*) in the late 1990s describe a difference in cell orientation of epitheliocytes compared to cells with an elongated morphology and more pronounced stress fibers.

More recent studies investigated the response of mesenchymal cells when exposed to conflicting guidance cues like mesoscale, cylindrical substrate curvature in the one direction and nanoscale contact guidance cues in form of directed collagen fibrils (*54*) or micropatterns (*134*) perpendicular to the curvature guidance. They found that on small convex surface curvatures ($\kappa \leq 1/1000\ \mu m^{-1}$; large cylinder radius) cells follow the chemical contact and/or nanoscale guidance, while for larger curvatures the curvature guidance becomes predominant, overruling the other contact guidance cues. For concave cylindrical topographies, however, the contact guidance cues overrule the curvature guidance cues for mesenchymal cells, indicating that cells are not only able to sense the degree of curvature but also distinguish between its sign.
This is in line with the observed differences in cell morphology and migration modes of mesenchymal stem cells on concave and convex topographies, described by Werner et al. on spherical (*97*) and cylindrical surfaces (*121*). On convex surfaces, the cell body has full contact to the surface, and the migration mode is described as “snail-like” with the speed and persistence being determined by the cell's perceived curvature (orientation on cylindrical surfaces). On convex spherical surfaces the nucleus was deformed and even indented by the actin fibers of the perinuclear cap. In contrast, on concave surfaces cells are observed to stretch upward lifting the nucleus, resulting in a “spider-like morphology” and an almost elliptical nucleus. Cell migration is described as fast, but non-aligned and non-persistent. When given the choice between bending over a convex curvature and lifting up (*121*), the same cells (mesenchymal stem cells) are described to tend to migrate in the direction where convex curvature can be avoided most efficiently.
Using their “hills-and-valleys landscape”, a sinusoidal surface, that presents modulations of cell-scale curvature in all directions, Pieuchot et al. (*120*) also showed that adherent cells tend to avoid convex regions of the substrate during migration and prefer to position themselves in concave valleys. The only exception was observed for epithelial cells growing in the center of large colonies.
All together these observations show that cells can sense not only the degree of curvature of the 2.5-D growth substrate, but also its sign. Moreover, it shows, that all adherent cells respond

to curvature as an external guidance cue and adapt their (re-) orientation and migration according to their perceived curvature.

Mechanism of Curvature Detection

As described in the previous paragraph, there is increasing evidence that cells can perceive and respond to curvature cues of their surroundings in various size scales. However, the mechanism of curvature detection remains elusive, not only since the whole scope of what is affected by substrate curvature is not yet fully understood. For instance, Li et al. (*170*) found that surface roughness in the size scale of single cells can increase high-affinity β1 integrin level of human ASCs (adipose-derived mesenchymal stem cells) without alteration the total β1 integrin level suggesting a curvature induced conformational change of integrins.

When Dunn and Heath (*166*) first observed the alignment of fibroblasts in the direction of minimal curvature, they proposed an involvement of actomyosin stress fibers in curvature detection and put forward the theory that the stress fibers cannot work in a bent state, which would limit their traction to the substrates and, therefore, influences the orientation behavior.

In 2009, Biton and Safran (*171*) addressed this observation and theory by Dunn and Heath, together with the in different publications described difference in cell orientation of epitheliocytes compared to cells with an elongated morphology and more pronounced stress fibers (*167*–*169*), in a theoretical model and presented a possible mechanism responsible for the observed cell behavior. They propose that cell orientation could be dependent on competition between stress fiber bending and deformation energy of the cell with the purpose of reducing the all-over elastic energy. The model predicts that cells, possessing less pronounced stress fiber network/higher cell rigidity, like epithelial cells would not avoid bending, while cells with more pronounced stress fibers, like fibroblasts would avoid bending over convex cylindrical curvatures, even for decreasing curvatures.

More recently, Bade et al. (*119*), “found that two distinct types of actin stress fibers respond differently to the convex curvature: the population below nucleus were shorter and aligned in the circumferential direction while the apical stress fibers, forming the nuclear actin cap, were longer and aligned along the cylinder axis.”[9] Upon regulation of cell contractility, using Rho activation, “they could observe the disassembly of apical stress fibers, and the thickening and stronger alignment in the circumferential direction of basal stress fibers. They speculate [, regarding the theory of Biton and Safran (*171*),] that the activation of Rho leads to a contractility-dominated response that overrides the bending-controlled response.

Another recent study from Werner et al. (*54*), suggests a mechanism based on their observations, of increased levels of energy demanding myosin light chain (MLC)

[9]Exact quote from Frey et al. (*1*)

phosphorylation in cells that cannot avoid bending (spherical substrates). They claim that it [might be] […] energetically more favorable for the cell to orient along minimal curvature since otherwise an energy demanding compensation mechanism (MLC phosphorylation) might be needed to maintain a stable and contractile cytoskeleton."[10]

Furthermore, the findings of Pieuchot et al. (*120*) in their study on curvotaxis suggest, "that the nucleus stiffness and its connection to the cytoskeleton is an additional important factor for cellular response to curvature besides the stress fiber system"[10], while they could not find an involvement of the microtubule network. They propose that the nucleus might be acting as a mechanical sensor leading the migrating cells toward concave curvature of the substratum, resulting in nuclear relaxation (and changes in gene expression). This proposed involvement of the nucleus is also supported by the previously published findings of Werner et al. (*97*), describing that the nucleus of cells on convex spherical surfaces is deformed and indented by the actin fibers of the perinuclear cap, which then potentially triggers a remodeling of the chromatin in the nucleus and the whole nucleus structure (*78*). This restructuring seems to be somehow unfavorable for the cell leading to the reorientation/migratory response.

All in all, there are several theories on what cell organelles are involved in the curvature perception of such mesoscale curvatures, but systematic studies are rare. Only a few studies, including Pieuchot et al. (*120*) systematically manipulated functional cell structures and observed the effect they have on their read-out (nucleus positioning).

In this work, therefore, pharmacological manipulation was utilized to manipulate different parts of the cell cytoskeleton, including acto-myosin and the microtubule network, additionally the substrate curvatures were varied, both aiming to systematically investigate the response of mesenchymal cells on the curvature perception of uniaxial curvatures.

Pharmacological Manipulation

To systematically investigate the involvement of structural molecules or pathways cell behavior and function different routes are deployed in cell biological research.

One possibility is genetical modification of the cells with various possible effects, including the expression of modified molecules or increased or decreased molecule expression. However, genetic modification using different transfection methods is highly complex (equipment, knowledge, safety precautions), time consuming (no one-fits-all solution) and not practicable for all cell types. Commonly used methods are often for instance not effective in primary cells and if transfection is possible the transfection efficiencies are relatively low (< 50%) and often cell viability is affected. (*172, 173*) Which altogether limits the cell types that can be investigated.

[10] Exact quote from Frey et al. (*1*).

Another, well established possibility is the use of small pharmacologically active molecules that have a special function, like activating or inhibiting pathways or stabilizing or destabilizing cellular structures. One of the probably best-known molecules is colchicine, the toxin of autumn crocus, known for its effect on microtubule resulting in cell cycle arrest. Colchicine binds to tubulin and inhibits its polymerization. Dhaliwas (*174*) gives a comprehensive overview of pharmacological activators and inhibitors used in research.
One objective of the present work was to conduct systematic cell studies to investigate the involvement of the actomyosin stress fibers as well as microtubule network on uniaxial curvature perception of mesenchymal cells. To pharmacologically manipulate the cytoskeletal components of interest four different small molecules were deployed: Blebbistatin and Rho Activator II (CN03) for interfering with the actomyosin contractility and Nocodazole and Paclitaxel (Taxol) for the microtubule network.

Blebbistatin is a myosin II inhibitor, binding to the myosin motor domain and thus hindering the interaction with actin, resulting in reduced cell contractility (*175*). Blebbistatin "blocks myosin II activity in an actin-detached state, thus preventing artifacts from the formation of strongly bound nonfunctional actomyosin complexes" (*176*). Moreover, Blebbistatin is known for its high specificity and rapid cell permeability, while the major limitation is presented by its light sensitivity and low solubility in aqueous solutions. (*176*) Together, these factors made Blebbistatin a "standard research tool for assessing the role of tension generation and other cytoskeletal activities in practically a biological process" (*175*) and numerous medical indications as described by Rauscher et al. (*175*). Studies using Blebbistatin to disrupt actomyosin contractility also stressed the interdependency of the different cytoskeletal components of cells (e.g. intermediate filaments and acto-myosin network (*177, 178*)).

CN03 or Rho Activator II by Cytoskeleton, Inc. (*179*) activates RhoA by selectively converting (deamination) glutamine-63 in the switch region of RhoGTPases, to glutamate, which blocks GAP-stimulated deactivation of RhoA. Subsequently, this blocked deactivation leads to reorganization of the actin-myosin network by increasing both the cytoskeletal contractility via the RhoA/ROCK pathway, as well as actin polymerization via RhoA/mDia (cf. RhoA Pathways, p. 15) (*115*). The action of CN03 is highly targeted, which makes it superior to other, indirect activators (e.g. LPA (Lysophosphatic acid)) concomitantly activate other signaling pathways (e.g. RAS, PI3K and PLC) (*179*)

Nocodazole inhibits microtubule dynamics and promotes tubulin depolymerization by binding to β-tubulin. (*174*) However, when depolymerizing the microtubule network, microtubule-bound GEF-H1 is released and activated, which subsequently activates the RhoGTPase RhoA (*117, 180, 181*) ultimately causing a simultaneous increase of cell contractility. This GEF-H1 realease couples the dynamics of the microtubule to Rho GTPase activation in both, normal

cell functions, as well as pathophysiological situations (*108*) like described previously (cf. Interaction with Other Cellular Structures and Functions, p. 16) and, therefore, it further stresses the interdependency of the different cytoskeletal components.

Paclitaxel, also known as Taxol, is a pharmacological active substance also used in chemotherapeutic agent in cancer therapy e.g. of ovarian, breast and lung cancer (on-label, US-FDA approved) (*182*). It stabilizes microtubules by binding to the N-terminus of β-tubulin on the internal surface of the microtubule inhibiting tubulin disassembly (*183*) and thus arrests the cells in mitosis via spindle-assembly checkpoint (*182*). As for the other small molecules paclitaxel-treatment also affects other cytoskeletal components: The previously described change in microtubule dynamics, therefore, is described to be accompanied by the formation of large central bundles of microtubules and intermediate filaments ("excluded from cell margins") (*184*) as well as the redistribution of f-actin forming circumferential bundles (*185, 186*).

As mentioned previously, the only study that systematically manipulated functional cell structures and observing the effect they have on their read-out (nucleus positioning) was conducted by Pieuchot et al. (*120*). They used a combination of small pharmacologically active molecules, siRNA as well as gene transfection summarized in Table 1.

Table 1 **Pharmacological Manipulation of Cellular Structures and their influence on curvotaxis.** Summarized from Pieuchot et al (*120*).

Manipulation	**Target**	**Effect on curvotaxis**
Cytochalasin D	f-actin (depolymerization)	Strong effect leading to homogenous cell distribution
Blebbistatin	Myosin II (blocking)	Strong effect leading to homogenous cell distribution
CK-666	Arp2/3 inhibition (actin nucleator involved in lamellipodia formation and haptotaxis, amongst others)	Strong effect leading to homogenous cell distribution
ML-141	Cd42 inhibition (actin polymerization regulation)	Strong effect leading to homogenous cell distribution
Nocodazole	Microtubule depolymerization	Slight increase in response
Taxol	Microtubule stabilization	No effect
siRNA	RhoA silencing	No strong impact (possibly due to incomplete extinction at protein level or redundancy with other Rho isoforms)
Rho inhibitor I	RhoGTPases inhibition	Strong effect leading to homogenous cell distribution
siRNA	Lamin A silencing	Significantly affects cells' ability to respond to curvature (data suggest that high lamin A levels are required for curvature induced nuclear movements and thus cell migration during curvotaxis.)
DN-KASH	LINC (dominant-negative Kash overexpression)	overexpression of DN-KASH strongly affects the cell response to curvature (homogenous cell distribution), the cells with highest expression presenting the strongest phenotype
siRNA	SUN1 silencing	strongly affects the cell response to curvature (homogenous cell distribution)

III. Experimental Part

The CurvChip – Fabrication and Characterization of a Model System

Theoretical Background to Photolithography and Use of a Low-cost Variation

Master structures of the CurvChip were generated using low-cost photolithography with thermal photoresist reflow using an in-house build, bench top flow hood, and solid-state photolithography tool, as described in Figure 8 A and our publications (Frey et al. (*2*) and Naggay and Frey et al. (*3*)).

In general, photolithography is a widely used tool for the generation of three-dimensional microstructures for different applications: A silicon wafer is coated with a photosensitive material, the photoresist, which is selectively exposed to light to generate the structures. This spatially distinct illumination is achieved by using a photomask, with opaque and transparent areas, that is positioned in the light path. Depending on the photoresist used, the exposed areas become more soluble (positive photoresist) or less soluble (negative photoresist, cross-linked by UV light). Subsequently, in both cases the more soluble areas can then be removed using a chemical called developer, the composition of which varies between different photoresists.

The major difference of the here used low-cost approach compared to conventional photolithography is the absence of a clean room and mask aligner. Cleanliness is of high importance for the outcome of the photolithography procedure. It does not only affect the uniformity of the photoresist layer during and after coating, but dust particles can also affect the illumination procedure by adding additional opaque areas (dust shadows) or increasing scattering and diffraction.

Instead of a clean room, a laminar flow bench is used to ensure a clean environment during all critical steps, including spin coating, baking, and exposure. Additionally, silicon wafers were cleaned prior to entering the laminar flow bench, and after removing the edge bead using a mild nitrogen-gas flow, and if necessary, a soft brush, to assure the absence of dust. The photomasks were freed from dust using a N_2-flow, or in case of chromium masks and more persistent contamination using acetone and isopropanol and clean room wipes without adding pressure to the mask.

These precautions are sufficient for generating topographies at the size of tens of micrometers to the mesoscale, as presented in this work, especially if applying the reflow procedure, which is able to eliminate small defects.

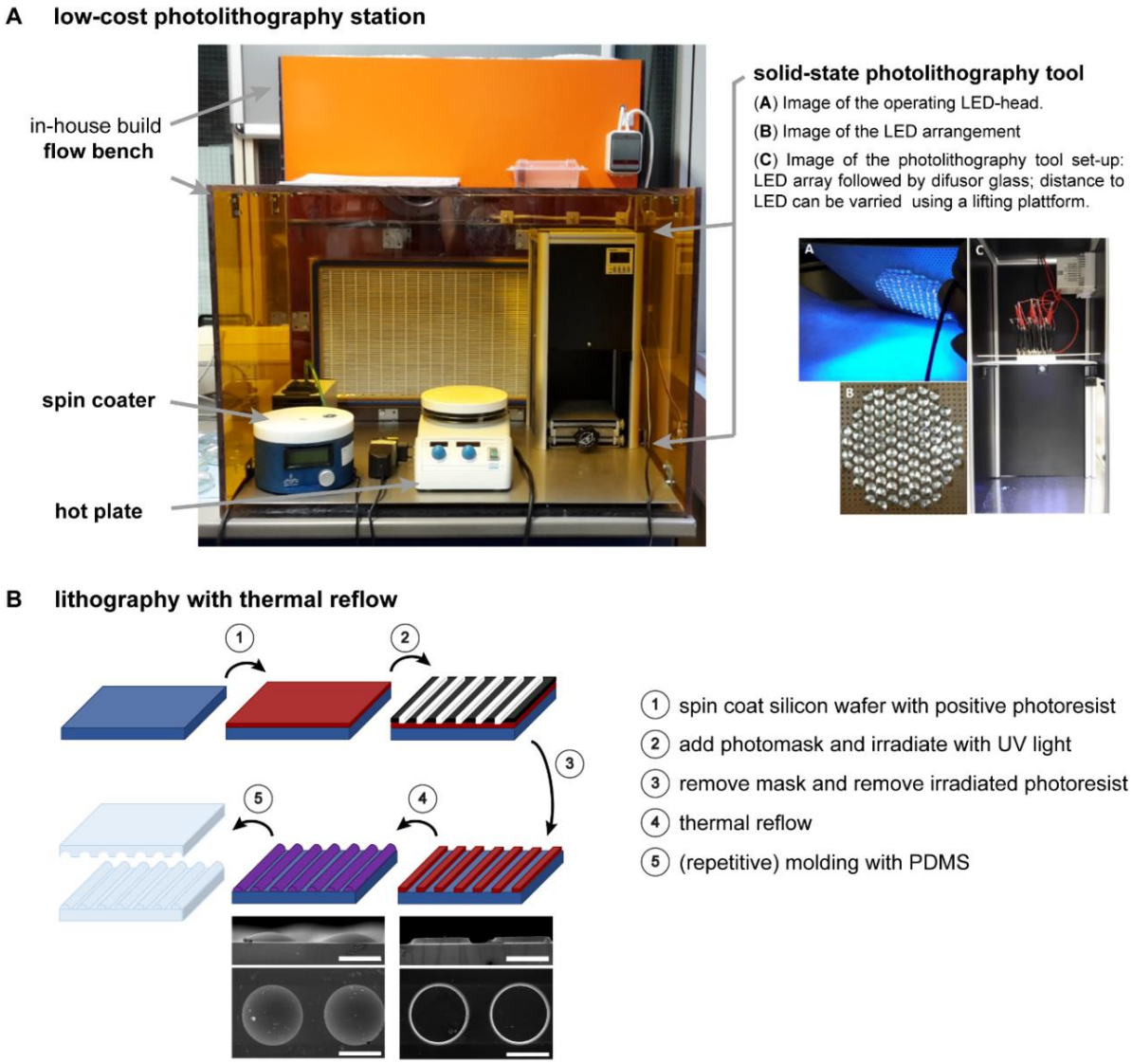

Figure 8 **Low-cost photolithography for generation of the CurvChip.** ***A*** In-house build low-cost, photolithography station, with bench-top laminar flow hood, spin coater, hot plate and LED photolithography system (images ***(B)***, and ***(C)*** adapted from Naggay and Frey et al. (*3*)). ***B*** Scheme of most crucial steps of photolithography with thermal reflow, including exemplary SEM images of circular structures before and after reflow, scale bar 100 µm. Adapted from Frey et al. (*2*)

The centerpiece of photolithography, however, is the mask aligner. Amongst others, it enables high accuracy alignment of the photomask for instance with positional marks of previously utilized masks, and precise adjustment of exposure parameters. The possible adaptions concerning the exposure range from modes to control the gap between mask and wafer, e.g. by vacuum or positive pressure or a combination (contact or proximity mode), to different exposure optics used to adjust various parameter of the exposure light for divers' applications. Using the low-cost lithography tool as presented in our previous publication (*3*) and shown in Figure 8 A, there is no possibility for mask alignment and only soft contact mode, where the mask is simply placed onto the wafer is possible. Furthermore, there is no sophisticated optical

pathway: To generate a more homogeneous illumination, the light emitted by the LEDs is scattered using a diffusor glass and then directly used for exposure. The intensity of the incident light and the exposure dosage can be varied by adjusting the working distance and/or the exposure time utilizing the integrated timer circuit.

Generally, the resolution of photolithographic procedures using contact or proximity modes, like presented here, is affected by different parameters, as shown in Equation 2 (*187* (p. 81)). The most important determinants however are, firstly, the distance between the mask and the resist. In contact mode the gap is approaching zero, in proximity mode there is a small gap between the mask and the resist surface, which induces diffraction and, therefore, reduces the resolution. To minimize the gap size in low-cost photolithography general cleanliness is important, as dust particles might increase the gap. Additionally, the edge bead is removed rigorously and in case of foil-photo masks an extra quartz microscopy slide is used to weight down the foil.

$$Resolution = b_{min} \cong \frac{3}{2} \sqrt[2]{\lambda \left(s + \frac{z}{2}\right)} \qquad \textbf{Equation 2}$$

with b_{min}: smallest structure width that can be achieved; λ: wavelength in nm; s: gap between the mask and the resist; z: resist thickness (187 (p. 81))

The second general key parameter is the utilized wavelength λ, which strongly affects the resolution as in every optical procedure. Therefore, photoresists that are sensitive to lower wavelength of the UV-VIS spectrum are used for the generation of smaller structures (e.g. i-mercury-spectral-line 365 nm).

Fabrication of CurvChip using Low-cost Photolithography with Thermal Reflow

The detailed standard operating procedure can be found in Chapter VIII Appendix, Part III: Supplementary Materials, p. 209 and is summarized here and schematically depicted in Figure 8 B.

Clean silicon wafers (Siegert Wafers) are heated to 200 °C for at least 30 minutes to fully passivate their surface and remove adsorbed water from the atmosphere. Immediately afterwards, HMDS (hexamethyldisilazane) is spin coated (Schaefer-Tec, KLM SCC-200) onto the silicon wafer as a coupling agent. The positive photoresist ma-P 1275 HV (micro resist technology) in the desired layer thickness (cf. Chapter VIII Appendix, Part III: Supplementary Materials, p. 209) is applied afterwards, followed by a soft bake step at 120 °C to dry the resist (Laboratory Heating plate, VLP Scientifica, AREX Digital). (*2*)

To generate the microstructure a photomask with the desired opaque/transparent structure needs to be placed on top of the photoresist (contact mode). To minimalize the gap between

the resist and the mask and, therefore, to reduce diffractive effects at the interfaces, the edge bead has to be removed prior to adding the photomask. To do so the wafer with dried photoresist is spun slowly on the spin coater, while the razor blade is brought into contact with the resist to mechanically remove it. The resulting abrasion is removed by means of a fine brush and nitrogen gas/clean pressurized air flow. (*2*)

After placing the photomask on the wafer, they are exposed to UV light at 375 nm using the low-cost photolithography tool with an LED array at maximum working distance (shown in Figure 8 A). For removing the UV-exposed photoresist, the developer ma-D331 (micro resist technology) is used, yielding classical, sharp edged lithographic structures. A post-developmental bake, inducing thermal reflow of the remaining photoresist is then used to generate smoothly curved topographies: The wafer is slowly heated above the melting temperature of the dried photoresist (here 140 °C) to allow thermal reflow. The curved shape is then generated by surface tension of the molten resist. (*2*)

Utilized Photomasks

Masks were designed for use with a positive photoresist, such as the ma-P 1275 HV, displaying the desired structures in opaque regions separated by transparent areas.

To demonstrate the outcome of different mask layouts in the CurvChip publication (*2*), low-cost printed foil-masks (printfactory.de), providing high resolution and high pigmented printing, were used. The mask layout included different opaque structures ranging from circles to squares and rectangles to lines arranged in arrays and further specified in Table 2. These arrays were cut in the size of a microscope slide and placed onto the photoresist, with the printing size facing the resist to minimize potential distance to the photoresist. To ensure a minimal gap between foil and wafer surface and to keep the foil in place a quartz microscopy slide (Aachener Quarz Glas) and two magnets in combination with a magnetic metal plate below the wafer, were used.

Better results, however, were achieved using chromium-masks on quartz glass or sodalime glass (Compugraphics Jena GmbH) having the specifications listed in Table 2. These masks were used for preparing cell culture substrates (except R= 20.9 µm and R= 59.3 µm cylindrical substrates, they were made using foil masks). Arrays with different spacings and structure dimensions were systematically arranged, as further described in Table 2.

Table 2 **Photomask specifications.** Foil-masks were mainly used to demonstrate the outcome of different mask layouts, published in (*2*). Cell culture substrates were made using chromium-masks, except for R= 20.9 µm and R= 59.3 µm cylindrical substrates, which were made using foil-masks.

Foil-Masks	
array specifications	1 cm × 1 cm spacing between opaque structures: 25 µm
circles	**diameter:** 50 µm
square	**length and width:** 50 µm
rectangle	**width:** 50 µm **length:** 100 µm; 200 µm; 400 µm; 800 µm
line	**width:** 50 µm **length:** 10 000 µm
array specifications	1.5 cm × 1 cm spacing between opaque structures: 25 µm
line	**width:** 25 µm to 500 µm in steps of 25 µm **length:** 15 000 µm
Chromium Mask	
technical specifications	
critical dimension tolerance	± 0.5 µm
defects	non-critical
writing grid	≤ 250 nm
array specifications	1 cm × 1 cm
line arrays – uniaxial curvature	
• narrow spacing	**width:** 15 µm; 25 µm; 50 µm; 100 µm to 300 µm in steps of 25 µm **spacing:** 25 µm
• wide spacing	**width:** 15 µm; 25 µm; 50 µm to 400 µm in steps of 50 µm **spacing:** 50 µm; 100 µm; 200 µm; 400 µm
circle arrays – spherical curvature	
• linear circle arrangement	**radii:** 50 µm; 100 µm; 150 µm; 200 µm **spacing:** 100 µm; 150 µm; 300 µm; 400 µm
• hexagonal circle arrangement	**radii:** 50 µm; 100 µm; 150 µm; 200 µm **spacing:** 100 µm; 150 µm; 300 µm; 400 µm

Soft Lithography with Polydimethylsiloxane (PDMS)

To generate versatile substrates with concave surface topographies the master wafer was molded using polydimethylsiloxane (PDMS, Sylgard 184; Dow Corning Inc.) in a curing agent to base ratio of 1:10 at 80 °C for one hour, yielding a PDMS substrate (first molding) with concave replicas of the master's topographies. For convex topographies, the resulting PDMS substrate (fist molding) was detached from the master and stored at 80 °C overnight to fully cure the PDMS and avoid crosslinking with the fresh PDMS used for the second molding step. In the second molding step the first mold is used as a master structure for the repeated PDMS molding. Detaching the two PDMS moldings, one yields, both, convex (second molding) and concave (first molding) PDMS substrates with the desired structure. (*1, 2*)

These PDMS surfaces were either used as cell culture substrates or to transfer the structures to other polymers via hot embossing.

Low-cost Hot Embossing

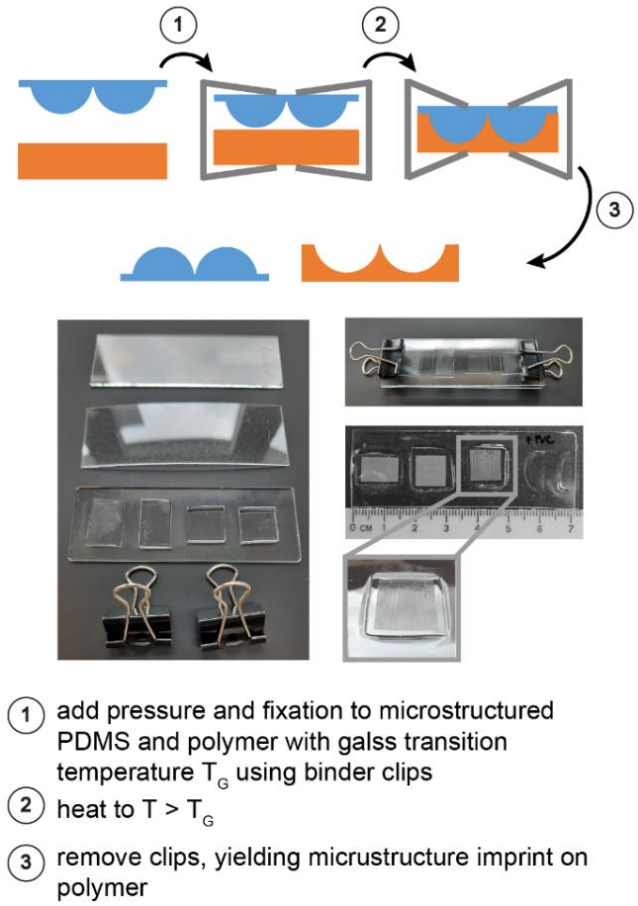

Figure 9 **Scheme of low-cost hot embossing**. Including photos for better visualization. Partially adapted from Frey et al. (*2*)

To transfer the structures in other polymers a variation of the low-cost hot embossing process described by Goral et al. (*188*) was used. The major difference in their and the here presented

approach compared to conventional hot embossing is the use of a standard laboratory oven for heating, PDMS molds as embossing mold and binder clips to generate the required force. In conventional hot embossing mostly metal molds are used, which are not only cost and time expensive to prepare but also limited in their design by the manufacturing processes.

As schematically depicted in Figure 9 and described in our publication (*2*), a polymer microscopy slide (e.g. commercial polyvinylchloride (PVC) microscope slides from Rinzl), self-made polystyrene (PS) slide or thermoplastic polyurethane elastomer (TPU) foil (made by solvent casting from Pellethane® 2363-55D) and the PDMS master-mold(s) of interest were fixed between two glass microscopy slides using ¾ inch binder clips (more or smaller binder clips can be added for increased pressure). This setup was then placed into an oven that was pre-heated to a temperature slightly above the glass transition temperature T_G of the polymer used (here we used 100 °C). Once the polymer reaches its T_G, the pressure of the binder clips is enough to emboss the polymer with the PDMS. (*2*)

Surface Characterization of PDMS Replicas

Both PDMS molded and hot embossed topographies were characterized using scanning electron microscopy (SEM). For determining the radius of curvature, the molded PDMS was cut, in case of linear structures, perpendicularly to the structure axis. Samples were mounted onto 90° specimen holders and sputter coated with gold (Polaron Equipment Limited, SEM coating unit E5100). Subsequently, the samples were imaged at 5 to 10 kV (Zeiss, DSM 962) with 0° and 30° tilting angle. (*1, 2*)

For the determination of the structure radius of curvature R, a circle was manually fitted to the topography's cutting edge of the PDMS molds. The manual fit was verified using the ImageJ contact angle plugin[11]. (*1*)

It is of note that the PDMS substrates exhibiting cylindrical structures with approx. 400 µm distance between the cylinders (cf. Figure 11 "cylindrical topographies", "wide", p. 51) were only visualized using light microscopy for determination of the radius of curvature R.

Surface roughness of PDMS samples was determined using a MultiMode AFM (Brucker, Nanoscope III) in Scansyst HR Mode. By means of Gwyddion 2.51, ten height profiles (without a preferred direction) of an image with a large (10-30 µm², 512 × 512 Pixel), and an image with

[11] accessible via https://imagej.nih.gov/ij/plugins/contact-angle.html; last accessed 20. Dez.2022.

a small (2-5 µm², 512 × 512 Pixel) scan area were used for determining the roughness. Root mean square (RMS) roughness and peak to valley (PV) roughness were determined. [12] (*1*)

Cell Studies

Selected Topographies for Cell Studies

Table 3 displays the topographies used in cell experiments and their specifications.

Most experiments using cylindrical topographies were done using substrates with three different radii of curvature (59.3 µm; 154.2 µm; 312 µm) and a flat PDMS substrate for comparison. This range allows the investigation of responses to uniaxial curvatures in the size scale of cells (fibroblast size: 80 µm (*189*)) and to curvatures significantly larger than fibroblast cell size (hundreds of micrometers).

For spherical topographies, comparable sizes regarding the radius of curvature R were selected. Additionally, different radii for the base structure were investigated. Therefore, four different topographies and a flat PDMS substrate were utilized (see Table 3).

[12] Determination of surface roughness was conducted as a part of the Master Thesis *"Investigation of optical resonators made of different microlenses for application as a compact refractive index sensor"* (original German title *"Untersuchung von optischen Resonatoren aus verschiedenen Mikrolinsen für die Anwendung als kompakter Brechungsindexsensor")* submitted by Janina Drews, in 2019 at the University of Tübingen, supervised by Prof. Dr. Marc Brecht and Achim Juninger.

Table 3 **Selected topographies for cell studies**; Radius of curvature R, distance d, height h, radius of the topography r (cf. Figure 11, p. 51) or rather width of cylinder base w, as well as half arc length $a_{0.5}$.

cylindrical topographies	**topography specification**
narrow spacing *(d: 25 µm)*	
• utilized for dose response relationship, cell type and donor variation, cell density and spacing variation, pharmacological manipulation and protein coating adjustment.	**R: 59.3 µm**; w: 96.1 µm; h: 24.2 µm **R: 154.2 µm**; w: 208.3 µm; h:40.2 µm **R: 312 µm**; w: 286.1 µm; h: 35.3 µm
narrow spacing *(d: 25 µm)*	
• utilized for dose response relationship (additional to above mentioned)	**R: 20.9 µm** **R: 76 µm** **R: 110.2 µm** **R: 118 µm** **R: 129.4 µm** **R: 160 µm** **R: 213.2 µm** **R: 255 µm**
wide spacing *(d: 400 µm)*	
• utilized for cell density and donor variation	**R: 63.5 µm**; w:114.2 µ; h: 34.4 µm **R: 166.8 µm**; w: 210.1 µm; h:39.4 µm **R: 401.3 µm**; w: 276.1 µm; h: 26.2 µm

spherical topographies	**topography specification**
• utilized for epithelial cell experiments (A431, MDCK); convex and concave	**R: 318.6 µm**; h: 47.9 µm; r: 188.7 µm; $a_{0.5}$: 202.0 µm; d: 400 µm (linear) **R: 193.2 µm**; h: 44.1 µm; r: 137.7 µm; $a_{0.5}$: 153.3 µm; d: 400 µm (linear) **R: 134.0 µm**; h: 6.8 µm; r: 51.0 µm; $a_{0.5}$: 51.3 µm; d: 400 µm (linear) **R: 62.7 µm**; h: 19.8 µm; r: 48.6 µm; $a_{0.5}$: 55.6 µm; d: 400 µm (linear)

Substrate Preparation for Systematic Cell Experiments

The arrays of the selected PDMS topographies were trimmed, and cleaned using sellotape to remove dust, followed by ethanol rinsing. The structures were then inserted into a well of a

6 Well plate (Cellstar, Greiner Bio-one) each. Subsequently, to increase surface wettability and hence improve cell adhesive protein adsorption (*190*), the well plate was treated with oxygen plasma (200 Watt with 11 sccm; Pico low pressure plasma system from Diener electronic) for 20 seconds. Directly afterwards, the PDMS was covered with 70 % (v/v) Ethanol for sterilization/disinfection of the surfaces. Using aseptic technique in the clean bench, the Ethanol was removed immediately to avoid PDMS swelling (contact duration absolute maximum 5 minutes), the substrates were washed with sterile phosphate-buffered saline (PBS) and subsequently incubated with the selected protein coating solution (see Table 4). After the indicated incubation time, the substrates were washed three times with sterile PBS to remove excess protein and cells were seeded. (*1*)

Table 4 **Overview of coating variations and use of different coatings throughout the work.** Abbreviations: hdF is short for human dermal fibroblasts, ASC for adipose-derived stem cells, MDCK for Mardin-Darby Canine Kidney cell line, and A431 is a human epidermoid carcinoma cell line.

Protein Coating	Conditions	Application
Fetal Calf Serum (Gibco)	20 % v/v in PBS; overnight at 7 °C	• Pharmacological cytoskeleton manipulation (hdF); • donor and cell type variation experiments using human adipose-derived stem cells (ASC), and hdF from a second donor
Fibronectin bovine serum, (Gibco)	10 µg mL^{-1} in PBS; 30 minutes at 37 °C	• variation in cell density (hdF) • variation in substrate spacing (hdF) • coating variation (hdF)
Collagen I rat tail, (Merck/ EMD Millipore)	50 µg mL^{-1} in PBS; 30 minutes at 37 °C, subsequent 1 % bovin serum albumin in PBS blocking for 10 min at room temperature	• coating variation (hdF) • studies using epithelial cells (MDCK and A431)
Laminin Engelbreth-Holm-Swarm murine sarcoma basement membrane, (Sigma Aldrich)	5 µg mL^{-1} in PBS; 2 hours at 37 °C	• coating variation (hdF)

Human Dermal Fibroblast Cultivation and Pharmacological Manipulation

Human dermal fibroblasts were kindly provided by M.D. habil. Dieter Kaufmann (University of Ulm, hdF1 and hdF2) and Prof. Dr. Petra Kluger (Kluger Lab, Reutlingen University, hdF3 and hdF4), detailed information on cell donors and origin can be found in Table 5.

Cells were cultivated in Dulbecco's Modified Eagle Medium (DMEM, 4.5 g L^{-1} D-Glucose, L-Glutamin without Pyruvat, Gibco) with 10 % (v/v) fetal calf serum (FCS, Gibco) and 1 % (v/v) Penicilin/Streptomycin (P/S; Gibco) at 37 °C and 5 % CO_2 in a humidified incubator. They were subcultivated when reaching confluency using Trypsin/EDTA (0.05 %). Medium was exchanged every two to three days. (*1*)

Table 5 **Overview of human dermal fibroblast with specifications.** Donor information, gender, age, body part of skin donation origin.

hdF indication	Short description	Donor information
hdF1	hdF, FL	Male, 32 years, prepuce
hdF2	hdF, VR	Male, 48 years, prepuce
hdF3	hdF 6/P	Male, 5 years, prepuce
hdF4	hdF 47	Male, 47 years, abdomen

For low density cell experiments, hdF was seeded on the substrates at a density of 2 000 cells per cm^2 to prevent the formation of local denser areas. In experiments without pharmacological manipulation, cells were cultivated for 24 hours and then fixed. (*1*)

For the reduction of cell contractility using the Myosin II inhibitor Blebbistatin (Sigma; dissolved in DMSO), cells were seeded and allowed to adhere for 30 minutes before Blebbistatin was added to a final concentration of 10 µM. Subsequently, cells were allowed to grow for 24 hours, fixed, and then stained. (*1*)

The Rho Activator II (CN03; Cytoskeleton, Inc.; dissolved in diH_2O, in the following mostly referred to as CN03) was used to enhance cell contraction via the Rho/ROCK pathway. Cells were cultivated for 24 hours on the PDMS substrates, and another 24 hours with serum deprivation, prior to substitution with serum-free medium containing 3 µg mL^{-1} CN03. After four hours the cells were fixed and stained. (*1*)

Depolymerization and stabilization of microtubule were achieved using Nocodazole (abcam; dissolved in DMSO) and Paclitaxel (Paclitaxel Sigma-Aldrich; dissolved in DMSO, in the following referred to as Taxol), respectively. In both cases, cells were cultivated on the substrates for 24 hours before the agents were added to a final concentration of 3 µM. Cells were fixed after 8 hours of incubation. (*1*)

Since a concentration of ≥ 0.5 % (v/v) DMSO is considered to be cytotoxic, the final concentration of DMSO in all experiments was below 0.3 % (v/v). (*191*); (*1*)

In cell experiments investigating nearly confluent cell layers (referred to as “high density”), hdF were seeded in a density between 3 500 to 5 500 cells per cm², subsequently cultivated until the cell layer on the flat PDMS became confluent (approximately after 7-10 days) and then fixed and stained. During cultivation the medium was replaced every two to three days.

Adipose-derived Stem Cell Cultivation

Human adipose-derived stem cells (ASCs) were kindly provided from Kluger Lab (Reutlingen University, cf. Chapter VIII Appendix, p. 214 for more information). ASCs were initially cultivated in serum-free MSC growth medium (MSCGM; PELOBiotech, #PB-C-MH-675-0511-XF) containing 5 % (v/v) human platelet lysate. For the investigation of the adaption behavior of the cells on curved substrates, cells were seeded in a density of approx. 10 000 cells/cm² in DMEM (Biochrom) with 10 % (v/v) FCS and 1 % (v/v) P/S onto the substrates. (*1*)

Mardin-Darby Canine Kidney (MDCK) Cell Cultivation

MDCK cells, were kindly provided by the Spatz Group (MPI for Medical Research, Heidelberg). This epithelial cell line is isolated from a cocker’s healthy kidney tubule and a commonly used model system utilized in different kinds of experiments, both in 2-D as well as in 3-D cell culture. (*192*)

Cells were cultivated in Minimum Essential Medium (MEM, Gibco), with 1 % (v/v) Sodium Pyruvat (100 mM, Gibco), 10 % (v/v) FCS, and 1 % (v/v) P/S at 37 °C and 5 % CO_2 in a humidified incubator. Cells were subcultivated twice a week at a confluency of about 90 % using Trypsin/EDTA (0.05 % (v/v)). Medium was changed every two to three days.

For experiments on the PDMS substrates cells were seeded in a density of approximately 41 600 cells per cm² and cultivated until confluency was reached and then fixed.

A431 Cell Line Cultivation

A431 cells, a human epidermoid carcinoma cell line, were kindly provided by Cavalcanti-Adam Group (Heidelberg University) and are a commonly used model cell line used in different applications. For instance, A431 are known to show an increased collective contractility when treated with EGF, based on their overexpression of the EGF receptor (*193*).

A431 cells were cultivated in DMEM with GlutaMAX (Gibco), 10 % (v/v) FCS, and 1 % (v/v) P/S at 37 °C and 5 % CO_2 in a humidified incubator. Splitting was performed once a week, when cells reached a confluency of about 75 % using Trypsin/EDTA (0.05 % (v/v)). Medium

was exchanged every two to three days. Cell density in experiments on the PDMS substrates was approximately 83 200 cells per cm^2. Cells were cultured until a confluent cell layer was reached on flat PDMS and then fixed.

Wound-healing Assessment for Epithelial Cells

For a better investigation and comparison of how A431 cells and MDCK cells are growing onto the convex micro-spherical segments a wound-healing assay was conducted. Therefore, cells were seeded in a density allowing good coverage of the surfaces after 48 hours. For A431 cells this density was 4×10^5 cells per mL, for MDCK cells 2×10^5 cells per mL. After 48 hours the cell layer was "scratched" using a pipet tip, to "wound" the cell monolayer in this area, followed by a medium exchange.

Using the Live Cell Analyzer JuLi™ Br (NanoEnTek Inc.), time-lapse images were recorded inside the incubator.

Immunostaining

For better visualization of the cells and cellular structures on the PDMS substrates, all investigated cells were fixed (4 % paraformaldehyde solution in PBS for 15 minutes), permeabilized using 0.1 % Triton X-100 (Sigma Aldrich) in PBS for 10 minutes and stained for F-actin (ActinGreen 488 Ready probes from molecular probes by life technologies in case of hdF, MDCK, and A431, or Flash Phalloidin Red 594 from Biolegend in case of ASC), and the nucleus (NucBlue Live Ready probes, molecular probes by life technologies, in case of hdF, MDCK, and A431 or DAPI, SERVA Electrophoresis, in case of ASC). (*1*)

In hdF1 samples with manipulated microtubule network as well as control samples without pharmacological manipulation, microtubule (β-tubulin) were also labeled utilizing the following protocol.

Fixed and permeabilized samples were blocked using 3 % (w/v) bovine serum albumin (BSA; biomol) in PBS-Tween 0.05 % (Tween-20, Sigma Aldrich, in PBS 0.05 % (v/v)). The primary antibody (mouse anti-β-tubulin, Tub41 mono clone tub 2.1; Sigma) was diluted 1:300 in PBS. To decrease the amount of volume needed, drops of 40 µL were placed on a Parafilm® in a 6 well plate and PDMS samples were flipped and placed on the drops. In order to assure humidified environment to avoid the evaporation of the antibody solution, the empty wells and spaces between the wells were filled with diH_2O and then incubated for one hour at room temperature. Subsequently, samples were removed and washed three times using PBS-Tween 0.05 % (v/v) with 1 % (w/v) BSA, for 5 minutes each. The secondary antibody (donkey anti-mouse Alexa 594, abcam) was used in a dilution of 1:400 in PBS and incubated for one hour in the dark, using the previously described drop-technique. Samples were then washed

three times, 5 minutes each using PBS. Finally, the staining of F-actin and the nucleus was performed as described above. (*1*)

Epithelial cell lines (MDCK and A431) were additionally stained for E-cadherin:
Fixed and permeabilized samples were blocked for a minimum of 30 minutes using 1 % BSA solution in PBS at room temperature. The first antibody (mouse anti-E-cadherin from BD Biosciences, 2 µg mL^{-1}) was incubated overnight at 7 °C in a humidified environment. To decrease the amount of volume needed, drops of 25 µL were placed on a Parafilm® in a 6 well plate and PDMS samples were flipped and placed on the drops. To assure humidified environment, the empty wells and spaces between the wells were filled with diH_2O. Substrates were washed three times, 5 minutes each, using blocking solution (1 % BSA in PBS). The secondary antibody (MDCK: goat anti-mouse CyTM3 from Jackson Immno Research Laboratories, INC; 1:1000 / A431: donkey anti-mouse Alexa 595 from abcam; 1:300) was incubated for two hours at room temperature in the dark, using 25 µL drops and the same drop-approach as described previously. Samples were washed using blocking solution and stained for Nuclei and F-actin as described above.
Until microscopic examination, all samples were stored at 7 °C covered with PBS and in the dark.

Proliferation Assay

The proliferation of cells on CurvChip substrates with cylindrical topographies was assessed at two time points after cell seeding (24 hours, 70 hours) using the Click-iT Plus EdU Assay Imaging Kit from Invitrogen, following the protocol and instructions from the manufacturer. The EdU assay is an alternative to the BrdU assay, using the nucleoside analogue of thymidine, EdU (5-ethynyl-2'-deoxyuridine). This nucleoside is incorporated into the DNA during DNA synthesis, while the detection is based on a click reaction, where a copper catalyzed covalent reaction between a picolyl azide (Alexa Fluor® dye) and an alkyne (EdU) is taking place. (*194*)
In short, for each time point cells were seeded on respective PDMS substrates. After 20 hours and 66 hours, respectively, the medium was replaced by growth medium containing 10 µM EdU. After an additional 4 hours of incubation, the samples were washed twice with 3 % (w/v) BSA in PBS, fixed and permeabilized. The EdU detection cocktail with Alexa Fluor® picolyl azide dye was applied and subsequently, all nuclei were stained using Hoechst 33342.
For detection fluorescence images were acquired as described in the Data acquisition and analysis section (p. 55), using the kit with Alexa Fluor® 594 nuclei of proliferating cells appeared red and blue (or purple in merged images), while the nuclei of non-proliferating cells were only stained blue.

Data Acquisition and Analysis

Fluorescence and Bright-field Microscopy

Since cells on a cell culture substrate are normally almost invisible, different contrast enhancing techniques have been developed, of which phase contrast microscopy utilizing the difference in refractive indices of cells and the surrounding aqueous medium, is the most common one. However, since the here used, curved PDMS topographies also act as micro-lenses, deviating the passing light, contrast enhancing methods, such as phase contrast, are impaired, strongly reducing the visibility of cells.

For this reason, all samples, except those used for time laps experiments, were fixed and immunohistochemically stained as described previously. Subsequently, they were imaged using an upright microscope with water emersion objectives (Zeiss Examiner Z.1; additional equipment listed in Table 6).

Using this setup further reduces the effect of light deviation from micro-lenses (PDMS substrate) during fluorescence microscopy, since the light does not need to pass the micro-lenses/substrate. Fluorescent z-stacks and tile images were recorded for cell characterization. Additionally, bright field, transmitted light tile-images of the same areas were recorded to be able to correlate the findings to the different substrate regions (curved topography or flat area between). Fluorescence z-stacks were combined using the Zeiss Axio Vision wavelet algorithm and then merged with the corresponding bright-field images. In the case of low density hdF and ASC, tile images were then stitched manually. (*1*)

For high density hdF experiments and epithelial cell experiments automated stitching was performed to align the tiles using the Zeiss Zen Blue software, subsequently the contrast algorithm was used to combine z-stacks, as it showed better results compared to the wavelet algorithm used for low density experiments. For epithelial cells several different extended depths of focus algorithms were applied, depending on what showed the best results.

Table 6 **Zeiss Examiner fluorescence microscope equipment.** HBO high pressure mercury lamp; Information on filter wavelength given in nm. BP short for band pass filter; FT short for Farb-Teiler (German for color splitter) dichromatic beam-splitter; NA short for numerical aperture; ∞/0 Infinity Color Corrected System / without cover glass correction.

Microscopy equipment	Specification
Fluorescent lamp	
Lamp housing	Ebq 100 isolated power supply with HBO 100 housing
Light source	Osram HBO 100 w/2
Fluorescence filter cubes	
Green fluorescence	BP 470/40; FT495; BP 525/50 (Zeiss set 38)
Blue fluorescence	G365; FT395 BP445/50 (Zeiss set 49)
Red fluorescence	TexasRed (probably comparable to Zeiss set 71: BP 592/24; FT615; BP675/100)
Emersion Objectives	
10x	W N-Achroplan; NA= 0.3; ∞/0
20x	W-Plan-Apochromat; NA= 1.0; DIC VIS IR; ∞/0
40x	W-Plan-Apochromat; NA= 1.0; DIC VIS IR; ∞/0
63x	W-Plan-Apochromat; NA= 1.0; VIS IR; ∞/0
Software	AxioVision
Camera	Axiocam MRm with 1x Optovar
Motorized Stage	MCU 2008

When using these images for further analysis of different parameters it is necessary to bear in mind that the curved regions are displayed distorted in microscopy images due to projection of the structure to a plane during the imaging process. This distortion is stronger for areas at the curvature edges compared to the structure central axis. Figure 10 A displays a schematic illustration of this projection bias and its correction. Figure 10 B and C show exemplary microscopy images for further visualization.

Correction of Projection-bias for Morphological Cell Analysis

To be able to analyze morphological parameters of cells growing on the curved topographies the projection bias caused by microscopical image acquisition needs to be corrected. Therefore, together with Michael Brunner of the Curio Group “Cognitive Systems” (Hochschule Reutlingen), a Python-based ImageJ plugin for the correction of the projection bias of microscopy images of cylindrical surfaces was developed. (*1*)

When topography boundaries, radius of curvature R of the topography, as well as the cell’s/nucleus’ outline are known (acquired like described below in Quantification of Cell and Nucleus Orientation on Cylindrical Topographies; p. 53, cf. Figure 10 B) the plugin projects the

outline into a flat plane eliminating the distortion by calculating the real distance b (length of circle arc) of each point of the outline (with measurable distance s) to the cylinder axis as indicated in Figure 10 and the Pseudocode in Chapter VIII Appendix, Part III: Supplementary Materials, p. 213. This procedure corrects the uniaxial distortion giving the new location of the cell outline point. This correction is done for every outline point yielding the undistorted outline. The corrected contour was then used to determine area and aspect ratio of cells and nuclei using the basic measurement functions of ImageJ. The area is calculated based on the spatially calibrated pixel size of the image. The aspect ratio is calculated from the proportion of major axis length to minor axis length of the best fitting ellipse. (*1*)

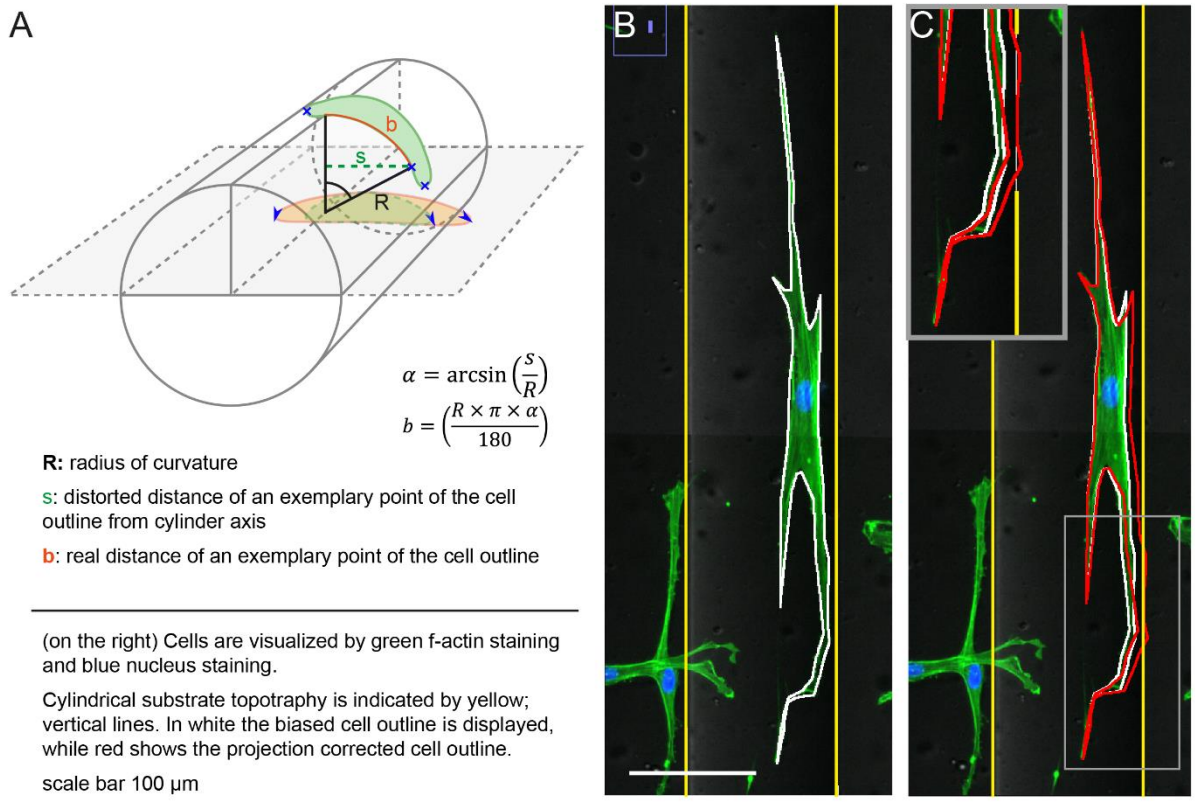

Figure 10 **Projection bias of microscopy images taken from cells on curved substrates.** ***A*** schematic illustration of microscopy projection bias and its correction. Depicted are a cylinder in grey lines with a cell (green) spreading on its surface. The projection plane is visualized in light grey with dashed outlines. The visible projection by microscopy is indicated by the green element in the projection plane (dashed outline), whereas the orange element in the projection plane indicates the corrected cell outline. By manually specifying the radius of curvature R of the cylinder, the ImageJ Plugin calculates the real distance b for every point of the cell outline (indicated by the blue x) with the measurable distance s to the cylinder axis. This procedure corrects the uniaxial distortion giving the new location of the cell outline point, visualized by the blue arrow heads in the projection plane. Adapted from Frey et al. (*1*) ***B*** shows an example of a cell (green with blue nucleus) with its distorted outline depicted in white, that is adhering on a cylindrical topography (yellow vertical lines). ***C*** displays the same cell as depicted

in ***B*** with the projection corrected cell outline (in red). The enlarged section gives a more detailed view on the difference between the biased, projected outline (white) and the corrected outline (red) and illustrates the stronger distortion for increasing distance to the cylinder axis.

Definition of Different Regions on Substrates used for Cell Culture

To correlate investigated (nucleus) parameter to different substrate properties, the substrates are divided in different regions, illustrated in Figure 11.

For hdF on uniaxial, cylindrical topographies, two regions were defined: Area (I), the curved area (later also referred to as “curv”) and area (II) the areas between the cylinders (below “btw”). For experiments with low cell density, nuclei situated in the transition zone of curvature to flat were considered to be part of area (II) and manually sorted out. To simplify automated nucleus detection, especially for high density cell experiments (except for orientation determination), the curved area (I) was reduced from its complete size to the central ⅓ (I_{HD}), where the projection bias is negligibly small, since projection correction would need manual adjustment which was not feasible for this high number of cells/nuclei.

For substrates with spherical topographies, the regions are allocated slightly different (visualized in Figure 11). Again, the curved area (I) is slightly reduced from its complete size of the whole curvature area (topography radius r is reduced by 10 %). The remaining part of the curved area, together with part of the flat area (topography radius r+ 20 µm) is then defined as “transition zone” and area (III) is the remaining flat area.

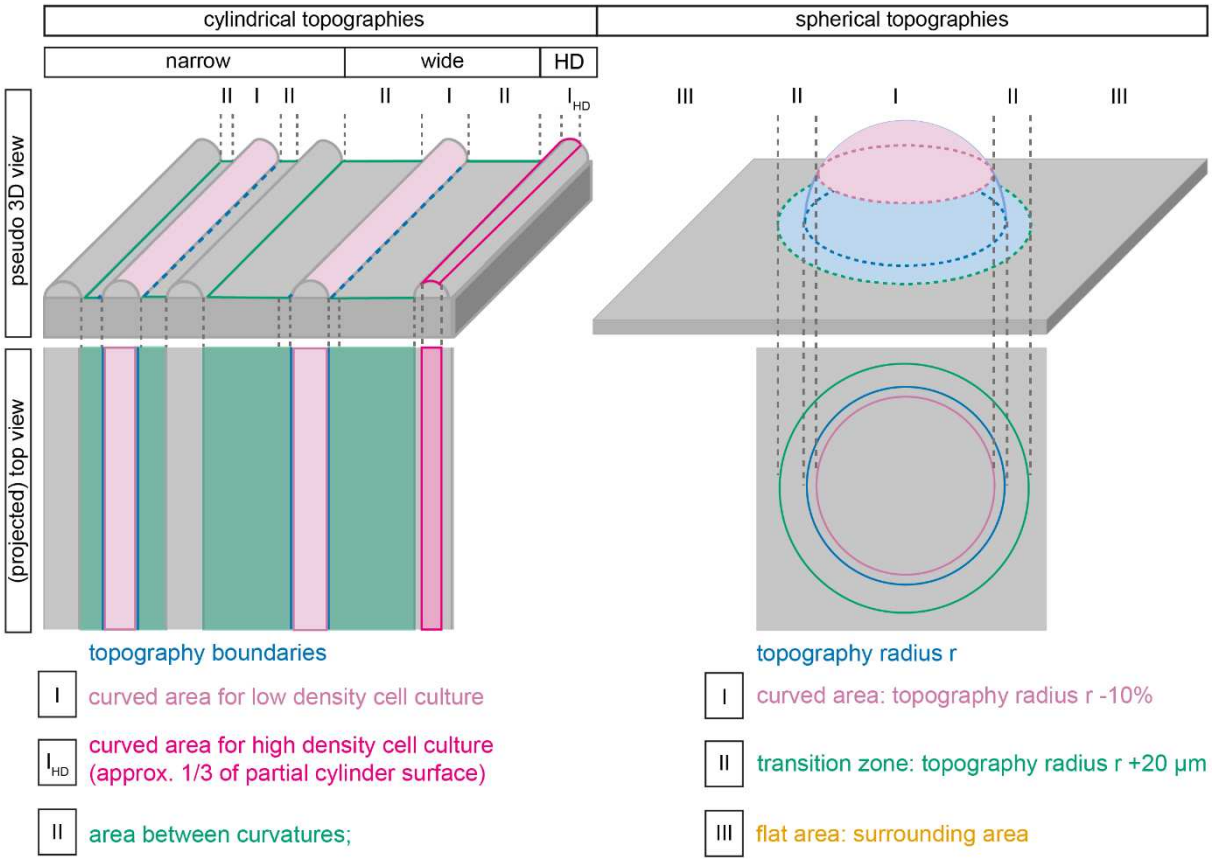

Figure 11 **Illustration of different substrate areas of topographies used for cell studies.** (***Left***) three kinds of different defined surfaces for substrates with cylindrical curvatures: depending on distance between curved areas and depending on cell density. For cylindrical topographies with narrow (approx. 25 µm) and wide (approx. 400 µm) topography spacings, two regions are defined curved area “curv” (I), and area between the curvatures “btw” (II). In case of high cell density (HD), except for orientation analysis, only the upper 1/3 of the partial cylinder surface is used (I_{HD}), since projection error is negligibly small in this area and projection correction would need manual adjustment which was not feasible for this high number of cells/nuclei. (***right***) Surface definition for spherical topographies. Here, three areas are defined: curved area (I), transition zone (II), including part of the curved topography, as well as the transition region from topography to flat, and part of the flat area, and (III) the flat area between the topographies. Illustrations are not in scale. Cylindrical topographies adapted from Frey et al. (*1*)

Nucleus Positioning and Density in Different Substrate Regions

To investigate if there is a preferred nucleus position, the nucleus density on different regions of the PDMS substrates was determined. The regions are illustrated in Figure 11. For experiments using dissociated cells (low density experiments on cylindrical substrates), nuclei that are positioned in the transition zone of curvature to flat were manually sorted out from the cells on the curvature (area (I)) and added to area (II). For experiments with almost confluent

cell layers (high density experiments, including cylindrical and spherical substrates) this sorting process was automated by decreasing the utilized curved area (area (I)), as described previously. Nucleus counts were normalized according to the investigated surface area size. Due to the projection bias induced during microscopy imaging the area sizes of the curved regions cannot be measured from the images but need to be calculated, as described below. (*1*)

For hdF cultivated in low density on substrates with cylindrical topographies, three imaging areas of approximately 17 to 23 mm² in total were analyzed. For epithelial cells on substrates with spherical topographies 15 structures were analyzed (total imaging areas approximately 2.5 mm² to 9 mm², depending on magnification used for image acquisition). (*1*)

In all cases, the mean and standard error of the mean were calculated and are displayed in a bar graph. (*1*)

Calculation of the Area of Different Surface Regions

For cylindrical topographies the topography width s or width s of the curved area of interest of the cylindrical topographies represents a “circle chord”. From the circle cord, together with the radius of curvature R, the circle arc b was calculated (Equation 3), which equals the corrected width of the curved area.

$$b = 2R \times \sin^{-1}\frac{s}{2R} \qquad \textbf{Equation 3}$$

$$A = b \times L \qquad \textbf{Equation 4}$$

with b: circle arc, R: topography radius of curvature; s: topography width, or circle chord, A: Area, L: topography length

The area size of the curved region, area (I), was then calculated from Equation 3 and Equation 4, considering the fact that $s_{(I)}$ is ¾ s of the whole topography (see Figure 11). Area (II) is then $A_{topography} - A_{(I)} + A_{flat\ area}$. As area (III) is not affected by the projection bias its size can be measured using ImageJ.

For spherical topographies with a radius of curvature R and a radius of the circular base r, and height h variations of the spherical cap were calculated as described in Equation 5.

$$M = \pi(r^2 + h^2) \qquad \textbf{Equation 5}$$

$$h = R \pm \sqrt[2]{R^2 - r^2} \qquad \textbf{Equation 6}$$

with M: spherical cap area, r: radius of circle base (topography base), h: topograhphy height, R: topography radius of curvature

For calculating the size of area (I) first $h_{(I)}$ was calculated as described in Equation 6 based on the definition that $r_{(I)}= r – 10$ % (see Figure 11). Area (II) was then calculated by $(M – M(I)) + (\pi (r_{(III)}^2 – r^2)$ with $r_{(III)}= r+ 20$ µm.

Quantification of Cell and Nucleus Orientation on Cylindrical Topographies

For anterior-posterior polarized cells growing on uniaxial curvatures (cylindrical topographies), it is possible to measure an angle φ between the cylinder axis and the cell elongation axis or the nucleus elongation axis. However, due to the previously described projection bias (cf. Figure 10, p. 49), the measured angle φ is different from the actual angle of orientation Ψ. As previously described by Kemkemer et al. (*106*), this angle of orientation Ψ can be calculated from the following parameter: the measurable angle between the cylinder axis and the cell/nucleus elongation axis φ, the cell/nucleus location on the cylinder in relation to the cylinder axis d, and the radius of curvature of the structure R, which equals the radius of the cylinder R (visualized in Figure 12 and described in Equation 7 to Equation 9). (*1*)

For determining these parameters, the boundaries of the curved topographical regions were marked using ImageJ's line selection tool and ROI manager. The outlines of cells, that were growing on the curved region completely, were marked manually using the polygon selection tool and added to the ROI manager. Afterwards, an ellipse was calculated from the cell-outline using the fit ellipse function of ImageJ and the orientation angle φ of the ellipse to the cylinder axis was measured. (*1*)

For determining nuclei outlines we isolated the corresponding channel, converted it to an 8-bit grey scale images and used the ImageJ standard threshold tool to manually set a threshold to distinguish between the background and the nuclei and generate a binary image. Subsequently, the analyze particle ImageJ function was used to detect the nuclei and add the outline to the ROI Manager. In the case of high-density cell layers, the Otsu method was used to automate threshold finding followed by "find edges" "sharpen" and "fill holes" commands. Watershed function was applied to separate nuclei, if necessary. The analyze particle function was again used to detect the nuclei and add the outline to the ROI manager. These outlines were then used to determine the orientation φ using the measurement function of ImageJ.

For all three described cases, the distance d from the ellipse center of mass (given by the measurement function of ImageJ) to the cylinder axis was determined by calculation using the positions of the curved topography boundaries.

The angle of orientation Ψ was then calculated by means of the relations given in Equation 7 to Equation 9. (*1*)

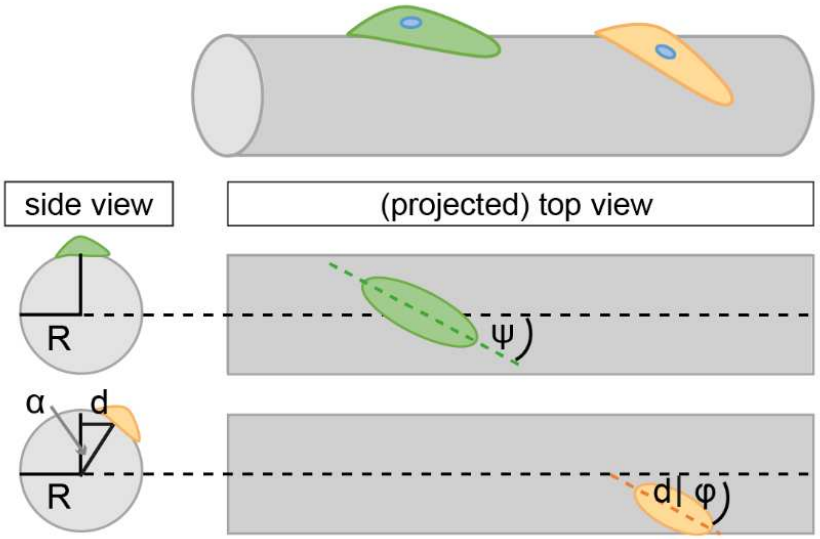

R: cylinder radius, equals radius of curvature of the substrates
φ: measured angle between cylinder axis and cell/nucleus axis of elongation
d: distance between cell/nucleus (center of mass) to cylinder axis with corresponding angle α
ψ: Angle of orientation without projection bias

Figure 12 **Schematic illustration of calculated correction of the angle of orientation due to projection bias.** (see also Equation 7 to Equation 9), Adapted from Frey et al. (*1*)

$$\tan \Psi = \frac{\tan \varphi}{\cos \alpha}$$ **Equation 7**

and

$$\sin \alpha = \frac{d}{R}$$ **Equation 8**

yielding:

$$\tan \Psi = \frac{\tan \varphi}{\sqrt[2]{1 - \left(\frac{d}{R}\right)^2}}$$ **Equation 9**

with R as the cylinder radius, φ as the measured angle between the cylinder axis and the cell/nucleus axis of elongation, d as the distance between the cell/nucleus (center of mass) to cylinder axis with corresponding angle α and Ψ as the angle of orientation without projection bias

Drawing of Nucleus Major Axis

To facilitate the visualization of nucleus orientation, a macro from the imageJ NIH website called “DrawParticleEllipseAxis.txt”, accessible via (*195*), was adapted and used to draw the major axis of the nuclei. The adapted code can be found in Chapter VIII Appendix, Part III: Supplementary Materials, p. 214.

Prior to running the macro, the nucleus fluorescence image needs to be converted to a greyscale 8-bit image (Image >type >8-bit), followed by the adjustment of the threshold (Image >Adjust >Threshold) yielding in a binary image of black nuclei on white background.

Additionally, since the macro is using no scale, the scale of the image needs to be removed (Analyze >Set Scale >Remove Scale), to draw the axis in the right scale.

Calculation of the Cell and Nucleus Perceived Curvature of Cells on Cylindrical Topographies

Assuming, the cell is in contact with the underlying substrate surface, all over its spreading area, the curvature the cell perceives k can be calculated, when knowing the angle of orientation Ψ and the radius of curvature R of the substrate topography following Equation 10, as previously described by Werner et al. (*121*). (*1*)

$$k = \frac{\sin^2 \Psi}{R} \qquad \textbf{Equation 10}$$

With k as cell perceived curvature, Ψ as angle of orientation and R as radius of curvature of the substrate topography.

This assumption is reasonable for cells adhering flat substrates, and convex curvatures but not always for concave topographies and also for the corresponding nuclei, as shown by Werner et al. (*97*). In their work they describe that cells on concave surfaces cells are observed to stretch upward, lifting the nucleus, resulting in a “spider-like morphology”.

Calculation of Pooled Cell Perceived Curvature of Cells on Cylindrical Topographies

To quantify the change of perceived curvature between different groups like cell type or types of pharmacological manipulation the pooled median cell perceived curvature (pooled k_{Med}) was calculated. For doing so we pooled all values of not-significantly different perceived curvatures of a defined group (e.g. same cell type or same pharmacological manipulation) and calculated the new median perceived curvature. (*1*)

In cases where there was only one significance between the three substrates (cf. Figure 24, p. 82 and Figure 30, p. 98) the perceived curvature of cells on the substrate with R=59.3 µm was excluded as analysis of all FCS-coated substrates indicates some kind of significant difference for this substrate (cf. Figure 19 C, p.73). (*1*)

Quantification of Cell Proliferation

Click-iT Plus Edu Imaging Kit from Invitrogen (Alexa Fluor® 594), was performed as described previously (Proliferation Assay p. 46) and subsequently, all nuclei were stained using Hoechst 33342. Yielding red stained nuclei of proliferating cells and counter-stained blue nuclei of all cells (or purple nuclei of proliferating cells and blue nuclei of non-proliferating cells in merged images).

For determination of the position dependent proliferation rate, several microscopic images were used. From each investigated area one brightfield image was taken to correlate the data

to special regions of interest (curved region “curv” or transition zone between the cylinders “btw”), additionally fluorescent tile and z-stack images were acquired. Fluorescence raw images which were then processed using Zeiss software (Zen blue) yielding one fluorescence image (2 channels, several tiles) of the investigated area. Using imageJ, ROI were defined based on the brightfield images. The channels of the fluorescence images were split and processed separately, while here the blue channel represented all nuclei and the red channel (Alexa Fluor® 594) only the EdU positive nuclei that were proliferating. After thresholding and selecting the right ROI, “Analyze Particles” was applied for both channels to quantify the total number of nuclei and the EdU positive ones in this ROI. The proliferation rate was determined by dividing EdU positive count of nuclei by total nucleus number on the corresponding ROI. For the analysis, from each substrate a minimum of 13 curved regions and transition zone (area between the curvatures) were quantified. For the flat PDMS used as control, 3 independent tile images (4×4) were used.

Time-Lapse Microscopy

Samples were prepared as described previously for other analyses. Life cell imaging was performed using the Live Cell Analyzr JuLi^{TM} Br (NanoEnTek Inc.), an incubator-compatible microscopy unit. The scope unit, containing a 4x objective and white LED can be placed into the incubator, providing stable and undisturbed growth conditions. Connected to the station unit, outside the incubator, the sample placed on the stage of the scope unit can now be focused via an LCD touch screen. Additionally, some adjustments like digital zoom, exposure, brightness can be made to optimize the image quality. For human dermal fibroblasts, no zoom was used, and the imaging frame was set to one image per 15 minutes. Since the JuLi^{TM} Br does not have any kind of fixation for samples placed on the stage or stage automatization, it is not possible to find the same spot after media exchange. Therefore, the maximum imaging time of one region is limited to about 2 to 3 days. Additionally, despite the digital adjustments that can be made concerning contrast, cell visualization remained challenging.

Statistical Analysis

Since the presented data are not distributed normally, the non-parametric Kruskal-Wallis test with Dunn’s post-hoc test was performed using the OriginPro’s App “Post-hoc Analysis for non-parametric tests”. Statistical significance was analyzed on four levels: not significant ns with $p > 0.05$, significant * with $p < 0.05$; highly significant ** $p < 0.01$ and most significant *** $p < 0.001$. Generally, the medians of the data sets were calculated and compared instead of means, indicated by the subscripted index Med (e.g. median of orientation angle ψ_{Med}). The only exception is the cell density determination, here we display the mean plus standard error of the mean (SE). (*1*)

IV. The CurvChip – A Model System

To systematically study the effect of mesoscale curvature on different cell types and elucidate the interdependencies of different microenvironmental factors, the CurvChip platform was developed. This topography platform is a 2.5 D model system with variable convex and concave three-dimensional structures, ranging from simplest structures that can be described by one defined surface curvature, comprising uniaxial curvatures with circular cross-section (i.e. cylindrical substrates) and positive gaussian curvatures with circular cross sections, i.e. partial spheres, to more complex, positive gaussian curvatures with square and rectangular basic shapes (i.e. "rods"). These curvatures are separated by flat areas, as depicted in Figure 13 and Figure 14. Chip parameter, like radius of curvature R, distance between the curved regions d and surface chemistry, can be systematically modified in straight forward procedures, allowing a profound analysis of different cell behavior and functions with varying CurvChip parameters.

The master structures of the CurvChip on silicon wafers (Figure 13 A, left image) were created using a low-cost photolithography system with a LED based illumination unit (cf. Figure 8 A, p. 34) (*3*), a positive photoresist (ma-P 1275 HV) in different thicknesses on silicon wafers, chromium and foil photomasks with different layouts and a post-developmental, thermal reflow procedure to create the curved structures by surface tension of the molten photoresist, as visualized in Figure 8 B. Depending on the utilized mask layout (cf. Table 2, p. 37) generated topographies can range from partial spheres, to (partial) cylindrical rods of various lengths like illustrated in Figure 13 B, but also more sophisticated patterns, like microfluidic channels, are possible using this method. Semi-spheres and cylinders are theoretically feasible by adjusting resist thickness and structure width to a ratio of 1:3 (height to width) (*196*), however the outcome also depends on the setup used.
Repeated PDMS casting of the master structures and then the first PDMS molds like depicted in Figure 8, allow the generation of convexly and concavely curved surface topography arrays (Figure 13 A middle and right top image). These soft PDMS arrays can either be applied as cell culture substrates, like done in the following sections, or they can be used to transfer the structures to other materials, for instance by hot embossing or further polymer molding using injection molding or cast molding (*2*) as well as hydrogel coating or molding (*197*). Using hydrogels, however, special considerations need to be made since the topographies are altered during hydrogel swelling.

Using low-cost hot embossing (cf. Figure 9, p. 38), a transfer to different polymers was verified, including PVC, PS and TPU (Pellethane® 2363-55D), all biomaterials utilized in different

biomedical applications. Figure 13 C shows exemplary SEM images of the transferred patterns using convex PDMS and PVC.

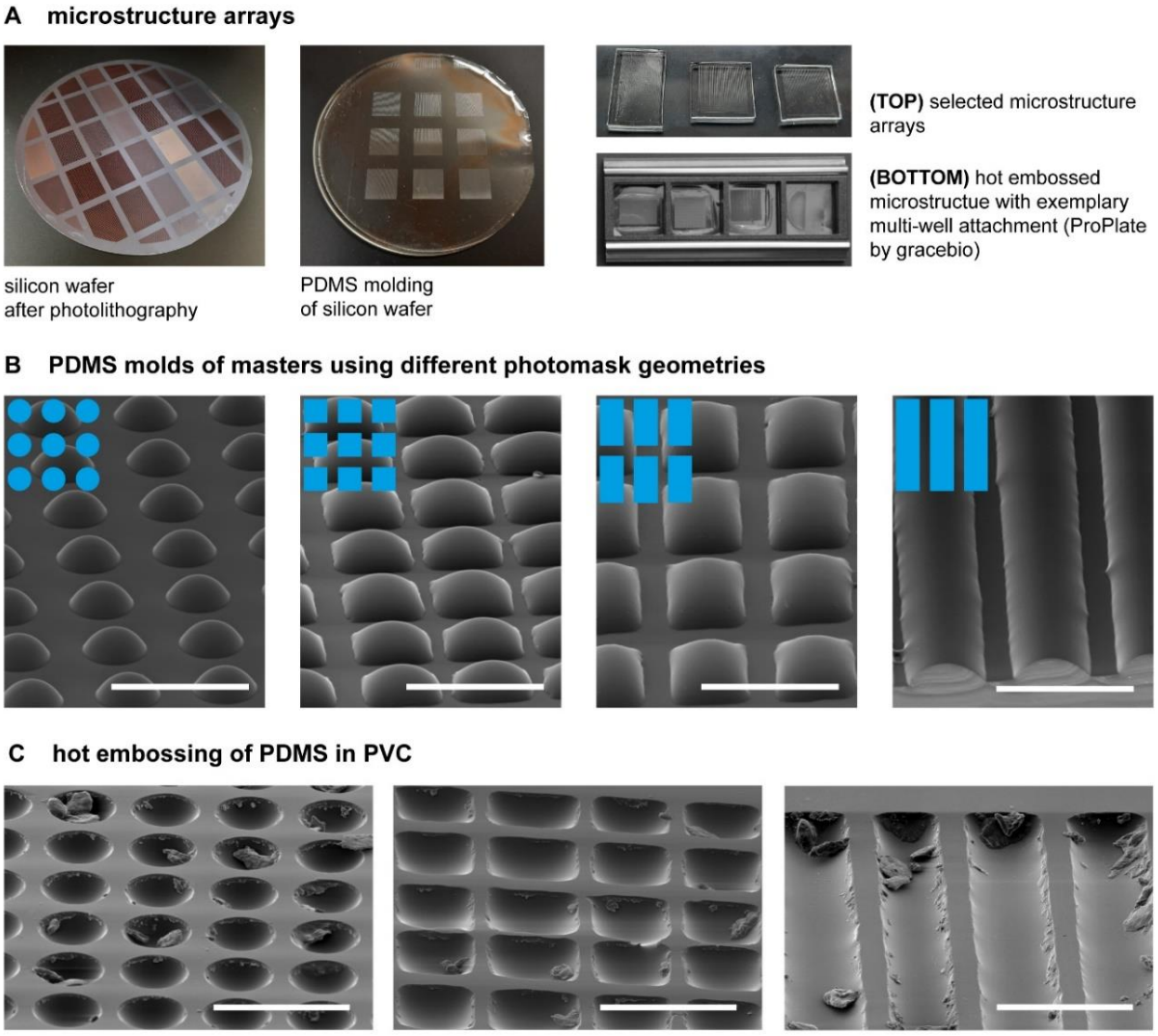

Figure 13 **Images of microstructure arrays of the CurvChip.** ***A*** Images of microstructures, left silicon wafer after photolithography, middle PDMS mold of a silicon wafer, right top selected microstructure arrays cut from PDMS, right bottom hot embossed microstructures with exemplary multi-well attachment (ProPlate by gracebio). (Image of silicon wafer and PMDS molding adapted from Frey et al (*1*)) ***B*** Tilted view of PDMS repetitive moldings with different microstructure geometries, generated by low-cost photolithography with different mask layouts, as indicated by blue structures in upper left corner. Only spherical microstructures were generated using a standard chromium mask, the other structures were made utilizing low-cost foil masks. ***C*** Tilted view of impressions of the in ***A*** shown PDMS moldings on PVC generated by low-cost hot embossing. Figure part B and C adapted from Frey et al. (*2*). Scale bars 100 µm.

The transfer of the CurvChip structures to medically relevant polymers allows an application-oriented biomaterial research approach by combining a set of topographies of interest with a pertinent material. TPU, for instance, is studied for an application in vascular grafts (*7, 198*), a

field where substrate curvature is obviously a factor that needs to be considered for cell material interactions like endothelialization.

Using arrays with cylindrical or spherical topographies, the CurvChip has mathematically well-defined surfaces, with one radius of curvature R describing the geometry of the topographies, unlike for sinusoidal, elliptical or more complex patterns (*120, 123, 127, 128, 145, 199*). Even though this situation might be more artificial compared to the situation in vivo, it enables the observed cellular behavior to be linked to the curvature of the underlying substratum more directly.
For the systematic cell studies, different partial-cylindrical topographies and partial-spherical topographies (later often referred to as cylindrical substrates or spherical substrates), with different spacing between the curved areas were manufactured, as listed in Table 3 (p. 41).
The radii of curvature R of the produced partial-cylinders (applied in mesenchymal cell studies of Chapter V) range from R= 20.9 µm to 401.3 µm. Spherical substrates (used for experiments using epithelial cells in Chapter VI) display radii of curvature R in the same size range (R= 62.7 µm to R= 318.6 µm).
Figure 14 A shows exemplary SEM images of both cylindrical and spherical PDMS surface structures. The images of the topography profiles were used to measure the curvature radius R by fitting a circle to the cross-section of the partial cylinders/spheres, as illustrated by the pink lines on SEM images of cylindrical topographies. To verify the circularity, we used the ImageJ plug-in contact angle giving us the same radii with a maximum of 0.16 µm deviation from the ideal circular shape. (*1*)

On this account, the surface roughness of the CurvChip model-system based on the PDMS moldings was determined using AFM. Figure 14 B shows an exemplary topography scan and roughness profile of the PDMS surface of a microstructure. Due to the thermal reflow process, the microstructures show a very low RMS roughness of about 1.8 nm (*1*) and RV roughness of 11.9 nm, which is much smoother compared to a 3-D printed structure using the Photonic Professional GT two photon 3-D Printer by Nanoscribe (RMS=7.5 nm, RV=32.7 nm; cf. *Chapter VIII Appendix, Part IV: Supplementary Material, p. 216*, Figure 76) and comparable to what Sun et al. (*200*) published for their microgroove substrates (RMS <5 nm), also produced by photolithography with thermal reflow.

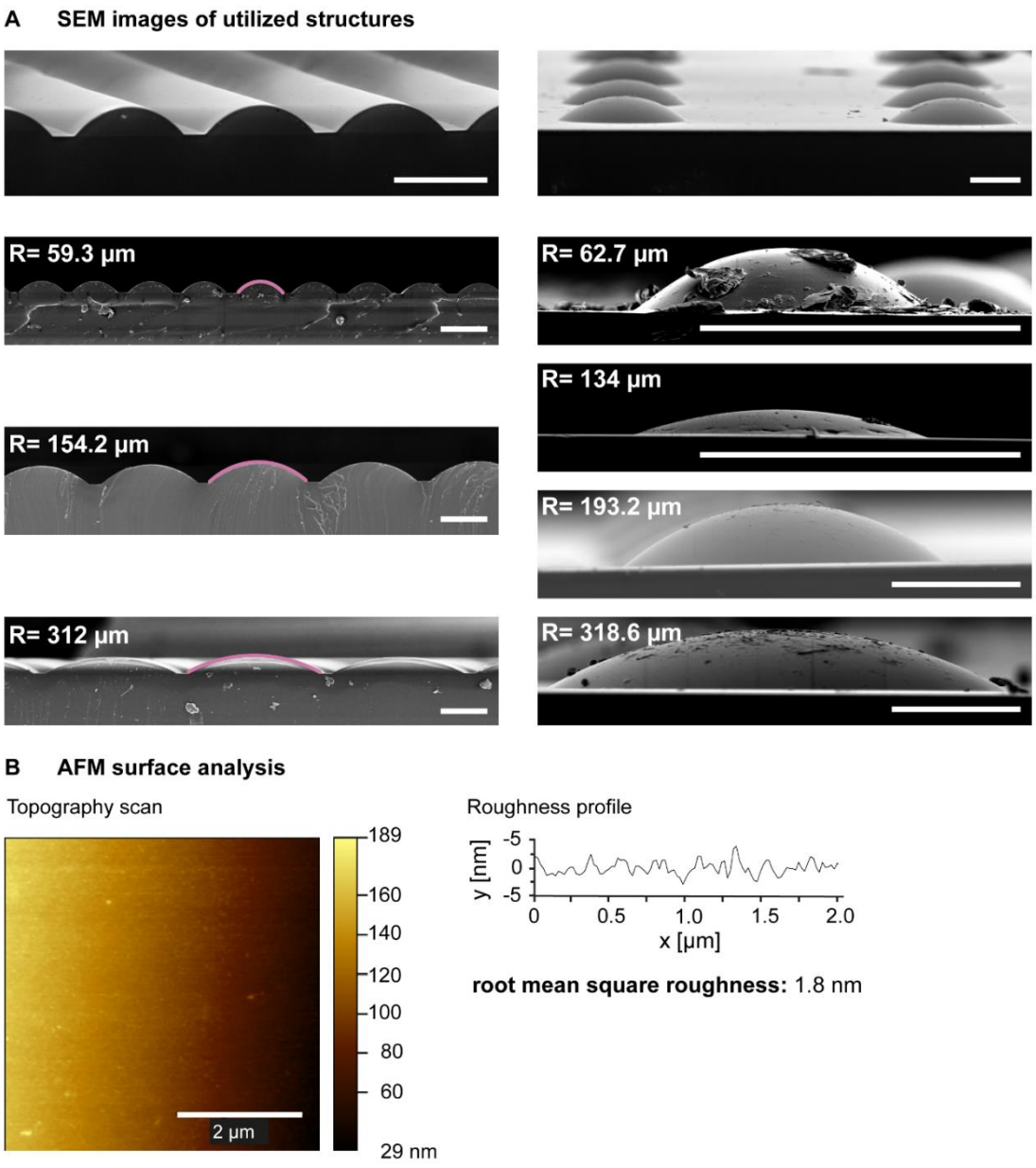

Figure 14 **Surface analysis of microstructures of the CurvChip**. ***A*** SEM images of utilized structures (***left***) cylindrical structures, (***right***) spherical structures. (***top row***) Tilted view, (***other rows***) cutting edge/side view. Scale bars 100 µm. ***B*** AFM surface analysis. (***left***) Exemplary topography scan and (***right***) roughness profile. SEM images from cylindrical structures and AFM surface analysis adapted from Frey et al. (*1*)

Using the CurvChip platform, it is, therefore, possible to exclude the interference of guidance cues on the nanometer-scale (*1, 54, 201*) without the need for post-processing of the PDMS moldings. This fact presents a clear advantage of the CurvChip compared to the cell culture chip deployed by Werner et al. (*54*) which was manufactured by FEMTOPrint by glass 3-D printing. Using their approach, the surface roughness of each PDMS mold needs to be decreased by applying a thin PDMS layer onto the chip using pressurized air flow, followed by 3 h of additional curing. However, no measured values for surface roughness are given, neither

by Werner et al. (*54*) nor for other approaches, like the glass capillaries in a PDMS foundation, used by Bade et al. (*119*), or the 3-D printed channels used by Jung et al. (*202*). In both cases, no data on roughness or surface finish of the capillaries or 3-D printed surfaces are indicated.

Consisting of highly defined surface topographies without the need of post-processing, together with the fact that, all of the applied methods can be conducted under normal laboratory conditions, without the need for expensive equipment, all in all, the CurvChip platform is an affordable, useful tool for basic and applied research in the area of cell response to topographies on the micro and meso scale, that opens up the field to a broader range of researchers, including small academic research or teaching laboratories (*3*).

V. Mesenchymal Cells on Uniaxial, Cylindrical Curvatures

Comparison of Cell Behavior Depending on Cell Density

When investigating cellular adaption of mesenchymal cells with pronounced stress fibers, like human dermal fibroblasts, in response to convex, cylindrically curved surface topographies, there are two options regarding cultivation density: firstly, in a sparse cell density where cells only have few to no cell-cell contacts or, secondly, in denser cell monolayers providing more cell-cell interactions. To study if there are differences in cell adaption to curved topographies depending on the cell density or number of neighboring cells, human dermal fibroblasts (hdF) were cultivated on the CurvChip model surfaces precoated with fibronectin either for 24 hours (low density) or until confluency (high density).

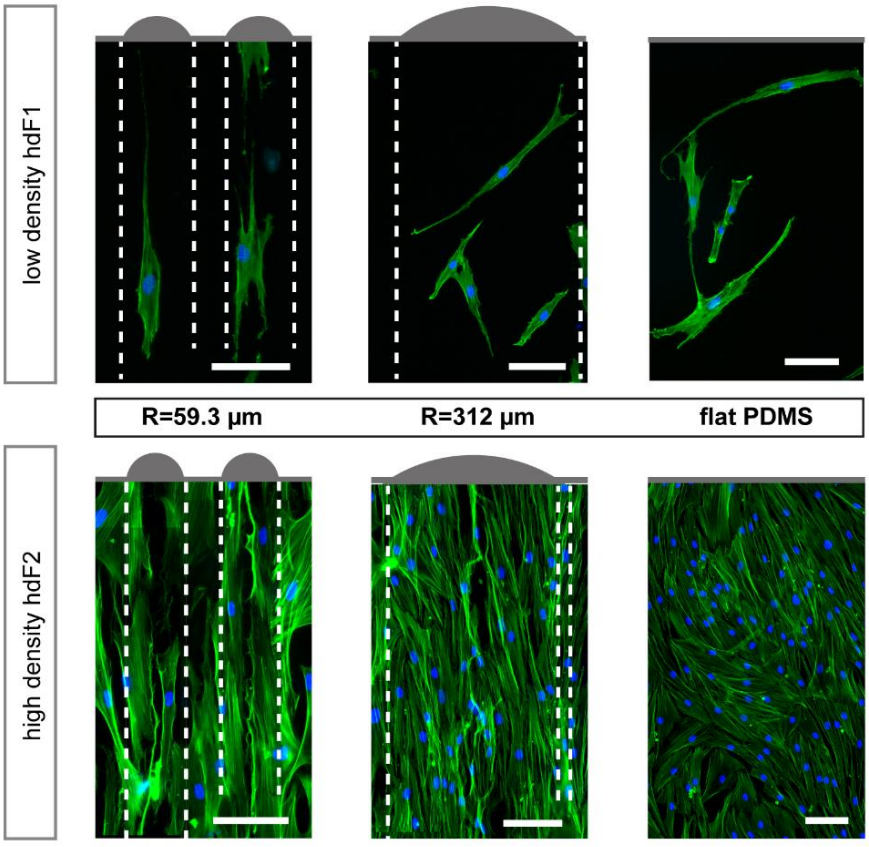

Figure 15 **Fluorescence microscopy images of hdF, cultivated in low and high density on PDMS substrates with cylindrical topographies of varying radii of curvature R and flat PDMS**. Surfaces are coated with fibronectin, f-actin is presented in green, nuclei in blue, dashed lines show topography boundaries and curved regions are indicated by (grey) partial circles at the upper image rim (not in scale). Scale bars 100 µm.

Examining these hdF on cylindrically curved, convex topographies, as presented in Figure 15, it can be observed that independent from cell density hdF principally align longitudinally, along

the cylinder axis, even on mesoscale cylindrical topographies (radius of curvature R=312 µm), larger than the cells (fibroblast size 80 µm (*189*)). Additionally, it can be seen that the manifestation of the longitudinal orientation of the hdF is depending on the underlying substrate curvature, with a more pronounced orientation along the axis for larger curvatures (smaller radii), which was previously only described for substrates with smaller radii of curvature (*106, 203*).

To quantify the observed orientation adaption, the angle of orientation ψ in relation to the cylinder axis (ψ=0°) was determined. The rose histograms in Figure 16 display the angle of orientation ψ of cells and nuclei. The cell orientation angles, for low density conditions, show an increasing deviation from ψ=0° with decreasing curvature (deviation from cylinder axis R= 59.3 µm<R= 154.2 µm<R= 312 µm), while cells on flat PDMS show no preferred orientation.

A comparable orientation adaptation can be observed for the orientation of the corresponding nuclei of the investigated cells, with a slight decrease in manifestation (cf. Figure 16). This decrease is also indicated by the median of the angle of orientation ψ_{Med} given in Table 7, where the values for median cell orientation angles are smaller compared to the values for the nucleus, i.e., the nucleus orientation shows a stronger deviation from the cylinder axis.
Since it is hard to distinguish individual hdF, when they are growing in a monolayer, only the nucleus' angle of orientation was determined for the high-density approach. Compared to the nucleus' orientation of sparsely seeded cells, the orientation behavior of nuclei in denser layers, is more pronounced:
For hdF growing low density on substrates with low curvature (R= 312 µm), about 31 % of nuclei are aligned in an angle between 0° and 15°, while for denser hdF layers 76 % of the nuclei are oriented in this range. This increased alignment along the minimal curvature (ψ=0°) becomes even more notable when comparing the median of the nucleus orientation (ψ_{Med}) for both approaches (Table 7): For small curvature substrates (R= 312 µm) the nucleus' ψ_{Med} for hdF cultivated in low density is 21.1° while it is 8.0° for nuclei of hdF cultivated in cell layers, a decrease that is statistically most significant ($p<0.001$). For high curvature substrates (R=59.3 µm) this decrease in nucleus ψ_{Med} is less prominent with 7.1° for hdF cultivated in low density and 4.8° for hdF in denser cell layers (no significant difference $p>0.05$).

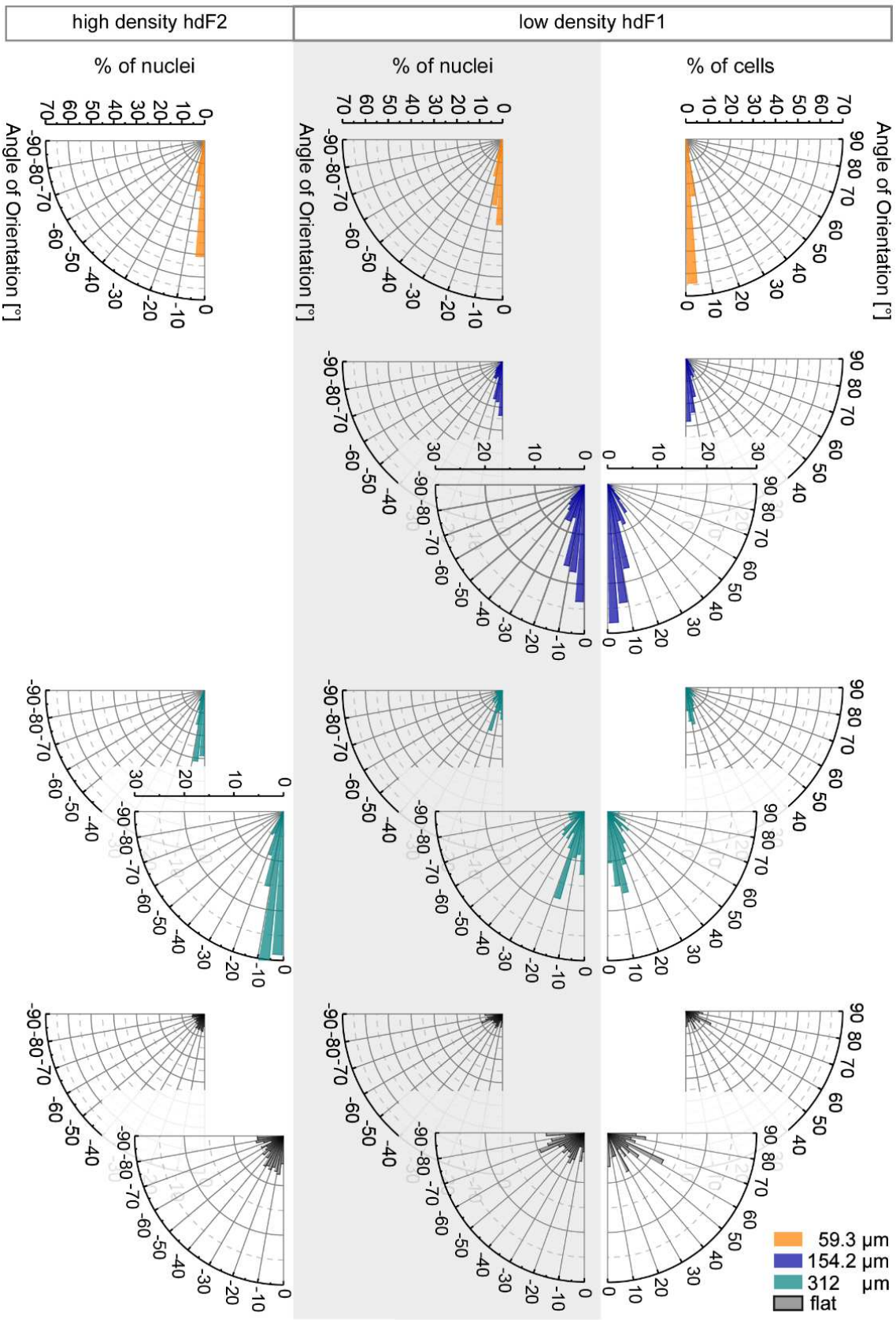

Figure 16 **Orientation of hdF cultivated in low and high density on cylindrically curved PDMS substrates and flat PDMS coated with fibronectin.** Rose Histograms show the percentage of cells or nuclei oriented in a certain angle in relation to the cylinder axis and dependent on the radius of curvature

R of the PDMS substrate. For the purpose of easier comparison of cell and nucleus orientation, nucleus angles of orientation are shown as negative values while cell orientation is displayed as positive value, resulting in mirrored display of cell and nucleus orientation. Bin size 5°, sample size low density (cells/nuclei): $n_{59.3\,\mu m}$= 129/129; $n_{154.2\,\mu m}$= 104/104; $n_{312\,\mu m}$= 126/124; n_{flat}=104/104; high density: $n_{59.3\,\mu m}$= 197; $n_{312\,\mu m}$= 276; n_{flat}= 604; To facilitate comparison and decreasing bias the axis scaling was kept the same and only adjusted in the diagrams overlapping the ones with larger scaling.

Table 7 **Median angle of orientation ψ_{Med} pertaining to hdF cultivated in varying cell densities on convex cylindrical topographies coated with fibronectin**. Asterix indicate statistical significance between low- and high-density nucleus orientation, (asterix) indicate statistical difference within high density approach (*p<0.05 significant; **p<0.005 highly significant; ***p<0.001 most significant), ns indicates p>0.05 not significant, using Kruskal-Wallis ANOVA.

Substratum Radius of curvature R	Angle of Orientation median ψ_{Med} [°]	
	Cell	**Nucleus**
Low density		
59.3 µm	3.2	7.1
154.2 µm	9.4	12.2
312 µm	17.9	21.1
flat	52.0	50.2
High density		
59.3 µm		4.8 ^{ns}
154.2 µm		-
312 µm		8.0 ***
flat		36.8 *
High density, wide distance between curvatures		
63.5 µm		6.8 ^{ns} (*)
166.8 µm		7.8 ***
401.3 µm		11.2 *** (***)
flat		40.7 * (^{ns})

An increased alignment to the cylinder axis (minimal curvature) with increasing cell density, is also described by Bade et al. (*119*), for mouse embryonic fibroblasts (MEF) and human vascular smooth muscle cells (hVSMC), both less polarized cell types than hdF, with a more pronounced change in the angle of orientation for hVSMC. These observations suggest the involvement of cell-cell contact in collective cell response to convex curvatures, which could be due to the circumstance that cell-cell contacts mechanically couple neighboring cells by enabling tension transmission (*38, 204*).

Liu et al. (*205*) suggest, that the key driving force of collective cell alignment on curved cylindrical topographies, as well as 2-D patterns of comparable dimensions (width=π R), is the in-plane shear stress, resulting from anisotropic nature of the single cell tension. They modelled the in-plane stresses of a cell layer and showed a correlation of osteoblast-like MC3T3-E1 cell polarization and alignment with the direction of the maximum principal stress., For cylinders this alignment and principal stress is along the cylinder axis, except for the cylinder ends where the edge effect dominates. Moreover, they argue that the "cytoskeleton cannot bear shear stress" and it, therefore, reorients along the maximum principal stress equaling zero shear stress. However, they do not address the difference between dense cell layers and sparsely growing cells as well as the in literature described change in actin alignment towards circumferential orientation of hVSMC upon Rho activation on cylinder with R=125 µm (*119*). This circumferential alignment was also described for MDCK cells growing on R<40 µm (*206*), as well as brain microvascular endothelial cells on capillaries with R<12.5 µm (*207*), showing that there seems to be difference for varying cell types, not addressed by their model.

Using a different kind of 2.5-D surfaces (hill and valley sinusoidal topographies, cf. Figure 6 A, p. 22), Pieuchot et al. (*120*) also describe a change in cell behavior of epithelial cells depending on their level of cell-cell contact: They found that cells at the leading edge of growing epithelium, as well as cells in low density cell clusters behaved comparable to mesenchymal cells by positioning their nucleus on the concave areas. This preference, however, is reduced for clusters of higher density, here, cells in the colony center of a growing epithelial layer show no preference for concave over convex regions. For MSCs in denser layers, on the contrary they describe that cells remain excluded from the convex areas, resulting in a three times higher density in concave areas compared to flat substrates.

All together, these findings, as well as the here presented results, suggest that cell-cell junction might play an important role in mediating collective cell response to curved topographies. One possible mode of action might be, by connecting the stress fibers of adjacent cells via adherence junctions, forming an extended stress fiber network with an increased effective length or other processes influencing cytoskeletal organization or mechanics which also might include other cytoskeletal components besides the actomyosin network. (*63*) This theory also leaves room for explaining the difference between mesenchymal and epithelial cells exhibiting a differently structured cytoskeleton (e.g. more fibrous actomyosin in mesenchymal cells vs. cortical actomyosin in epithelia) as well as variations in their composition (e.g. intermediate filaments).

Comparison of the Cell Behavior in Dense Layers Depending on the Space Between the Cylindrical Curvatures

Broders et al. (*204*) describe a size dependent effect of the areas between cylindrically curved (concave) channels regarding the observed uplifting of the epithelial layer in the channels. To exclude the factor that the phenomenon of stronger longitudinal hdF alignment in the denser approach could also be an effect of the spacing between the cylinders, it was investigated, whether the nucleus orientation is affected when the distance between the cylinders (transition zone) is increased from 25 µm to 400 µm.

The microscopy images in Figure 17 show, that on the larger transition zones, nematic patterns[13] begin to form, comparable to a conventional 2-D culture (cf. flat in Figure 15 and Figure 17). The present results, moreover, show, that the formation of these ordering structures, seems to be disturbed by the cylindrical, convex curvatures protruding from the 2-D plane: On the curvatures, an alignment with the cylinder axis seems to be favored over the helical patterns in different angles resulting from local misalignment of the nematic structures. This observation is confirmed by the rose histograms of nucleus orientation of cells growing on curvatures in Figure 17, as well as the nucleus median angles of orientation ψ_{Med} listed in Table 7 (p. 65). The nucleus median angles of orientation ψ_{Med}, of for intermediate and low curvature cylindrical substrates with wide distance, show a significant ($p<0.01$) decrease of ψ_{Med} compared to the median angle of orientation of the low-density approach with narrow transition zones ($\psi_{Med}=7.8°$ for R=166.8 µm, and $\psi_{Med}=11.2°$ for R=401.3 µm compared to $\psi_{Med}=12.2°$ for R=154.2 µm, and $\psi_{Med}=21.1°$ for R=312 µm). However, also significant differences ($p<0.05$ for R=63.5 µm, $p<0.001$ for R=401.3 µm) can be observed between the two high-density approaches (transition zone width 25 µm and 400 µm).

This change for intermediate curvatures could be due to the change in transition zone width, but more likely it is an effect of the difference in the radius of curvature R between the two kinds of substrates (narrow vs wide spacing, 59.3 µm vs. 63.5 µm and 312 µm vs. 401.3 µm).

[13] Nematic patterning is a form of order on a larger scale than the single entities resulting from a collective motion. This type of ordering can be observed for amoeboid and migrating cells like human dermal fibroblasts, melanocytes, and adipocytes, among others, as an effect of polar symmetry (*208*) which was first described by Elsdale in 1968 (*209*).

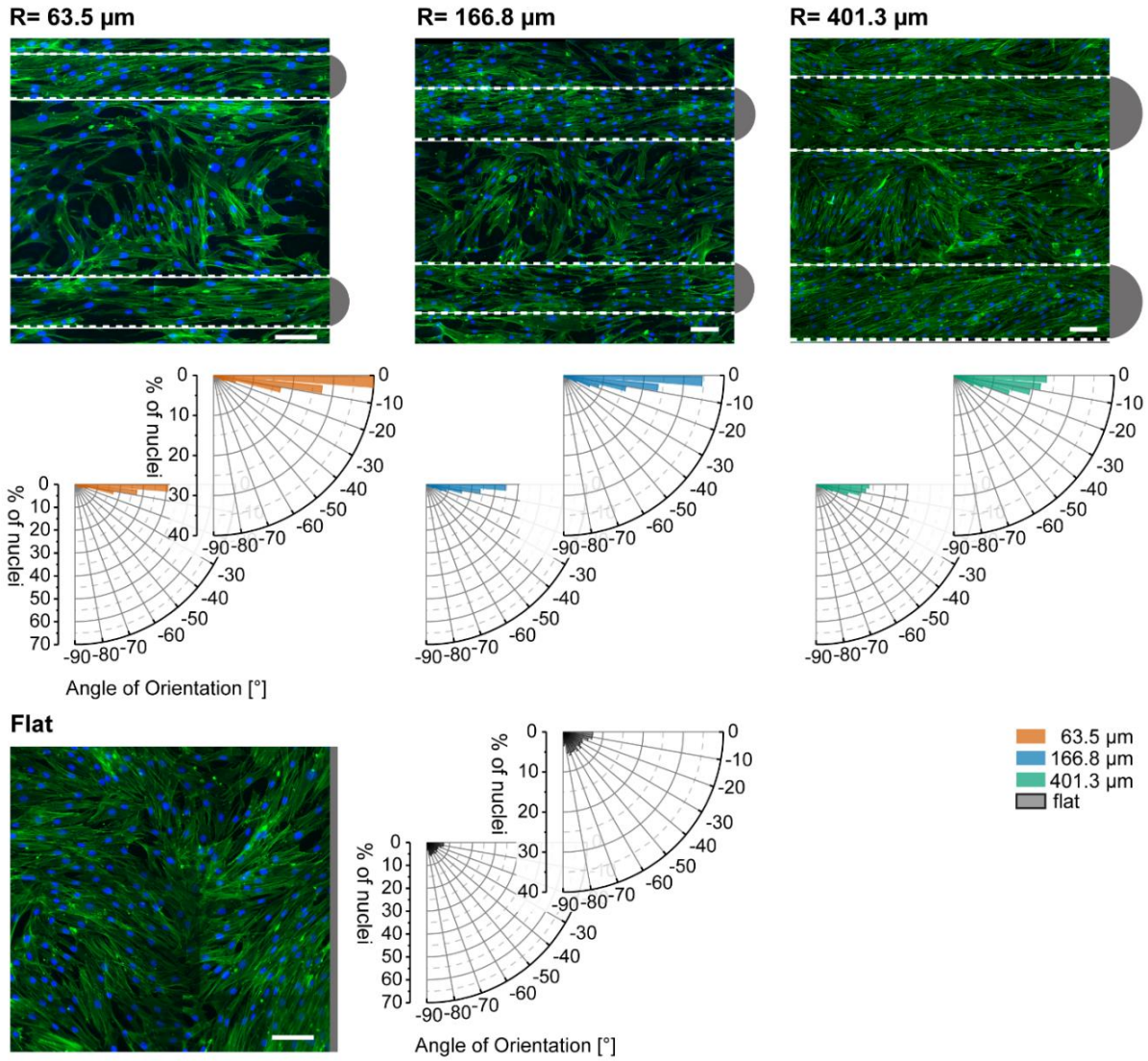

Figure 17 **hdF3 monolayers on fibronectin-coated, cylindrical CurvChip substrates of varying radius of curvature R and with wide (400 µm) distance between the convexities.** Flat PDMS is shown as an control surface. Fluorescence images show f-actin (green) and nuclei (blue), cylinder boundaries are indicated by dashed lines and for better distinction partial circles (not in scale) are added to the cylinder areas. Scale bars 100 µm. Rose histogramms display the percentage of nuclei of cells growing on the curvatures, oriented in a certain angle in relation to the cylinder axis and dependent on the radius of curvature of the PDMS substrate. An angle of zero means perfect alignment with substrate cylinder axis. For better visualization with other rose plots of nuclei, nucleus angles of orientation are always shown as negative values. Bin size 5°, sample size high density: $n_{63.5\,\mu m}$= 459; $n_{166.8\,\mu m}$= 645; $n_{401.3\,\mu m}$= 1055; n_{flat}= 1184; To facilitate comparison with other figures and decreasing confusion the axis scaling was kept the same and only adjusted in the diagrams overlapping the ones with larger scaling.

Examining this increased alignment for dense cell monolayers from the active nematics point of view, Bade et al. (*119*) claim, that this disturbance is not predicted by the theory of nematics. Moreover, they say that the theory “suggests that cells, the ‘nematogens’ in this system, would

wrap cylinders in helical patterns with various pitch angles because the isolated cells aligned in random directions on large cylinders. Because the cylinder would not induce any deformation of the two-dimensional nematic (that is, no bend or splay), no orientation angle would be preferable over another" (*119* (p. 6)). However, this statement is in contrast to the findings displayed in their work as well as the present work. In the present low-density approach, "isolated" cells do not align randomly on cylindrical substrates with a radius of R≤312 µm, as clearly displayed by the rose histograms in Figure 16, as well as the median angle of orientation ψ_{Med}= 17.9° or 21.1° for respectively hdF1 and nuclei on substrates with cylindrical topographies R=312 µm. Random orientation, on the contrary, would be reflected by ψ_{Med} of approximately 45°. In their study, Bade et al. (*119*) only show data for radii of curvatures of R= 200 µm, which still show a mean angle of orientation of approximately 19° and 25° for MEF and hVSMC, respectively. They claim that this preferred orientation is lost for larger R but show no data. Therefore, for the presented data and radii of curvature the cylindrical topographies do induce a preferred orientation in cells growing in a low density, which could induce a preferred orientation in a denser layer.

Nevertheless, these findings do not explain the increased alignment for denser cell monolayers compared to sparsely growing cells. Comparable to the here presented strong alignment along the cylinder axis, Duclos et al. (*91*) describe, in their work on perfect nematic order in confined monolayers, that the alignment of spindle-shaped NIH-3T3 cells in micropatterned stripes with a width smaller than the cells correlation length (500 µm for NIH-3T3 cells) was perfectly ordered. More importantly, they also observed that this ordering did not emerge within the stripes but was a boundary effect, initiated at the boundaries of the microstructures, with which the cells aligned, and that this alignment propagated through the whole strip with increasing density or for wider strips within the corresponding correlation length.

This boundary effect could also be an explanation for the increased alignment on convex cylinders in the present work: The substrates with partial convex cylinders have a sort of boundary, that could induce this ordering effect: the strongly quasi-concave curved groove, resulting in the region where the curved area meets the flat zones.

However, an effect caused by the cylindrical curvature can also not be eliminated completely, since the simulation of Pearce (*210*) shows that an active nematic on a cylinder surface aligns with the lowest principle curvature, which is along the cylinder axis due to favorable elastic energy, unless, when the nematogens have a non-zero spontaneous curvature, then an alignment at an angle accommodating their curvature would be favorable. Concerning the deformation of this nematic alignment, Pearce (*210*) states that their stability "primarily [depends] on the nature of the active stress, with extensile active nematics being unstable to bend deformations and contractile active nematics being unstable to splay deformations" (*210*

(p. 4)), which results in defects that are either aligned perpendicularly (extensile) or parallel (contractile) to the nematic.
To distinguish between the different effects affecting collective cell alignment more studies would be necessary, starting, for instance, with cultivating hdF on whole cylinders with radii between approx. 60 µm and 400 µm, to be able to compare the angle of orientation with those on partial cylindrical 2.5-D topographies and rule out the boundary effect.

However, to be able to understand how cell collectives perceive and react to curved topographies it is also necessary to understand more about how single cells behave on uniaxial curvatures. Therefore, the following investigations using mesenchymal cells were mainly conducted using cells in low density to minimize cell-cell contact and its unknown correlated effects. In some cases, comparisons to hdF in confluent layers are made.

Characterization of the Behavior of Sparsely Growing hdF on FCS-coated Cylindrical Topographies

Aiming to further characterize the cellular adaption of sparsely growing cells on cylindrical substrates with increasing radius of curvature, FCS-coated substrates with cylinder radius of curvature in the rage from R=20.9 µm to 312 µm were investigated.

Nucleus Preferred Position on Cylindrical Topographies of the CurvChip

On the utilized cylindrical substrates cells have two ways of avoiding curvature, firstly by placing themselves in the transition zones between the curvatures, and secondly by adapting their orientation on the cylinders along the cylinder axis. Comparable to what Pieuchot et al. (*120*) analyzed using sinusoidal hill and valley topographies, the nucleus positioning was investigated on the here used cylindrical CurvChip substrates with 25 µm distance between the cylinders.

Figure 18 A shows the nucleus density according to their position on the cylindrical substrates either on the cylindrical curvatures “curv” or in the narrow transition zones between the convexities “btw”.

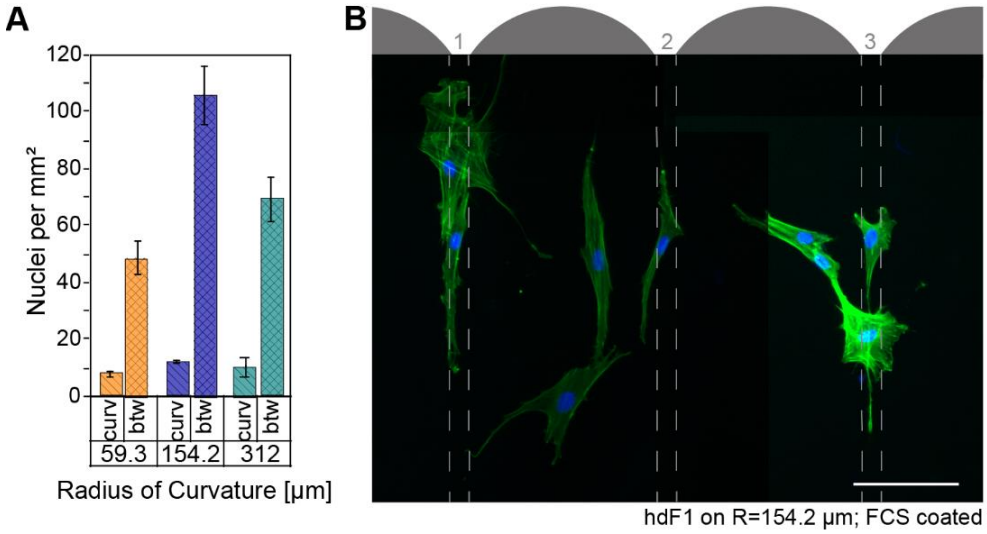

Figure 18 **Nucleus density of hdF1 on cylindrical CurvChip substrates coated with FCS.** ***A*** Nucleus density (Mean ±SE). Curv indicates nucleus density on curved regions (i.e. 8.0 nuclei per mm² for R= 59.3 µm; 12.1 nuclei per mm² for R= 154.2 µm and 10.3 nuclei per mm² for R= 312 µm), btw nucleus density in transition zones between the convex curved regions of the substrates (i.e. 48.6 nuclei per mm² for R= 59.3 µm; 105.9 nuclei per mm² for R= 154.2 µm, 69.2 nuclei per mm² for R= 312 µm substrates). Sample size $n_{59.3\,\mu m}$= 443; $n_{154.4\,\mu m}$= 416; $n_{312\,\mu m}$= 390. Adapted from Frey et al. (*1*) ***B*** Exemplary fluorescence image (f-actin green, nuclei blue) of cells positioning their nuclei in/over the

area between the cylinders. Topography boundaries indicated by dashed lines and curved regions of the substrates are emphasized by partial, grey, spheres (not in scale).. Scale bar 100 µm.

The results show a higher density in the area between the curvatures, meaning that sparsely growing hdF1 seem to avoid positioning their nucleus on curvatures and prefer the region between the convexities.
Additionally to this general preference, in the present work, a slight trend increase in nucleus density on the curved regions of the substrates can be observed with decreasing curvature (increasing radius of curvature R) of the substrates (cf. Figure 18; mean density: 8.0 nuclei per mm² for R= 59.3 µm; 12.1 nuclei per mm² for R= 154.2 µm and 10.3 nuclei per mm² for R= 312 µm). The nucleus density between the convexities also changes with increasing curvature radius R (mean density: 48.6 nuclei per mm² for R= 59.3 µm; 105.9 nuclei per mm² for R= 154.2 µm, 69.2 nuclei per mm² for R= 312 µm substrates), indicating the highest overall cell density for R=154.2 µm substrates. This results in ratios of mean nucleus density curv to btw of 0.16 (R= 59.3 µm); 0.11 (R= 154.2 µm) and 0.14 (R= 312 µm), indicating the overall cell distribution seems to be relative independent from underlying radius of curvature.

These results are comparable to what Pieuchot et al. (*120*) observe for different cells on hill and valley topographies with varying parameters. They showed that cells preferred positioning the nucleus over the convex regions and conclude that this positioning minimizes the nuclear stress (*120*).

Taking a closer look on the cells in the transition zones, as shown in Figure 18 B, some of the hdF on the CurvChip substrates seem to be spanning over the concave gap between the cylindrical curvatures, while others seem to prefer positioning the nucleus in the transition area between curvature and flat area.
The uplifting of cells in concave curvatures was also described by Werner et al. (*97, 211*). They found that sparsely growing mesenchymal cells in concave topographies of varying mesoscale sizes, like partial spheres and cylinders, avoid bending by lifting the cell body up.

The following sections, however, focus on the cells' second way of adaption when growing on cylindrical curvatures, the reorientation along the cylinder axis.

Curvature-induced Cell Alignment on Cylindrical Topographies

As described previously for stronger curvatures κ (1/R of approx. 1/5°µm to 1/150 µm) (*106, 203*), and already shown in the rose histograms in Figure 16 for hdF cultivated on fibronectin-coated substrates, the deviation from axial alignment for sparsely growing hdF1 increases with decreasing curvature κ (increasing radius of curvature R). Displayed in Figure 19 A, the

present work shows that this orientation response continues for smaller substrate curvatures κ, compared to the previously in literature described curvatures.

The median angle of orientation ψ_{Med} (cell) for the smallest curvature (R=312 µm, ψ_{Med}=29.0°) is still (significantly) different from the randomly oriented of hdF1 cultivated on flat PDMS, with ψ_{Med} 47.5° (ideal random orientation 45°). (*1*) This observation is especially remarkable as the radius of curvature of 312 µm is almost four times larger than the cells size itself (approx. 80 µm (*189*)).

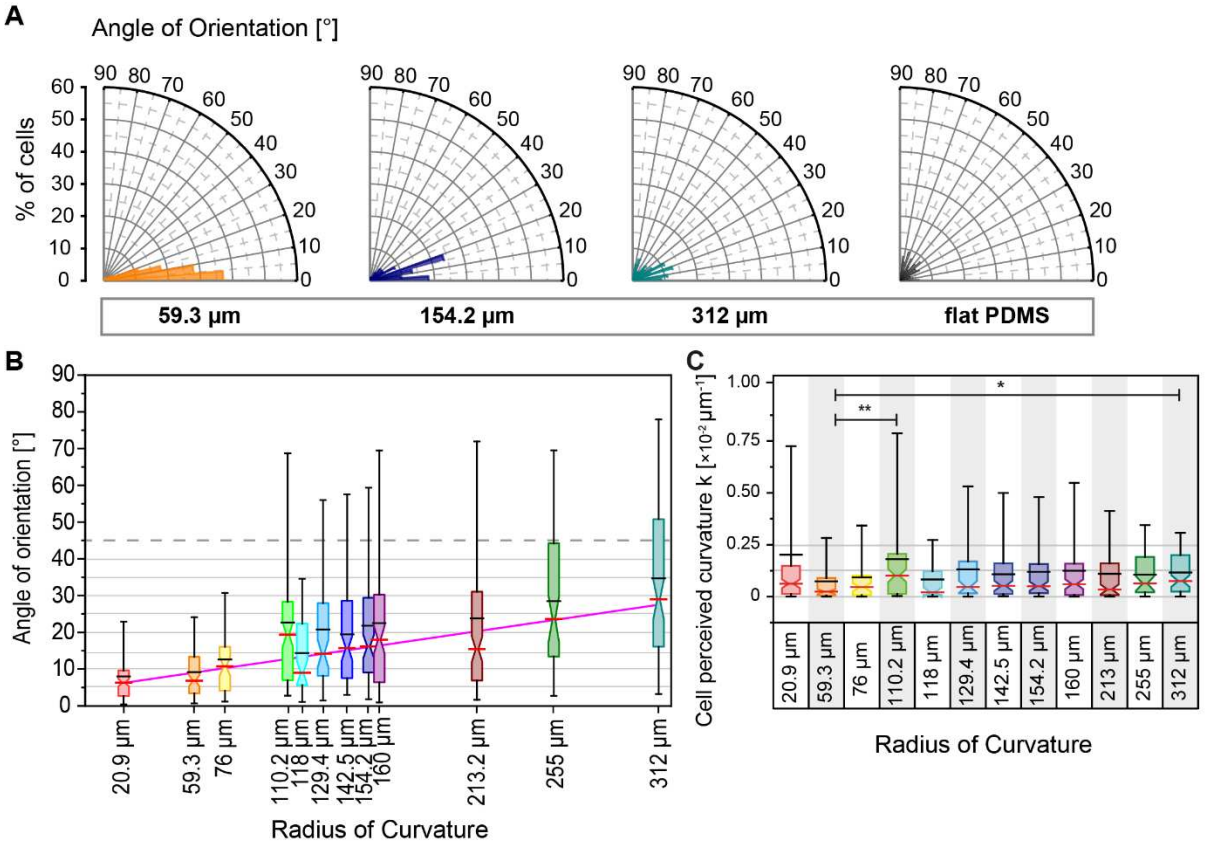

Figure 19 **Dose Response characteristics for hdF1 orientation with increasing radii of curvature R of cylindrical CurvChip substrate coated with FCS.** ***A*** Rose histograms display the percentage of cells oriented in a certain angle in relation to the cylinder axis and dependent on the radius of curvature of the cylindrical PDMS substrate topography. An angle of zero represents perfect alignment with substrate cylinder axis. Bin size 5°. ***B*** Notched box plots of cell angle of orientation as scaled values of the substrate radius of curvature R, median angles of orientations are listed in Table 23 in the Appendix (p. 217). In color box plots show the 25th and 75th percentile, the red horizontal lines indicate the medians, the black horizontal lines the mean, and the whiskers display the 5th and 95th percentile. The pink line represents the linear fit of the median values, Pearson R 0.89707, while the dashed grey line indicates 45° (random orientation). ***C*** Notched box plots of cell perceived curvature k. Description of the boxes as previously stated for B. Asterix indicates statistical significance *p<0.05 significant; **p<0.005 highly significant, using Kruskal-Wallis ANOVA. Sample size $n_{20.9\ µm}$= 117; $n_{59.3\ µm}$= 100; $n_{76\ µm}$= 53;

$n_{110.2\ \mu m}$= 92; $n_{118\ \mu m}$= 63; $n_{129.4\ \mu m}$= 71; $n_{142.5\ \mu m}$= 93; $n_{154.2\ \mu m}$= 104; $n_{160\ \mu m}$= 100; $n_{213.2\ \mu m}$= 117; $n_{255\ \mu m}$= 58; $n_{312\ \mu m}$= 101; n_{flat}= 118. All figure parts adapted from Frey et al. (*1*)

To investigate this dose response relationship between uniaxial curvature and cell orientation in more detail, the angles of orientation ψ were plotted against the substrate's radius of curvature R, using box plots shown in Figure 19 B. Noteworthy is, that, in the range from 20.9 µm to 312 µm, this relationship between the median cell angles of orientation ψ_{Med} and the corresponding radius of curvature (listed in Table 23 in the Appendix) can be estimated with a linear regression line (Pearson R 0.89707; adjusted R^2 0.78521), as indicated by the pink line in Figure 19 B. This regression line suggests, that for increasing radius of curvature, the cell angle of orientation ψ (deviation from cylinder axis) is increasing in a constant manner. (*1*)

This correlation has never been reported before[14], and suggests, that there is some kind of internal setpoint determining the optimal orientation and, therefore, perceived curvature. Like also suggested by Kemkemer et al. (*106*) when describing cell orientation using the automated controller model (cf. Chapter II, Objectives, Curvature Detection: Orientation, Positioning and Migration on Substrates with Curvature).

When calculating and plotting the curvatures k, that the cells perceive when oriented in a specific angle ψ, the presence of this setpoint becomes even more apparent (Figure 19 C).

Generally, "when a cell is oriented along the cylinder axis ((ψ= 0°) the perceived curvature k is zero, whereas for convex substrate curvature [, like the ones investigated here,] the perceived curvature k increases when the cellular orientation deviates from this cylinder axis [(Equation 10, p. 55).] When the cell is oriented perpendicularly to the cylinder axis (ψ= 90°), the curvature k is equal to the curvature of the cylinder κ (κ= 1/R). For instance, if a cell on the R= 312 µm substrate is oriented in ψ= 90° the cell perceives a curvature k= 1/(312 µm) ≈ 0,0032 μm^{-1}. If another cell on this substrate (R= 312 µm) is oriented in ψ= 45°, it perceives a curvature of k=0.5/(312 µm) ≈ 0.0016 μm^{-1}."[15]

Figure 19 C displays the distribution of cell perceived curvature k of hdF1 on the differently curved substrates: "The distribution of perceived curvatures varies within a certain range but only the cells on the R= 59.3 µm substrate show a significantly (p< 0.05) different median perceived curvature k_{Med} compared to the cells on two other substrates"[15] (i.e. R= 110.2 µm, and 312 µm), indicating that the median cell perceived curvature (k_{Med}) seems to be independent of substrate curvature. (*1*)

[14] Meaning before publication of results in Frey et al. (*1*).
[15] Exact quote from Frey et al. (*1*).

When pooling all not significantly different cell perceived curvature data and calculating the median cell perceived curvature (pooled k_{Med}), a value of 0.55 $\times 10^{-3}$ μm^{-1} can be determined, which is equivalent to a median perceived radius of curvature of R= 1807.6 µm (Table 9, p. 82; $hdF1^{all}$). This value can be seen as an approximation of the internal setpoint of cell perceived curvature and implies that hdF1 can perceive curvatures of this magnitude, which, in this case, equals a size of about 22-times their average cell length (*189*). (*1*)

Fitting more realistic, sigmoidal dose response curves to hdF1 median cellular angles of orientation ψ_{Med} obtained from either R=20.9 µm to 312 µm ($hdF1^{ALL}$) cylindrical substrates or R=59.3 µm, 154.2 µm and 312 µm (hdF1) cylindrical substrates, with an upper limit of 45° (random orientation) and a lower limit of 0° (perfect alignment), results in the graphs displayed in Figure 20. These sigmoidal dose response curves verify that the linear regression is a good approximation for the dose response course. Moreover, when comparing the results of the two datasets also shows that using only three radii of curvature (i.e. 59.3 µm; 154.2 µm and 312 µm) already generates a good approximation of the dose response relationship (DRR).
The sigmoidal curves also give a more plausible approximation of how the cellular orientation adaption for radii of curvature out of the investigated range might look like, with the reservation that the perception mechanism does not change for smaller or larger substrate curvatures.

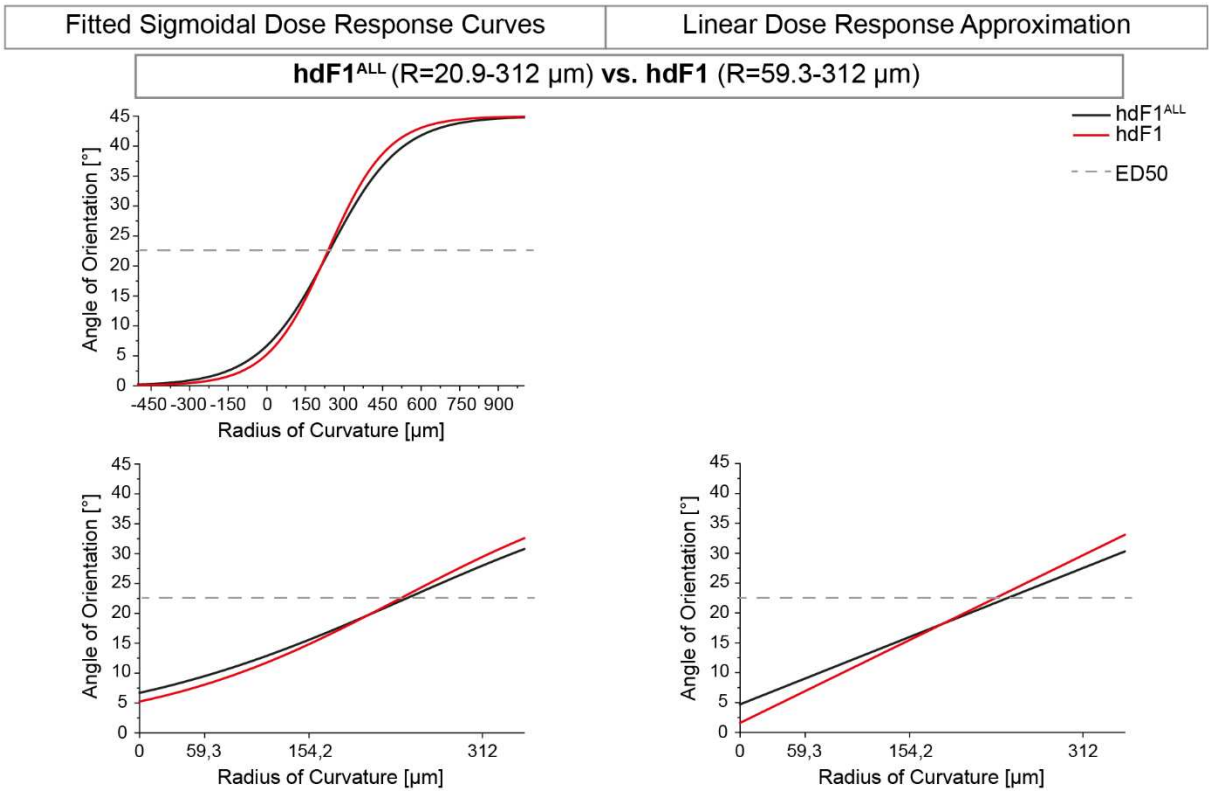

Figure 20 **Cell orientation of hdF1 on cylindrically curved CurvChip substrates with increasing radii of curvature R displayed as dose response relationship.** ***(left)*** Sigmoidal Dose response fit to median angles of orientation (ψ_{Med}) of the, in Figure 19 B, shown orientation distributions, with upper

boundary set to 45° (random orientation) and lower boundary 0° (perfect alignment with cylinder axis). First graph shows whole sigmoidal curve, while the second graph shows the relevant section (R=0-350 µm). ***(right)*** extrapolated linear approximation of the dose response relationship for the investigated section. Linear fit of ψ_{Med} of cells on either twelve substrates with cylindrical topographies with radii of curvature R ranging from 20.9 µm to 312 µm (hdF1^{ALL}) or three substrates with R=59.3 µm, 154.2 µm and 312 µm (hdF1). Intersections with 22.5° dotted line represent half maximal effective dose ED50. Please note, for purposes of better visualization the data points of ψ_{Med} are not included in the fitted graphs. The goodness of the fits is listed in Table 8 (p. 81).

The fact that for ultimately low radius of curvature $\lim_{R\to 0} f(R)$ the alignment varies from perfect alignment is in line with the concept of an automated controller system that has been suggested to be involved in the cellular response to external stimuli, like electrical fields, periodically stretched fields, microgrooves and also curved surfaces (*106*). In the present work, hdF orient their long axis of the cell along the minimal substrate curvature, and the strength of the cell response is dependent on the substrate curvature. However, as described by Kemkemer et al. (*165*) “noise is an unavoidable component of real-world systems” originating from external factors as well as intrinsic properties of the controller components. The in Figure 20, fitted sigmoidal dose response curve, indicated deviation from perfect alignment for $\lim_{R\to 0} f(R)$ (i.e. angle of orientation of approx. 5° to 7° for R=0 (y-intersection)) can be seen as this kind of noise. And albeit engineers try to avoid noise in their technical signal transductions, in biological systems, however, Kemkemer et al. (*165*) describe that this noise might also impose an advantage as it is able to optimize the function of the system, as described for the search mode of white blood cells.

Cell and Nucleus Alignment

To further characterize the difference in cell and nucleus orientation adaption, like shown in Figure 16 (p. 64) for hdF on FN-coated substrates, the difference $\Delta\Psi$ between nucear ψ and cellular ψ of hdF1 on FCS-coated substrates was calculated and are displayed in Figure 21. Median $\Delta\Psi$ are listed next to the graph. Due to the connection of the nucleus to the cytoskeleton, the nucleus orientation in anterior-posterior polarized mesenchymal cells like fibroblasts, is always more or less aligned with the orientation of the cell (*74, 78*). This alignment is also visualized in the heatmaps in Figure 77 (Chapter VIII Appendix, Part V: Supplementary Materials, p. 218).

The alignment difference $\Delta\Psi$ enables a distinction, whether the nucleus or the cell is oriented more axial compared to the other one. Since stronger axial alignment is represented by smaller angles of orientation, this results in positive (Cell ψ< Nucleus ψ) or negative values (cell is less aligned). For cells on flat substrates, however only the absolute value is relevant, since their

angles are measured according to a hypothetical axis and not the cylinder axis as it is done for cylindrical substrates.

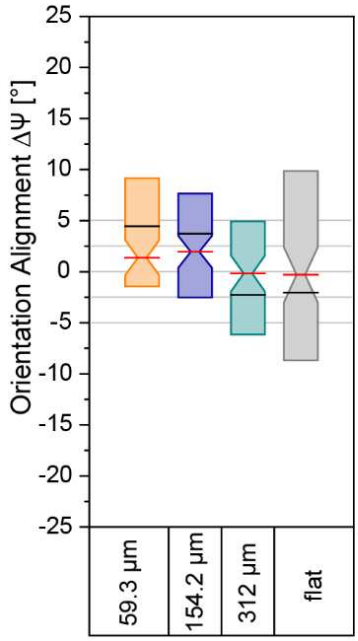

Radius of curvature R	median ΔΨ (Nucleus - Cell)
59.3 µm	1.37°
154.2 µm	1.97°
312 µm	-0.18°
flat	-0.30°

Figure 21 **Difference of cell to nucleus alignment in relation to cylinder axis ΔΨ of hdF1 on FCS-coated cylindrical CurvChip substrates with varying radius of curvature R.** Cell angle of orientation subtracted from nucleus angle of orientation, positive value indicates nucleus is less aligned with the cylinder axis compared to the cell, negative value indicates nucleus is stronger aligned with the cylinder axis than the cell, higher deviation from 0 indicates stronger misalignment of the nucleus and cell orientation. Boxes show 25th and 75th percentile, median line in red, and mean line in black. Grey lines connecting the different graphs are for better comparison. Median values are displayed in the table on the right.

The distribution width (interquartile range IQR) of the cell/nucleus alignment of hdF1 on different substrates decreases on convex cylindrical substrates compared to flat PDMS indicating an overall increased alignment. Additionally, the median ΔΨ is shifted towards positive values for decreasing radius of curvature, indicating that there is a trend towards a stronger alignment of the cell compared to the nucleus on stronger curved substrates.

This trend could be a simple arithmetic shift that is resulting from the curvature induced elimination of values, where the cell is less aligned by increasing curvature, however, it could also point to an impaired reorientation of the nucleus in the cell caused by the substrate curvature.

Donor and Cell type Variation

Dose Response Relationship

To rule out that the observed dose-response behavior of hdF1 is a particularity of the special donor, a second donor of human dermal fibroblasts (hdF2) and another mesenchymal cell-type, human adipose derived stem cells (ASC) were cultivated on three different cylindrical topographies, covering the relevant range of curvatures (R=59.3 µm; R=154.2 µm and R= 312 µm), as well as on flat PDMS as a control surface. All surfaces were coated with FCS prior cell seeding.

Figure 22 A shows the superimposed rose histograms of the cell angle of orientation on the different substrates. All display the same characteristic decrease in axial cell orientation for increasing radii of curvature. Figure 22 B shows the angles of orientation as box plots as a function of substrate cylinder radius R. The ψ_{Med} of cells on R= 59.3 µm substrates range from 10.9 µm, over 7.9 µm to 3.7 µm for hdF1, hdF2 and ASC respectively. For cells on cylindrical topographies with R= 312 µm ψ_{Med} ranges from 27.7 µm (hdF1) over 21.6 µm (hdF2) to 30.0 µm (ASC). (*1*)

The linear dose response approximations (Figure 22 B, pink line) also show the characteristic linearity, that is comparable to the one previously shown in Figure 19 for hdF1 in a range from 20.9 to 312 µm with a strong linear correlation (Pearson R 0.9353 for hdF2 and 0.99924 for ASC, adjusted R^2 can be found in Table 8, p. 81). (*1*)

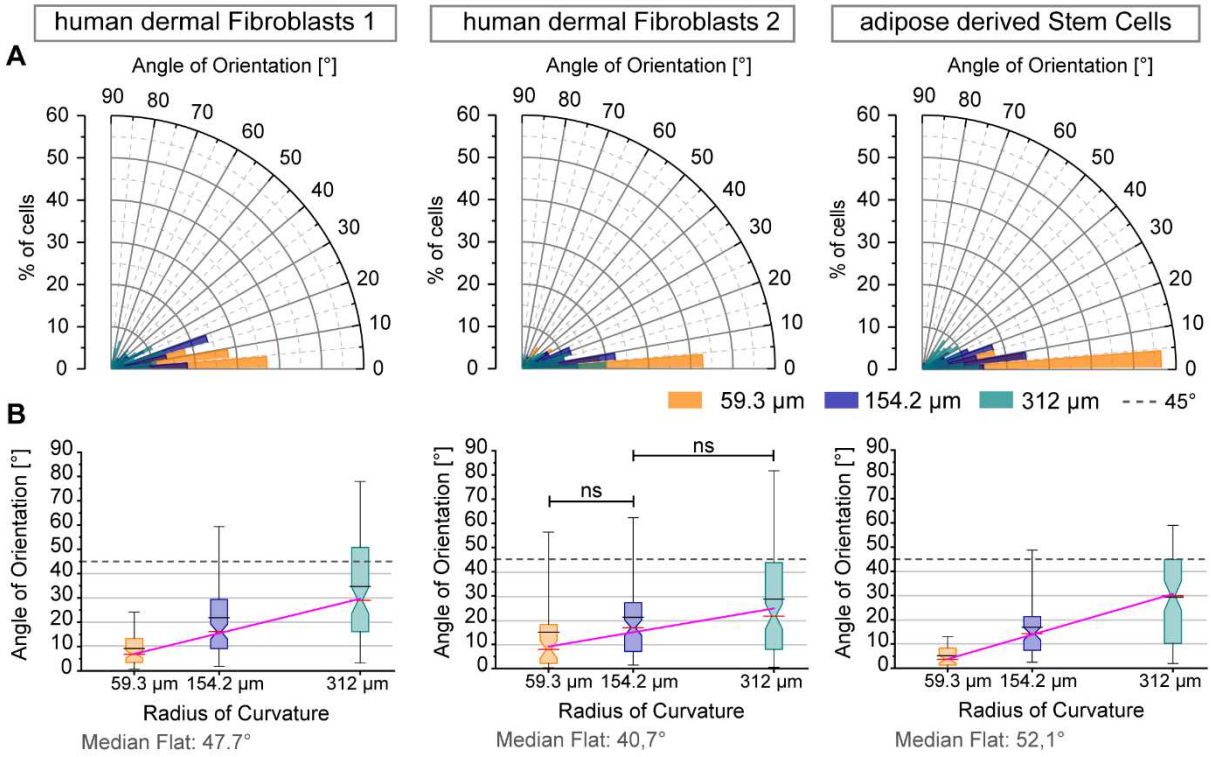

Figure 22 **Donor and cell type variation of cell orientation on cylindrical CurvChip substrates coated with FCS**. Two donors of human dermal fibroblasts (hdF) and one donor of adipose derived

stem cells (ASCs), sparsely growing on FCS-coated PDMS CurvChip substrates with cylindrical curvatures of varying radii. hdF1 data is displayed for better comparison and is identical to the data shown in Figure 19. ***A*** Superimposed rose histograms of cell orientation angle, displaying the percentage of cells oriented in a certain angle in relation to the cylinder axis and dependent on the radius of curvature of the PDMS substrate topography. An angle of zero represents perfect alignment with substrate cylinder axis. Bin size 5°. ***B*** Angle of orientation as a function of radius of curvature and linear dose response relationship approximation of median angle of orientation. In color notched box plots, showing 25th and 75th percentile, the red lines and notch indicate the medians, the black lines the means of each cell orientation distribution. Whiskers display the 5th to 95th percentile range. The pink lines represent the linear fit of the median values, Pearson R $_{hdF1}$: 0.99844; Pearson R $_{hdF2}$: 0.9353; Pearson R $_{ASC}$: 0.99924. Dashed lines display 45°, the expected orientation value for ideal random orientation. Median flat values (below the graphs) report the actual median values of our sample on flat PDMS. ns indicates not significant differences ($p>0.05$) tested with Kruskal-Wallis with Dunn's post-hoc test. Sample size hdF1: $n_{59.3\,\mu m}= 100$; $n_{154.2\,\mu m}= 104$; $n_{312\,\mu m}= 101$; $n_{flat}= 118$; hdF2: $n_{59.3\,\mu m}= 49$; $n_{154.2\,\mu m}= 99$; $n_{312\,\mu m}= 116$; $n_{flat}= 106$; ASC: $n_{59.3\,\mu m}= 46$; $n_{154.2\,\mu m}= 69$; $n_{312\,\mu m}= 82$; $n_{flat}= 107$; Part B adapted from Frey et al. (*1*)

When superimposing the resulting regression lines, like shown in Figure 23 in the right column, it becomes clear, that the linear approximations also exhibit differences, that could be in relation to the underlying perception mechanism. In the given situation, a shift of the dose response relationship (DRR) curve to the left, compared to hdF1, either by an increase in slope or an increase in y-intercept, can be interpreted as a decrease in curvature avoidance, as for the same alignment (angle of orientation) a lower radius of curvature (higher curvature) is needed. Respectively, a shift to the right, either by a decrease in slope or an increase in y-intercept would, therefore, mean an increase in sensitivity or avoidance as the same radius of curvature causes stronger alignment (lower angle of orientation).

Taking a closer look at the plotted linear approximation in Figure 23 right column shows, that the lines intersect in the relevant section, which leads to a situation that is difficult to interpret. This situation is caused since not only the slope but also the y-intercept is changing simultaneously.

This challenge also stresses the clear limitations of the approximations (both linear and sigmoidal) used to visualize the possible connections.

As mentioned previously, the change in y-intercept can be interpreted as a deviation form ideal alignment or in terms of the automated controller concept "noise" of the cell response. A change of this noise, therefore, should also reflect cell internal processes. However, regarding the linear DRR approximation in Figure 23 right column, an extrapolation beyond the investigated range is not reasonable as it is not expected that the linearity continues. However, the measure of the half maximal response (ED50) characteristic for dose response curves, is a common measure in drug related dose-response studies indicating drug efficacy, can here

be interpreted as a measure of curvature sensitivity/avoidance: Lower ED50 values indicate lower sensitivity or more tolerance to bending. Graphical analyzation gives the following sequence: *hdF1 ≤ ASC < hdF2*. And as the values lie within the examined range of 59.3 µm to 312 µm this sequence should be representative, even for the linear dose response approximations.

For a more realistic representation of the DRR, especially outside of the linear range, also sinusoidal dose response curves were fitted to the median angles of orientation ψ_{Med} (cell) of the three investigated radii, like described previously. The curves are visualized in Figure 23 left column, while the first graph represents the whole dose-response curves and the second displays the relevant sections of these curves. Comparing the linear and sigmoidal fits of ψ_{Med} depending on R, shows again, that for the investigated range the linear approximation and the sigmoidal fit are comparable, as previously shown for hdF1 (Figure 20, p. 75): The relative progression of the curves is almost identical, resulting in the same sequence of ED50 values.

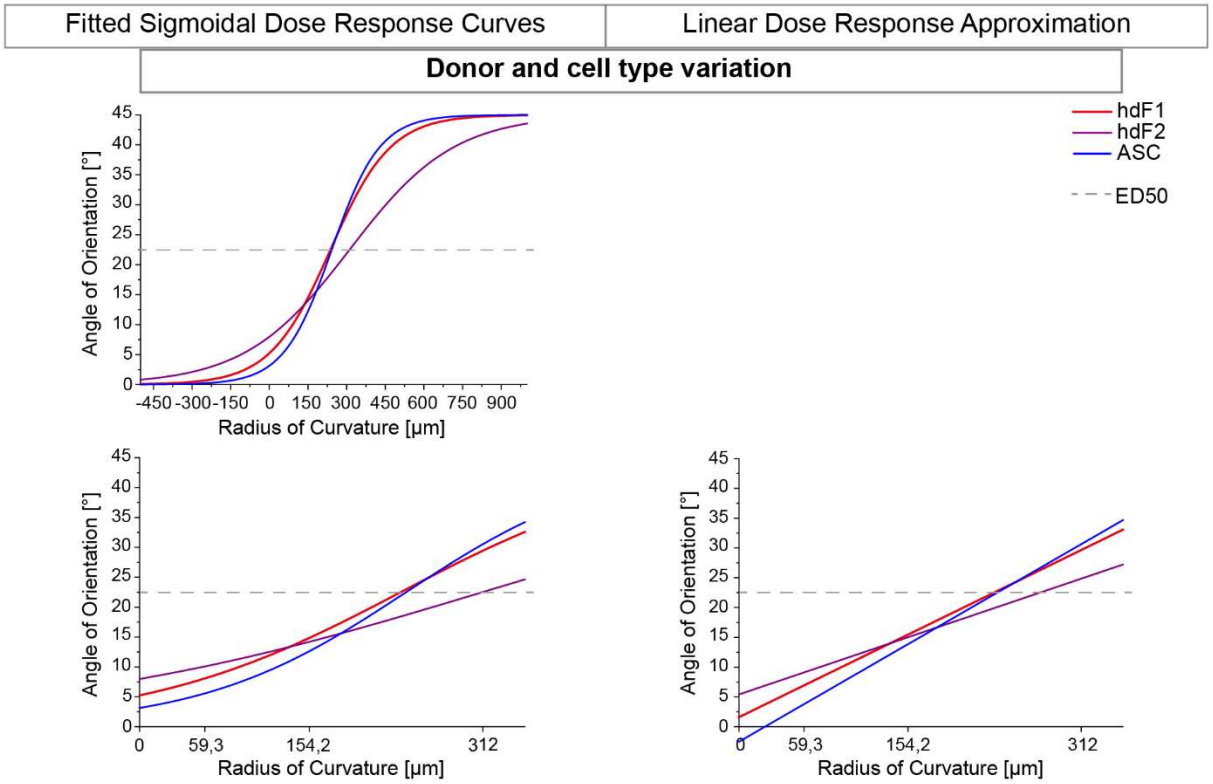

Figure 23 **Cell orientation of hdF1, hdF2 and ASC on cylindrically curved, FCS-coated CurvChip substrates with increasing radii of curvature R displayed as dose response relationship.** ***(left)*** Sigmoidal Dose Response fitted to median angles of orientation, with upper boundary set to 45° (random orientation) and lower boundary 0° (perfect alignment). First graph in each condition shows whole sigmoidal curve, while the second graph shows the relevant section (R=0-350 µm). ***(right)*** extrapolated linear approximation of the dose response relationship for the investigated section. Linear fit of ψ_{Med} of cells on R=59.3 µm; 154.2 µm and 312 µm cylindrical substrates under the specified conditions. Colors represent different conditions as indicated in upper right corner. Intersection with 22.5° dotted line

represents half maximal effective dose ED50. Please note, for purposes of better visualization the data points of ψ_{Med} are not included in the fitted graphs.

The goodness of both fits (linear and sigmoidal) is also confirmed by the high coefficient of determination (R^2 adjusted, see Table 8, p. 81). Examining the previously addressed y-intercepts or noise, which reflect a measure of deviation from ideal alignment, gives the following sequence: *hdF2 > hdF1 > ASC*.
For a simpler/more ideal comparison of dose-response relationships one would expect the values of ED50 and y-intercept to be the same, the present situation, however, is more complex. Compared to hdF1, ASC for instance seem to have a decreased curvature avoidance/sensitivity for small radii of curvature (which is strong curvatures) and a more pronounced avoidance for R ≥ 261.5 µm (intersection with hdF1).
Generally, these results could indicate, that there might be a donor and/or cell type variation in dose response relationships, while the general characteristics, however, are comparable: In all cases, the orientation response decreased for increasing radius of curvature (decreasing curvature). Moreover, it is of note that the variation between the two fibroblast donors (both from adult male prepuce) is stronger than the cell type variation between hdF1 and adipose derived stem cells.

Table 8 **Goodness of linear fit and sigmoidal fit for the radius of curvature/adjustment of the cell angle of orientation-relationship of donor and cell type variation.** Corresponding visualizations are shown in Figure 20 and Figure 23.

Cell specification	**adjusted R^2**	
	Linear Fit Ψ/Radius of curvature	**Sigmoidal Fit** Ψ/Radius of curvature
hdF1^{all}	0.78521	0.77582
hdF1	0.99375	0.97199
hdF2	0.74956	0.73819
ASC	0.99696	0.96223

Cell Perceived Curvature

When looking at the distribution of cell perceived curvatures k of hdF2 and ASC (Figure 24), the low variation again consolidates the previous finding for hdF1, shown in Figure 19 C (p. 73): the perceived curvature seems to be independent of substrate curvature. (*1*)

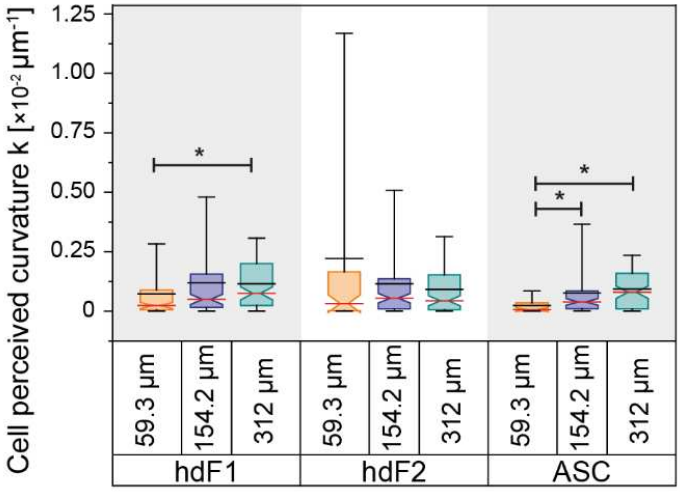

Figure 24 **Cell perceived curvature k of hdF1, hdF2 and ASC on cylindrical, FCS-coated CurvChip substrates with varying radius of curvature R.** Notched Box plots of the cell perceived curvature k of hdF1, hdF2 and ASC on three different, cylindrically curved surface topographies. Radius of curvature as indicated (59.3 µm, 154.2 µm, 312 µm). Notched box plots of 25th to 75th percentile. The red line indicates median, the black line the mean, whiskers display the 5th to 95th percentile range. Sample size hdF1: $n_{59.3\,\mu m}$= 100; $n_{154.2\,\mu m}$= 104; $n_{312\,\mu m}$= 101; hdF2: $n_{59.3\,\mu m}$= 49; $n_{154.2\,\mu m}$= 99; $n_{312\,\mu m}$= 116; ASC: $n_{59.3\,\mu m}$= 46; $n_{154.2\,\mu m}$= 69; $n_{312\,\mu m}$= 82; * significant difference ($p< 0.05$) analyzed by Kruskal-Wallis with Dunn's post-hoc test. Adapted from Frey et al. (*1*)

Table 9 **Pooled median cell perceived curvature (pooled k_{Med}) of hdF1, hdF2 and ASC.** If not indicated differently cells on R= 59.3 µm, 154.2 µm, and 312 µm substrates were used. #calculated from all medians without significant difference as indicated in Figure 24 and Figure 19 C ($hdF1^{all}$); ns means no significant difference ($p>0.05$) using Kruskal-Wallis ANOVA. StDev stands for standard deviation. Adapted from Frey et al. (*1*)

Cell type	Cell perceived median curvature [$\times10^{-3}$ µm^{-1}]	StDev [$\times10^{-3}$ µm^{-1}]	Cell perceived median radius [µm]
$hdF1^{all\,\#}$	0.55	1.7	1 807.6 ^{ns}
hdF1$^{\#}$	0.60	1.4	1 671.4 ^{ns}
hdF2	0.43	2.2	2 307.4 ^{ns}
ASC$^{\#}$	0.53	1.0	1 888.1 ^{ns}

When pooling all not significantly different data from one cell type and calculating the median perceived curvatures (pooled k_{Med}; Table 9) of the cell, there is a slight variation between the different cell origins. (*1*) These differences are expectable based on the variation in DRR and could be indicative for a cell-type/donor specific variation of the internal setpoint. However, when testing for significance, the deviations are not statistically different ($p>0.05$) from each

other, which could indicate that the differences could only show normal biological variation and would decrease for increasing sample size.

Certainly, however, one can conclude that the internal setpoint, wherever it has its origin, is met when the cell orients in an angle where the cell perceives a radius of curvature somewhere between 1671 µm and 2307 µm for cells (1449 µm for nuclei).
As stated previously, this observation would mean, conversely, that cells must be able to perceive curvatures of this magnitude (about 20 to 29 times the average hdF cell length (*189*)). To achieve this perception, cells would need a highly sensitive detection mechanism.

This theory is supported by the findings of van der Putten et al. (*134*) whose results suggest that human myofibroblasts are able to perceive convex, uniaxial radii of curvatures up to approx. 2500 µm.

Summary of Characteristics found for sparsely growing mesenchymal cells

In summary, the above presented results show that mesenchymal cells, independent from donor or tissue origin, prefer to avoid curvature by either positioning between the narrow cylinder structures or by adapting their orientation on the cylindrical curvatures.
The orientational deviation from cylinder axis increases with increasing radius of curvature. Calculating the perceived curvature for the varying angles or orientation suggests the presence of an internal setpoint. This setpoint seems to be reached when mesenchymal cells perceive a curvature of about 1671 µm to 2307 µm for cells (1449 µm for nuclei), which is about 20 to 29 times the average hdF cell length (*189*). This observation indicates the need for a highly sensitive detection mechanism.
This interpretation is supported by the findings of van der Putten et al. (*134*), whose results suggest that human myofibroblasts are able to perceive convex, uniaxial radii of curvatures up to approx. 2500 µm. Together, the findings of van der Putten et al. (*134*), and the in this work presented results suggest that the internal setpoint could be the limit of curvature detection.
Further comparison of nucleus and cell alignment showed that there is a trend towards a stronger axial alignment of the cell compared to the nucleus on stronger curved substrates. Which could by an arithmetic shift that is resulting from the curvature induced elimination of values where the cell is less aligned by increasing curvature, however, it could also point to an impaired reorientation of the nucleus in the cell caused by the substrate curvature.

Effect of Pharmacological Manipulation on Cell Alignment of Sparsely Growing hdF1 on Cylindrical Curvatures

As described in Chapter II Objectives, (Curvature Detection: Orientation, Positioning and Migration on Substrates with Curvature, pp. 25) in more detail previous studies and theoretical models (*166, 171*) suggest an involvement of the contractility state of the actomyosin network and a competition between stress fiber bending and shear stress effect resulting from deformation energy of the cell, with the purpose of reducing the all-over elastic energy. Varying orientation of different cell types is explained based on the dominating energy in the cell: when stress fiber bending associated energy dominates over deformation energy, like it is thought for fibroblasts exhibiting thick stress fiber bundles, a cell is expected to orient longitudinal, along the cylinder axis. Whereas epithelial cells, having relatively thin stress fibers, are predicted to align perpendicularly, in order to partially compensate the dominant contractility-based shear stress by the extension resulting from bending.

More recent publications (*54, 120*) establish the theory that orientation behavior is more a curvature avoidance mechanism. For instance, in situations where curvature cannot be avoided, like convex partial spheres, a compensation mechanism (myosin phosphorylation) was observed to set in necessary to maintain a stable and contractile cytoskeleton, which is energetically demanding and, therefore, unfavorable for cells (*54*). In another situation an involvement of the nucleus, its interplay with the cytoskeleton and the favorably relaxed mechanical state of the nucleus was described to be involved in the avoidance reaction to curved topographies they call “curvotaxis” (*120*).

Systematic Investigation of Involvement of the Cytoskeleton in Curvature Perception

To systematically examine the involvement of the stress fiber, microtubule network, as well as the nucleus in the underlying curvature perception process of cells on cylindrical substrates, pharmacological manipulation of the stress fibers (Blebbistatin/Rho Activator II CN03) and the microtubule network (Nocodazole/Taxol) of hdF1 on cylindrical CurvChip substrates, pre-coated with FCS, was conducted. (*1*)

In short, Blebbistatin is a myosin II inhibitor hindering the interaction with actin, resulting in a reduced cell contractility (*175*), while CN03 is a RhoA activatior which then increases the cytoskeletal contractility via the RhoA/ROCK pathway (*179*). Nocodazole causes depolymerization of the microtubule network, which causes the release and activation of microtubule-bound GEF-H1, which itself activates RhoGTPase RhoA (*117, 180, 181*) causing a simultaneous increase of cell contractility. Taxol stabilizes microtubules by binding to β-tubulin (*183*). This change in microtubule dynamics is accompanied by the formation of large

central bundles of microtubules (*184*) and the redistribution of f-actin forming circumferential bundles (*185, 186*).
The effect of the different manipulation agents on cell and nucleus orientation, the cell/nucleus alignment, the dose response relationship and the perceived curvature of hdF on FCS-coated CurvChip substrates were assessed trying to elucidate the involvement of different cell components in the perception mechanism. Moreover, the impact of both curvature exposure and pharmacological manipulation on morphological adaption was investigated and compared.

Figure 25 shows exemplary fluorescence images of hdF1 on substrates with varying curvature before (w/o) and after the treatment with indicated pharmacological agents: “hdF without pharmacological manipulation possess a spindle-shape morphology with pronounced anterior-posterior polarization and elongation. After treatment with Blebbistatin [(inhibitor of cellular contraction)] […], the cells adopt a more dendritic morphology with many thin protrusions. Increased cell contractility by RhoA activation, either by the Rho Activator II […] CN03 or Nocodazole (microtubule depolymerization with simultaneous RhoA activation (*117*)) leads to a more rhomboid, smooth muscle cell-like morphology, which seems to be even more distinct for Nocodazole (absence of microtubule) compared to CN03. Treatment with Taxol, which is known to stabilize the microtubule, however, induced an epithelioid morphology, with decreased elongation, less pronounced stress fibers and more cortical actin compared to hdF1 without treatment.”[16]

[16] Exact quote from Frey et al. (*1*).

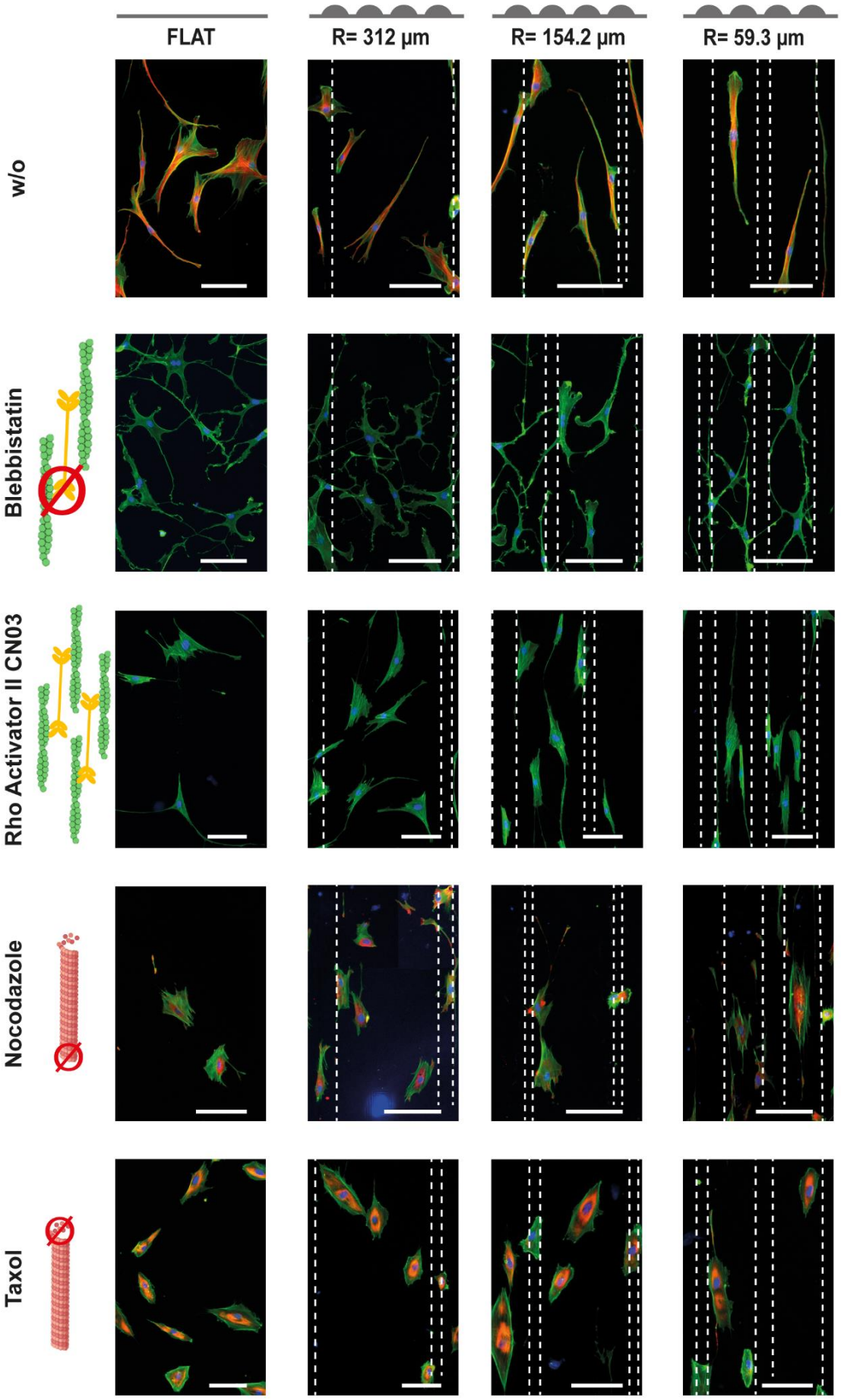
FLAT
R= 312 µm
R= 154.2 µm
R= 59.3 µm
w/o
Blebbistatin
Rho Activator II CN03
Nocodazole
Taxol

← Figure 25 **Fluorescence images of pharmacologically treated hdF1 on different CurvChip substrates with cylindrical topographies and flat PDMS, all coated with FCS.** F-actin in green, nuclei blue and if stained microtubule in red. From left to right substrate curvature is increasing, the dashed lines indicate topography boundaries. First row shows hdF1 without (w/o) pharmacological manipulation, row two hdF1 with impaired stress fiber formation/cell contractility by Blebbistatin-treatment. The third-row displays hdF1 with increased cell contractility due to Rho/ROCK pathway activation by Rho Activator II CN03. Row four shows hdF1 after microtubule depolymerization using Nocodazole, which simultaneously leads to Rho/ROCK pathway activation. The last, fifth row shows hdF1 with Taxol stabilized microtubule. Scale bars 100 µm. For a more detailed view, larger versions of the same images can be found in the Appendix, Part V, pp. 219-223. Adapted from Frey et al. (*1*)

Effect on the Nucleus Density in Different Substrate Regions

Like previously mentioned, on the here utilized cylindrical substrates cells have two ways of avoiding curvature, firstly by placing themselves in the transition zones between the curvatures, and secondly by adapting their orientation on the cylinders along the cylinder axis. Figure 26 shows the nucleus density according to their position on the cylindrical substrates with “curv” meaning on cylindrical curvature and “btw” in the narrow transition zones between the convexities.

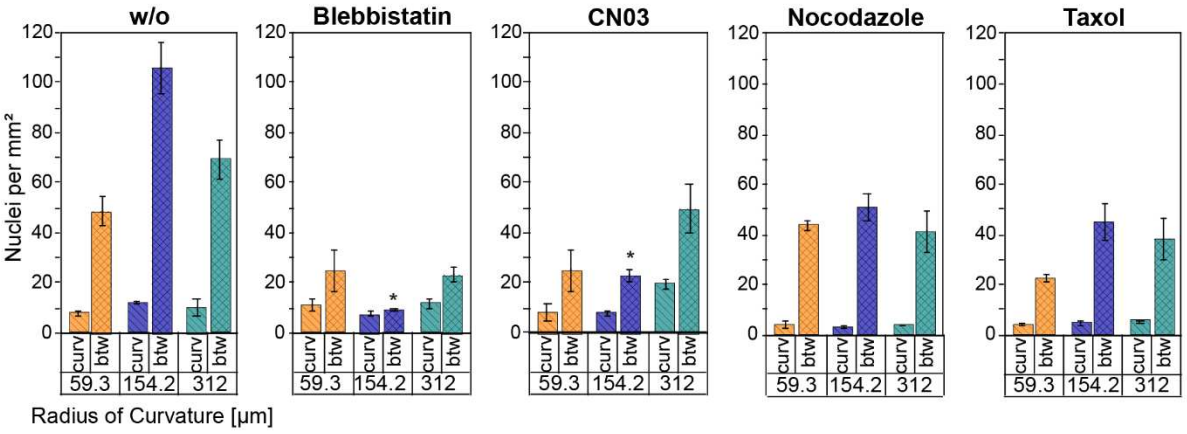

Figure 26 **Nucleus preferred positioning on or between cylindrical regions of FCS-coated CurvChip substrates depending on pharmacological manipulation of the cytoskeleton and cylinder radius of curvature R.** Nucleus density (Mean ±SE). Curv indicates nucleus density on curved regions, btw nucleus density in transition zones between the convex curved regions of the substrates: w/o displays hdF1 without treatment, other pharmacological manipulations as indicated. Sample size w/o: $n_{59.3\,\mu m}$= 443; $n_{154.4\,\mu m}$= 416; $n_{312\,\mu m}$= 390. Blebbistatin: $n_{59.3\,\mu m}$= 287; $n_{154.4\,\mu m}$= 151; $n_{312\,\mu m}$= 220. CN03: $n_{59.3\,\mu m}$= 391; $n_{154.4\,\mu m}$= 254; $n_{312\,\mu m}$= 534. Nocodazole: $n_{59.3\,\mu m}$= 457; $n_{154.4\,\mu m}$= 194;

$n_{312\ \mu m}$= 273. Taxol: $n_{59.3\ \mu m}$= 263; $n_{154.4\ \mu m}$= 229; $n_{312\ \mu m}$= 215. * significant difference to w/o (p<0:05) One-way ANOVA with Dunn-Sidak post-hoc test. Adapted from Frey et al. (*1*)

Comparing the preferred nucleus positioning of hdF1 without pharmacological manipulation with hdF1 after treatment with different pharmacological agents (Figure 26; mean ± SE) shows: Pharmacological manipulation decreases the mean nucleus density in the transition zones (btw), but this trend is only significant for Blebbistatin (R= 154.2 µm, 9.1 nuclei per mm²; p<0.05) and CN03 (R= 154.2 µm, 22.9 nuclei per mm²; p<0.05) treatment. While nucleus density adaption on curvatures is even less prominent, with a slight increase in mean density for manipulation of the cell contractility using Blebbistatin and CN03, and a more noticeable decrease in mean density for both microtubule depolymerization and stabilization, however these findings are again not statistically significant (p>0.05). (*1*)

For better comparison the ratio of nucleus density on curved regions (curv) to nucleus density in areas between the cylinders (btw) was calculated, as listed in Table 10, with a higher value representing a higher relative density of cells on the curvatures. Compared to untreated cells, Blebbistatin followed by CN03 seems to increase the number of cells on the curvature, whereas the effect of Taxol is neglectable, and Nocodazole-treatment decreases the number of cells on curved regions.

Table 10 **Ratio of nucleus density for hdF1 growing on curved regions and between cylinders, dependent on pharmacological manipulation and radius of curvature R of the cylindrical CurvChip topographies.** Calculated from mean densities as visualized in Figure 26.

Substratum	**Ratio of nucleus densities**				
Radius of	(curved regions/area between cylinders)				
curvature R	**w/o**	**Blebbistatin**	**CN03**	**Nocodazole**	**Taxol**
59.3 µm	0.16	0.44	0.33	0.08	0.16
154.2 µm	0.11	0.81	0.35	0.06	0.10
312 µm	0.14	0.50	0.39	0.08	0.14

Altogether, pharmacological manipulation of the cytoskeleton of cells on cylindrically curved substrates has an observable but not statistically significant effect on nucleus density distribution. This observed effect might be related to the fact that relocation to the transition zones is not the only way of curvature avoidance on cylindrical substrates. However, when forming the ratio of density on curvatures to nucleuss density in areas between the curvatures for each condition one can see that Blebbistatin-treatment as well as CN03-treatment seem to decrease curvature avoidance, whereas nocodazole seems to have the opposite effect.

These results suggest that not only the acto-myosin network but also the microtubules might be important for avoiding curvature by reorientation on the cylindrical curvatures and, therefore, when they are manipulated, the first way of curvature avoidance, relocation to the transition zone, seems to be increased, hence the reduced nucleus density on the curvatures. Furthermore, this interpretation is also in line with what Pieuchot et al. (*120*) observed for nocodazole-treated cells using their hill and valley topographies.

Effect on Cell and Nucleus Orientation

To investigate the effect of pharmacological manipulation on the (re-)orientation along the cylinder axis, cell and nucleus orientation adaption after pharmacological manipulation was investigated. Generally, an increased median angle of orientation ψ_{Med} shows a lower curvature avoidance or sensitivity for curvature, as this results in a higher perceived curvature. A decreased ψ_{Med} on the contrary displays an increased curvature avoidance or sensitivity.
"The results, [visualized in Figure 27,] […] indicate that the effect of stress fiber and microtubule manipulation on [adaption of] cell orientation […] [are] small."[17] The overall characteristics of increasing cell ψ_{Med} with increasing radius of curvature R (or decreasing axial orientation with decreasing substrate curvature κ) do not seem to be affected by pharmacological manipulation. (*1*)

Statistical analysis of the cellular median angles of orientation ψ_{Med} (Figure 27 A), show only few significant ($p< 0.05$) changes compared to cells without pharmacological manipulation: The median cell angle of orientation ψ_{Med} of hdF1 treated with Blebbistatin (myosin-II inhibitor) on R= 59.3 µm cylinders is significantly increased (ψ_{Med}= 10.5°) compared to non-treated hdF (ψ_{Med}= 6.8°), indicating that a reduced contractility by Blebbistatin shifts the orientation distribution towards larger angles of orientation (stronger perceived bending due to increased curvature). An increase in cell contractility, evoked by the Rho activator II CN03-treatment, on the contrary, induces a trend towards smaller orientation angles (increased sensitivity/bending avoidance), as indicated by the highly significant ($p< 0.005$) reduction of ψ_{Med} on R= 154.2 µm substrates (ψ_{Med}= 11.4° instead of 16.1°). (*1*)

This trend towards smaller median cell angles of orientation ψ_{Med} in cases of increased contractility can also be observed for the cells with depolymerized microtubules simultaneously causing an increase in cell contractility, as induced by Nocodazole. This observed trend is underlined by the highly significant ($p<0.005$) decrease of ψ_{Med} on R= 312 µm substrates from ψ_{Med}=29.0° (w/o) to 17.4° (Nocodazole). Interestingly, cells with stabilized microtubule network,

[17] Exact quote from Frey et al. (*1*).

a result of Taxol-treatment, also show ψ_{Med} shifts towards smaller cell orientation angles (increased sensitivity/bending avoidance), without any statistically significant adaption. (*1*)

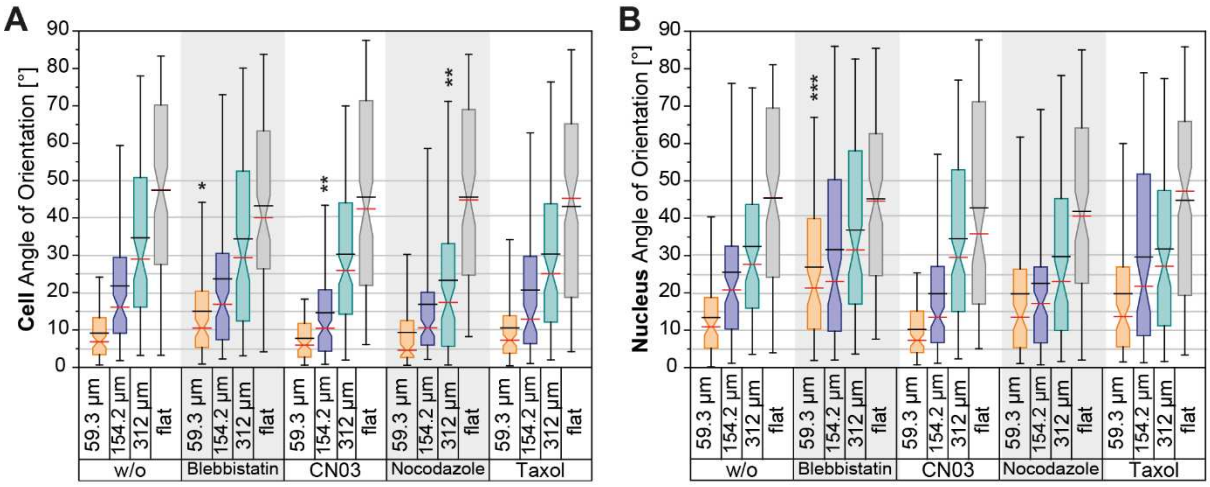

Figure 27 **Effect of pharmacological manipulation on cell** (***A***) **and nucleus** (***B***) **angle of orientation of sparsely growing hdF1 on FCS-coated cylindrical CurvChip topographies with indicated radii of curvatures R.** Notched box plots, with boxes showing the 25th and 75th percentiles, the red lines indicate the median and the black lines display the mean, whisker show the 5th and 95th percentile range. Sample size cell/nucleus $n_{w/o}$= 100-118/95-117; $n_{Blebbistatin}$= 99-110/98-110; n_{CN03}= 115-171/115-171; $n_{Nocodazole}$= 101-104/98-101; n_{Taxol}= 100-131/100-131; * Significant ($p< 0.05$), ** highly significant ($p<0.005$), *** most significant ($p<0.001$) to w/o ; ns not significant ($p> 0.05$) as indicated; Kruskal-Wallis with Dunn's post-hoc test. Adapted from Frey et al. (*1*)

Since nucleus positioning and rotation within the cell is also directly affected by both actomyosin and microtubule networks (*74, 76*) and latest results suggest an involvement of the nucleus in "curvotaxis" (*120*), the orientation adaption of nuclei in response to pharmacological manipulation and substrate curvature were also investigated and are displayed in Figure 27 B. The effect of the manipulation on nucleus orientation, is even less distinct for the different pharmacological manipulation as it is for cell orientation. (*1*)

The reduced contractility by Blebbistatin-treatment also causes a shift in nucleus orientation towards larger angles of orientation on cylinders with lowest radius of curvature/strongest curvature (most significant $p<0.001$ for R=59.3 µm). Moreover, for nuclei this trend is also observable on the other curved substrates. Like also described for cell orientation, CN03-induced increased contractility leads to a shift of the median towards smaller angles, however, for nuclei this trend is not statistically significant. (*1*)

While the results upon manipulation of the stress fiber system are comparable between nucleus and cell orientation, interference with microtubules demonstrate diverse tendencies in nucleus orientation adaption. Microtubules' depolymerization, in combination with an

increased contractility caused by Nocodazole, results in a tendential increase in nuclear median orientation angle ψ_{Med} on the large curvature (R= 59.3 µm, lower avoidance) but a tendency towards lower median angles on R= 154.2 µm and 312 µm substrates (increased avoidance). Microtubule stabilization by means of Taxol, on the other hand, shows a trend towards larger median nuclear angles of orientation ψ_{Med} (decreased curvature avoidance) on strongly and intermediately curved substrates (R= 59.3 µm and R=154.2 µm). (*1*)

Altogether, the fact that the effects of pharmacological manipulation on cell and nucleus orientation are relatively weak indicates that the underlying mechanism for orientation perception and adaption seems to be highly robust. Yet, statistically non-significant tendencies can be observed for every pharmacological manipulation: Myosin inhibition by Blebbistatin induces a shift towards larger median orientation angle ψ_{Med} (decreased curvature avoidance) for both cells and nuclei. The ψ_{Med} of cells with Rho activation by CN03 tend to be smaller (increased curvature avoidance), nucleus ψ_{Med} adaption is not so distinct. The manipulation of microtubules does not show clear tendencies and indicate differences in cell and nucleus adaption. Taxol-treatment induces an increased avoidance (smaller median angle of orientation ψ_{Med}) for cells but a decreased curvature avoidance, larger ψ_{Med}, for nuclei, while Nocodazole-treatment shows inconclusive adaption behavior for nuclei on differently curved substrates. (*1*)

Effect on the Alignment of Cell and Nucleus

To investigate the above-mentioned difference in cell and nucleus orientation adaption, the difference between the angle of orientation of nuclei ψ_{Nuc} and cells ψ_{Cell}, $\Delta\Psi$, was calculated (ψ_{Nuc} subtracted by ψ_{Cell}) and displayed in Figure 28, the corresponding medians are listed in Table 11. As previously stated, the difference enables a distinction, whether the nucleus or the cell is oriented more axial compared to the other one resulting in either a positive (ψ_{Cell} is more aligned) or negative value ($\psi_{Cell} > \psi_{Nuc}$). Furthermore, the distribution of the values indicated by the box plot width (interquartile range IQR) enables an estimation of the overall intensity of the deviation between nucleus and cell orientation. For cells on flat substrates, however, the sign of the value is irrelevant, since the angles are measured according to a hypothetical axis and not the cylinder axis, as done for cylindrical substrates.

The distribution (IQR) of the cell/nucleus alignment of hdF1 on different substrates decreases on convex cylindrical curvature compared to flat PDMS indicating an increased alignment. This increased alignment on curved substrates compared to flat PDMS is also visible for the investigated pharmacological manipulations, except for CN03.

However, when comparing the different pharmacological manipulations with the w/o condition shows, the IQR is increased by all pharmacological manipulations on all substrates, indicating

a decreased nucleus cell alignment. The only exception is RhoA activation by CN03: The distribution width of cell/nucleus alignment on flat PDMS and R=59.3 µm treated with CN03 is decreased compared to hdF1 without treatment, indicating a better alignment on these substrates. Moreover, the increase in IQR on R=154.2 µm and R=312 µm is smaller compared to the other manipulation conditions.

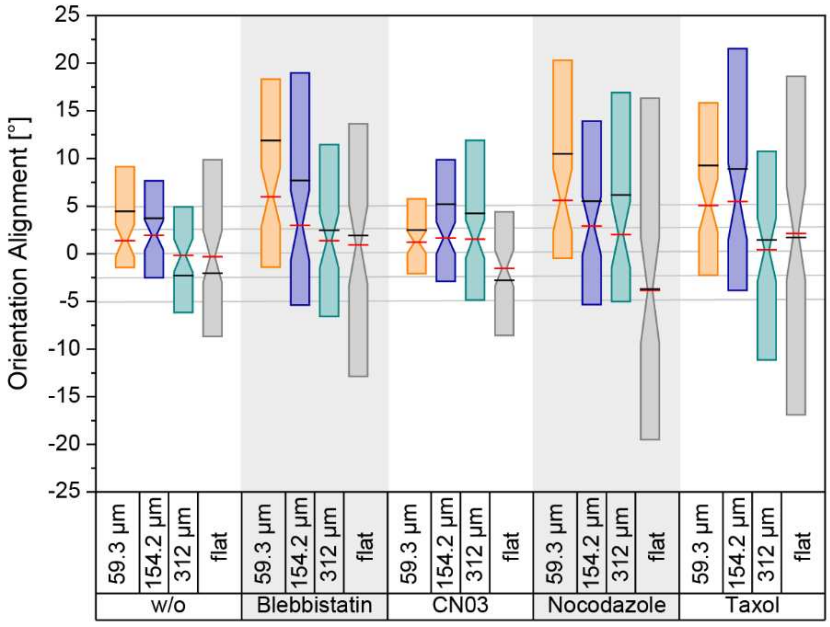

Figure 28 **Difference of cell to nucleus alignment in relation to cylinder axis ΔΨ of hdF1 on FCS-coated CurvChip substrates with varying radius of curvature R or flat PDMS.** Cell angle of orientation ψ_{CELL} subtracted from nucleus angle of orientation ψ_{NUC} ($\Delta\Psi=\psi_{NUC} - \psi_{CELL}$), positive value indicates nucleus is less aligned compared to the cell, negative value indicates nucleus is stronger aligned than the cell, higher deviation from 0 indicates stronger misalignment of the nucleus and cell orientation. Boxes show 25th and 75th percentile, median line in red and mean line in black. Grey lines connecting the different graphs are for better comparison and indicate a difference of 5; 0; -5. Median values are displayed in Table 11. Sample size range $n_{w/o}$=95-117; $n_{Blebbistatin}$=98-110; n_{CN03}=115-171; $n_{Nocodazole}$=98-101; n_{Taxol}=100-131.

Taking a closer look at the median ΔΨ (cf. Table 11) shows, for hdF1 without pharmacological manipulation, the median ΔΨ decreases with increasing radius of curvature (decreasing curvature). Interestingly, this shift towards larger median ΔΨ is also observable for all pharmacological manipulations, although hdF1 treated with CN03 causing a decrease in ΔΨ distribution again shows some deviations from this trend.

Generally, pharmacologically manipulated hdF1 show a tendency to be stronger aligned with the cylinder axis than their nuclei, independent from substrate radius of curvature or type of manipulation, as shown by median ΔΨ>0. This tendency could indicate an impaired nucleus rotation mechanism caused by curvature or a varying curvature sensitivity.

Furthermore, the median difference between nucleus and cell alignment is strongly increased when manipulating the microtubule network and decreasing cell contractility, which can be explained by the fact that both, a functional microtubule and stress fiber network are needed for the reorientation and positioning of the nucleus (*74*). This proposed explanation is also in line with the observed tendency of a decreased median $\Delta\Psi$ for CN03-treated cells. They have a functional microtubule system and increased cell contractility, which should hence result in stronger reorientation and cell-nucleus alignment.

On flat PDMS, however, all pharmacological manipulations shift median cell/nucleus alignment, as indicated by an increased median $|\Delta\Psi|$, indicating an effect of pharmacological manipulation on the alignment mechanism. It is unclear, why the median $|\Delta\Psi|$ of CN03-treated hdF1 on flat PDMS is also increased, since the opposite would be expected based on the above-mentioned theory involving a functional microtubule system and increased cell contractility, and like it is also indicated by the decreased interquartile range.

Table 11 **Median difference of nucleus and cell alignment in relation to cylinder axis $\Delta\Psi$ of pharmacologically manipulated hdF growing on cylindrical CurvChip substrates with FCS coating and varying radius of curvature R.** The median calculated from ψ_{Nuc}- ψ_{Cell} from each cell. A positive value indicates nucleus is less aligned compared to the cell, a negative value indicates nucleus is stronger aligned than the cell, higher deviation from zero indicates stronger misalignment of the nucleus and cell orientation. Caution: For flat PDMS only the absolute values is relevant, since here the angles are measured in relation to a hypothetical axis.

Radius of curvature R	w/o	Blebbistatin	CN03	Nocodazole	Taxol
59.3 µm	1.37	5.99	1.22	5.60	5.08
154.2 µm	1.96	2.98	1.66	3.40	5.48
312 µm	-0.18	1.39	1.54	2.02	0.42
flat	-0.30	0.93	-1.52	-3.84	2.14

Altogether, one can conclude, that both stress fibers and microtubule seem to be involved in the cell/nucleus alignment response on curvature, and that all pharmacological agents seem to negatively interfere with the cell-nucleus alignment indicated by an increased $|\Delta\Psi|$. Results suggest that this interference might be caused by an impaired nucleus rotation or a varying curvature sensitivity of the nucleus, mostly. On flat PDMS the influence of microtubule depolymerization has the strongest effect on cell/nucleus alignment, represented by a wide IQR and a large $|\Delta\Psi|$, on curved surfaces however, the alignment is comparable to the one resulting from Blebbistatin-treatment.

Effect on the Dose-Response Relationship

With changing angle of orientation also the dose-response relationship (DRR) is affected. Like described before and visualized in Figure 19 for hdF1 and Figure 22 for donor and cell type variation, this relationship can be approximated by a linear regression line in the observed range of radius of curvature (R=59.3 µm to 312 µm). Figure 29 A visualizes this relationship for hdF1 before and after different pharmacological treatments.

If publications (*166, 171*), suggesting an involvement of the cytoskeletal stress fiber system in curvature perception, are valid, one would expect that the DRR of pharmacologically manipulated hdF, reflect the different states of cellular stress caused by the corresponding treatment. In the given situation, a shift of the DRR curve to the left, compared to hdF1 w/o, can be interpreted as a decrease in curvature avoidance. Based on the theory of stress fiber-involvement in the perception mechanism, this observation would be expected for a decreased amount of stress fibers resulting in a lower contractility, like it is caused by Blebbistatin-treatment. Respectively, a DRR shift to the right, would, therefore, mean an increase in sensitivity or avoidance as the same radius of curvature causes stronger alignment (lower angle of orientation), which would be expected for CN03-treatment, and if stress fibers are involved, also for Nocodazole.

Looking at the plotted regression lines for cell orientation response in Figure 29 A, and the sigmoidal cell DRR fit of the relevant area in Figure 29 D again validates the goodness of the linear approximation: The relative course of the curves is almost identical. The goodness of both fits is also confirmed by the high coefficient of determination (R^2 adjusted, see Table 12).

Furthermore, the ED50 sequence, a measure for curvature sensitivity, with lower values indicating lower sensitivity (causing cells to tolerate stronger bending), is the same for both linear and sigmoidal fit: *Blebbistatin* ≤ *w/o* < *Taxol* ≤ *CN03* << *Nocodazole*. However, for the course outside the linear area, the linear approximation and the sigmoidal fit have notable differences. These differences, however, were expected, since the linearity is not thought to continue endlessly. Interestingly, the sequence of the previously addressed y-intercepts of the sigmoidal fit, a value for the inherent system noise or deviation form ideal alignment, is the same compared to ED50: *Blebbistatin* > *w/o* ≥ *Taxol* > *CN03* ≥ *Nocodazole*.

Generally, the ED50 sequence for cell orientation is mostly consistent with what is expected based on the theories of stress fiber involvement in the perception mechanism.

What is unexpected based on the previously published findings and suggested mechanism, however, is the difference between the hdF1 w/o and the dose-response curve for hdF1 treated with Taxol. The deviation is comparable to the difference between hdF1 w/o and treatment

with CN03, especially with increasing radius of curvature, representing an increase in sensitivity.

Rovensky, et al. (*167*) describe, that epithelioid cells with cortical, circular actin bundles and, therefore, reduced stress fibers, as also induced by Taxol (*185*) (cf. Figure 25, p. 87), have a tendency to bend around cylinders with a reduced elongation and orientation along the substrate axis. This finding would be reflected by an increase in ψ_{Med} and, therefore, a reduced sensitivity (DRR shift to the left). Nothing, however, is reported about the microtubule state in the epithelioid cells used by Rovensky et al. (*167*). This discrepancy again suggests that functional microtubules might be important for the cell response to uniaxial curvature.

Another interesting observation is, that the curves of hdF1 w/o and Blebbistatin-treatment intersect in the observed range (at approx. R=305 µm and ψ=29°). This intersection could be interpreted in a way, that for larger R treatment with Blebbistatin causes an increase curvature sensitivity, whereas for R<305 µm a decrease in sensitivity takes place. One can only speculate about the meaning, if there is one, but one possible explanation could be that above this threshold the influence of the (reduced) actomyosin dependent cytoskeletal contractility on the response to curvature decreases while other factors might gain in importance. More studies would be needed to be able to make a more substantiated statement.

The more realistic sigmoidal fit or the DRR, was also conducted for cell ψ_{Med} against the curvature κ=1/R (cf. Appendix Part V: Supplementary Materials; Figure 83 B and D, p. 224). Since the goodness of fit (cf. Chapter VIII Appendix Part V: Supplementary Materials; Table 25, p. 225) is better for the curves that take the radius of curvature into account compared to those factoring in the curvature, and the using the radius of curvature R is more intuitive compared to the curvature, only those using the radius of curvature are discussed here.

Based on the indications that the nucleus might play an important role in the cell response to uniaxial curvature, sigmoidal dose response curves were also fitted to nuclear ψ_{Med} of hdF on differently curved substrates and under different pharmacological manipulations, as shown in Figure 29 C and E. As expected, the DRR of the nucleus differ from cell DRR. To a certain extent unexpected is, that the influence of the different pharmacological agents differs in their sequence depending on the radius of curvature R, as also depicted by the intersections of the different conditions. For ultimately small R ($\lim_{R\to 0} f(R)$, represented by y-intercept) Blebbistatin, Taxol and nocodazole decreased nucleus curvature sensitivity compared to w/o (sequence: Blebbistatin> Taxol> Nocodazole> w/o> CN03), while on larger substrate radii of curvature R (represented by ED50: Blebbistatin< Taxol< w/o< CN03< Nocodazole), Nocodazole changes its influence and is now (large R) increasing curvature sensitivity.

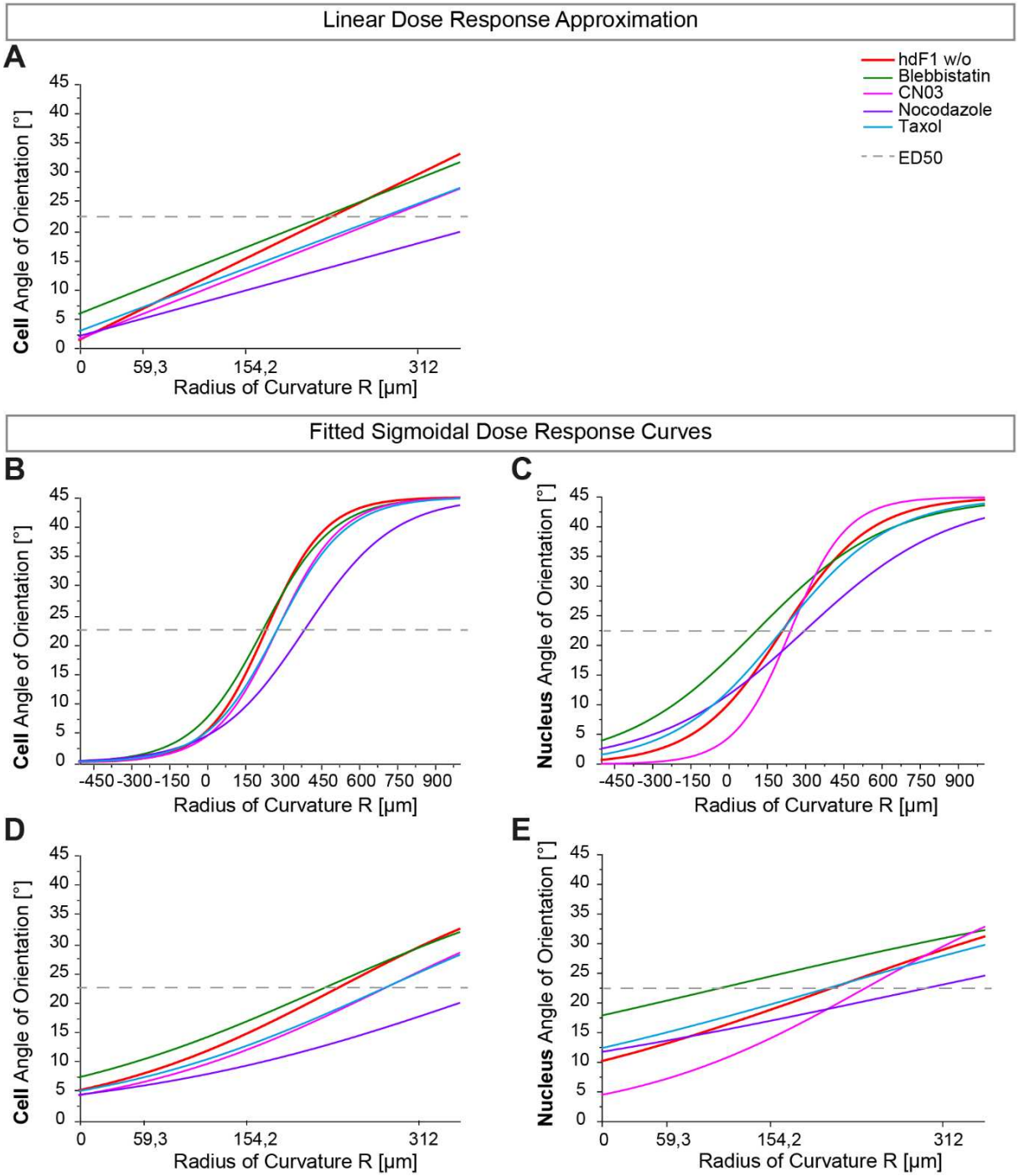

Figure 29 **Cell and nucleus response to cylindrical CurvChip surfaces with increasing radii of curvature R and with and without pharmacological manipulation displayed as dose response relationships**. ***A*** extrapolated linear approximation of the dose response relationship for the investigated section. Linear fit of ψ_{Med} of cells on R=59.3 µm; 154.2 µm and 312 µm cylindrical substrates under the specified conditions. ***B-E*** Sigmoidal Dose Response fit to median Angles of orientation, with upper boundary set to 45° (random orientation) and lower boundary 0° (perfect alignment). ***B*** and ***C*** show the whole curves, ***D*** and ***E*** show relevant section. ***A***, ***B*** and ***D*** cell angle of orientation. ***C*** and ***E*** for nucleus angle of orientation. Colors represent different conditions as indicated in upper right corner. Intersection with 22.5° dotted line represents half maximal effective dose ED50.

Please note, for purposes of better visualization the data points of ψ_{Med} are not included in the fitted graphs. The goodness of the fits is listed in Table 12.

Generally, Taxol has the least pronounced effect on the nucleus, with a slight decrease in curvature avoidance for large and intermediate substrate curvatures (κ=1/59.3 μm^{-1} to 1/154.2 μm^{-1}) and a weak increase in avoidance for small curvatures. Contractility inhibition using Blebbistatin on the contrary shows a clear decrease in curvature avoidance, although the effect is decreasing with increasing R. This decrease can also be observed for CN03-treatment: a pronounced increase in curvature avoidance on small radii of curvature, that is decreasing with increasing R. While the DRR of nuclei from Nocodazole-treated cells show the opposite, a weak effect on substrates with small radii of curvature and a pronounced curvature avoidance for larger R.

Table 12 **Goodness of linear fit and sigmoidal fit for the relationship of the adjustment of the median angel of orientation ψ_{Med} for changing radius of curvature R, as visualized in Figure 29**.

	adjusted R^2		
Condition	**Linear Fit *Cell*** Ψ/Radius of curvature	**Sigmoidal Fit *Cell*** Ψ/Radius of curvature	**Sigmoidal fit *Nucleus*** Ψ/Radius of curvature
hdF1 w/o	0.99375	0.97199	0.75101
Blebbistatin	0.99461	0.99999	0.88933
CN03	0.99465	0.99393	0.99993
Nocodazole	0.97769	0.93256	0.99778
Taxol	0.99293	0.99939	0.85705

These findings suggest that for increasing radius of curvature the status of the stress fiber system might become less important for the nucleus orientation, while the presence or absence of microtubule seems to be increasingly relevant.

Effect on the Median Perceived Curvature and Effect on the Pooled Perceived Curvature

As they are directly related and, therefore, an increase in angle of orientation results in a higher perceived curvature k (lower perceived radius), the changes in perceived curvature, shown in Figure 30, are similarly small as to those concerning the angle of orientation, shown in Figure 27. Only a few significant changes were recognizable, which is again suggestive of a highly robust mechanism, as stated previously. (*1*)

Statistically non-significant tendencies, already described for the adaption of the angle of orientation, could also be observed for every pharmacological manipulation: Blebbistatin

induced a shift towards higher cell and nucleus perceived curvature, while the perceived curvature of cells with Rho activation by CN03 tend to be smaller (lower ψ_{Med}). Since cells with stabilized microtubule network, as a result of Taxol-treatment, also show tendencies of shifts towards smaller k_{Med} or median cell orientation angles ψ_{Med} it is not clear if the effect of Nocodazole (shift towards smaller ψ_{Med}) is only caused by the concomitant Rho activation (by release of microtubule bound GEF-H1) or if there is an effect caused by an impaired microtubule network. (*1*)

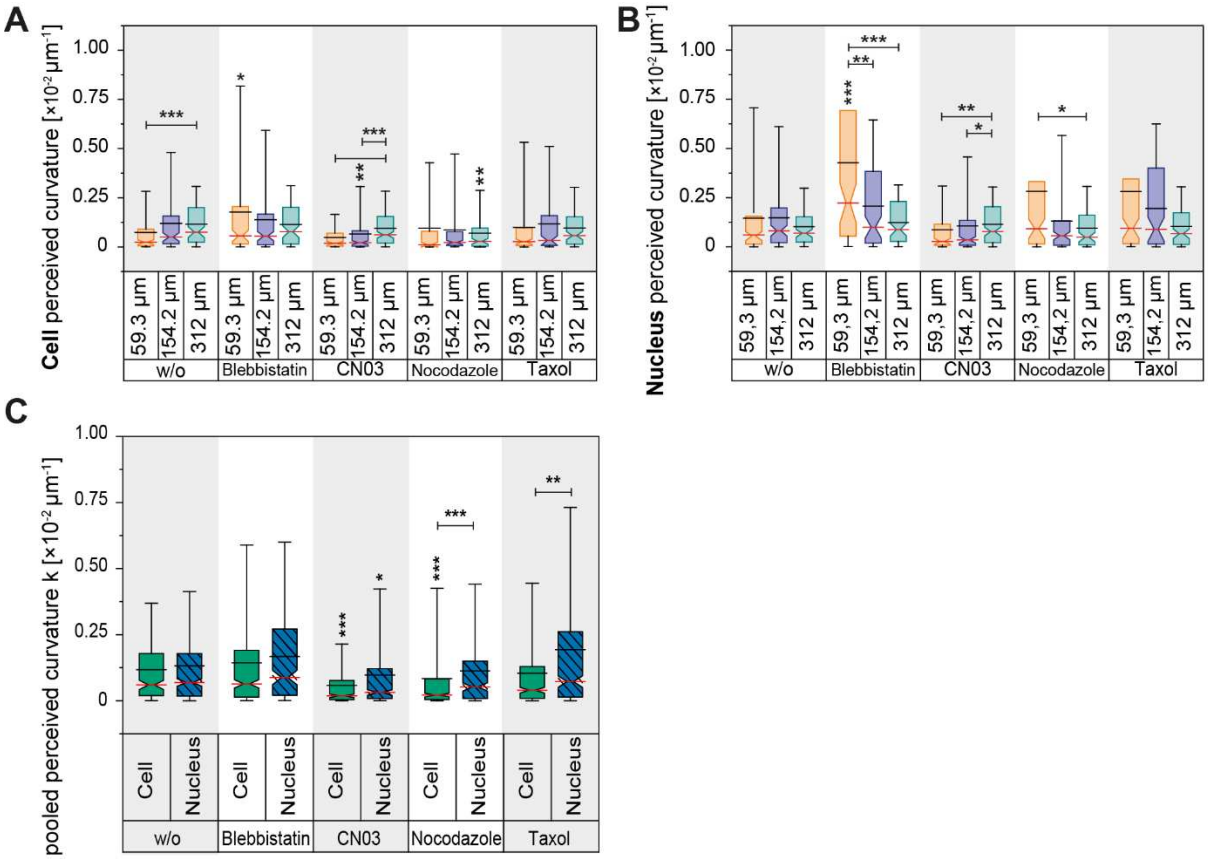

Figure 30 **Effect of pharmacological manipulation on cell** (***A***) **and nucleus** (***B***) **perceived curvature k as well as on pooled median perceived curvature** (***C***) **of sparsely growing hdF1 on FCS-coated cylindrical CurvChip substrates with different radii of curvature R**. Median values for ***C*** are displayed in Table 13. Notched box plots Boxes showing the 25th and 75th percentiles, the red lines indicate the median and the black lines display the mean, whisker show the 5th and 95th percentile range. Sample size cell/nucleus $n_{w/o}$= 100-118/95-117; $n_{Blebbistatin}$= 99-110/98-110; n_{CN03}= 115-171/115-171; $n_{Nocodazole}$= 101-104/98-101; n_{Taxol}= 100-131/100-131; * Significant ($p< 0.05$), ** highly significant ($p<0.005$), *** most significant ($p<0.001$) to w/o or as indicated; ns not significant ($p> 0.05$) as indicated; Kruskal-Wallis with Dunn's post-hoc test. All figure parts adapted from Frey et al. (*1*)

Interpreting these trends in terms of curvature sensitivity and avoidance: Blebbistatin-treatment seems to decrease the curvature sensitivity of both cell and nucleus by shifting their orientation towards larger perceived curvature (larger angles of orientation ψ_{Med}, equals stronger bending by larger curvature) compared to hdF1 w/o, and thus decrease the curvature avoidance. Rho

activation by CN03 induces an increase in curvature sensitivity for the cell, or in other words, an enhanced curvature avoidance, and the same can be observed for Nocodazole as well as for Taxol-treatment of hdF1. Nuclei of Taxol-treated cells, however, are shifted to a decreased curvature avoidance (larger angles of orientation ψ, equals smaller perceived curvature), while the nuclei of cells treated with Nocodazole and CN03 do show mixed tendencies. (*1*)

As the perceived curvature seems to reflect an internal setpoint a cell aims to reach (or possibly the limit of curvature perception), the pooled median perceived curvature (pooled k_{Med}), was calculated for both cell and nucleus like described before, as a measure for this internal setpoint. The results are displayed in Figure 30 C and Table 13. (*1*)
Only pharmacological manipulations known to increase cell contractility (CN03 and Nocodazole) lead to significant ($p<0.001$) changes in pooled cell k_{Med}, independent from microtubule polymerization state: In these cases, larger radii of curvature are perceived (that is smaller curvatures) compared to w/o, showing an increased curvature avoidance, or increased setpoint. The pooled k_{Med} upon treatment with the pharmacological agents, again show a weaker adaption for the perceived curvatures of the nuclei compared to cells' pooled k_{Med}. Notable, however, is the difference between CN03, which increases cellular contractility via the RhoA/ROCK pathway and Nocodazole, increasing contractility due to depolymerization of microtubule, sequentially also activating the RhoA/ROCK pathway: While both significantly affect cell orientation and thus cell perceived curvature, the nucleus orientation is only significantly affected when microtubules are still intact. (*1*)
When comparing all pooled cell k_{Med} and corresponding pooled nucleus k_{Med} (Figure 30, as indicated and Table 13 asterisks in brackets) we can observe a trend towards a higher perceived curvature (smaller radius) for nuclei compared to the cell, which was also indicated by the cell nucleus alignment (pp. 91). When the microtubule network is manipulated, this trend becomes highly significant which could be explained by the fact that the functional microtubule network is known to be involved in nucleus rotation within the cell (*74, 212*). (*1*)

The finding, that enhanced cell contractility via the RhoA/ROCK pathway (CN03 and Nocodazole) decreases the pooled cell k_{Med} seem to consolidate previous assumptions that the stress fiber system generating cell contractility, enforced by the Rho/ROCK pathway, is somehow involved in the curvature perception mechanism, or maybe even in defining the internal setpoint (*166, 171*). (*1*)
However, three things are noteworthy: Firstly that interfering with the myosin II-dependent contractility using Blebbistatin, only shows a significant effect on small substrate radii of curvature, secondly that neither Blebbistatin, nor Taxol, which induced change of F-actin pattern towards more ring-like cortical actin (*185, 186*), show a significant effect on the cell

(pooled) perceived curvature, and thirdly, the fact that Taxol-treatment caused an increase in curvature avoidance for cell (not for nucleus) while previously published results on epithelioid cells suggest otherwise (*167*). These observations suggest that there is no exclusive involvement of the stress fiber system in curvature sensation/avoidance reaction. (*1*)

Certainly, "the strongest effects, especially on cell orientation and perceived curvature, were observed when the cell contractility was increased, and the underlying increased stress fiber formation was in both cases caused by an activation of RhoA."[18] Therefore, an involvement of other RhoA downstream effectors or effect of the stress fiber system on other cell organelles should not be disregarded. (*1*)

Table 13 **Pooled median perceived curvature of pharmacological manipulated human dermal fibroblasts and corresponding nuclei on cylindrical CurvChip surfaces coated with FCS.** If not indicated differently cells/nuclei on 59.3 µm 154.2 µm and 312 µm substrates were used. The values were calculated from all medians without significant difference as indicated in Figure 30; StDev stands for standard deviation. * Significant ($p<0.05$), *** most significant ($p<0.001$) difference to hdF1 without pharmacological manipulation (w/o), (**) highly significant ($p<0.01$); (***) most significant ($p<0.001$) difference between cell and nucleus perceived curvature, Kruskal-Wallis with Dunn's post-hoc test. Adapted from Frey et al. (*1*)

Pharmacological manipulation	***Cell* perceived median curvature** [$\times 10^{-3}$ µm^{-1}]	**StDev** [$\times 10^{-3}$ µm^{-1}]	***Cell* perceived median radius** [µm]
hdF1 w/o	0.60	1.36	1 666.7
Blebbistatin	0.64	1.97	1 562.5
CN03	0.18 ***	0.98	5 555.6 ***
Nocodazole	0.22 ***	1.63	4 545.5 *** (***)
Taxol	0.40	1.55	2 500.0 (**)
Pharmacological manipulation	***Nucleus* perceived median curvature** [$\times 10^{-3}$ µm^{-1}]	**StDev** [$\times 10^{-3}$ µm^{-1}]	***Nucleus* perceived median radius** [µm]
hdF1 w/o	0.69	1.89	1 449.3
Blebbistatin	0.88	1.87	1 136.4
CN03	0.31 *	1.52	3 225.8 *
Nocodazole	0.52	1.45	1 923.1 (***)
Taxol	0.72	2.84	1 388.8 (**)

[18] Exact quote from Frey et al. (*1*).

Effect on Morphological Characteristics

Cell spreading area and nucleus area

"Various physiological and signaling cell functions are generally known to be interrelated with morphological adaptions of the cell, as well as the nucleus. Moreover, interferences with cell morphology also cause functional changes"[19], including cell fate decisions like apoptosis, cell differentiation and carcinogenicity (*62, 96, 98*). The cytoskeleton is responsible for many kinds of morphological adaptions, which can also be observed in Figure 25 (p. 87), therefore, the analysis of the cell and nucleus morphology can give insights in the cell and nucleus mechanical state. For instance, the nucleus is directly coupled to different cytoskeletal components, which are affecting its orientation, shape and even its size. By investigating the cell and nucleus adaption on curvature compared to flat substrates with and without pharmacological manipulation additional information on the mechanism of cell curvature perception might be found for example by allowing conclusions regarding the mechanical state of the cell.

"When quantifying morphological adaptions on curved substrates, one needs to be aware that the cells are projected in a 2-D plane during imaging process, which induces a projection bias that needs to be corrected. To do so, we developed and established an ImageJ plug in to correct the projected area of a cell or nucleus on a cylindrical substrate"[19] (compare Figure 10, p. 49).

Figure 31 visualizes the quantified changes in cell and nucleus morphology by cultivation on curvature with and without pharmacological manipulation of the cytoskeleton. However, these quantifications always need to be seen in relation to the fluorescence images displayed in Figure 25 (p. 87), as only the combination of information on cytoskeletal arrangement, given by the fluorescence images, together with the quantified parameter allows for a profound interpretation of the results.

The comparison of the cell spreading area (A_{CELL}; Figure 31 A) of cells on cylindrically curved PDMS and flat PDMS shows, that hdF on curvatures tend to be smaller compared to those on flat substrates: "While the decrease of the median cell spreading area for cells on larger curvatures (small radii, median A_{CELL}= 2705.1 µm² on R= 59.3 µm) is minor[20], the decrease for smaller curvatures (larger radii; median A_{CELL}= 2526.6 µm² on R= 154.2 µm and median A_{CELL}= 2282.7 µm² on R= 312 µm) are statistically significant ($p<0.05$ for R= 154.2 µm and

[19] Exact quote from Frey et al. (*1*).

[20] median is approx. 250µm² smaller, which is considered to be in the area of normal variation consindering cell outlines are fitted manually

$p<0.001$ for R= 312 µm) compared to […] cell area [on flat substrates] (median A_{CELL}= 2926.4 µm²)."[21] The gradation that can be observed between the differently curved substrates, however, is not statistically significant. (*1*)

Moreover, the median nucleus projected area (A_{NUC}; Figure 31 C), is also significantly ($p<0.001$) smaller on curved topographies (median A_{NUC}= 201.3 µm² to 214.5 µm²) compared to flat PDMS (median A_{NUC}= 243.5 µm²), with no significant differences between the different radii of curvature. This observation is particularly interesting, as the nucleus shape is known to be related to (compressive) forces emerging from the cytoskeleton (*78*), amongst others. (*1*)

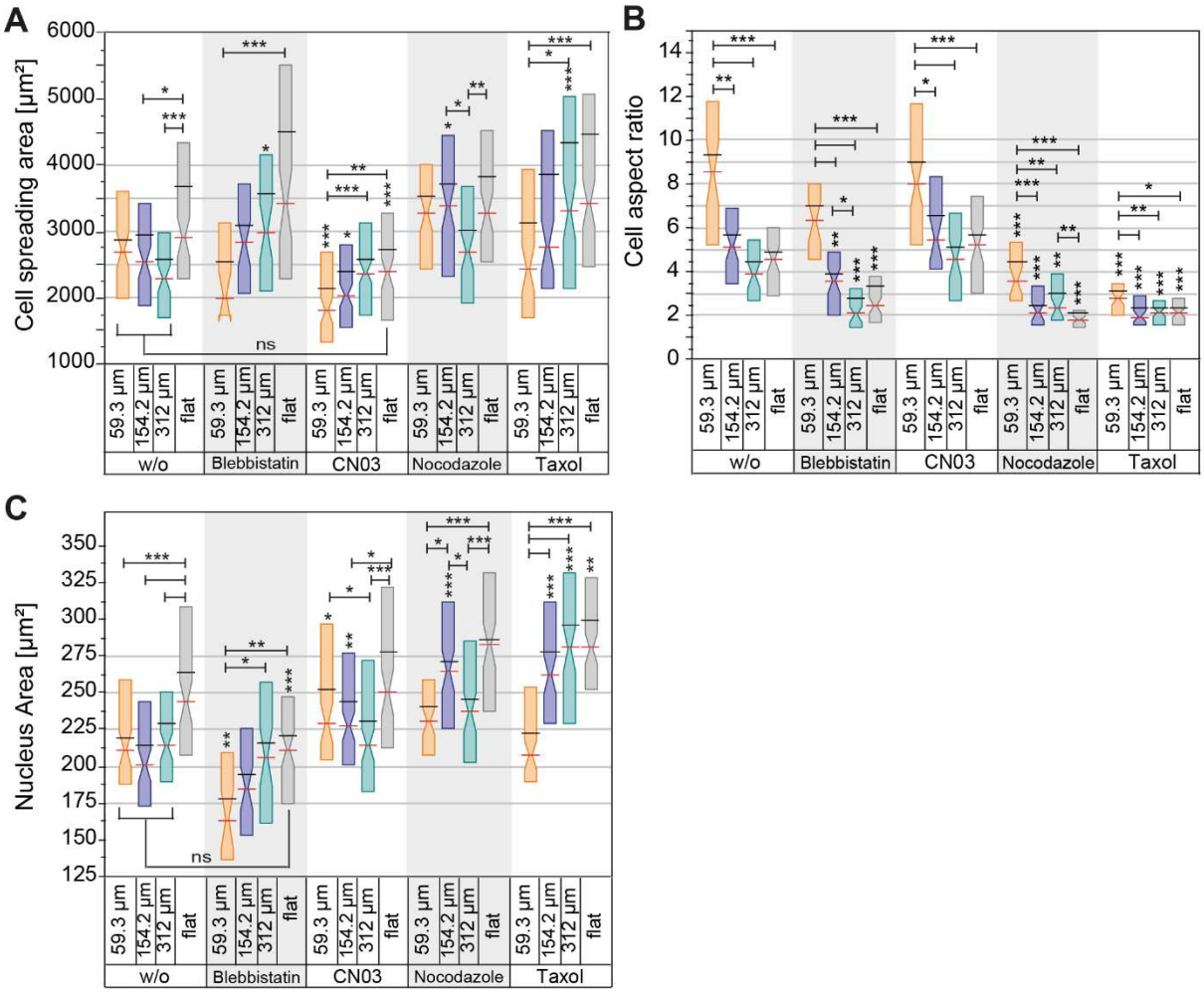

Figure 31 **Morphological adaption of cell and nucleus upon pharmacological manipulation of hdF1 growing on cylindrical CurvChip surface topographies coated with FCS**. Notched Box plots of ***A*** Cell spreading area (A_{CELL}) corrected for projection bias and ***B*** Cell Aspect ratio (AR), corrected for projection bias. Aspect ratio= Major axis/Minor axis. ***C*** Notched Box plots of Nuclei projected area (A_{NUC}), corrected for projection bias. w/o indicates hdF1 without pharmacological treatment. Boxes display 25th and 75th percentiles, the red lines the medians, and the black line the mean. * ($p<0.05$) significant, ** ($p<0.005$) highly significant, *** ($p<0.001$) most significant to w/o; * significant ($p<0.05$),

[21] Exact quote from Frey et al. (*1*).

** ($p<0,005$) highly significant, *** ($p<0.001$) most significant as indicated; ns not significant ($p>0.05$) as indicated; Kruskal-Wallis with Dunn's post-hoc test. Sample size range $n_{w/o}$= 84-118; $n_{Blebbistatin}$=33-99; n_{CN03}=114-171; $n_{Nocodazole}$=77-104; n_{Taxol}=100-131; Sample size aspect ratio: $n_{w/o}$= 49-69; $n_{Blebbistatin}$= 34-82; n_{CN03}= 45-88; $n_{Nocodazole}$= 45-68; n_{Taxol}= 54-81; All figure parts adapted from Frey et al. (*1*)

Results show that myosin inhibition with Blebbistatin of cells on flat PDMS, is related to an increase in A_{CELL} (median A_{CELL}= 3416.7 µm²; not significant $p>0.05$). This is a trend, that can also be observed for cells on cylindrical PDMS with R=154.2 µm and 312 µm). On R=59.3 µm cylindrical substrates, on the contrary, a decrease in A_{CELL} compared to non-treated cells on the same substrates can be observed. Comparing these findings with the fluorescence images in Figure 25 shows where this area increase might most likely come from. Cells have a more dendritic morphology, with long protrusions reaching out in all directions, adding up to a tendential increase in cell spreading area. (*1*)
The nucleus projected area A_{NUC} in these cytoskeletally more relaxed cells, is decreased for all substrates, with significant changes compared to non-treated cells for flat and R=59.3 µm substrates ($p<0.001$ and $p<0.005$, respectively)., the projected area of the nuclei on cylindrical substrates without manipulation are comparable (not significantly different $p>0.05$) to the median A_{NUC} of hdF1 treated with Blebbistatin and growing on flat PDMS. (*1*)

On the contrary, CN03-treatment of cells leads to a significantly reduced cell spreading area compared to untreated hdF1 for all substrates except R=312 µm cylinders. This observation complies with the more rhomboid cell morphology seen in Figure 25., the resulting median A_{CELL} for flat PDMS is comparable (not significantly different $p>0.05$) to hdF1 without pharmacological treatment on curved substrates. (*1*)
The effect of CN03-treatment on the nucleus projected area shows an increase in median A_{NUC}. This change is significant for R=59.3 µm and R=154.2 µm substrates (with an A_{NUC} of 228.8 µm and 227.0 µm, respectively) and minor for R=312 µm and flat PDMS. (*1*)

When microtubules are additionally depolymerized (Nocodazole), which simultaneously causes an increase of cell contractility, the, for CN03 reported reduction of cell spreading area A_{CELL}, cannot be observed. On the contrary, an increase in median A_{CELL} compared to hdF1 w/o can found for all substrates, which is statistically significant for R=154.2 µm ($p<0.05$) substrate. This spreading area increase would not be expected based on the fluorescence images in Figure 25, showing an even more rhomboid phenotype compared to the CN03-treated cells. (*1*)
The median A_{NUC} is comparable or even larger than the values of CN03-treated cells, the differences, except for cells on R= 154.2 µm substrates, are not significant compared to non-treated cells' nuclei. (*1*)

Microtubule stabilization using Taxol causes a more epithelioid phenotype with increased cortical actin. Moreover, Taxol-treatment also causes an increase in median cell spreading area for substrates with a radius of curvature greater or equal to 154.2 µm, including flat PDMS, whereas on R=59.3 µm cylindrical substrates median A_{CELL} is slightly decreased (median A_{CELL}= 2436.0 µm vs. 2705.1 µm, p>0.05). (*1*)

Compared to cells without pharmacological treatment the nucleus projected area A_{NUC} of Taxol-treated cells is significantly increased on smaller curvatures substrates (κ= 1/154.2 µm^{-1}, 1/312 µm^{-1}; p< 0.001) and flat (p< 0.005), with median A_{NUC} of 261.7 µm², 280.7 µm² and 280.3 µm², respectively (compared to median hdF1 A_{NUC} w/o of 201.3 µm², 214.5 µm² and 243.5 µm² respectively). Nuclei on large curvatures (κ=1/59.3 µm^{-1} with median A_{NUC}= 208.0 µm²) show a minor decrease in median A_{NUC}. (*1*)

Altogether, the results show a decrease in cell spreading area (A_{CELL}) and nucleus projection area (A_{NUC}) of not pharmacologically manipulated hdF1 on curved substrates compared to flat PDMS., the median A_{NUC} of cells on curvatures are comparable (not significantly different) to nucleus area of Blebbistatin-treated hdF1 on the flat PDMS. This observation suggests that the decrease in A_{NUC} induced by substrate curvature could be related to a decrease in cell contractility. (*1*)

However, nucleus shape adaption is not only affected by normal compressive forces resulting from the perinuclear actin cap, which causes the nucleus projected area to increase with increasing compression, also lateral compressive forces caused by central actomyosin filaments are involved (*77, 78*)(cf. Chapter I, Biophysical Factors). Additionally, increased nuclear stress can also cause nuclear remodeling and, therefore, cause a decrease in nuclear area (*79*). (*1*)

Cell area decrease, like also observed on cylindrically curved substrates, is often associated with increasing cell contractility but also with cell elongation. While cell elongation itself is often described to be related to a decrease in contractility due to the suggested link between elongation and downregulated cytoskeletal tension, which is thought to facilitate outward polymerization of actin during spreading (*82, 213*). Therefore, another morphological parameter of interest, especially in cell types with mesenchymal phenotype, having an anterior-posterior polarized morphology, is cell elongation. (*1*)

Cell aspect ratio as a measure of elongation

To quantify the changes in cell elongation, the aspect ratio (AR) of major to minor axis of the ellipse fitted to the projection-corrected cell outline obtained by our ImageJ plugin was determined using the basic ImageJ functions. The AR distributions are visualized in Figure 31 B. (*1*)

Independent from pharmacological manipulation the cell elongation is strongest for hdF1 growing on substrate with the highest curvature (R=59.3 µm), with a high statistical significance ($p<0.001$, except for Taxol $p<0.05$) compared to the median elongation of cells cultivated on flat PDMS surfaces. "HdF1 on substrates with smaller curvature than R=59.3 µm[, however,] show no significant change in the median aspect ratio compared to cells growing on flat PDMS (except for AR of Nocodazole-treated cells on R= 312 µm)."[22] (*1*)

When inhibiting cell contractility using Blebbistatin, the cell aspect ratio of hdF on low curvature substrates (R= 312 µm; R= 154.2 µm) and flat PDMS is significantly reduced. This reduction needs to be considered with caution. Reduction of intracellular contractility by Blebbistatin or other agents, such as the Rho inhibitor Y27362 leads to the formation of multiple thin protrusions (*213*), which usually is indicative for elongation. However, these protrusions are formed in multiple directions (cf. Figure 25, p. 87) which, therefore, can decrease the direction dependent parameter "aspect ratio". (*1*)

When microtubules are manipulated, independent from the type of manipulation, a decrease in cell elongation can be observed. Moreover, in this case also the median elongation of hdF1 on R=59.3 µm is significantly reduced compared to hdF1 without pharmacological treatment. Unlike the AR reduction for Blebbistatin-treatment, the reduced AR for microtubule manipulation is in line with what can be observed in the fluorescence images in Figure 25.

"Increased cell contractility with an intact microtubule network by CN03, however, does not significantly affect cell elongation, only a minor trend towards stronger elongation for low curvature substrates and flat PDMS can be noted. (*1*)

Based on the fact, that an increase in cell elongation, which would be indicative for a reduced cell contractility (*82*), is only observable for cells on the substrate with the largest curvature (R=59.3 µm) and not for the other two curvatures a general, curvature induced decrease in cell contractility causing the decrease in nucleus projected area is considered unlikely. Therefore, a nucleus remodeling due to an increased nuclear stress induced by the curved substrate is suggested to be the reason for decreased nuclear projected area, especially on substrates larger than R=59.3 µm.

Summary of Characteristics Found by Pharmacological Manipulation

In summary, the overall effect of stress fiber and microtubule manipulation on the adaption of hdF is small and the overall characteristics are not affected.

[22] Exact quote from Frey et al. (*1*).

Table 14 summarizes the effect of pharmacological manipulation on cell and nucleus of hdF growing on cylindrical CurvChip surfaces. The strongest effects are observed when the cell contractility is increased, independent from the state of the microtubule.

Table 14 **Summary of cell and nucleus responses to pharmacological manipulation.** Indication always compared to hdF without treatment: ↑ symbolizes a clear increase, ↓ a clear decrease, ↑↓ different response for strong curvatures compared to weak curvatures, ↗ tendential increase, ↘ tendential decrease, → no change (if symbol is **bold** observation is statistically significant). # nucleus is always less aligned with cylinder axis compared to cell

	Density ratio curv to btw	**Cell Ψ_{Med}**	**Nucleus Ψ_{Med}**	**Cell/nucleus alignment# $\Delta\Psi_{Med}$**	**Pooled cell perceived median R**	**Pooled nucleus perceived median R**
Blebbistatin	↑	↑	↑	↑	↗	↘
CN03	↑	↓	↓	↘	**↑**	**↑**
Nocodazole	↓	↓	↑↓	↑	**↑**	↑
Taxol	→	↓	↗	↑	↑	→

Discussion: Derived Suggestions for the Underlying Mechanism

Based on the presented results one can conclude that the curvature perception mechanism must be extremely robust and highly sensitive. Additionally, the independence of the cell median perceived curvature k from substrate curvature suggests the existence of an internal setpoint (at κ=1/1670-1/2310 μm^{-1}) mesenchymal cells aim to meet, further stressing the need of a very sensitive curvature perception mechanism. This need for a sensitive perception mechanism is supported by the findings of van der Putten et al. (*134*) whose results suggest that human myofibroblasts are able to perceive convex, uniaxial radii of curvatures up to approx. 2500 µm. Which altogether suggests that the internal setpoint could be the limit of curvature detection. (*1*)

Moreover, an exclusive involvement of the stress fiber system, in the curvature perception mechanism, like it was proposed in literature (*166, 171*), is improbable as the effect of stress fiber disruption by Blebbistatin and the f-actin reorganization following microtubule stabilization with Taxol is comparatively weak, as well as the fact that Nocodazole-treatment decreases the ratio of cell density on curvatures to density between curvatures, while CN03 treatment does not. (*1*)

Moreover, results show that Taxol-treatment causes an increase in curvature avoidance by reorientation for cell (not for nucleus), while previously published results on epithelioid cells, with a cortical actin-ring suggest otherwise (*167*). Nothing, however, is reported about the

microtubule state in the epithelioid cells used in literature (*167*), further suggesting that functional microtubules might be important for the cell response to uniaxial curvature.
Another interesting observation is, that the dose response curves of hdF1 w/o and Blebbistatin-treatment intersect in the observed range, one possible explanation could be that above this intersection/threshold the influence of the (reduced) actomyosin dependent cytoskeletal contractility on the response to curvature decreases while other factors might gain in importance.

In line with literature (*120*) the results indicate an importance of the nucleus mechanical state in cell response to curvature and an involvement of both the stress fiber system and the microtubule in the reorientation response of the curvature. (*1*)

Stress Shielding of the Nucleus

Based on the strong effect of RhoA activation, either by CN03 or Nocodazole-induced microtubule depolymerization, an involvement of other down-stream effectors of RhoA or / and the effect of RhoA activation on other cell components needs to be considered. (*1*)
One possible downstream effector of interest might be PRK1 (Protein kinase N1 PKN or protein kinase c-related kinases PKR) (*214*), as its activation is described to lead to a disassembly or perinuclear collapse of the intermediate filament (IF) network (*109, 110, 215*). Confirmatively, this intermediate filament remodeling, is also described in literature for microtubule depolymerization (*216, 217*). Altogether, this interrelation indicates that the intermediate filament network is also affected by RhoA activation and might, therefore, be of interest regarding the curvature perception mechanism, especially since, one of the major functions of IF, was shown to be the protection of the cell and nucleus from deformation (*81, 218–221*).
However, the suggested effect of the IF is thought to be rather indirect: IF disassembling or structural change could affect the mechanical integrity of the cell and, therefore, cause a decrease in nuclear mechanical shielding by IF (*218–221*). In combination with the increased contractility and, therefore, nucleus compression induced by RhoA/ROCK, the collapsed IF could further cause an increase in nucleus deformation or mechanical stress, which could then lead to a reorientation of the cell and nucleus. (*1*)
Therefore, the suggested pivotal effect caused of pharmacological RhoA activation is thought to be attributed to the nucleus and its mechanical state, which is in line with the suggested mechanism of Pieuchot et al. (*120*) for their sinusoidal hill and valley substrates. (*1*)
A possible scenario involving intermediate filaments could be, that upon RhoA activation the nucleus is not only increasingly compressed by stronger acto-myosin contractility and the curvature of the substrate, but also the stress shielding by vimentin could be negatively affected, further increasing the stress on the nucleus. (*1*)

This suggested involvement of the intermediate filament network can even explain why Taxol-treated cells behave differently from other epithelioid cells since intermediate filaments are described to collapse and form large central bundles upon Taxol-treatment (*184*). This finding together with the impaired nucleus rotation due to microtubule stabilization could increase the stress on the nucleus and, therefore, induce the observed cell reorientation. (*1*)

Furthermore, the microtubule network itself is also described to be involved in stabilizing the cell nucleus against compression and deformation (*81*) providing an alternative and/or complementary scenario that is further stressed by comparing the effect of CN03- and Nocodazole-treatment, since the difference can directly be related to microtubule presence or absence:
Comparing the results concerning nucleus (re-) orientation of CN03- and Nocodazole-treated hdF1 in more detail (cf. Figure 27, p. 90), some additional differences in orientation adaption can be observed:

The effect of CN03 and Nocodazole nuclei of hdF1 growing on small radii substrates and large radius substrates differs. For small radii (R=59.3 µm), CN03-treatment causes a decrease in the nucleus ψ_{Med} compared to hdF1 w/o (increased axial alignment), while the ψ_{Med} of nuclei from Nocodazole-treated cells shows a slight increase (decreased axial orientation). (*1*)

While the tendencies on R=312 µm are inversed: CN03 seems to minorly increase median nucleus' angle of orientation compared to nuclei of hdF1 w/o and Nocodazole decreases the median nucleus' angle of orientation. (*1*)

This difference between CN03 and Nocodazole-treatment is also nicely visualized by the fitted sigmoidal DRR progress of CN03- and Nocodazole-treated hdF1 (cf. Figure 29; p. 96): the curves intersect at approx. 206 µm suggesting a changed effect of the pharmacological agents on curvature perception mechanism depending on substrate curvature.

And since the major difference between CN03- and Nocodazole-treatment is the presence or absence of a functional of microtubule network, it can be suggested that microtubule in hdF1 on strong curvatures and weak curvatures might have a different importance in the perception mechanism.
One possible explanation could comprise the different involvement of stress fibers and microtubule in nucleus reorientation on differently curved substrates, since it is known that cytoskeletal requirements for nucleus rotation varies for different cell types and experimental conditions (*74*). The hypothesis that microtubule might be more important for nucleus rotation on small substrate radii of curvature, however, is contradicted by the results of Blebbistatin-treatment, where reduced contractility causes a strong increase in nucleus orientation angle

on R=59.3 µm, while when microtubule would be mainly responsible for nucleus rotation, a weaker reaction would be expected, since microtubule are not known to be affected by Blebbistatin.

Therefore, a second, more likely explanation, that is consistent with literature (*81*), might be, that the lacking microtubule network (further) impacts the stress shielding of the nucleus, causing a stronger deformation of the nucleus for Nocodazole compared to CN03 conditions with intact microtubule network. Meaning that, due to the increased contractility and the lacking microtubule, the nucleus becomes more deformed even by weaker substrate curvature (increasing R, increased sensitivity for substratum curvature). (*1*)

For a comparable compressing force on all substrates, the nucleus would be much more deformed by R=59.3 µm substrate compared to 154.2 µm or 312 µm, as exemplarily visualized in Figure 32 for a hypothetical non-elongated nucleus with A_{NUC}=250 µm.

This assumption leads to the consideration that the resulting bend deformation could cause a steric hindrance for nucleus rotation, which then could explain the difference between nuclei of Nocodazole-treated cells on R=59.3 µm and R=312 µm: On all radii of curvature, the nucleus deformation is increased due to the lack of microtubule shielding, but the deformation varies in extent based on the size ratio of the nucleus dimension to the substrate radius of curvature. To reduce the stress on the nucleus the cell tries to reorient the nucleus but, the deformation caused by the compression of the nucleus to the substrate additionally sterically hinders the already impaired (lack of microtubule) reorientation by rotation, especially for strongly curved substrates.

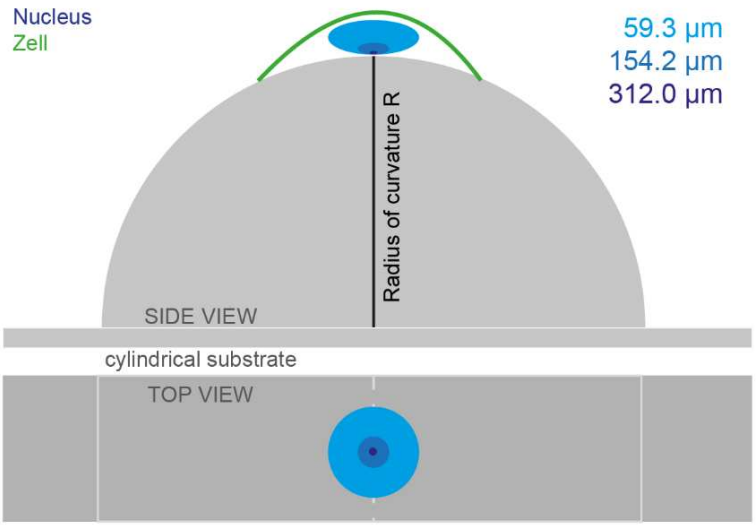

Figure 32 **Schematic representation of the size relationship between a hypothetical circular nucleus (projected A_{NUC} 250 µm², diameter 17.8 µm) and R=59.3 µm, 154.2 µm and 312 µm cylindrical substrates, to visualize the difference in nucleus deformation potentially emerging from the different substrates' radii of curvature.** For better comparison the nucleus diameter was

adapted and the size of the cylindrical substrate was kept the same. Resulting different sized nuclei were superimposed. ***Side view (top)**:* cylindrical substrate is represented as a semi-cylinder visualized using a semi-circle protruding from a plane. Zell is exemplarily indicated by the green arc for R=59.3 µm. ***Top view (bottom)**:* cylinder boundaries are indicated by light grey lines; cylinder axis is visualized by a dashed light grey line. Ratios of nucleus diameter to radius of curvature are approximately 3.3 (R=59.3 µm), 8.6 (R=154.2 µm) and 17.5 (R=312 µm).

Another, third, possibility that could explain the difference between nuclei of Nocodazole-treated cells on R=59.3 µm and R=312 µm is also in relation to the reduced stress shielding by lack of microtubule but also involves an adversely affected stress fiber contractility on strong curved substrates versus weakly curved substrates: Here, the reduced stress shielding on R=59.3 µm substrates, caused by lacking microtubule network, would be less notable, since the stress fiber contractility is assumed to be decreased, based on a conclusion drawn from the increased AR and the correlation of decreased contractility and increased elongation indicated by Roca-Cusachs et al. (*82*). Whereas on R=312 µm stress fiber contractility is not impaired (no increased cell aspect ratio) and, therefore, the stress on the nucleus is further increased, resulting in a stronger reorientation response on weak curvatures compared to strong curved substrates.

For further information on the involvement of the nucleus as mechanosensor the presented data on the nucleus area (Figure 31 C) was investigated. “One would expect the nucleus […] [to have an increased area] due to increased compression onto the curved substrate, and proposed decreased stress shielding, all compared to hdF1 without pharmacological treatment (w/o). This trend can be observed for both CN03- and Nocodazole-treated cells on the curved substrates.”[23] Interestingly, the median A_{NUC} of hdF on R=59.3 µm is independent from the presence of microtubule, while A_{NUC} on R=154.3 µm and R=312 µm cylinders as well as flat PDMS is increased when microtubules are lacking indicating that the third possible explanation might be depicting the situation best. (*1*)

Additionally, an increase in nucleus area can also be observed for cells treated with Taxol. “As a result of the F-actin reorganization upon Taxol-treatment, forming a cortical actin ring [(cf. Figure 25, p. 87 and (*185, 186*))], stress fiber formation is expected to be decreased, reducing the [normal, compressive force] […] of the perinuclear actin cap on the nucleus,”[23] as well as the lateral compressive force on the nucleus by cell elongation. Regarding the previously described potential increase of stress on the nucleus due to the intermediate filament reorganization (*184*), and/or the microtubule reorganization, this theory is line with our hypothesis, that reduced shielding together with still remaining compression by adhesion could

[23] Exact quote from Frey et al. (*1*).

be contributing to the increased nucleus area as well as the observable tendency of increased pooled k_{Med} of the cell (Figure 30 C and Table 13) compared to hdF1 w/o. (*1*)

Admittedly, "there is no study investigating the direct influence of intermediate filaments on curvature perception. Holle et al. (*222*), however, observed an enhanced alignment and directionality of Panc-1 cell migration along grooved substrata (width 2 and 4 µm, depth 200 nm and 350 nm) by destabilization of the intermediate filament network, indicating an involvement of intermediate filaments in contact guidance on sharp edged topographies." [24]
And although, some publications (*223, 224*) "found an increase in nuclear deformation by nanopillars upon depolymerization of intermediate filaments,"[25] literature also indicates that intermediate filaments are the mainly responsible for mechanical nucleus homeostasis (*221*), while actin and microtubule seem to be able compensate for parts of the intermediate filament actions and functions, when it is deficient (described for mesenchymal stem cells (*225*)). (*1*)
These findings, together with the here presented results and the literature based indication that the microtubule network is also described to be involved in stabilizing the cell nucleus against compression and deformation (*81*), show that further studies are necessary in order to distinguish between the role of intermediate filaments and microtubule in nucleus stress shielding, especially in situations comparable to the present one, where the potential deformation also comes from below the nucleus.

Important Role of Microtubule in Cell Reorientation on Curved Substrates

Independent from nucleus stress shielding, an intact microtubule network seems to have an important role in cell response to uniaxial substrate curvature, like indicated by the results from nucleus positioning and orientation (summarized in Table 14, p. 106). (*1*)
Based on the presented results (Figure 27, Figure 30, Table 9, and Table 11), showing that the nucleus is always less aligned with the cylinder, resulting in a larger (pooled) nucleus perceived curvature k_{Med} compared to cell k_{Med} and a positive $\Delta\Psi$, it is possible to conclude that the stress on the nucleus caused by its bending over this larger curvature (compared to cell perceived) is stronger compared to the stress the whole cell perceives (bends over smaller curvature). (*1*)
The nuclei of cells with RhoA activation (CN03, Nocodazole) perceive lower pooled k_{Med} (higher pooled perceived radii of curvature) than nuclei of hdF1 without pharmacological manipulation (w/o). Which is again in line with the previously described hypothesis that RhoA activation increases the stress on the nucleus, driving this reorientation, to reduce unfavorable nucleus

[24] Exact quote from Frey et al. (*1*).
[25] Exact quote from Frey et al. (*1*).

deformation by the substrate curvature and compressive forces. Whereas, when the microtubule network is manipulated, either by depolymerization (Nocodazole) or stabilization (Taxol), the difference between cell and nucleus perceived curvature becomes highly significant ($p<0.005$), indicating the importance of an intact microtubule network in this reorientation response and, therefore, its response to substratum uniaxial curvature. (*1*)

A possible explanation for this observation is the circumstance that microtubule and actin are both involved in nuclear rotation and repositioning inside the cell (*74*), and in order to reorient the nucleus (to decrease the stress) the cell reorients its cytoskeletal components resulting in smaller angle of orientation and, therefore, an increased alignment with the cylinder axis.
If the actomyosin and the microtubule network are intact (CN03) the reorientation is the strongest for both the cell and the nucleus. While, when the microtubule network is depolymerized, the results suggest that the mechanism causing nucleus reorientation is impaired, as both actin and microtubule are known to be involved. This suggested impaired nucleus reorientation, therefore, causes a reduced reorientation based on an impaired nucleus orientation. (*1*)
This theory can also explain the unexpected cell behavior of Taxol-treated cells compared to other epithelioid cells, which are described to exhibit a weaker curvature avoidance(*167*): Since the microtubule and the actin cytoskeleton are redistributed and reorganized by the microtubule stabilizing agent Taxol, the alignment of nucleus and cell orientation is decreased, in a way that the nucleus perceives an increased curvature. This increased nucleus perceived curvature triggers a reorientation of the cell in order to reorient the nucleus, but due to the stabilization of the microtubule network the nucleus rotation mechanism is impaired, resulting in the here described increased curvature avoidance of the cell. (*1*)
Additionally, cells on the CurvChip cylinder arrays also have a second possibility of avoiding curvature, besides (re-)orientation along the cylinder axis: they can position themselves in the transition zones between the cylinders. Evaluation of nucleus density on the two areas (Figure 26) further stresses the importance of the microtubule network in cell reaction to curvature, as an impaired microtubule network, in both cases, stabilized and depolymerized, decreased the nucleus density on the curved areas. This decreased nucleus density on the curved areas indicates, that with an undisturbed microtubule cytoskeleton the nucleus can be reoriented to reduce its deformation, if this reorientation of the nucleus is not possible the entire avoidance of the curved regions, by positioning in the transition zones, might be even more favorable. (*1*)

Interpretation of Morphological Adaptions of hdF Evoked by Substrate Curvature

As stated previously cell morphological changes can be indicative for cell internal processes. Therefore, comparing the morphological adaption of hdF1 and their nuclei on curved

substrates without pharmacological manipulation to the adaptions resulting from different pharmacological agents, can give some inside on the internal processes that are evoked by substratum uniaxial curvatures. (*1*)

The nucleus area for instance changes depending on different factors: “First, nuclear [normal] compression can cause an increase in the nucleus projected area [, either during cell spreading, or by increased contractility of the stress fibers in the perinuclear actin cap.] Second, lateral compression during cell elongation can induce a more elongated, smaller nucleus (in terms of projection area).(*77, 78*) Third, increased [nuclear] stress can also cause nuclear remodeling and, therefore, cause a decrease in nucleus area (*79*). ”[26] While cell area decrease is often related with increasing cell contractility but also with cell elongation. (*1*)

The here presented results show a decrease in both cell spreading area (A_{CELL}) and nucleus projection area (A_{NUC}) of not pharmacologically manipulated hdF1 (w/o; Figure 31 A and B) by substrate curvature. Interestingly, the median A_{NUC} of cells on curvature is comparable [($p>0.05$)] […] to the median nucleus area of Blebbistatin-treated hdF1 on the flat substrate, suggesting a reduction cell contractility induced by substratum curvature to be causal for the reduced A_{NUC}. (*1*)

However, the results of cell elongation analysis (aspect ratio AR) are not in line with this theory, since literature describes an interdependence between reduced cell contractility and increased cell elongation (*82, 213*). The increase in cell elongation, however, is only observable for cells on the substrate with the largest curvature (R= 59.3 µm; Figure 31 C) and not for the other two curvatures. On this basis, nucleus remodeling due to an increased nuclear stress, induced by the curved substrates, could be responsible for the decreased nuclear projected area, especially for R> 59.3 µm.

This hypothesis is supported by the decreased cell area that can also be observed, as it indicates an increased cell contractility (A_{CELL} on curvatures is not significantly different from CN03-treated A_{CELL} on flat, Figure 31 A). Furthermore, this increase in cell contractility is in line with the here suggested cell adaption to uniaxial curvature, whose driving force is to reorient the nucleus in order to reduce its curvature induced stress, since for the rotation of the nucleus the cell stress fibers as well as the microtubule are needed.

Based on the above, a nucleus remodeling is also expected to take place upon longer cultivation duration of CN03- (currently 4 hours; hdF1 w/o 24h) and Nocodazole-treated (currently 8 hours) cells on the curved substrates, since Philip and Dahl (*79*) described a time

[26] Exact quote from Frey et al. (*1*).

dependent change of nuclear remodeling with an increase in nuclear area after 14 hours of cultivation and a subsequent area decrease after 24 hours of stress induction.

An additionally notable morphological feature is, that in all cultivation conditions, independent from the type of manipulation, cells on R=59.3 µm cylindrical substrates are observed to be most elongated compared to the hdF1 on other substrates of the same condition.
This elongation is strongly affected by Nocodazole and Taxol, probably due to the role of undisturbed microtubule network in cell shape (*226, 227*), but even cells with pharmacologically manipulated microtubule on R=59.3 µm substrates are significantly more elongated compared to other substrates.
Interestingly, the substrate curvature of 1/59.3 μm^{-1} is in the range of cell size (approx. 80 µm (*189*)), a size relation that Li et al. (*170*) report to cause an activation of β_1 integrin in mesenchymal stem cells. Furthermore, β_1 integrin engagement is described to promote cell protrusions via Rac/Arp2/3 (*65*). This finding might indicate that the suggested reduced cell contractility on R=59.3 µm substrates is not based on the often-cited hypothesis, that stress fibers cannot work in a bend position (*166*), but based on a down regulation in relation to cell protrusion formation, an often-described phenomenon also discussed by DeMali et al. (*228*).

Suggested Mechanism and its Conformity with Suggestions from Literature

In summary, the here suggested curvature perception mechanism, based on the presented results, comprises the nucleus as a central mechanosensing unit as well as the cytoskeletal components, including actin-myosin filaments, microtubule and intermediate filaments, acting in a way to reduce unfavorable stress on the nucleus. The involvement of all cytoskeletal components in this mechanism might explain the, in this work found, robustness against pharmacological manipulation of single components. Which can further be supported by the interdependency of the cytoskeletal components, their mutual regulation (e.g. based on RhoA/ROCK pathway (*215*)), and the fact that some deficiencies can possibly be compensated for by the remaining components (*225*).
Moreover, the mechanism needs to be highly sensitive, in order to perceive curvatures in the range of κ=1/1670-1/2310 μm^{-1} for mesenchymal cells (Table 9) and this range also seems to form some kind of internal setpoint.

Discussion with Regards to Suggestions from Literature

Like mentioned previously, the high sensitivity is confirmed by results from van der Putten, et al. (*134*) showing that human myofibroblasts are able to perceive curvatures down to κ=1/2500 μm^{-1}. Which also suggests that the internal setpoint could be the perception limit.

Pieuchot et al. (*120*) also assume that the nucleus with its connection to the cytoskeleton acts as a mechanosensor and that a mechanically relaxed state of the nucleus, like when it is placed in concave regions, is more favorable for the cell. These findings fully support each other albeit they are based on completely different types of substrate systems: on the CurvChip cylindrical substrates the cells have two ways of avoiding curvature, either by reorientation along the cylinder axis or by positioning in the flat transition zones of the substrate, while on the sinusoidal hill and valley surfaces of Pieuchot et al. (*120*) the only way of avoiding curvature is to place the nucleus over the valleys.

Using similar substrates to the here used CurvChip surfaces with uniaxial curvature, as well as spherical substrates for comparison, Werner et al. (*54*) observed reduced F-actin levels and higher phosphorylated myosin II in human bone marrow stem cells (hBMSCs) on spherical substrates compared to cylindrical substrates ($R < 100$ µm) and increasing myosin II phosphorylation for increasing cylinder curvature. In accordance with the theory that stress-fibers cannot work in a bent formation (*166*), "they conclude that cells enhance the myosin II phosphorylation to maintain a contractile cytoskeleton on curved substrates and that reorientation is more likely a "curvature avoidance" since the phosphorylation is energetically demanding."[27] (*1*)
Taking their study together with the here presented observations and proposed mechanism, one can also suggest that increased myosin II phosphorylation on cylindrical substrates is caused by the need to actively reorient or "rescue" the nucleus to reduce its deformation. "Moreover, the limiting factor in Dunn and Heaths (*166*) observation could also be explained by the nucleus deformation and not by impaired stress fiber formation due to bending."[27] (*1*)

Using a cylindrical substrate, Bade et al. (*119*) observed that human vascular smooth muscle cells (hVSMCs) show a weaker orientation along the cylinder axis compared to mouse embryonic fibroblasts (MEFs). They also describe an increase of circumferentially aligned basal stress fibers in hVSMCs upon Rho activation using CN03, but did not show the results for MEFs. Both observations indicate that hVSMCs seem to respond differently compared to mesenchymal stem cells or fibroblasts, and it would, therefore, be evident if the way of protecting the nucleus form deforming is also different for this cell type. For instance, the increasing amount of basal stress fibers could lift up the nucleus and/or simply shield it, and the simultaneous decrease in apical stress fibers further reduces the stress on the nucleus. Additionally, the finding of increase in apical stress fibers shows that stress fibers can work in

[27] Exact quote from Frey et al. (*1*).

a bend configuration, which further supports the theory that the nucleus is the central unit for curvature sensation and avoidance.

Effect of Protein Coatings on Cell Alignment of Sparsely Growing hdF1 on Cylindrical Curvatures

In vivo the extracellular matrix is composed of different types of proteins, changing in composition and ratio depending on the tissue type, age and other factors. Both biochemical composition as well as biophysical properties, like ECM mechanics but also ligand density are known to influence cell behavior and functions (cf. Chapter I; The Extracellular Environment – a Complex System). These include stem cell differentiation, morphology adaption, and changes in migration (speed and persistence) and proliferation (*44, 45*) as well as protein expression (e.g. collagenase (*45*), alpha smooth muscle actin (*35*), integrin subunits (*229*)). Furthermore, modulated mechanotransduction due to changed ligand receptor interaction based on varying protein coatings has already been shown to be causal for the stem cell differentiation (*25*), morphology, and migration adaption of different cell types on flat and micro-structured substrates (*44*) as well as hydrogel contracture (*42*). The present chapter aims to investigate if the choice of ECM affects cellular perception of uniaxial cylindrical convex curvatures.

Besides coating the convex cylindrical CurvChip surfaces with fetal calf serum (FCS; 20 % v/v) the most commonly used adhesion proteins were applied, comprising fibronectin, collagen I and laminin. FCS was used based on two considerations both describing its suitability as a reference surface. Firstly, emerging from the fact that when substrates are not precoating with any specific protein, as it is often done in cell cultivation, cells encounter a surface coated with proteins adhering form the culture media which mostly contains FCS, resulting in a comparable surface coating as used here. Certainly, assumed that the surface properties affecting protein adsorption are comparable. Secondly and maybe less relevant for the present approach, the FCS coating is best representing the surface cells encounter after implantation of a biomaterial, as serum proteins will adhere on the surface within seconds after blood contact. Generally, FCS consists of a mixture of various proteins. Alongside albumin, the main protein in serum, FCS includes the two cell adhesion proteins vitronectin (*230*) and (plasma-) fibronectin (*231*). Since literature indicates an impaired adsorption of fibronectin from serum, cell adhesion is thought to be mediated mainly by vitronectin (*232–234*).

Comparing the hdF1 growing on the different coatings, like shown in Figure 33, only minor differences can be seen in comparison to the FCS reference surfaces: Cells on fibronectin and collagen I seem to have stronger pronounced stress fibers, while hdF on collagen I and laminin seem to have an increasing amount of long, thin protrusions and an increasing presence of filopodia.

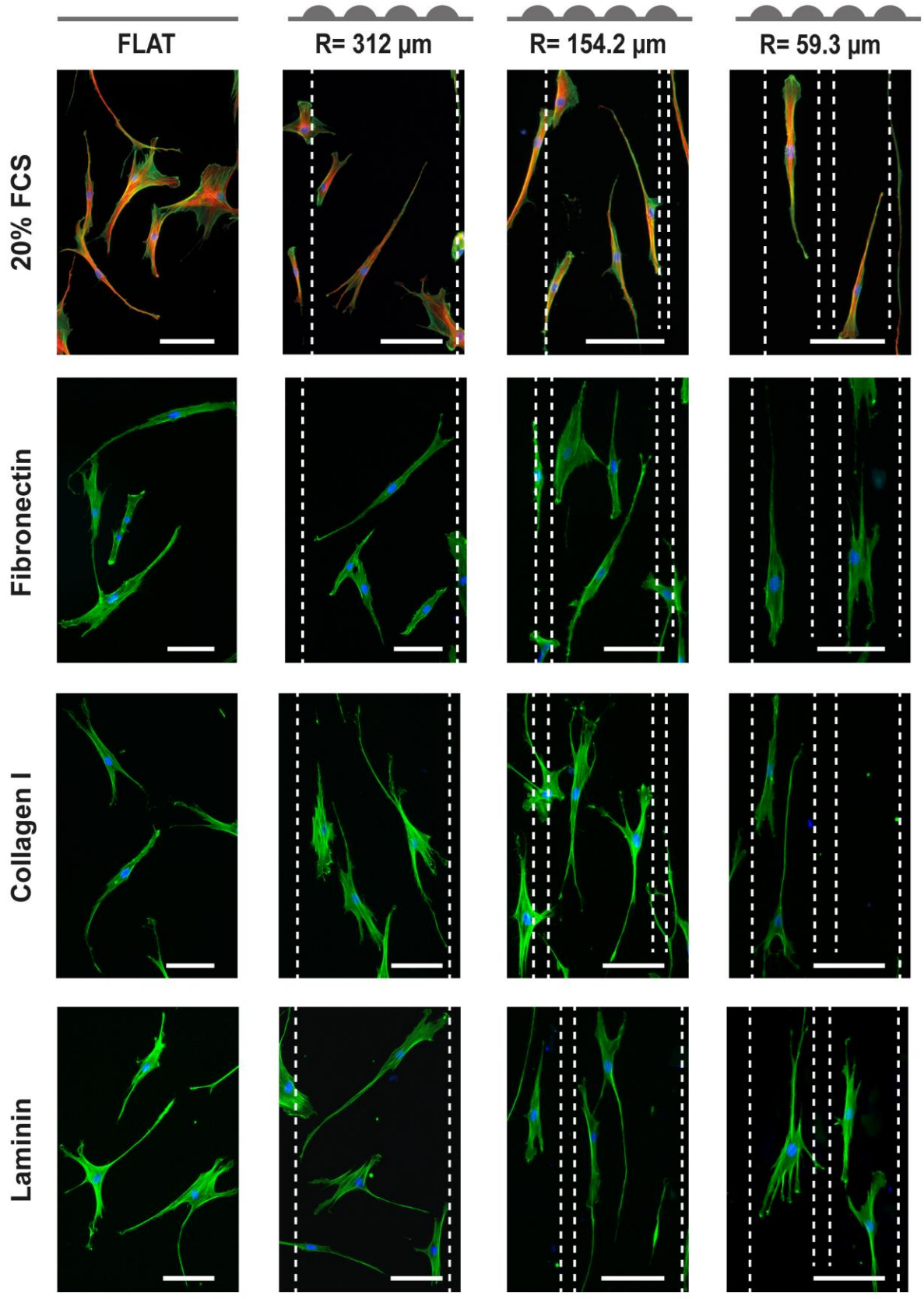

Figure 33 **Fluorescence images of hdF1 on cylindrical CurvChip surfaces with varying radii of curvature R and different surface protein coatings as indicated.** F-actin in green, nuclei blue and (if stained) microtubule in red. From left to right substrate radius of curvature R is decreasing, resulting in

an increasing surface curvature κ. The dashed lines point out topography boundaries. Protein used for surface coating is indicated on the left. Scale bars 100 µm

Effect on Nucleus Density in different substrate regions

Analyzing the preferred nucleus positioning on cylindrical, convex, curved substrates with varying protein coatings, Figure 34, shows that the density in the transition zones "btw" is decreased for the different coatings compared to FCS. The strongest decrease can be observed for R=154.2 µm substrates coated with collagen I ($p<0.001$) and laminin ($p<0.05$) with regard to the control surface. This reduction is accompanied by a reduced overall cell density on collagen and laminin.

The strongest adaptions on the curved regions are taking place on R=59.3 µm curvatures, while the other cylinder radii are only affected minorly: For fibronectin- and collagen I-coated surfaces, an increase of cell density (mean ± SE: 18.5±1.78 and 25.0±7.1 nuclei per mm², respectively) on the curvatures compared to FCS-coated surfaces (8.0±1.2 nuclei per mm²) can be observed. While this increase is not statistically significant for fibronectin ($p>0.05$) the change collagen I is significant ($p<0.001$).

This finding suggests that both fibronectin and collagen I-coating affects the cell cytoskeleton and nucleus in a way improving cell and nucleus curvature resistance, e.g. by enhancing the second way of curvature avoidance, axial orientation, which causes the increase in nucleus density on curved regions.

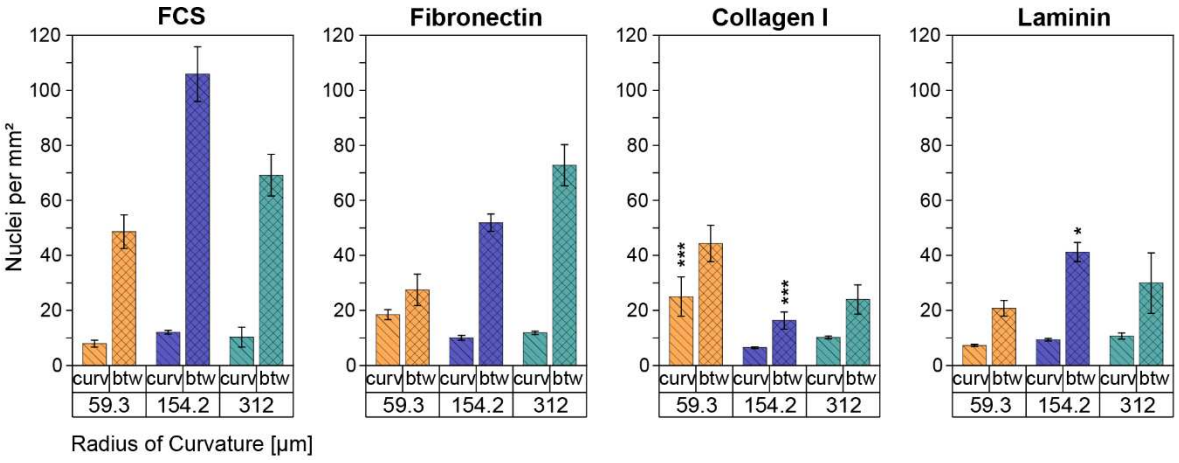

Figure 34 **Nucleus density on curvatures and area between the curvatures of CurvChip cylindrical substrates with varying protein coatings and radii of curvature R.** Nucleus density (Mean ±SE). Curv indicates nucleus density on curved regions, btw nucleus density in zones between the convex curved regions of the substrates. Sample sizes FCS: $n_{59.3\,\mu m}= 443$; $n_{154.4\,\mu m}= 416$; $n_{312\,\mu m}= 390$. FN $n_{59.3\,\mu m}= 402$; $n_{154.4\,\mu m}= 279$; $n_{312\,\mu m}= 276$. Col I: $n_{59.3\,\mu m}= 457$; $n_{154.4\,\mu m}= 153$; $n_{312\,\mu m}= 178$, Laminin $n_{59.3\,\mu m}= 208$; $n_{154.4\,\mu m}= 240$; $n_{312\,\mu m}= 199$. Mean ±SE for flat PDMS (FCS 15.3 ±1.49 nuclei per mm², fibronectin 12.2 ±0.24 nuclei per mm², collagen I 10.4 ±1.02 nuclei per mm², laminin 10.2 ±1.13 nuclei

per mm²) are not significantly different from each other. *significantly different from FCS (* p<0.05; ** p<0.005; *** p<0.001) One-way ANOVA with Dunn-Sidak post-hoc test.

When comparing the ratios of nucleus density on curved regions to nucleus density in areas between the cylinders, as listed in Table 15, one can see that the effect of collagen I is generally the strongest regarding an increase in nucleus density on curved area, while the effect of Fibronectin on lower curvatures, in relation to FCS-coating, is negligible.

Table 15 **Ratio of nucleus density for hdF1 growing on curved regions and between surfaces with cylindrical topographies of varying radius of curvature R and protein coating**. Calculated from mean densities as visualized in Figure 34

Substratum	**Ratio of cell densities**			
Radius of	(curved regions/area between cylinders)			
curvature R	**FCS**	**FN**	**Collagen I**	**Laminin**
59.3 µm	0.16	0.67	0.56	0.35
154.2 µm	0.11	0.16	0.40	0.23
312 µm	0.14	0.16	0.42	0.35

Effect on Cell and Nucleus Orientation

To investigate the effect of varying protein coating on the (re-)orientation of cells and nuclei along the cylinder axis of cylindrical curvatures, cell and nucleus angle of orientation ψ was quantified and visualized in Figure 35. Although the most observable adjustments of the medians are not statistically significant, some tendencies can be seen.

Compared to FCS-coated substrates, the median cell angle of orientation ψ_{Med} is decreased on all curved substrates coated with fibronectin and collagen, representing a more pronounced axial orientation or increased curvature avoidance. Cells on laminin-coated surfaces show comparable angles of orientation with cells on FCS-coatings, only for substrates with R=312 µm cylinders a decrease in the ψ_{Med} can be observed.

Nucleus'angles of orientation (cf. Figure 35 B) display comparable trends to those observed for the cell on fibronectin and collagen I, where the median nucleus alignment with the cylinder axis is increased (smaller nucleus ψ_{Med}) compared to FCS-coating. Nucleus adaption on laminin-coating, however, is stronger compared to cell adaption, with about the same median angle of orientation between laminin- and FCS-coating on R=59.3 µm and an increased nucleus alignment on laminin-coated R=154.2 µm and R=312 µm substrates (decreased nucleus ψ_{Med}).

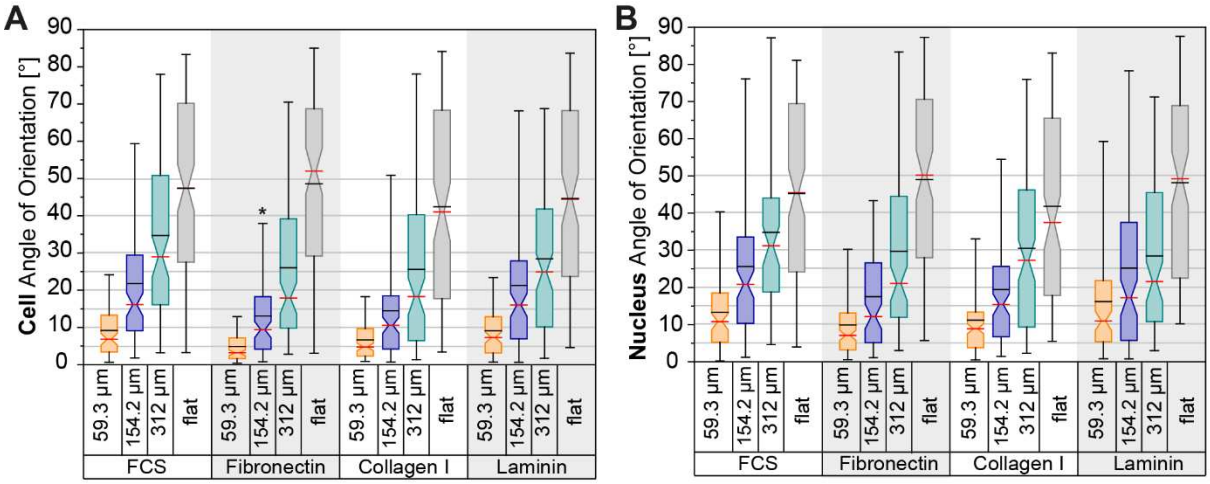

Figure 35 **Effect of varying protein coating on cell and nucleus orientation of hdF1 on cylindrically curved CurvChip topographies with different radii of curvature R.** Notched box plots Boxes showing the 25th and 75th percentiles, the red lines indicate the median and the black lines display the mean, whisker show the 5th and 95th percentile range. Sample size cell/nucleus n_{FCS}= 100-118/95-117; $n_{Fibronectin}$=104-129 /104-129; $n_{Collagen\ i}$= 110-131/106-116; $n_{Laminin}$=100-111/100-111; * Significant ($p< 0.05$), ** highly significant ($p<0.005$), *** most significant ($p<0.001$) to w/o; Kruskal-Wallis with Dunn's post-hoc test.

To examine the difference between nucleus and cell alignment the difference of the angle of orientation of nucleus and cell ΔΨ was calculated and displayed in Figure 36 (median ΔΨ in Table 16).

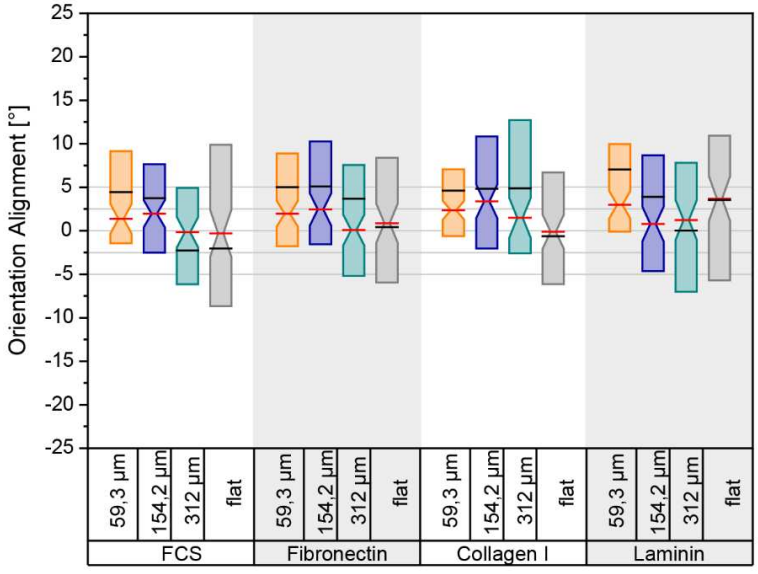

Figure 36 **Difference ΔΨ of cell to nucleus alignment in relation to cylinder axis on cylindrical CurvChip substrates with varying surface coating and radii of curvature R.** Cell angle of orientation ψ_{CELL} subtracted from nucleus angle of orientation ψ_{NUC} ($\Delta\Psi=\psi_{NUC} - \psi_{CELL}$), positive value indicates nucleus is less aligned compared to the cell, negative value indicates nucleus is stronger aligned than

the cell, higher deviation from 0 indicates stronger misalignment of the nucleus and cell orientation. Boxes show 25th and 75th percentile, median line in red and mean line in black. Grey lines connecting the different graphs are for better comparison and indicate a difference of 5; 0; -5. Median values are displayed in Table 16. Sample size range n_{FCS}=95-117; n_{FN}=104-128; n_{COL}=106-131; n_{LAM}=100-112.

The interquartile range (IQR) of hdF1 on flat PDMS is decreased for all protein coatings compared to FCS-coating, resulting in an almost symmetrical distribution for collagen I and fibronectin-coating and a to positive values shifted distribution for laminin. The median $|\Delta\Psi|$ is minorly increased for fibronectin and stronger increased for laminin, s

The trend for decreased IQR on curved substrates compared to flat PDMS, like it can be observed for FCS-coating, is not so prominent for fibronectin- and laminin-coating as it is for FCS. On collagen I-coating this general trend can only be seen for R=59.3 µm, which might be a result from the already decreased IQR on flat for the different coatings compared to FCS. Moreover, median $\Delta\Psi$, is increased by all coatings compared to FCS, with two exceptions (fibronectin R=312 µm and Laminin R=154.2 µm). For fibronectin-coating this increase is weak, whereas it is more prominent for collagen I as well as laminin-coating. This difference can be interpreted in a way that protein coatings decrease cell-nucleus alignment causing the nucleus to be less aligned with the cylinder axis, as indicated by the shift towards larger positive values for median $\Delta\Psi$. However, in most cases this shift is more likely caused by the reduction of strong misalignment of cell and nucleus where the nucleus is stronger axially aligned compared to the cell (high negative $\Delta\Psi$) as also indicated by the asymmetry of the boxes.

Table 16 **Median difference $\Delta\Psi$ of nucleus and cell alignment on cylindrical CurvChip substrates with varying curvatures and protein coatings**. Cell angle of orientation subtracted from Nucleus angle of orientation ($\Delta\Psi=\psi_{NUC} - \psi_{CELL}$), positive value indicates nucleus is less aligned compared to the cell, negative value indicates nucleus is stronger aligned than the cell, higher deviation from 0 indicates stronger misalignment of the nucleus and cell orientation. Caution: For flat PDMS only the absolute values is relevant, since here the angles are measured in relation to a hypothetical axis.

Radius of curvature R	FCS	Fibronectin	Collagen I	Laminin
59.3 µm	1.37°	1.96°	2.36°	3.00°
154.2 µm	1.96°	2.45°	3.38°	0.77°
312 µm	-0.18°	0.08°	1.48°	1.24°
flat	-0.30°	0.87°	-0.12°	3.69°

Effect on Dose Response Relationship

Investigating the cell and nucleus sigmoidal DRR of hdF growing on differently coated substrates with increasing radius of curvature, as visualized in Figure 37, one can see that, on

cylinders larger than, or equal to R=154.2 µm, all protein coatings increased cellular sensitivity/avoidance to curvature in relation to FCS-coating, resulting in a shift of the curves to the right of the DRR of hdF1 on FCS. For R<154.2 µm, on the contrary, the DRR curve of laminin-coating is slightly shifted to the left of the FCS DRR curve, but this adaption is minor and, therefore, not seen as reliable.

The overall trend of the nucleus response is comparable to the adaption observed for the whole cell: for all protein coatings the curvature-avoidance is increased, resulting in a smaller angle of orientation for the same underlying curvature. While for laminin the effect of increasing nuclear curvature-avoidance compared to FCS-coating is getting stronger with increasing radius of curvature of the underlying substrate, the effect of increasing nuclear curvature-avoidance on collagen I-coating seems to be decreasing with increasing radius of curvature.

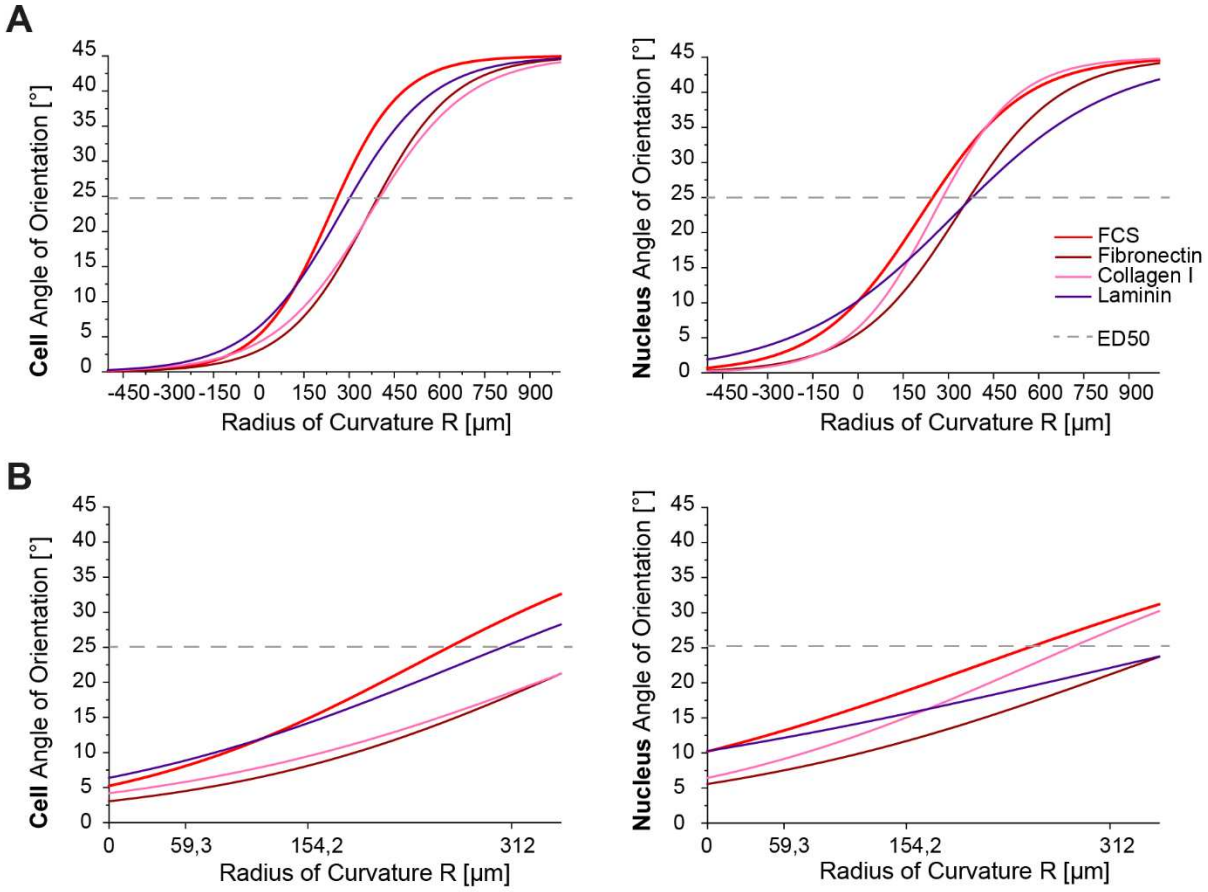

Figure 37 **Orientation of hdF1 and their nuclei on cylindrical CurvChip substrates with increasing radii of curvature R and varying protein coatings displayed as dose response relationships.** Sigmoidal Dose Response fit to median angles of orientation ψ_{Med}, with upper boundary set to 45° (random orientation) and lower boundary 0° (perfect alignment). ***A*** shows the whole curves, ***B*** shows relevant section. ***Left column*** cell angle of orientation, ***right column*** nucleus angle of orientation. Colors represent different substrate coatings as indicated. Intersection with 22.5° dotted line represents

half maximal effective dose ED50. Please note: for purposes of better visualization the data points of ψ_{Med} are not included in the fitted graphs.

Based on the deviation from DRR of hdF1 on FCS substrates, fibronectin-coating shows the strongest effect over the investigated range of radii of curvature for both cell and nucleus adaption. Corresponding to this observation, the sequence resulting from ED50 analysis is *FCS < Laminin << Fibronectin ≈ Collagen I* for cell orientation adaption and *FCS < Collagen I << Fibronectin ≈ Laminin* for nucleus adaption.
The y-intercept sequences, representing the noise of the detection system or deviation from perfect alignment are *Laminin > FCS > Collagen I > Fibronectin* for cells and *Laminin ≈ FCS > Collagen I > Fibronectin.* Indicating a decrease in noise for collagen I and fibronectin.

Effect on Median Perceived Curvature

Regarding the cell perceived curvature k (Figure 38 A), a general decrease in median perceived curvature can be observed for all coatings compared to the FCS reference. The strongest effect can be observed for fibronectin-coating, with significant differences for R=59.3 µm ($p<0.001$) and R=154.2 µm ($p<0.005$). This strong effect for fibronectin-coating also results in the fact that the median cell perceived curvature is significantly different for all investigated radii of curvature, making it impossible to combine the values to calculate a pooled k_{Med}. The reduction of median perceived curvature on the collagen I-coating is also significant on R=154.2 µm and 312 µm ($p<0.05$) compared to the FCS-coating, while laminin-coating does not induce significant changes in median cell perceived curvature, only a minor median increase on R=59.3 µm cylinders and a minor median reduction on R=312 µm substrates.

The adaption of the median nucleus perceived curvature k_{Med} (Figure 38 B) is, like previously described for the angle of orientation, also less pronounced compared to the cell adaption. Only fibronectin-coating evoked a significant decrease of median nucleus perceived curvature on R=154.2 µm ($p<0.05$), compared to the nucleus k_{Med} on FCS-coated substrate of the same radius, while the reduced nucleus k_{Med} on the other substrates is not significant. On collagen I-coated substrates, in comparison with FCS-coated substrates, also only non-significant trends towards a decreased nucleus k_{Med} can be observed on R=59.3 µm and R=154.2 µm. The same applies to laminin-coated surfaces with R=154.2 µm and 312 µm compared to the nuclei of cells on FCS-coated substrates with the same radii of curvature.

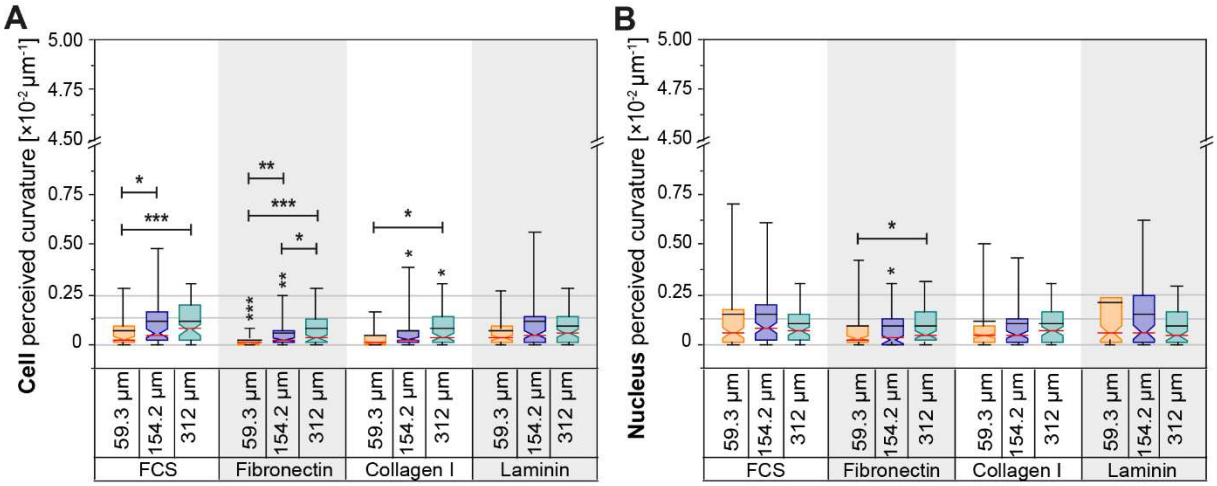

Figure 38 **Effect of varying protein coatings on cell and nucleus perceived curvature k on cylindrical CurvChip substrates with different radii of curvature R.** Notched box plots Boxes showing the 25th and 75th percentiles, the red lines indicate the median and the black lines display the mean, whisker show the 5th and 95th percentile range. ***A*** displays the cell perceived curvature data, ***B*** the plots of the nucleus perceived curvature. Sample size cell/nucleus n_{FCS}= 100-118/95-117; $n_{Fibronectin}$=104-129 /104-129; $n_{Collagen\ i}$= 110-131/106-116; $n_{Laminin}$=100-111/100-111; * Significant ($p< 0.05$), ** highly significant ($p<0.005$), *** most significant ($p<0.001$) to FCS or as indicated; ns not significant ($p> 0.05$) as indicated; Kruskal-Wallis with Dunn's post-hoc test.

Pooling the median perceived curvatures of cells and nuclei on different protein coatings to calculate the pooled k_{Med} is not as straight forward as for the different pharmacological manipulations, since in some cases multiple pooling combinations or no pooling at all were possible based on which substrates to exclude due to the significant difference to the other curved substrates with the same coating. All different combinations of not significantly different perceived curvatures of the same coating were pooled and the calculated pooled k_{Med} are listed in Table 17. The findings corroborate that all protein coatings lead to a decrease in the perceived curvature k, and the strongest effect on both cell and nucleus perceived curvature is caused by fibronectin and collagen I-coating, while laminin only induces statistically non-significant effects.

Table 17 **Pooled median perceived curvature of hdF1 and their nuclei growing on cylindrical CurvChip substrates with varying protein coatings.** The values were calculated from all medians without significant difference as indicated in Figure 38; as specified in some cases more than one combination was possible; StDev stands for standard deviation. * Significant ($p<0.05$), *** most significant ($p<0.001$) difference to hdF on FCS-coating, Kruskal-Wallis with Dunn's post-hoc test.

Protein Coating	***Cell* perceived median curvature** [$\times 10^{-3}$ µm^{-1}]	**StDev** [$\times 10^{-3}$ µm^{-1}]	***Cell* perceived median radius** [µm]
FCS	0.60	1.36	1666.7
Fibronectin			
59.3 µm	0.05	-	20 000.0 ***
154.2 µm	0.17	-	5 882.4 ***
312 µm	0.30	-	3 333.4
Collagen I			
59.3 und 154.2 µm	0.17	0.99	5 882.4 ***
154.2 und 312 µm	0.26	1.10	3 846.2 ***
Laminin	0.44	1.26	2272.7
Protein coating	***Nucleus* perceived median curvature** [$\times 10^{-3}$ µm^{-1}]	**StDev** [$\times 10^{-3}$ µm^{-1}]	***Nucleus* perceived median radius** [µm]
FCS	0.69	1.89	1 449.3
Fibronectin			
59.3 und 154.2 µm	0.27	1.86	3 703.7 ***
154.2 und 312 µm	0.36	1.14	2 777.8
Collagen I	0.46	1.74	2 173.9 *
Laminin	0.53	2.40	1 886.8

Effect on Morphological Parameter

To further characterize the effect the different protein coatings, have on the cytoskeleton, nucleus and their mechanical state, their morphological adaptions, also visualized in the fluorescence images in Figure 33 (p. 118) were quantified. Figure 39 displays the projection bias corrected (cf. p. 48 and Figure 10, p. 49) quantifications of cell and nucleus morphology. Regarding the median cell spreading area (Figure 39 A), interestingly, mixed trends can be observed. While for fibronectin-coating, compared to FCS-coating, no statistically significant changes are observable, the median cell spreading area shows a trend for decreased median A_{CELL} for R=59.3 µm and 154.2 µm, and increased of R=312 µm substratum.

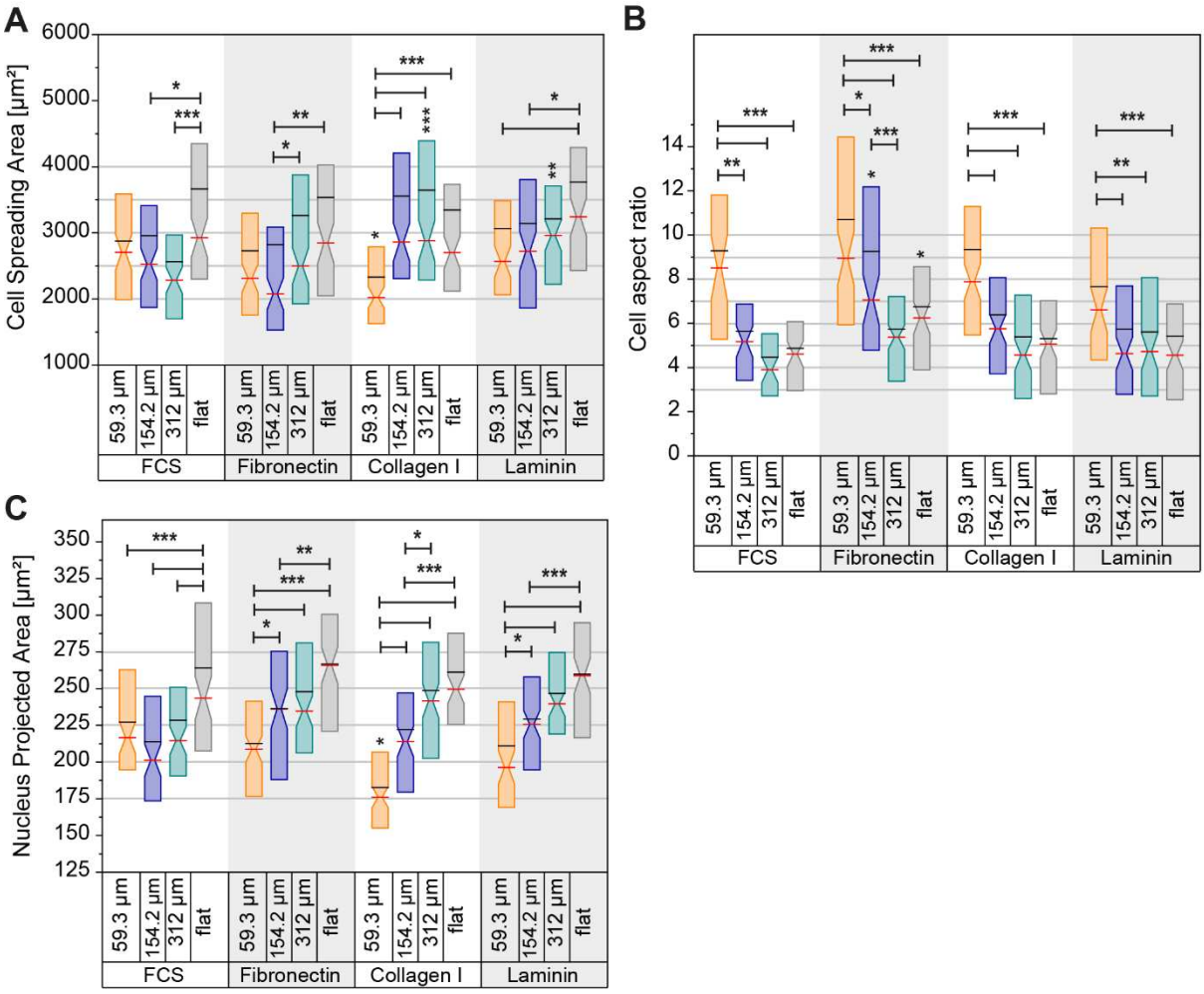

Figure 39 **Effect of varying protein coating on morphological parameter of hdF1 cultivated on cylindrical CurvChip substrates with different radii of curvature R.** ***A*** Cell spreading area (A_{CELL}) corrected for projection bias and ***B*** Cell Aspect ratio (AR), corrected for projection bias. Aspect ratio= Major axis/Minor axis. ***C*** Notched Box plots of Nuclei Area (A_{NUC}), corrected for projection bias. w/o indicates hdF1 without pharmacological treatment. Boxes display 25th and 75th percentiles, the red lines the medians, and the black line the mean. * ($p<0.05$) significant, ** ($p<0.005$) highly significant, *** ($p<0.001$) most significant to w/o; * significant ($p<0.05$), ** ($p<0,005$) highly significant, *** ($p<0.001$) most significant as indicated; ns not significant ($p>0.05$) as indicated; Kruskal-Wallis with Dunn's post-hoc test. Sample size range n_{FCS}= 88-118; $n_{Fibronectin}$=102-129; $n_{Collagen\ i}$= 106-130; $n_{Laminin}$=91-111

For the collagen I-coating, showing a comparable effect to fibronectin in previously investigated parameter, a decrease in cell spreading area can be observed for R=59.3 µm ($p<0.05$) and flat PDMS ($p>0.05$), while hdF on R=154.2 µm ($p>0.05$) and 312 µm ($p<0.001$) cylindrical substrates median spreading area is increased compared to cells on FCS.

A comparable trend can be observed for laminin coating. Compared to FCS-coating the median spreading area on laminin-coating is reduced for R=59.3 µm ($p>0.05$) and increased for R=154.2 µm ($p>0.05$) and R=312 µm ($p<0.005$). The increase in median spreading area

observed on collagen I and laminin might be due to the, in Figure 33 observable, increase in thin protrusions observed for both collagen I and laminin surface coating.

Comparing the findings on cell spreading area with those on cell aspect ratio (AR) in Figure 39 B shows two trends: The change of the surface coating induces a tendential decreased median elongation and spreading area in hdF growing on substrates with large cylindrical curvatures (κ=1/59.3 μm^{-1}) and an increase of median AR and A_{CELL} on hdF growing on small cylindrical curvatures (κ=1/312 μm^{-1}).
In more detail, the decrease in A_{CELL} on R=59.3 µm substrates coated with fibronectin, collagen I and laminin compared to FCS are accompanied by a minor increase in median AR on fibronectin (AR=8.9) and a minor decrease for collagen I and laminin (AR=7.8 and 6.6, respectively), but all medians are not significantly different to the corresponding median AR of hdF on FCS-coating (AR=8.5). While the median AR on fibronectin and collagen I, and collagen I and laminin are not significantly different from each other. Together these observations suggest that the decreased A_{CELL} is caused by a reduced cell elongation.
On R=154.2 µm, an increase of median AR could be observed for fibronectin (AR=7.1; $p<0.05$) and collagen I (AR=5.7; $p>0.05$) coating, in relation to cells on FCS-coating-(AR=5.2), while the median A_{CELL} is decreased for fibronectin and increased for collagen I coated substrates. Laminin-coating induces a non-significant decreased median AR (AR=4.6) together with a median A_{CELL} increase. The median AR of the coatings with fibronectin, collagen I and laminin, however, are not significantly different from each other. On the contrary to these rather inconclusive changes for hdF median AR on R=154.2 µm, the median AR on R=312 µm is increased for all coatings (FN AR= 5.4, COL I AR=4.6, LAM AR=4.7) compared to FCS (AR=3.9), which is accompanied by an increase in median cell spreading area, meaning that the increased area is a result of an increased cell elongation.

Investigation of the median nucleus projection area (A_{NUC}) also shows two major tendencies: On substrates with large curvatures (κ=1/59.3 μm^{-1}) changing the coating induces a decrease in median nucleus area, while on substrates with radii of curvature larger than the cell size (R=154.2 µm and 312 µm) and flat PDMS an increase in median nucleus projected area can be observed.
The only significantly different median ($p<0.05$) compared to the FCS-coating however can be observed for the decreased median of A_{NUC} on R=59.3 µm coated with collagen I, all other medians are not significantly different ($p>0.05$).

Discussion

Generally, the biochemical composition of the extracellular matrix, and, therefore, also substrate coating, is known to be able to affect the mechanical state of the cells (*25, 235*). However, since cells display multiple integrins and proteins bind and activate more than one integrin a detailed understanding of specific intracellular signals is challenging and a direct conclusion on cytoskeletal adaption is not easily possible. A comparison with the results from pharmacologically manipulated hdF1 on FCS-coatings might be helpful to gain additional insight.

Before doing so, however, it needs to be emphasized, that although the protein coatings, besides FCS, are made of defined protein solutions, the surface cells encounter most likely vary and change over time. This change is due to multiple factors, including the use physisorption for coating, the utilization of FCS containing medium, which includes the cell adhesion proteins vitronectin and fibronectin (*230, 231*), protein-protein interactions (*17*), as well as cellular remodeling including the binding of soluble fibronectin and subsequent fibronectin fibril formation (*40, 236*) as well as protein synthesis.

The present work, together with the results from other researcher (*120*) suggests that the nucleus seems to be the mechanosensor responsible for curvature perception and that the cell reorients its cytoskeleton and, therefore, its polarization orientation in order to reorient the nucleus to decrease the stress and deformation acting upon it. To achieve this rotation of the nucleus both stress fibers and a functional microtubule network seems to be necessary. Results also indicate that the stress of the curvature on the nucleus induces a remodeling of the nucleus, decreasing its projected area on FCS-coating without pharmacological manipulation.

Comparison of results from variation in protein coating to results from pharmacological manipulation of the cytoskeleton

Angle of orientation

Comparing the results of the median cell angles of orientation of hdF on different coatings (Figure 35, p. 121) with those resulting from pharmacological manipulation of the cytoskeletal components (Figure 27, p. 90; for better comparison cf. Chapter VIII Appendix, Part V: Supplementary Materials Figure 84, p. 226) shows that both, fibronectin and collagen I-coating, increase the median axial cell alignment comparable to the alignment achieved by RhoA activation either by CN03 or Nocodazole induced release of GEF-H1. The increased median axial alignment observed for fibronectin is even stronger than the increased alignment achieved by RhoA activation using CN03, especially for R=312 µm.

For nucleus median orientation again, the effect of fibronectin and collagen I-coating seem to be comparable, and for R=312 µm the effect of fibronectin-coating is even stronger than the RhoA induced increase in nucleus axial alignment caused by CN03.
Laminin-coating, on the contrary, only has a minor effect on median cell orientation: ψ_{Med} is only decreased on R=312 µm substrates and is identical with FCS for both R=154.2 µm and 59.3 µm substrates. Interestingly, this adaption on R=312 µm substrate is comparable the one observed after Taxol induced microtubule stabilization, but regarding the overall distributions it is also comparable to FCS-coating without pharmacological manipulation.
For the adaption of the nuclear ψ_{Med} n, a decrease of the median orientation for laminin-coated R=154.2 µm and 312 µm can be observed, while the adaption on R=312 µm is as strong as the one on fibronectin-coating and FCS-coating after Nocodazole-treatment. Interestingly, cells growing on laminin-coating seem to show a stronger reorientation adaption for nuclei compared to the cell adaption of the median, which can only be observed for Blebbistatin- and CN03-treated hdF on, and only on R=59.3 µm. In all other conditions the cell orientation is always affected stronger.

Taken together, the different coatings show comparable orientation adaption as seen for hdF after Rho A activation, indicating that the coating increases stress fiber formation and cell contractility, which is, most likely, an effect of an increased ligand density presented to the cell. An increased density was shown to affect cellular mechanotransduction including the Rho/Rock pathway (*29, 92*), as well as MSC response to hill and valley topographies (*120*).

When considering the applied concentration of the cell adhesive components in the different coating solution, at first, an increased ligand density from FCS (20% FCS: 40-80 µm mL^{-1} FN and VN, each) to fibronectin (10 µm mL^{-1}), and collagen I (50 µm mL^{-1}) seems to be conflicting. However, one needs to consider that FCS contains a mixture of proteins, including cell adhesive and non-adhesive proteins, all competing for adsorption onto the substrate. This competition negatively affects the overall adsorption of cell-adhesion proteins. In the presence of serum concentrations above 2 % (v/v) fibronectin adsorption was reported to be reduced by more than 90 %, while the concentration of vitronectin adsorption at 10 % (v/v) serum was reported to be higher compared to fibronectin (*233*). Altogether, this finding suggests that the reported orientation adaption could mainly be due to the influence of an increase in ligand density.

However, a more diverse reaction of cells between the different coatings was expected, since varying optimal densities are described for different proteins (*25*), and, moreover, different ECM proteins are known to interact with varying (integrin) receptors (*27*), which are described to evoke various reactions. These reactions include, for instance, fibroblast to myofibroblast

transition (FMT) (*237–239*), or migration (*240*). The main integrin receptors responsible for the fibronectin interaction with cells, for example, are $\alpha_5\beta_1$ also known as fibronectin receptor and $\alpha_v\beta_3$ which is also called vitronectin receptor. While cell adhesion to collagen is reported to be mainly mediated by $\alpha_2\beta_1$ (*42*), although an interaction with other β1-integrins is also reported.

Cell and Nucleus Dose Response Relationships

When comparing the dose response curves resulting from different coating conditions, the underlying more diverse responses become visible more clearly. Moreover, some interesting resemblances for coating variation and pharmacological manipulations are displayed.

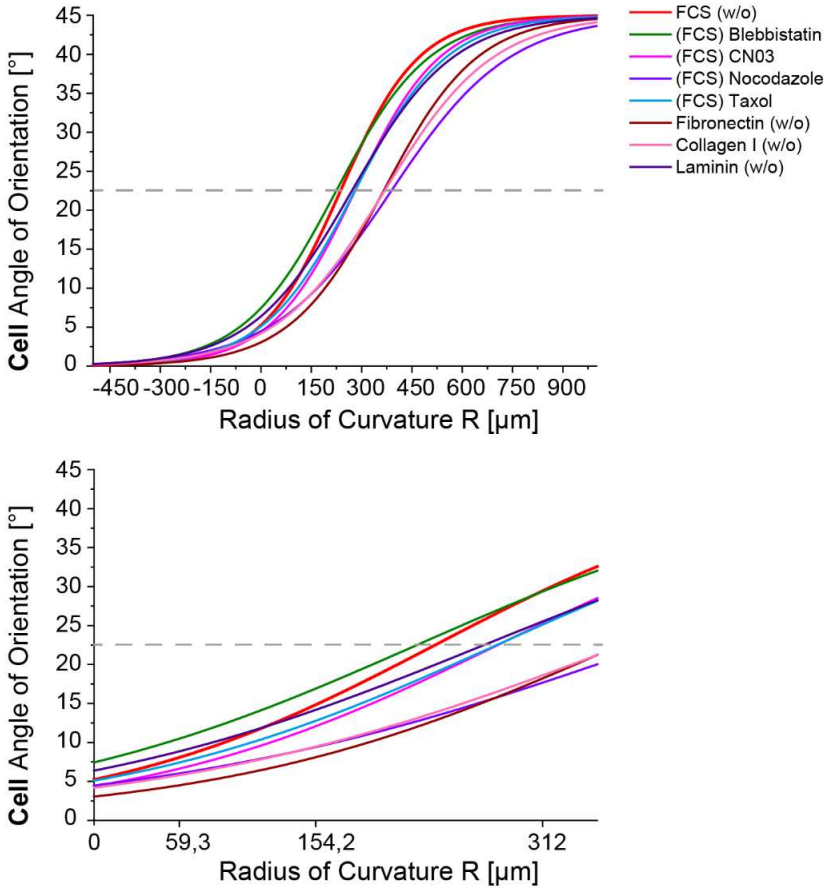

Figure 40 **Orientation of hdF1 on cylindrically curved CurvChip substrates with increasing radius of curvature R under varying conditions displayed as sigmoidal dose response relationships.** Conditions as indicated by the colors in upper right corner, FCS is short for fetal calf serum coating of the substrates, while w/o indicates that no pharmacological manipulation was applied. The first graph shows the whole curve where the upper limit is set to 45° (equals median angle for random orientation) and the lower limit is set to 0°. The second graph displays the DRR in the investigated range. Please note: for purposes of better visualization the data points of ψ_{Med} are not included in the fitted graphs.

For increasing radius of curvature (R>155 µm) three groups of similar cellular DRR progressions can be identified, as visualized in Figure 40. The first cluster, with the lowest

sensitivity to curvature comprises FCS without (w/o) and with Blebbistatin-treatment. The second group, showing a similar course and, therefore, sensitivity to curvature, includes cells growing on FCS-coated substrates treated with CN03, to activate RhoA, hdF1 on FCS treated with Taxol, to stabilize the microtubule, and hdF1 growing on laminin-coated substrates. The highest sensitivity for curvature is attributed to the third group, containing Nocodazole-treated hdF1 growing on FCS-coated surfaces, to depolymerize the microtubule leading to a simultaneous activation of RhoA, as well as hdF1 growing on collagen I- and fibronectin-coated substrates.
Like mentioned initially, this clustering is only visible for substrate radii of curvature larger than about 155 µm, which is also displayed by the ED50 sequence (Bebbistatin < FCS (w/o) < Laminin < Taxol ≈ *CN03* < *Collagen I* ≈ *Fibronectin* < *Nocodazole)*. The sequence of the y-intercept (Blebbistatin > Laminin > FCS (w/o) ≈ *Taxol* < *Nocodazole* ≈ *CN03* ≈ *Collagen I* > *Fibronectin)* represents the status for smaller substrate radii of curvature, and indicates the deviation from ideal alignment, which seems to be increased for Blebbistatin-treatment of hdF on FCS and hdF on laminin-coating, while all other conditions decrease the noise/deviation, with the strongest effect for fibronectin coating.

However, the main conclusion that can be drawn from this observation is about the strength gradation of the effect the different coatings have, and interestingly fibronectin- and collagen I-coating have a stronger effect compared to a simple RhoA activation by CN03. Their effect is comparable to Nocodazole-treatment, where the lack of microtubule was suggested to further increase the stress on the nucleus.

Since previously reported findings and literature indicate that the most important mechanosensor involved in curvature perception or curvotaxis seems to be the nucleus, and that the cell's reorientation is used to reduce the stress on the nucleus, the comparison of nucleus dose response relationships of pharmacologically manipulated hdF1 growing on FCS and of hdF1 growing on different protein coatings, as visualized in Figure 41, might give more information.
Nuclei of hdF1 on growing on FCS and treated with Blebbistatin show a strong effect in reducing the nucleus curvature sensitivity/avoidance in the investigated range of substrate radii of curvature, while coating the substrates with fibronectin causes the opposite extreme, a clear and strong increase in nuclear curvature avoidance over the whole investigated range of substrate radii of curvature. Interestingly, the other coatings and pharmacological manipulations seem to pair up, where always two conditions seem to be inducing a comparable progression of the nucleus DRR: nucleus adaption of hdF1 on laminin-coating shows a similar nuclear DRR like those of Nocodazole-treated hdF1 on FCS-coating, and, therefore, are

suggested to have an increased nuclear stress and an impaired reorientation mechanism. They both show an increased nucleus curvature avoidance with higher radius of curvature. Nuclei of hdF1 on collagen I-coated substrates, on the contrary, show a comparable DRR to nuclei of CN03-treated cells on FCS-coatings over the whole investigated range of R. CN03 is thought to increase the stress on the nucleus without affecting the reorientation mechanism of the nucleus in the cell. In the section of smaller substrate radii of curvature (approx. R< 60 µm) the response of collagen I and CN03 is also comparable to nuclei of cells on fibronectin-coatings, for increasing R, however, the curvature avoidance decreases.

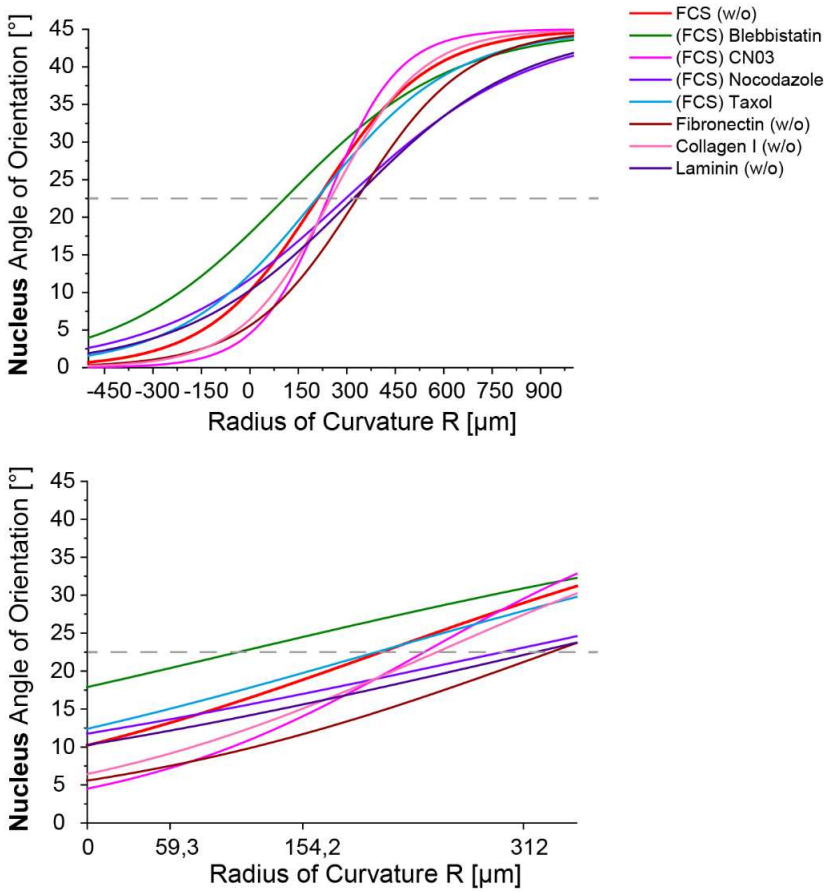

Figure 41 **Orientation of nuclei of hdF1 on cylindrically curved CurvChip substrates with increasing radius of curvature R under varying conditions, displayed as sigmoidal dose response relationship.** Conditions as indicated by the colors in upper right corner, FCS is short for fetal calf serum coating of the substrates, while w/o indicates that no pharmacological manipulation was applied. The first graph shows the whole curve where the upper limit is set to 45° (equals median angle for random orientation) and the lower limit is set to 0°. The second graph displays the DRR in the investigated range. Please note, for purposes of better visualization the data points of ψ_{Med} are not included in the fitted graphs.

The extreme effect of fibronectin-coating on nucleus DRR, exceeding all other examined conditions, might be associated with the in literature relatively well described roles of $\alpha_5\beta_1$ and $\alpha_v\beta_3$ integrins, also known as fibronectin-receptor and vitronectin-receptor, respectively.

Both receptors are described to be involved in cell adhesion on fibronectin substrates, and $\alpha_5\beta_1$ is associated with high RhoA activity and mediating adhesion strength and stress fiber formation via Rho/ROCK pathway, $\alpha_v\beta_3$ integrin is described to be responsible for mechanotransduction, by reinforcing the integrin-cytoskeleton linkage causing low levels of Rho activation (*26, 65, 66*).

Taking a closer look to more detailed findings from literature, moreover, indicates that α_5 integrin is the most important, if not the only, integrin necessary for mechano-response on different ECM-coatings (fibronectin, collagen I and IV and laminin) (*25, 42*), even though α_5 integrin has not been shown to directly interact to laminin and collagen (*27*). However, the interaction of fibroblasts with fibronectin using $\alpha_v\beta_3$, and probably also subsequently activated $\alpha_5\beta_1$ (*42, 241*), has been described to be able to initiate the activation and fibroblast to myofibroblast transition (FMT) (*237, 239, 241*), which is linked to the expression of alpha smooth muscle actin (αSMA) and increased contractility needed in wound healing. This transition could be involved in this strong nucleus reorientation response induced by fibronectin. However, more tests would be necessary to confirm this hypothesis.

The similarity of the course of CN03 and collagen I-coating can also be well integrated into what has already been described in literature. Cells cultivated on collagen gels in the presence of fibronectin in the serum are known to be highly contractile, although there are indications that the contractility is mostly mediated by the fibronectin, which is present in the medium and can bind to cells as well as collagen itself (*40, 42*). The weaker effect compared to fibronectin-coating could, therefore, be explained by two possible circumstances. Firstly, the decreased fibronectin density on the collagen pre-coated substrates, or, secondly, the fact that FMT seems to be impaired when cells are exposed to collagen and/or express $\alpha_2\beta_1$, a collagen I binding integrin (*27, 35, 238*).

The comparable DRR progression of nuclei of hdF1 growing on laminin with nuclei of hdF1 on FCS with Nocodazole-treatment, on the other side is surprising, since nocodazole causes microtubule to depolymerize, which is together with the resulting RhoA activation thought to increase the stress on the nucleus and, therefore, causing this increased effect on larger R. However, this observation is not an effect that would be associated with a protein coating. Fibroblasts are reported to adhere to laminin even in the absence of fibronectin (*242*) and are reported to have a varying composition of the adhesion complex and be more motile compared to fibroblast growing on fibronectin-coatings (*240*). Which is in line with the difference

compared to fibronectin-coating but gives no further explanation concerning the similar course with Nocodazole-treated cells. Results, however, suggest, that laminin might induce some cytoskeletal reorganizations, possibly involving the microtubule network. This possibility is also supported by the decrease in cell/nucleus alignment (median $|\Delta\Psi|$ is increased increased), pointing to an interference with the components involved in nucleus rotation.

Morphological Parameter

As described previously, the results on orientation adaption indicate that the increase in curvature avoidance is related to a RhoA dependent cytoskeletal remodeling with increasing contractility. This increase in contractility also causes changes in morphological parameters. Comparing the effects of protein coatings with those of pharmacological manipulation (cf. Chapter VIII Appendix Part V: Supplementary Materials, Figure 85, p. 227) shows, that coating-based increase in contractility and CN03-treatment evoke comparable changes in cell spreading and aspect ratio.

However, the effect on the nucleus might be of more interest, with two possible outcomes: A stronger compression of the nucleus by apical stress fibers, is could result in an increased nuclear projected area, comparable to CN03-treatment (increased nucleus area; Figure 39, p. 127), or a further decreased nucleus area caused by stress induced nuclear remodeling and chromatin condensation (*78*), like described previously for the decreased nuclear projected area of hdF1 on flat FCS-coated PDMS and curved substrates.

Interestingly, all coatings induce an (non-significant) increase in nucleus projected area for all substrates except R=59.3 µm, while nuclei on R=59.3 µm show a decrease in nucleus projected area.

The reason for why the additional stress on the nucleus caused by the deformation by substrate curvature does not affect nucleus remodeling on substrates with smaller curvature (higher R), is probably due to the relation of nucleus size and cylindrical radius of curvature, visualized in Figure 32 (p. 109). An approximated area of 250 µm² (of hdF1 on flat PDMS) would mean a diameter of 17.8 µm assuming a theoretical circular nucleus shape. This aproximated diameter is about three times smaller than R=59.3 µm and about nine times smaller than R=154.2 µm.

Additionally, Li et al. (*170*), describe a curvature dependent activation of β_1 integrin for cells (MSC) growing on micro-scale curvatures that are comparable to cell size. This activation might also occur on R=59.3 µm cylindrical substrates, which then could additionally affect cytoskeletal contractility and nuclear compression in the presence of a high density of ligands. However, this hypothesis needs to be seen with caution, as the increase in activated β_1 integrin was analyzed after 14 days of cultivation on the surfaces, hdF1 here were only cultivated for

24 hours. Additionally, it is unclear if this activation also happens in fibroblasts. However, investigating the activation state of integrin β_1 on defined curved substrates of various radii would be an interesting research aspect that could be addressed in future using the CurvChip platform.

In summary, variation of the substrate coating non-significantly increases cell density on curved areas and enhances cell and nucleus reorientation along the axis of the cylindrical microstructure. The major trend can simply be explained by an increase in ECM ligands compared to FCS. But the more diverse adaptions that become visible when comparing the dose-response curves (radius of curvature-median orientation adaption curves) indicate that, albeit then general robustness of the cell response, cell orientation response differs between the varying proteins.

Effect of Different Topography Parameters Besides Radius of Curvature

Using the here presented CurvChip substrates with cylindrical topographies one needs to be aware that when changing the radius of curvature also other parameter can vary. Sometimes these adaptions are based on a variation of the photomask layout, like done for the manufacturing of wider distances between the cylinders. On the other side, there are also more unintentional variations, like the cylinder height, that are related to the manufacturing procedure and the limited photoresist thickness and resolvable aspect ratio.

In the present chapter, the influence of the distance between the curvatures and the height of the partial cylinders on cell curvature perception and morphological adaption are investigated. All substrates used were coated with fibronectin.

Distance Between Cylindrical Curvatures

Like previously tested for dense hdF layers, the present paragraph investigates if there is an effect of the distance between the cylindrical convexities on cellular curvature perception and morphological adaption of sparsely growing hdF1 on the curved substrate regions.

Substrates with narrow distances (approx. 25 µm) have a radius of curvature of R= 59.3 µm, R= 154.2 µm and R= 312 µm, while cylindrical substrates with wide spacings (approx. 400 µm) all have slightly higher radii of curvature (R= 63.5 µm, R= 166.8 µm and R= 401.3 µm). Figure 42 shows exemplary hdF1 on cylindrical PDMS surfaces of the CurvChip and flat PDMS as a control, as well as normalized rose histograms of cell angle of orientation of cells on the cylindrical areas. Both images and rose histograms show no indication of an influence of distance width. In both cases there is a curvature dependent increase in deviation from axial alignment with decreasing curvature (increasing radius of curvature R).

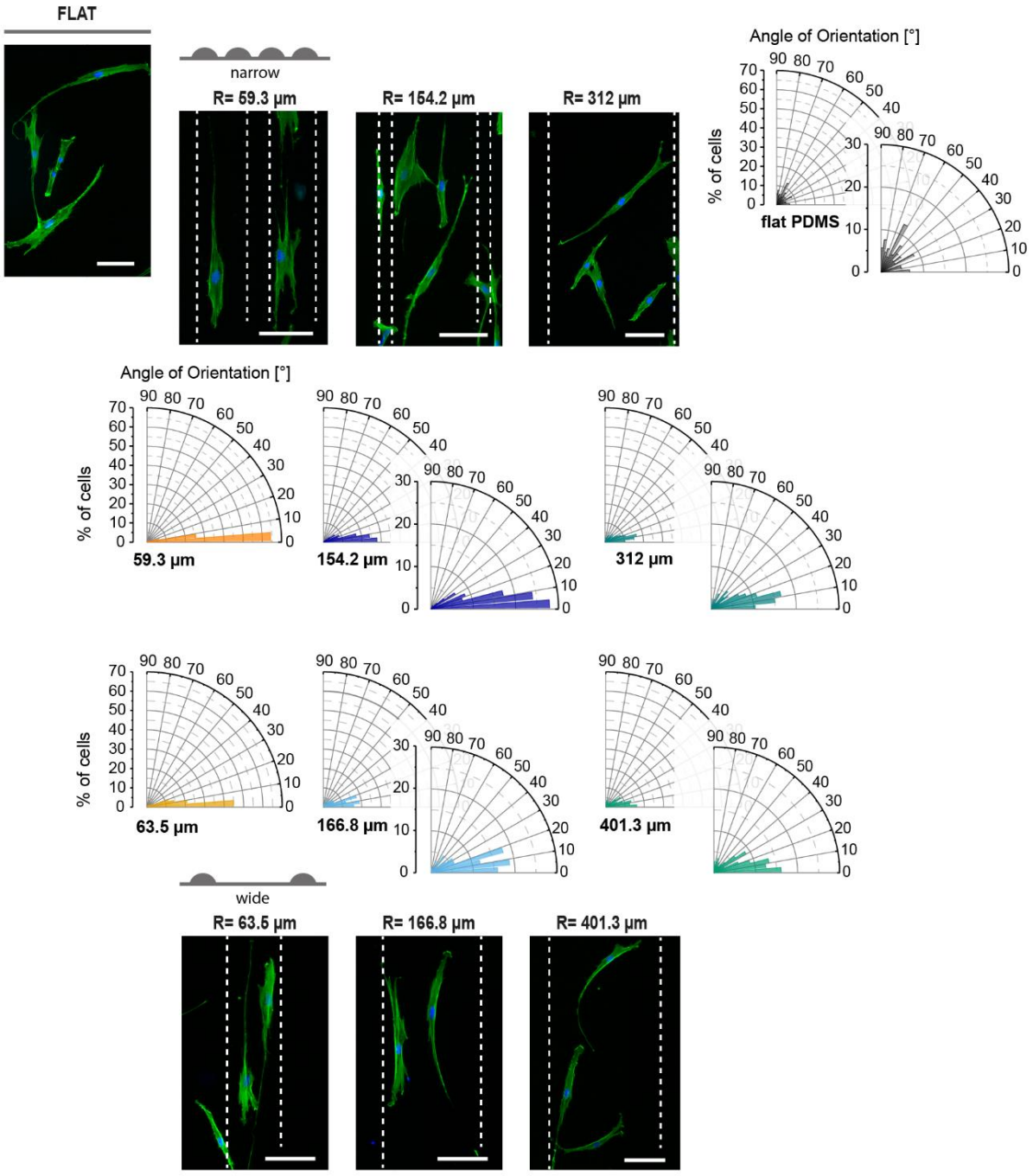

Figure 42 **Fluorescence microscopy images and rose histograms of hdF1, cultivated in low density on fibronectin-coated CurvChip substrates with convex cylindrical curvatures of varying radii of curvature R and spacing between the cylindrical curvatures (narrow/wide).** Flat PDMS was used as a control substrate, narrow distance is about 25 µm while wide distance is about 400 µm. Fluorescence images show F-actin stained green; the nuclei stained blue, dashed lines indicate the boundaries of the cylinders. Scale bar 100 µm. Rose histograms show the percentage of cells or nuclei oriented in a certain angle in relation to the cylinder axis (0°) and dependent on the radius of curvature of the PDMS substrate topography. Bin size 5°; sample size $n_{59.3\,\mu m}$= 129; $n_{154.2\,\mu m}$= 104; $n_{312\,\mu m}$= 126; n_{flat}=104; $n_{63.5\,\mu m}$= 105; $n_{166.8\,\mu m}$= 101; $n_{401.3\,\mu m}$= 112; To facilitate comparison and decreasing

confusion the axis scaling was kept the same and only adjusted in the diagrams overlapping the ones with larger scaling.

When investigating the nucleus density (Figure 43 A) either on the cylindrical curvatures ("curv") or on the areas between the curvatures ("btw"), for substrates with narrow spacing the cell density between the structures is always higher compared to the curved regions, like described previously. This distribution is especially prominent for R=154.2 µm and R= 312µm substrates. For substrates with wide spacings, the nucleus density between the curved regions is significantly reduced ($p<0.001$) for intermediate and large radii (R=166.8 µm and R=401.3 µm), compared to narrow spacing.
In other words, hdF preferentially position themselves in the quasi-concave regions between the structures that are formed for narrow spacing cylinders, whereas this preference is negated when spacing width increases. This observation is in line with what Pieuchot et al. (*120*) and Werner et al. describe concerning concave regions of a substrate: Werner et al. (*97, 211*) found that sparsely growing mesenchymal cells in concave topographies of varying mesoscale sizes, like partial spheres and cylinders, avoid bending by lifting the cell body up. Comparable to this observation, some of the hdF on our CurvChip substrates also seem to be spanning over the concave gap between the cylindrical curvatures (Figure 43 B, $2^{nd}/4^{th}$ area btw) while others seem to prefer an orientation along the cylinder axis positioning the nucleus in the transition area in-between curvature and flat area.

To investigate if the second way of curvature avoidance of cells, namely reorientation of the cell and nuclei on the curved regions is also affected by spacing width, the cell and nucleus orientation on cylindrical topographies with varying distances between the cylinders and comparable radii of curvature were analyzed. The results in Figure 44 show a tendential increase of cell and nucleus orientation angle for wide spacing compared to narrow spacing. However, displaying the orientation values in scale and sorted by ascending radius of curvature (Figure 45) suggests, that this increase is rather an effect of the larger radii of curvature than of the spacing width between the curvatures.

When evaluating the alignment of nucleus and cell orientation (orientation difference; Figure 44, right graph) there is no significant difference between the alignment on substrates with narrow and wide spacing, however the median orientation difference is always larger on substrates with wide spacing (2.9° to 3.4°) compared to cells on narrow spacing cylindrical substrates (0.1° to 2.5°) indicating that nucleus orientation on wide spaced curvatures might be slightly weaker compared to nuclei of cells on narrow topographies.

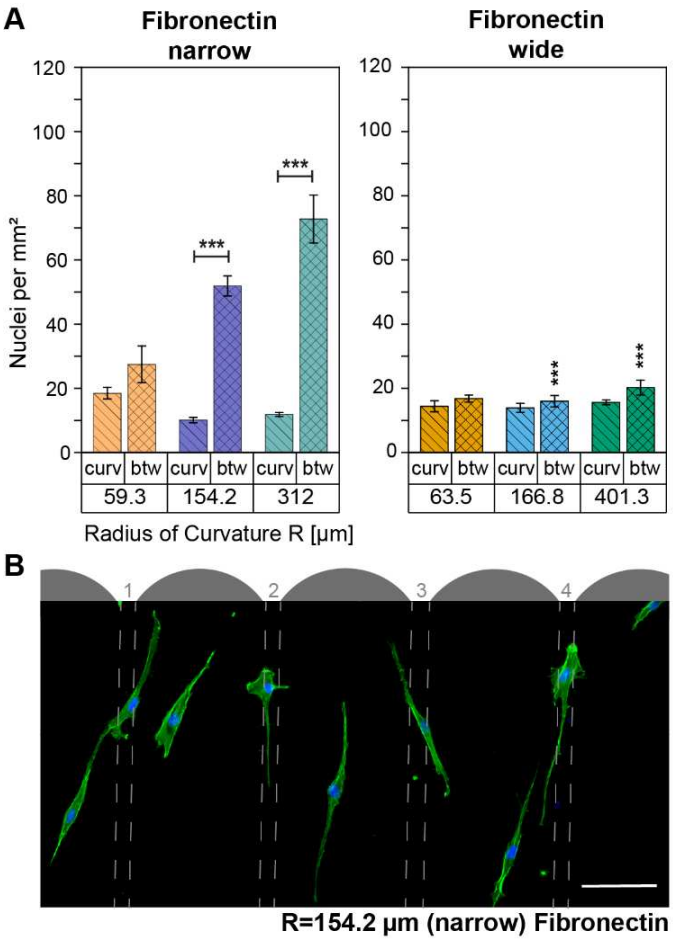

Figure 43 **Effect of varying space between cylindrical curvatures on nucleus density of hdF1 in different substrate areas and for cylindrical CurvChip topographies with varying radii of curvature R, coated with fibronectin.** ***A*** Nucleus density (Mean ±SE). Curv indicates nucleus density on curved regions, btw nucleus density in transition zones between the convex curved regions of the substrates, narrow indicates a spacing of 25 µm, wide 400 µm. Mean density ±SE of hdF1 on flat PDMS coated with fibronectin is 12.2 ±0.24 nuclei per mm². Significant differences to corresponding density of the other condition are indicated by *, significant differences to different area in same condition are indicated by * (*p<0.05; **p<0.005; ***p<0.001) calculated by one-way ANOVA with Dunn's post-hoc test. ***B*** Exemplary fluorescence image (f-actin green, nuclei blue) of cells positioning their nuclei in/over the (narrow) area between the cylinders. Topography boundaries indicated by dashed lines and curved regions of the substrates are emphasized by partial, grey, spheres (not in scale). Scale bar 100 µm. Both figure parts adapted from Frey et al. (*1*)

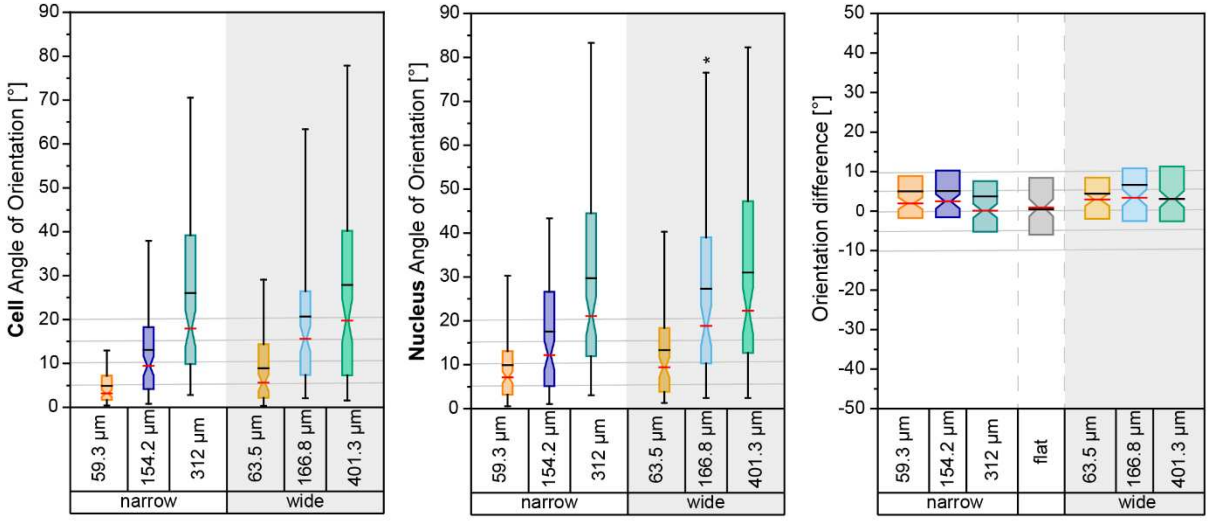

Figure 44 **Effect of varying space between convex cylindrical curvatures of the CurvChip on cell and nucleus orientation**. Substrates were coated with fibronectin. Orientation difference (nucleus subtracted by cell angle of orientation) displays nucleus and cell alignment with values larger than one indicating a lower axial alignment of the nucleus compared to cell alignment with the cylinder axis. Notched box plots Boxes showing the 25th and 75th percentiles, the red lines indicate the median and the black lines display the mean, whisker show the 5th and 95th percentile range. Sample size cell and nucleus $n_{59.3\ \mu m}$=129; $n_{154.2\ \mu m}$=104; $n_{312\ \mu m}$=126; $n_{63.5\ \mu m}$=105; $n_{166.8\ \mu m}$=101; $n_{401.3\ \mu m}$=112; * Significant ($p< 0.05$), ** highly significant ($p<0.005$), *** most significant ($p<0.001$) to comparable substrate in other condition; Kruskal-Wallis with Dunn's post-hoc test. Graphs of Cell and Nucleus Angle of Orientation adapted from Frey et al. (*1*)

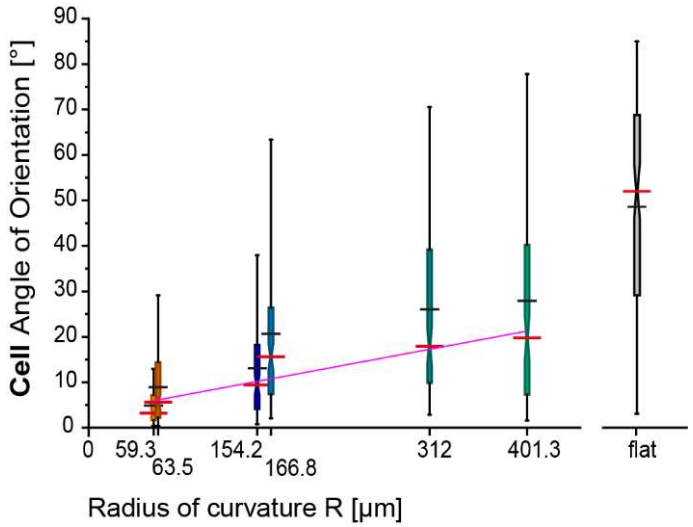

Figure 45 **Cell angle of orientation of hdF1 on fibronectin-coated CurvChip substrates with cylindrical curvatures of varying radius of curvature R and varying distances.** Boxes are displayed in scale, 59.3 µm 154.2 µm and 312 µm narrow space between cylinders (approx. 25 µm), 63.5 µm, 166.8 µm, 401.3 µm wide distance (approx. 400 µm). Notched box plots Boxes showing the 25th and 75th percentiles, the red lines indicate the median and the black lines display the mean, whisker show

the 5th and 95th percentile range. Sample size cell and nucleus $n_{59.3\ \mu m}$=129; $n_{154.2\ \mu m}$=104; $n_{312\ \mu m}$=126; $n_{63.5\ \mu m}$=105; $n_{166.8\ \mu m}$=101; $n_{401.3\ \mu m}$=112; linear fit of medians is indicated by pink line (Pearson R 0.923); Adapted from Frey et al. (*1*)

Especially for cells migrating from narrow "confined" spaces onto the cylinders, it is imaginable that their cell morphology might be persistently affected. To investigate this theory, the cell and nucleus morphology on curveted substrate regions with varying spacing was also evaluated as displayed in Figure 46.

Concerning cell spreading area, a tendential increase (not significant $p>0.05$) between cells on cylindrical topographies of comparable radius of curvature with narrow and wide spacing are observable. However, since the overall trend of increasing area with increasing radius of curvature is visible independent from spacing width, it is more likely, that this observed increase for wider spacings is caused by the larger radius of curvature rather than increased spacing width.

Regarding the nucleus projected area, also a minor increase in median values can be observed for wide spacings but also no significant differences ($p>0.05$) could be determined.

For cell elongation, measured by the aspect ratio, again, no significant differences could be observed between narrow and wide spacings. The elongation seems to constantly decrease for increasing radius of curvature.

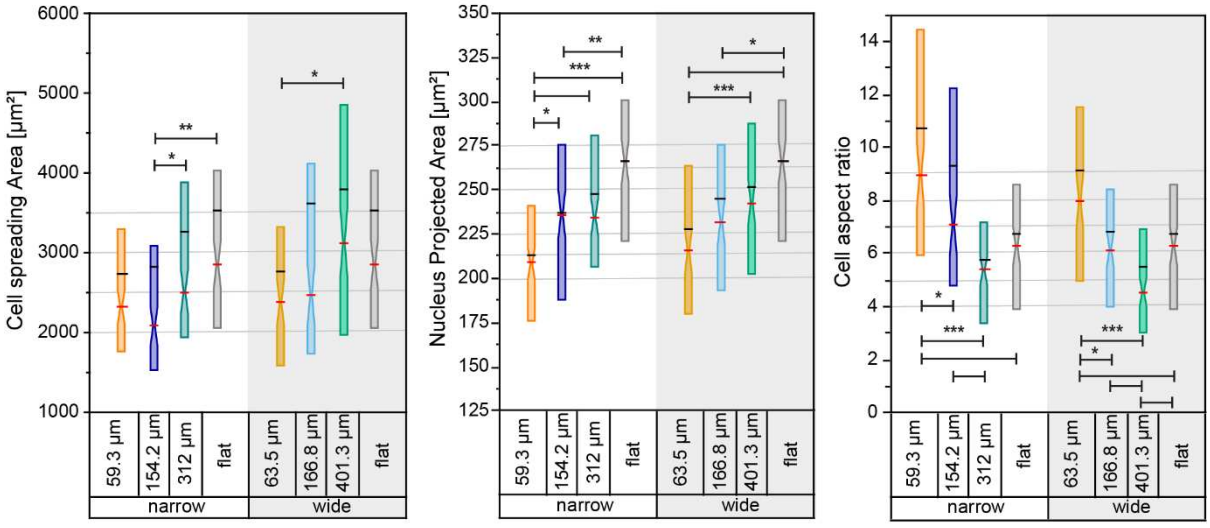

Figure 46 **Morphological adaptions of hdF1 on cylindrical, fibronectin-coated CurvChip substrates with varying radius of curvature R and spacing between the cylinders**. Narrow equals approx. 25 µm, wide approx. 400 µm. Notched box plots Boxes showing the 25th and 75th percentiles, the red lines indicate the median and the black lines display the mean. Sample size cell/nucleus $n_{59.3\ \mu m}$=125/129; $n_{154.2\ \mu m}$=104/102; $n_{312\ \mu m}$=126/126; $n_{63.5\ \mu m}$=91/103; $n_{166.8\ \mu m}$=101; $n_{401.3\ \mu m}$=112;

n_{flat}=104/104 * Significant ($p< 0.05$), ** highly significant ($p<0.005$), *** most significant ($p<0.001$) to comparable substrate in other condition or as indicated; Kruskal-Wallis with Dunn's post-hoc test.

All together it can be concluded that the width of the spacing between the cylindrical convexities does not affect cell orientation and morphological parameter of hdF on fibronectin-coated PDMS cylindrical topographies. However, there seems to be a trend towards stronger cell/nucleus alignment on substrates with narrow spacings.
A possible explanation might be that this stronger alignment is formed in the narrow gaps between the cylinders before cells migrate onto the curvatures, for instance due to the spacial confinement or due to an increase in stress fiber formation, which might be necessary for spanning over the gaps.
Moreover, a clear effect on nucleus density in the transition zones can be observed: Increasing the width of the area between the curvatures reduces the ability of the cell to place the nucleus over or in a concave region to reduce the stress, which seems to be the driving force for the increased density in density in narrow areas between the cylinders (*120*). When cells can choose between curved areas and flat, wide transition zones, only a negligible, non-significant, preference for flat over curved surfaces can be observed.
Pieuchot et al. (*120*) using sinusoidal hill and valley topographies with varying parameter also describe that cells show a preferred positioning of the nucleus over the convex regions and when increasing the sinusoidal topographies' period, while maintaining a constant period to amplitude ratio, they found, that the preference of nuclei for valleys over hills is strongly reduced. Certainly, in this case not only the distance between the hills increases, but also the curvature and height of the structures changes. Therefore, a direct comparison of the two situations is not possible, however, the analogy is still worth mentioning.

Comparison with Cells Growing in More Dense Layers

Like previously shown in Figure 16 and Figure 17 (p. 64 and 68, respectively), as well as Table 7 (p. 65) cells in denser layers on cylindrical curvatures are even more aligned compared to sparsely growing cells. And this axial alignment seems to be independent from the distance between the cylinders. However, other parameters of hdF/nuclei in densely growing layers on these different substrates were not further characterized. Therefore, in the following paragraph the nucleus density as well as nucleus projected area (A_{NUC}), of hdF3 on cylindrical substrates with wide and narrow space between the cylinders was investigated.

For both parameters, only the top 1/3 of cylindrical microstructures was analyzed. The main reason for this approach is that projection correction would need manual adjustment, which was not feasible for the high number of nuclei (n=230-300). Moreover, since projection error,

usually responsible for the necessary correction of the projection bias, (cf. Figure 10) is negligibly small in the analyzed top 1/3 area, this strategy was pursued. To maintain better comparability this reduced area was also used for the determination of nucleus density.
For substrates with narrow cylindrical microstructures, the mean nucleus density (Figure 47 A, left) on areas between the cylinders (BTW) is higher in all cases, compared to the density on cylindrical curvatures (CURV; top 1/3). This difference is statistically significant for R= 59.3 µm and 154.2 µm ($p<0.05$), and comparable to what can be observed for sparsely growing hdF1 (Figure 43, p. 140). This finding suggests that hdF in denser layers still seem to prefer positioning their nuclei in the quasi-concave narrow area between the cylinders over the convex curvatures. Pieuchot et al. (*120*), also investigated how MSC in denser layers (90% confluency) position on their hill and valley topographies and also describe that cells remain excluded from the convex areas resulting in a three times higher density in concave areas compared to flat substrates. In comparison to that, on cylindrical substrates the effect is not that strong, but still the density in the narrow quasi-concave areas between the cylinders is higher compared to flat PDMS ($p>0.05$, except for R=154.2 µm substrate).

The difference between the two approaches is most likely due to the uniaxiality of the curvature for cylindrical substrates, where cells can also avoid curvature by reorientation along the cylinder axis, which they are shown to do (cf. Figure 16, Figure 17 and Table 7). Interestingly, for epithelial cells growing in denser clusters and colony centers, curvature does not seem to have an influence on nucleus positioning. However, epithelial cells have a different cytoskeletal organization with strong cell-cell contacts and are generally described to behave differently on uniaxial curvatures compared to mesenchymal cells. Yevick et al. (*206*), for instance observe a circumferential alignment for MDCK cells growing on R<40 µm cylinders (*206*), which was also described for brain microvascular endothelial cells on capillaries with R<12.5 µm (*207*), as well as single epithelioid cells with cortical, circular actin bundles on R<25 µm (*167*).

When comparing dense and sparse growth conditions in narrow cylindrical substrates more closely, for increasing density one can observe a decrease of the preference for quasi-concave transition zones (“btw”) compared to the convex curvatures. This decrease can nicely be quantified by the density ratio of curved to areas between the curvature listed in Table 18. But, this trend might most likely be an effect of cells growing into free spaces.

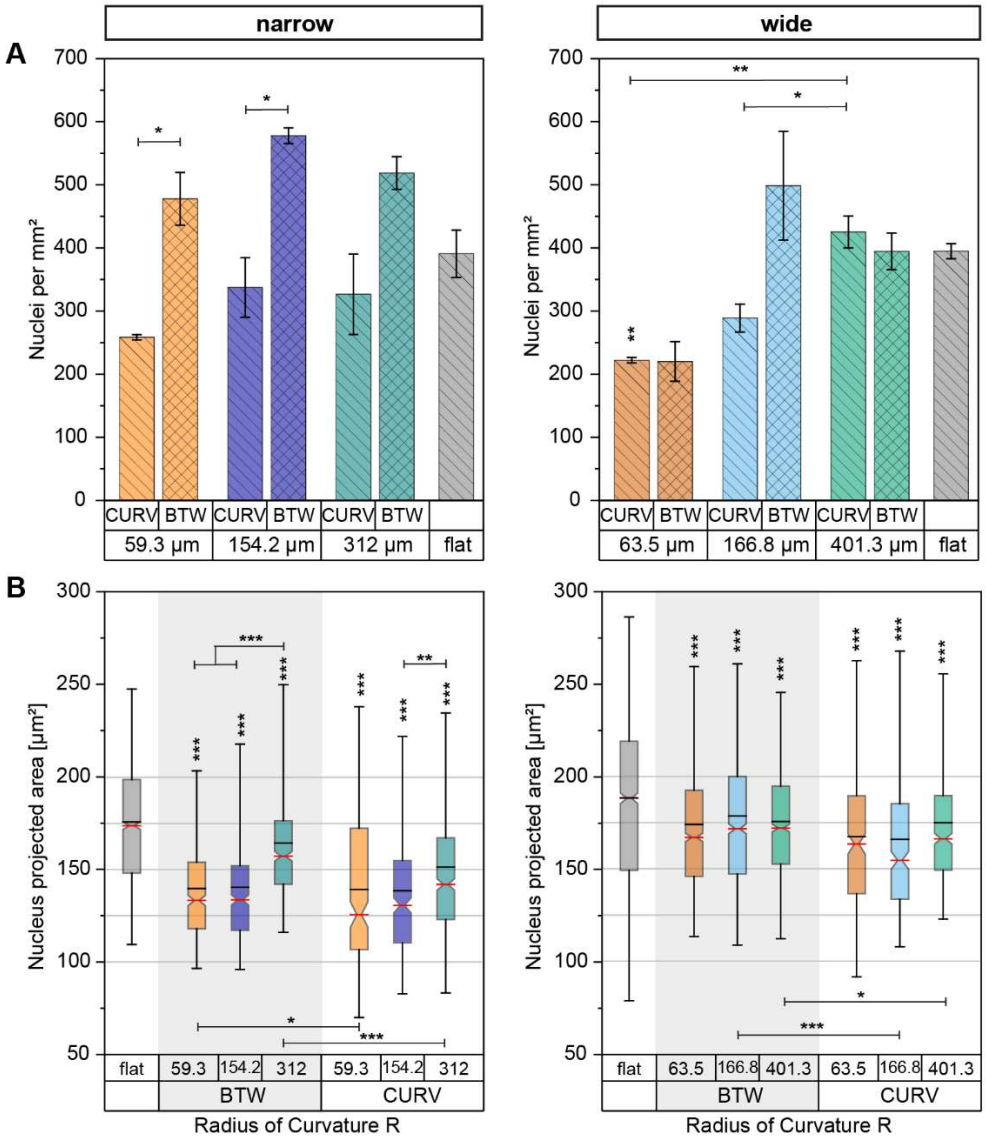

Figure 47 **Nucleus density** (*A*) **and nucleus' projected area** (*B*) **of hdF3 growing in dense layers on fibronectin-coated, cylindrical CurvChip substrates of varying radius of curvature R and space between the cylinders**. For both analyses only the top 1/3 of cylindrical microstructures was used, since projection error is negligibly small in this area. Projection correction would need manual adjustment which was not feasible for this high number of nuclei. Space between the cylinders (BTW) varies between 25 µm (narrow, left column) and 400 µm width (wide, right column). ***A*** *Nucleus density* (mean± SE) of nuclei on convex cylindrical curvatures of indicated radius of curvature R (CURV) or on the area between the curved regions (BTW). * statistical significance (*p<0.05; **p<0.005; ***p<0.001) of means as indicated or compared to flat PDMS (control substrate); one-way ANOVA with Dunn-Sidak post-hoc test. Sample sizes FN (narrow) $n_{59.3\,\mu m}$= 402; $n_{154.4\,\mu m}$= 279; $n_{312\,\mu m}$= 276 cells. FN (wide) $n_{59.3\,\mu m}$= 303; $n_{154.4\,\mu m}$= 294; $n_{312\,\mu m}$= 339. **B** *Nucleus projected area (*of top 1/3 curved area), notched box indicates 25th to 75th percentile whiskers indicate 5th to 95th percentile. The median line is shown in red, while the black line indicates the mean. Sample size for CURV area $n_{=59.3/63.5\,\mu m}$=230; $n_{154.2/166.8\,\mu m}$=290, $n_{=312/401.3\,\mu m}$=500, for BTW areas $n_{59.3/154.2/312\,\mu m}$=350; $n_{63.5/166.8/401.3\,\mu m}$=1000; flat PDMS

n=1500 each. * statistical significance (*p<0.05; **p<0.005; ***p<0.001) as indicated or compared to flat PDMS control; tested with Kruskal-Wallis with Dunn's post-hoc test.

Table 18 **Ratio of nucleus density on curved regions and between cylinders for hdF growing in dense and sparse conditions on CurvChip substrates with narrow and wide space between the cylinders, coated with fibronectin**. (narrow 25 µm/ wide400 µm) Calculated from mean densities as visualized in Figure 43 and Figure 47 A.

Substratum	**Radius of curvature R**	**Ratio of cell density** (curved regions/area between cylinders)	
		Low density	**High density**
narrow	**59.3 µm**	0.67	0.54
	154.2 µm	0.16	0.58
	312 µm	0.16	0.63
wide	**63.5 µm**	0.8	1.01
	166.8 µm	0.87	0.58
	401.3 µm	0.77	1.74

Furthermore, like also observed for sparsely growing hdF (Figure 43), the preference is also lost, when the area between the curvatures is increased from approx. 25 µm to 400 µm. Nucleus mean densities on R=66.5 µm and 401.3 µm, show comparable mean density for curv and btw and the difference between the mean density in the two surface areas on R=166.8 µm substrates is also not significant (p>0.05). Moreover, the density on curved regions (top 1/3) is significantly decreased for small R (large curvatures) compared to flat, and increases with increasing radius (decreasing curvature), a tendency that is observable independent form cylinder distance, but only significant for substrates with wide spaces between the cylinders.

Data on nucleus projected area in Figure 47 B show, that the median nucleus area (A_{NUC}) is significantly (p<0.05) decreased on substrates with cylindrical topographies independent from position on substrates (on top 1/3 curvatures or in areas between cylinders) as well as from size of the area between the cylinders. Furthermore, nuclei of hdF3 in dense layers are smaller compared to nuclei of hdF1 growing in low density. However, this difference in nuclear area is most likely an effect of different donors, like also indicated by the exemplary comparison of nucleus projection area of hdF1 and hdF2 on flat PDMS under varying conditions in Figure 87 (Chapter VIII Appendix, Part V: Supplementary Materials; p.228).
Regardless, differences between the different substrates for hdF3 growing in dense layers are still detectable, with smallest median A_{NUC} on cylindrical topographies with narrow area between the curvature and largest median A_{NUC} for nuclei in areas between the curvatures of

substrates with wide spacings. On curvatures with narrow space between the cylinders, nuclei show an increasing median projected area for increasing radius, while only R=154.2 µm and 312 µm are significantly different ($p<0.005$). This increase was also observed for sparsely growing hdF on the same substrates. Furthermore, for R=59.3 µm and 312 µm, nuclei of hdF3 in narrow spacings between the cylinders show a significantly larger median A_{NUC} compared to the corresponding median nuclei area on curvatures. And interestingly, the median A_{NUC} of nuclei between R=59.3 µm and 154.2 µm cylinders are significantly ($p<0.001$) smaller compared to nuclei between R=312 µm microstructures. For substrates with wide spacing between the cylinders also significant differences between the two areas are detectable, while nuclei on curved regions are again smaller compared to nuclei in areas between the cylinders. However, unlike for sparsely growing hdF1, the different radii of curvature show no significant impact on nucleus area.

In conclusion, for hdF growing in dense layers the distance between the cylinder seem to influence nucleus projected area, with larger median A_{NUC} for cells on substrates with wider distances compared to narrow cylinders, an effect that could not be observed for sparsely growing hdF1. Furthermore, the effect of cylinder distance on nucleus density in denser layers is comparable to the effect on sparsely growing cells and what Pieuchot et al. (*120*) described for MSC in dense layers, albeit the effect on cylindrical substrates is weaker compared to the sinusoidal hill and valley substrates of their approach.

Structure Height of Cylindrical Curvatures

Due to the fabrication method with limited aspect ratio and photoresist layer thickness the surface topographies are not semi-cylinders but partial cylinders of varying height. Therefore, when sorting the microstructures by ascending height h (mean ± standard deviation) a different sequence is yielded compared to sorting by increasing radius of curvature R (R≙h): 59.3 µm≙24.2 µm±0.3 µm; 401.3 µm≙26.2 µm±0.9 µm; 63.5 µm≙34.4 µm±1.1 µm; 312 µm≙35.3 µm±0.3 µm; 166.8 µm≙39.4 µm±3.2 µm; 154.2 µm≙40.2 µm±0.7 µm.

To further characterize the factors influencing cell behavior of sparsely growing hdF1 on cylindrical convex surface topographies, the present paragraph investigates if there is an influence of the topography height using fibronectin-coated PDMS substrates with additional variation in the space between the cylinders (25 µm for R=59.3 µm, 154.2 µm and 312 µm; 400 µm for 63.5 µm, 166.8 µm and 401.3 µm).

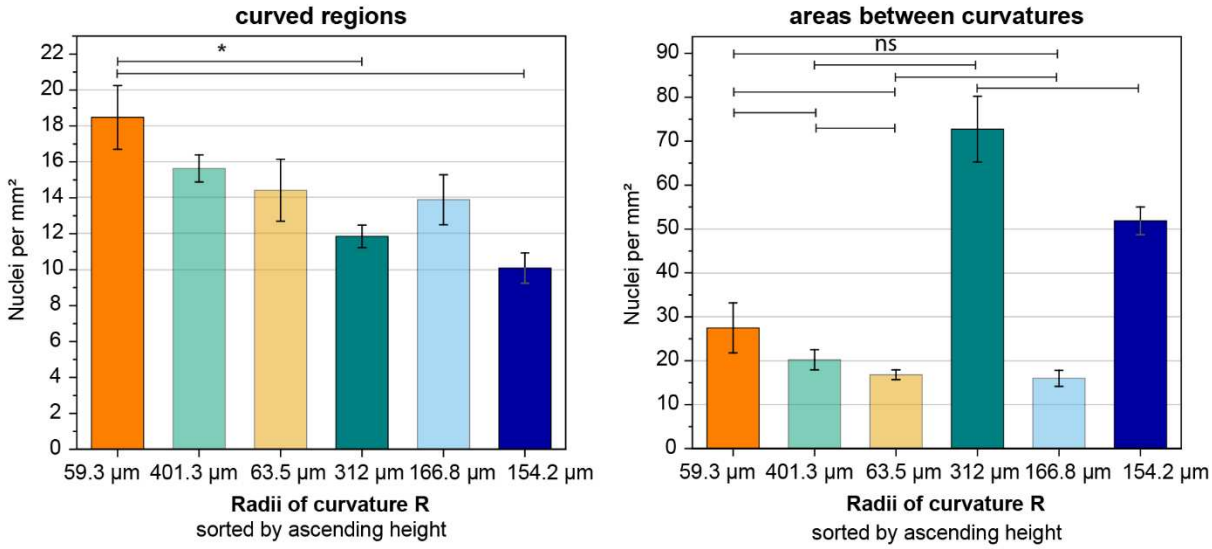

Figure 48 **Nucleus density on fibronectin-coated cylindrical CurvChip substrates of varying radius of curvature and structure height, sorted by ascending height**. Nucleus density (Mean ±SE). *Caution:* ordinate axis scales vary between the two graphs. Radius of curvature R and corresponding height (R≙h) 59.3 µm≙24.2 µm; 401.3 µm≙26.2 µm; 63.5 µm≙34.4 µm; 312 µm≙35.3 µm; 166.8 µm≙39.4 µm; 154.2 µm≙40.2 µm. Areas between the curvatures vary from 25 µm to 400 µm width, while substrates with wide distance between the cylinders are displayed transparently. Sample sizes FN (narrow) $n_{59.3\,\mu m}$= 402; $n_{154.4\,\mu m}$= 279; $n_{312\,\mu m}$= 276 cells. FN (wide) $n_{59.3\,\mu m}$= 303; $n_{154.4\,\mu m}$= 294; $n_{312\,\mu m}$= 339. * significant (*p<0.05); ns not significant, one-way ANOVA with Dunn's post-hoc test.

The dependence of the nucleus density (curved regions and areas between curvatures) from structure height was investigated first. Figure 48 shows bar graphs (mean ± standard error of the mean), visualizing the results in an ascending-height dependent sorting. The density on the cylindrical microstructures seems to decrease with increasing cylinder height, which suggests a direct dependency of density on structure height, but, except for the difference between R=59.3 µm and R=312 µm, and R=59.3 µm and R=154.2 µm, the observed differences are not statistically significant.

Interestingly, a comparable trend can also be observed for the density in the areas between the curvatures of wide spacing substrates (R=401.3 µm; 166.8 µm; 63.5 µm). For narrow spacing substrates, on the contrary, this height-dependency is not visible, moreover here density seems to depend on cylinder radius.

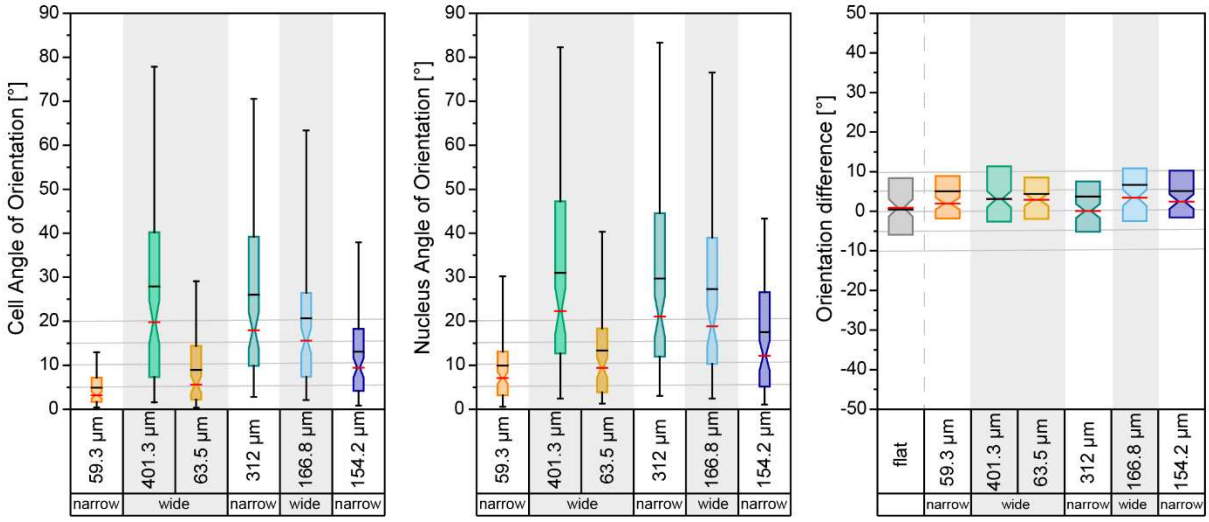

Figure 49 **Cell and nucleus orientation on fibronectin-coated, cylindrical CurvChip substrates of varying radius of curvature R and structure height h, sorted by ascending height.** Orientation difference ($\Delta\Psi=\psi_{NUC} - \psi_{CELL}$) displays nucleus and cell alignment with values larger than one indicating a lower axial alignment of the nucleus compared to cell alignment with the cylinder axis. Notched box plots Boxes showing the 25th and 75th percentiles, the red lines indicate the median and the black lines display the mean, whisker show the 5th and 95th percentile range. Sample size cell and nucleus $n_{59.3\ \mu m}$=129; $n_{154.2\ \mu m}$=104; $n_{312\ \mu m}$=126; $n_{63.5\ \mu m}$=105; $n_{166.8\ \mu m}$=101; $n_{401.3\ \mu m}$=112; Radius of curvature R and corresponding height (R≙h) 59.3 µm≙24.2 µm; 401.3 µm≙26.2 µm; 63.5 µm≙34.4 µm; 312 µm≙35.3 µm; 166.8 µm≙39.4 µm; 154.2 µm≙40.2 µm. Areas between the curvatures vary from approx. 25 µm “narrow” to approx. 400 µm width “wide”.

No correlation can be observed for the dependency of cell and nucleus angle of orientation on curvatures from structure height, visualized in Figure 49, neither for cell, nor for nucleus orientation.

Moreover, the cell/nucleus alignment (Figure 49, right), as well as morphological parameter (cell spreading area, nucleus projection area, cell aspect ratio, Figure 50) also do not present a dependency on structure height.

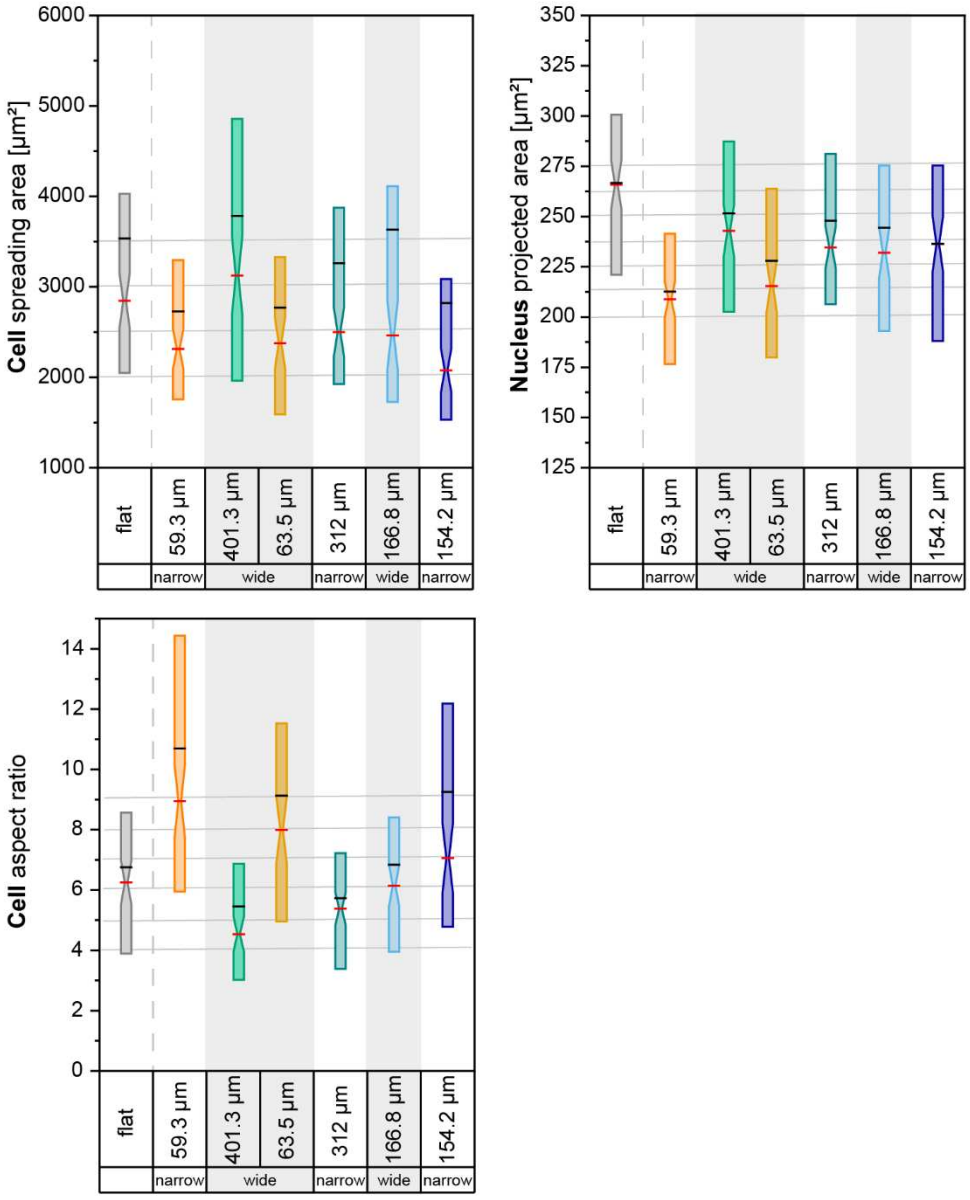

Figure 50 **Morphological adaptions of hdF on cylindrical, fibronectin-coated CurvChip substrates of varying radius of curvature and structure height, sorted by ascending height.** Notched box plots Boxes showing the 25th and 75th percentiles, the red lines indicate the median and the black lines display the mean. Sample size cell/nucleus $n_{59.3\ \mu m}$=125/129; $n_{154.2\ \mu m}$=104/102; $n_{312\ \mu m}$=126/126; $n_{63.5\ \mu m}$=91/103; $n_{166.8\ \mu m}$=101; $n_{401.3\ \mu m}$=112; n_{flat}=104/104 * Significant ($p< 0.05$), ** highly significant ($p<0.005$), *** most significant ($p<0.001$) to comparable substrate in other condition or as indicated; Kruskal-Wallis with Dunn's post-hoc test.

Altogether, structure height seems to be a non-essential parameter regarding cell orientation adaption on cylindrical surfaces. The only parameter that shows a dependency on structure height is the nucleus density, yet only the density on R=59.3 µm cylindrical curvature shows significant ($p<0.05$) differences in relation to the other substrates. And in sparsely growing cell culture conditions the cell morphology on the curvature is not affected by the variation in height.

Structure Height of Cylindrical Substrates with Varying Protein-Coatings

Like shown in the previous paragraph structure height seems to have an effect the nucleus density on cylindrical areas ("curv") coated with fibronectin. Since protein coating was also shown to influence nucleus density the present paragraph investigates if there is an effect of the coating on height-dependent nucleus density, visualized in the bar graphs in Figure 51 (mean ± SE).

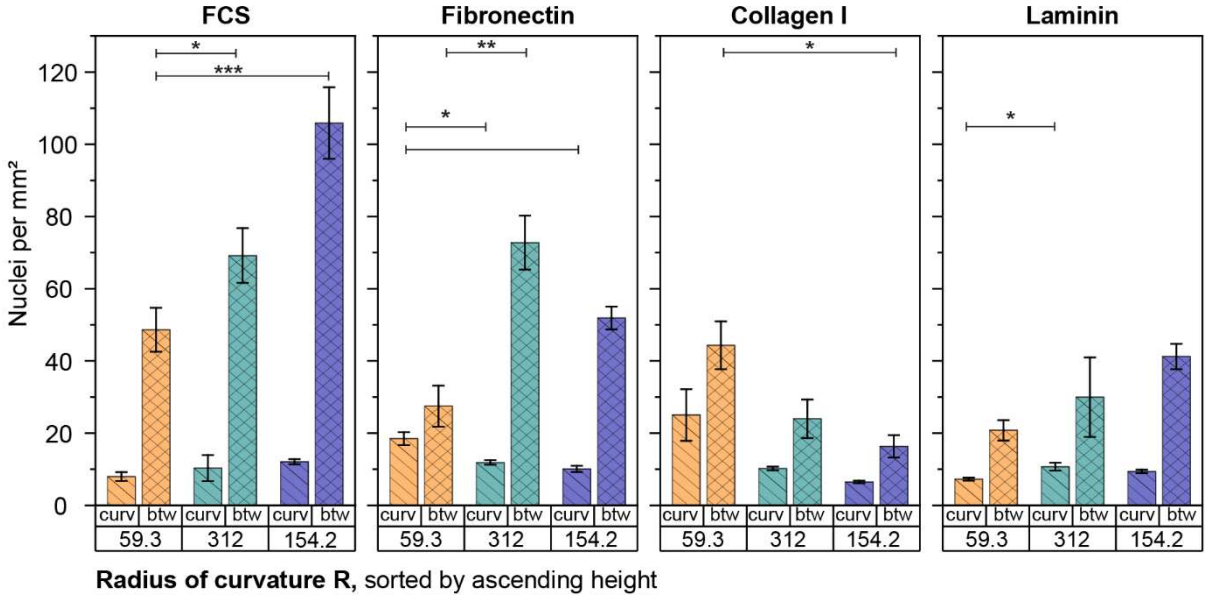

Figure 51 **Coating dependent nucleus density on cylindrical CurvChip topographies of varying radius of curvature R and structure height h, sorted by ascending height.** Nucleus density (Mean ±SE); Radius of curvature R [µm] and corresponding height [µm] (R≙h) 59.3 µm≙24.2 µm; 312 µm≙35.3 µm; 154.2 µm≙40.2 µm. Sample sizes FCS: $n_{59.3\,\mu m}$= 443; $n_{154.4\,\mu m}$= 416; $n_{312\,\mu m}$= 390. FN $n_{59.3\,\mu m}$= 402; $n_{154.4\,\mu m}$= 279; $n_{312\,\mu m}$= 276. Col I: $n_{59.3\,\mu m}$= 457; $n_{154.4\,\mu m}$= 153; $n_{312\,\mu m}$= 178, Laminin $n_{59.3\,\mu m}$= 208; $n_{154.4\,\mu m}$= 240; $n_{312\,\mu m}$= 199. Mean ±SE for flat PDMS (FCS 15.3 ±1.49 nuclei per mm², fibronectin 12.2 ±0.24 nuclei per mm², collagen I 10.4 ±1.02 nuclei per mm², laminin 10.2 ±1.13 nuclei per mm²) are not significantly different from each other. *significantly different from FCS (* $p<0.05$; ** $p<0.005$; *** $p<0.001$) One-way ANOVA with Dunn-Sidak post-hoc test.

Like described previously for fibronectin-coating the density on curved regions (curv) of the substrates, significantly ($p<0.05$) decreases with increasing topography height, while no correlation could be observed among the nucleus density between the cylinders (btw) and topography height.

For collagen I-coated cylindrical substrates a comparable trend ($p>0.05$) for the curved regions (curv) could be observed. Additionally, the density of nuclei in the between-areas (btw) of collagen I-coated substrates is also found to be decreasing with increasing height, while only the difference of the density between the lowest to the highest topographies are statistically significant ($p<0.05$).

On the contrary, for hdF1 on FCS and laminin-coated cylindrical substrates the nucleus density in the area between the cylinders (btw) is showing an increase with increasing topography height, which is significant for FCS. This increase in density with increasing topography height can also be surmised for FCS-coated curved regions (curv; $p>0.05$) while this trend cannot be observed on laminin-coated surfaces, where the density on R=312 µm substrates (intermediate height h=35.3 µm) shows the highest nucleus density and is significantly ($p<0.05$) different to the density on the lowest topography (R=59.3 µm).

In summary, height seems to be a determining factor for the density change on FCS, collagen I and maybe also laminin-coated areas between the cylinders, while for fibronectin it seems to be the radius of curvature.
On the cylindrically curved areas, however height seems to be the limiting factor for hdF on fibronectin and collagen I-coating, while this trend seems to be reversed for FCS-coating (no significant differences), where mean density (slightly) increases with increasing microstructure height. For collagen I and laminin, interestingly the observable trends coincide with a decrease in overall density on the different substrates, while for flat PDMS also a slight, non-significant decrease in nucleus density (collagen I 10.4 ±1.02 nuclei per mm², laminin 10.2 ±1.13 nuclei per mm²) can be observed compared to FCS (15.3 ±1.49 nuclei per mm²) and fibronectin (12.2 ±0.24 nuclei per mm²), also visualized in Figure 88 (Chapter VIII Appendix, Part V: Supplementary Materials; p. 229). Which might indicate an effect of the different protein coatings on initial cell adhesion and/or cell proliferation, like described for other cell types (*243*). Besides the cell density, there is no indication that other parameters of cells on the curvature are affected by structure height.

Comparison with hdF Growing in More Dense Layers

When comparing denser and less dense hdF layers on fibronectin (cf. Figure 52), interestingly, for denser cell layers the previously, for sparsely growing hdF1 described density decrease with increasing cylinder height cannot be observed. Moreover, only regarding the substrates with narrow spacings (non-transparent bars in Figure 52) the opposite trend ($p>0.05$) can be observed: increasing mean density for increasing structure height for both curved areas and areas between the cylinders. Comparable to what was observed for sparsely growing hdF1 on narrow substrates coated with FCS (cf. Figure 51). The increase with increasing height might indicate that cells prefer to place their nuclei in deeper concavities, however, also an affected cell proliferation could be resulting in this difference.
Furthermore, on curvatures of substrates with wide spacings, the radius of curvature seems to be the influencing factor on nucleus density, with statistically significant differences between R=401.3 µm and R=63.5 µm as well as R=166.8 µm.

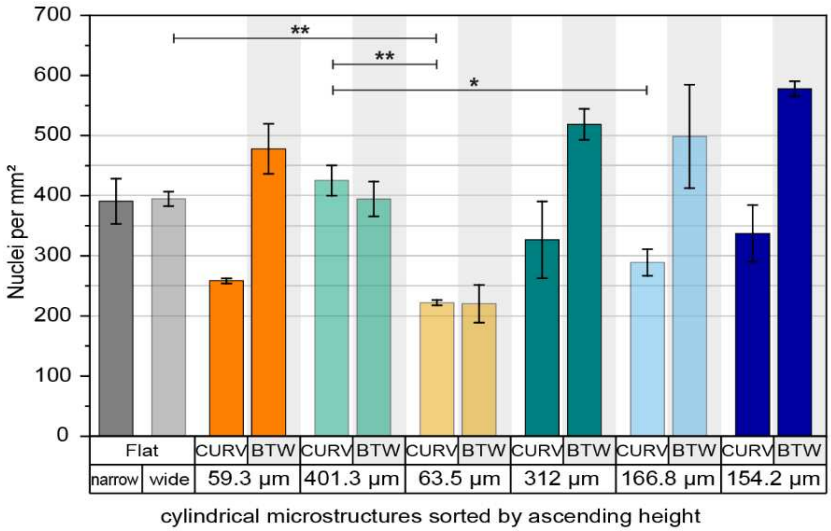

Figure 52 **Nucleus density of hdF3 growing in denser layers on cylindrical, fibronectin-coated CurvChip substrates with varying radius of curvature R, structure distance and height h, sorted by ascending height.** Nucleus density (Mean ±SE) of the top 1/3 of cylindrical microstructures was used. Indicated numbers represent cylinder radius of curvature and substrates with wide distance (approx. 400 µm) between the cylinders are displayed transparently, narrow distance (approx. 25 µm). Radius of curvature R and corresponding height (R≙h) 59.3 µm≙24.2 µm; 401.3 µm≙26.2 µm; 63.5 µm≙34.4 µm; 312 µm≙35.3 µm; 166.8 µm≙39.4 µm; 154.2 µm≙40.2 µm. *significant difference as indicated (* $p<0.05$; ** $p<0.005$; *** $p<0.001$) One-way ANOVA with Dunn-Sidak post-hoc test.

Discussion

Altogether, the height of the cylindrical microstructures seems to have no influence on cell/nucleus orientation or morphological parameter. However, nucleus positioning, and, therefore, density, on the different areas of cylindrical substrates is affected by the variation in microstructure height, especially for cylinders with narrow (25 µm) flat areas between them, resulting in quasi-convex structures. And interestingly, different surface coatings seem to evoke different trends (mostly $p>0.05$) for nucleus density of sparsely growing hdF1 with increasing microstructure height, as summarized in Table 19.

Moreover, for denser hdF3 layers on fibronectin-coated substrates, the trend of sparsely growing hdF (decreasing density with increasing height) is reversed, which could be a result of different cell proliferation on the different substrates and substrate areas.

Pieuchot et al. (*120*) also investigated the influence of different surface parameter on nucleus positioning on their sinusoidal hill and valley substrates and found that for decreasing surface amplitude (representing decreasing valley depth/height of the hills), while keeping the period constant, the nucleus preference for valleys over hill areas decreases. Which in other words means that for increasing amplitudes, representing deeper valleys and higher hills

respectively, an increasing percentage of nuclei are positioned in the valleys and, therefore, a decreasing percentage of cells is positioned on the hills.

Table 19 **Trends for nucleus density observed for increasing microstructure height of cylindrical CurvChip surfaces with 25 µm space between the cylinders.** HD stands for cells growing in high density, CURV stands for the trend on curved surface areas, BTW is short for area between the curvatures; ↑ indicates increase with increasing h, ↓ decrease; ↑→ indicates that increase is not observable for higher structures, R shows that the main influence seems to be the radius of curvature, not structure height.

	FCS	**Fibronectin**	**Fibronectin** HD	**Collagen I**	**Laminin**
CURV	↑	↓	↑	↓	↑→
BTW	↑	R	↑	↓	↑

Comparing these results to the here presented work, is not easy, since it is important to consider that for sinusoidal topographies the amplitude change also affects other surface parameters, like resulting substratum curvature, with higher curvature for larger amplitude. For the cylindrical surfaces of the CurvChip on the other side, structure height is not directly related to curvature or other parameters (R≙h: 59.3 µm≙24.2 µm; 312 µm≙35.3 µm; 154.2 µm≙40.2 µm, cf. Table 3, p. 41), enabling a separation of the two parameter and, therefore, more detailed study of the effect of surface parameter on cell behavior. Additionally, Pieuchot et al. (*120*) present their data normalized to total nucleus number (% of nuclei), which is feasible, since the substrate areas are comparable in size for their sinusoidal topographies, and a higher percentage of cells in an area can be considered equal to a higher density. However, for the cylindrical CurvChip surfaces with narrow spacing the difference between the curved regions and flat regions between the cylinders is high: For R=312 µm the cylinder surface area is approximately 13 times larger than the flat area, for R=154.2 µm this factor is approx. 8, and 4 for R=59.3 µm substrates. This factor was considered and, therefore, data is displayed as nucleus density in the present work. For reasons of completeness the results of the present work, displayed as a percentage of total nucleus number, can be found in the Appendix (Figure 89, p.230). In short, disregarding the difference in area affects the observable trends, for instance cells do not show the characteristic preference of concave narrow areas over cylindrical curvatures and only nuclei on fibronectin-coating show a dependency on structure height.

All in all, comparison and interpretation of the differences is not easy: for fibronectin-coating, the results of the two attempts vary, as Pieuchot et al. (*120*) found an increasing percentage of cells in the valleys for larger amplitudes (larger curvature), while the present work indicates

an increasing density with decreasing curvature in the area between the cylinders. However, regarding the convexly curved regions, where the present work found a decreasing density for increasing height, the two attempts show the same trend. Still, for constant cell count, a density increase in one area should cause a density decrease in the other area, but since the cells are known to proliferate the cell number is not constant. Which is no problem when considering the percentage of nuclei, however for density this results in not correlated trends for curved areas and areas between the cylinders. Furthermore, comparing the trends for hdF3 in high density with those of sparsely growing hdF1 indicates that proliferation might be affected differently by different substrates, which also seems to be the case for different protein coatings.

Nevertheless, it is interesting that coatings that are considered less adhesive (FCS, Laminin) show the opposite trend in height-dependent density distribution on the microstructures compared to coatings considered to mediate strong adhesion.

Proliferation of hdF on Cylindrical Topographies

Cell proliferation is a basic cell function, highly regulated in normal cells compared to cancer. And extracellular surrounding is known to influence cell proliferation by multiple different signals ranging from growth factors to cell-cell contacts and different kinds of stresses impacting the cell (*78, 82, 244, 245*). Cell morphological changes affecting nucleus size for instance have been shown to affect cell proliferation (*78, 82*).
Since the previously presented results on nucleus density indicate a different proliferation based on the underlying topography and area of the topography and, moreover, a decrease in nucleus projected area that is suggested to be caused by nuclear remodeling and DNA condensation can be observed, the present paragraph investigates the proliferation of hdF on fibronectin-coated CurvChip cylindrical topographies and narrow area between the cylinders.

Proliferation was assessed using an EdU assay at two time points, 24 hours and 70 hours after cell seeding to observe if there is a difference for sparsely growing cells compared to hdF in denser layers. Figure 53 shows box plots of the investigated conditions and time points, as well as two exemplary fluorescence images enabling a better comparison in terms of nucleus density, of the differences between the two time points.
Generally, as expected, proliferation significantly ($p<0.001$) deceases with increasing cultivation duration, since cell density is increased causing contact inhibition.
At the first time point, after 24 hours, the median proliferation rate on curved regions (curv) gradually decreases with decreasing radius of curvature: while R=312 µm and R=154.2 µm shows a higher and R=59.3 µm shows the same median proliferation rate compared to flat PDMS substrate. In areas between the curvatures (btw), the median proliferation rate was reduced compared to flat PDMS for R=59.3 µm substrates, while for the areas between R=154.2 µm and 312 µm cylinders, the proliferation rate was increased in relation to flat PDMS. The highest median proliferation rate was determined for the area between R=154.3 µm cylinders, which is interestingly the highest topography (R≙h: 59.3 µm≙24.2 µm; 312 µm≙35.3 µm; 154.2 µm≙40.2 µm). However, all observed differences are not statistically significant.

For the second time point, 70 hours after seeding, interestingly, the gradual increase of the median proliferation rate on the curved areas with increasing radius of curvature was maintained. However, all curvatures showed an increase in median proliferation rate compared to flat PDMS. For the areas between the curvatures the median proliferation rate is also increased in relation to flat PDMS and a gradation for increasing median proliferation rate with increasing radius of curvature can be observed, while the difference between the medians of

R=154.2 µm and R=312 µm is negligibly small. Again, all observed differences are not statistically significant.

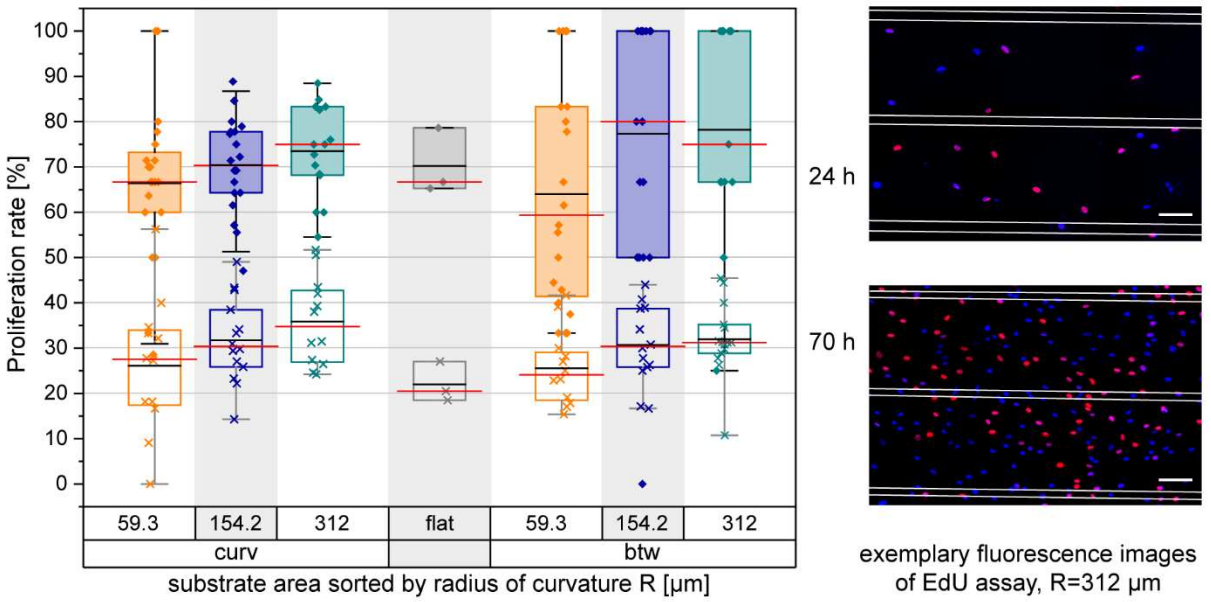

Figure 53 **Proliferation of hdF3 on cylindrically curved CurvChip substrates of varying radii of curvature R and area between the curvatures of 25 µm**. hdF3 were cultured on fibronectin-coated substrates for 20 hours and 66 hours before EdU proliferation assay performance, endpoint was 24 and 70 hours respectively. Curv indicates curved areas of the CurvChip substrates, while btw stands for area between the cylindrical curvatures. Boxes show the 25th and 75th percentile, median (red) and mean line (black), whiskers indicate 5th to 95th percentile. Exemplary fluorescence images for estimated evaluation of nucleus density at the two time points, nuclei of proliferated cells (red), other nuclei (blue). Scale bar 100 µm. For 70 hours compared to 24 hours the proliferation rate was significantly decreased ($p<0.001$), except for flat PDMS substrate. Kruskal-Wallis with Dunn's post-hoc test.In summary, although the differences are not significant, the results suggest that cell proliferation might be affected by substrate curvature. This suggestion is in line with the findings on decreased nuclear projected area on curvature compared to flat PDMS (Figure 39 C, p. 127) and literature derived findings that proliferation is correlated with nuclear volume and chromatin condensation (*78, 82*). Whereas, based on literature findings, the decreased nuclear area observed on curvatures compared to flat PDMS would be indicative for a reduced proliferation, which contradicts the observations of an increased proliferation rate compared to flat PDMS for both timepoints.

The difference in proliferation for the areas between the cylindrical microstructures after 24 hours, moreover, suggest an influence of structure height or probably more correct depth of the quasi-concave areas, which might also explain the change in nucleus density between sparsely growing hdF (Figure 48, density decreases with increasing microstructure height) and hdF in dense layers (Figure 52, nucleus density increase with increasing microstructure height)

on narrow cylindrical substrates, which also accompanied by an increased total density for increasing structure height.

Proliferation Location

Unfortunately, from the results of the EdU assay one cannot easily distinguish where the cell proliferation really takes place and if there is any preference, since cells could be migrating onto the curvatures after proliferating in the areas between the cylinders or vice versa. But, analyzing sequences of time lapse images of cells was not successful for all radii of curvature, since the contrast is not good and contrast enhancing microscopy methods do not work properly due to light deviation by topographies acting as microlenses. The only surface with acceptable visualization of cells on the cylindrical areas and between the structures was R=312 µm as shown in Figure 54. Additionally, it was decided not to use live cell dyes, as these can themselves influence cell behavior (*246*). The exemplary time-lapse sequence of hdF on R=312 µm cylindrical substrates (Figure 54), however, indicates that mitosis does take place in both areas, on curved topographies as well as in quasi-concave areas between the cylinders and no preference is apparent. This observation is also in line with the comparable median proliferation rate in both areas of R=312 µm substrates.

Additionally, it could be observed that cell division can also take place perpendicularly to the cylinder axis, as indicated by the blue boxed mitosis in Figure 54 (t=3-5). However, most of the cell divisions seem to take place longitudinally to the cylinder axis (division axis perpendicular). For a more detailed and quantitative observation, the imaging technique would need to be optimized.

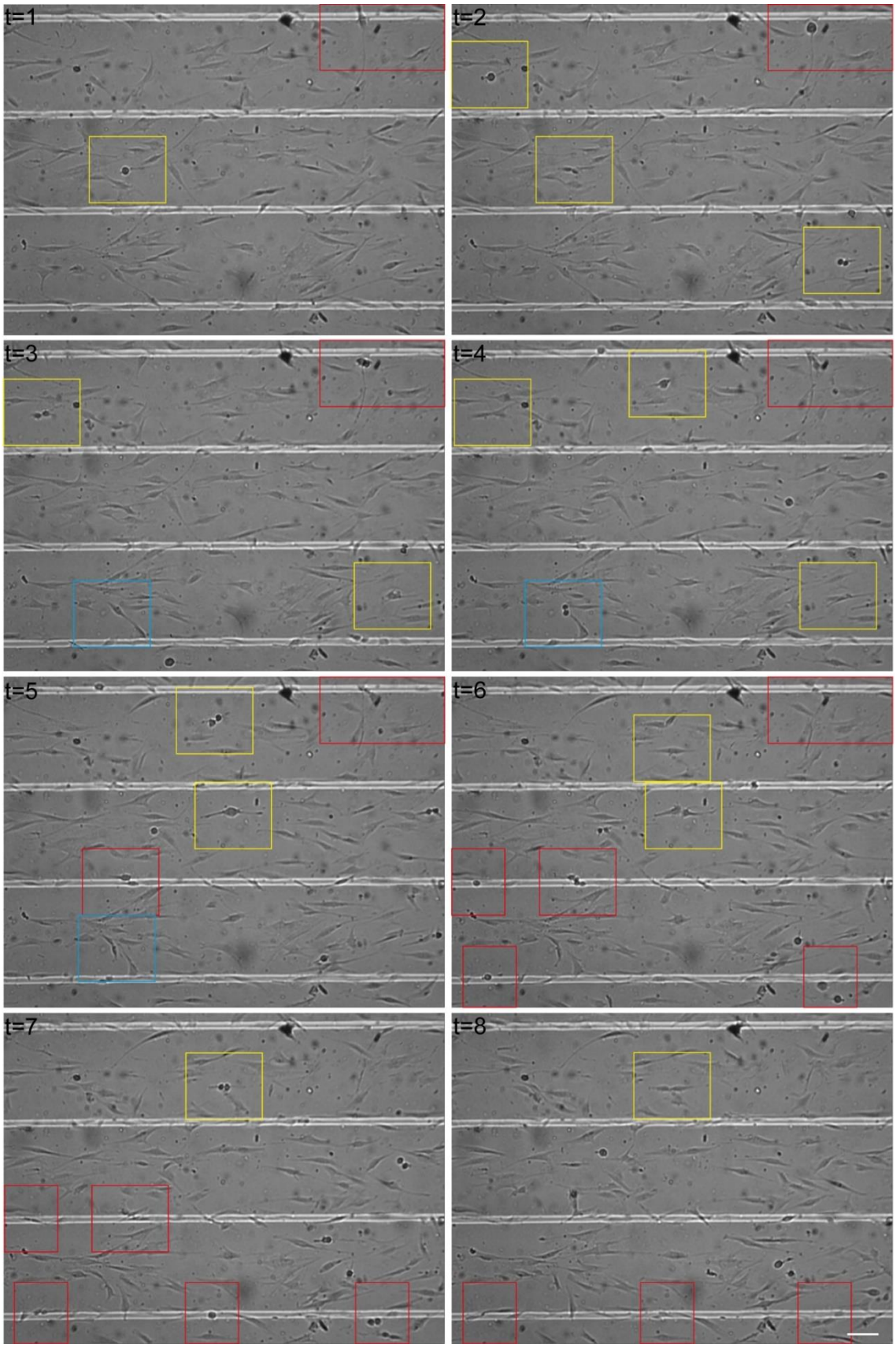

Figure 54 **Representative time-lapse sequence of hdF proliferation on fibronectin-coated cylindrical CurvChip substrate with R=312 µm**. Time-lapse recordings were performed using JuLi^{TM}Br Life Cell Analyzer without digital zoom and frame rate of one picture per 15 minutes, t displays

relative time point in the presented sequence. Red boxes mark mitosis in or near transition zones, while yellow boxes indicate mitosis taking place on convex curvatures. Blue box indicates that cell division also takes place perpendicular to cylinder axis. Scale bar 100 µm.

Summary and Conclusion of Findings Obtained from Studies Using Mesenchymal Cells on Uniaxial Curvatures

In summary, results show that cell behavior of mesenchymal cells on uniaxial curvature is independent from cell type or origin and donor (cf. Figure 22 to Figure 24). When given the possibility mesenchymal cells prefer to position in the quasi-concave areas between (narrow) cylindrical curvatures (cf. Figure 18), independent of cell density. For increasing cylinder distance (from approx. 25 µm to 400 µm), however, this preference is lost (cf. Figure 43), which is again found to be independent from overall cell density (cf. Figure 47). Moreover, for sparsely growing mesenchymal cells the topography height also seems to affect the preference of cell positioning on the curved regions (cf. Figure 48), while this is not the case for cells growing in overall denser cell layers (cf. Figure 52). On the contrary, structure height was shown not to affect mesenchymal cell orientation on cylindrical curvatures (cf. Figure 49).

On cylindrical curvatures ranging down to $\kappa=1/312\ \mu m^{-1}$, mesenchymal cells show a preferred axial orientation that was shown to increase with increasing substratum curvature (decreasing radius of curvature) (cf. Figure 19), as well as with increasing cell density (cf. Figure 17). The reason for the observed increased axial orientation of denser cell layers, however, remains elusive and was not within the scope of the present work. More tests, for instance, using whole cylinders to exclude a “boundary effect” (cf. Comparison of the Cell Behavior in Dense Layers Depending on the Space Between the Cylindrical Curvatures, p. 67 and Duclos et al. (*91*)) would be necessary.

For sparsely growing mesenchymal cells, it was found that they seem to orient along the cylinder axis to meet some kind of internal setpoint that can be described as a perceived curvature k of about $k=1/1671\ \mu m^{-1}$ to $k=1/2307\ \mu m^{-1}$ (cf. Figure 19, Figure 24, Table 9). Together with literature findings (*134*), the results indicate that the setpoint might be the limit of curvature perception, which moreover stresses the necessity of a highly sensitive detection mechanism. (*1*)

By pharmacologically manipulating the cytoskeleton of human dermal fibroblasts (hdF) it was found that both a reduced and increased cell contractility, by Blebbistatin or Rho Activator CN03 increases the cell density on curvatures compared to between curvatures, while microtubule depolymerization (which simultaneously activates Rho) caused by Nocodazole-treatment reduced cell density on curvatures compared to between curvatures. This finding indicates that an exclusive involvement of the stress fiber system in the curvature perception

mechanism, like it was proposed in literature (*166, 171*), is improbable (cf. Figure 26 and Table 10). (*1*)
Further investigation of cell orientation behavior of pharmacologically manipulated hdF showed that the curvature perception seems to be a highly robust mechanism, which seems to comprise the nucleus as a central mechanosensing unit while the cytoskeletal components, including actin filaments, microtubule and intermediate filaments, acting in a way to reduce unfavorable stress on the nucleus. (*1*)
The involvement of all cytoskeletal components in this mechanism might explain the here found robustness against pharmacological manipulation of single components (cf. Figure 27 and Figure 30). Which can further be explained by the interdependency of the cytoskeletal components, their mutual regulation (e.g. based on RhoA/ROCK pathway (*215*)) and the fact that some deficiencies can possibly be compensated for by the remaining components (*225*). (*1*)

In a second approach the effect of different protein substrate coatings on mesenchymal cell orientation on cylindrical substrates was observed, i.e. fibronectin, collagen I and laminin additional to the initially used FCS.
When varying the substrate coating a non-significant increase in cell density on curved areas (cf. Figure 34) and an enhanced cell and nucleus reorientation along the axis of the cylindrical microstructure could be observed (cf. Figure 35). This major trend can simply be explained by an increase in ECM ligand density compared to FCS. An increased ligand density is known to affect cellular mechanotransduction including the Rho/Rock pathway (*29, 92*), as well as MSC response to hill and valley topographies (*120*).
However, more diverse adaptions become visible when comparing the dose-response curves (radius of curvature-median orientation adaption curves; cf. Figure 40 and Figure 41) indicating that, albeit then general robustness of the cell response, cell orientation response differs between the varying proteins.

Since the presented results on nucleus density indicate a different proliferation based on the underlying topography and area of the topography (cf. Comparison with hdF Growing in More Dense Layers; p.152) and, moreover, a decrease in nucleus projected area (cf. Figure 31) that is suggested to be caused by nuclear remodeling and DNA condensation can be observed, proliferation of hdF on fibronectin-coated CurvChip cylindrical topographies and narrow area between the cylinders was investigated. Results show a non-significant increase in median proliferation rate of hdF on cylindrical substrates compared to flat PDMS for 24 hours as well as 70 hours after cell seeding (cf. Figure 53), independent from position on the substrate, with the only exception being cells growing between cylinders with R=59.3 µm.

The difference in proliferation for the areas between the cylindrical microstructures after 24 hours, moreover, suggest an influence of structure height

The exemplary time-lapse sequence of hdF on R=312 µm cylindrical substrates (Figure 54), confirms that mitosis does take place in both areas, on curved topographies as well as in quasi-concave areas between the cylinders and no preference is apparent. Additionally, it could be observed that, cell division can also take place perpendicularly to the cylinder axis, most of the cell divisions, however, seem to take place longitudinally to the cylinder axis (division axis perpendicular).

VI. Epithelial Cells on Spherical Curvatures

Mesenchymal and epithelial cells differ in many aspects, including their polarity and cell-cell contact (*31*). In vivo, many epithelial cells are growing in quasi-2-D environments, as there is only little to no space for extracellular matrix between the tightly coupled cells of an epithelial monolayer growing on the basal lamina. This tight coupling of neighboring cells involves different types of cell-cell contacts that do also couple the neighboring cells mechanically as well as chemically by allowing the exchange of stresses as well as small molecules (cf. Chapter I, Theoretical Background, Biochemical Factors and (*37, 38, 247*)). Therefore, their dynamics vary strongly compared to mesenchymal cells, as they often act as a collective body rather than densely growing single cells.

Many studies investigating the dynamics of epithelial cell layers use two-dimensional, spherical confinements, while most studies using 2.5-D curved environments deploy uniaxial curvatures like channels, or sinusoidal wavy patterns. (*144, 147, 204, 248, 249*)

In the present work, CurvChip substrates with spherical curvatures of varying radius of curvature, structure height and topography radius (cf. Table 3, p.41 and Figure 11, p. 51) were used to study the dynamic as well as general cell behavior on of epithelial cells on micro-structured curved surfaces. Healthy, renal epithelial cells form cockle spaniel (MDCK cell line) where used as it is a commonly used epithelial model cell line with apical-basal polarity and retained transport and barrier function. Moreover, the cell line has already been used in 2-D as well as 2.5-D and 3-D experiments (*192, 204, 250, 251*). While A431 cells, a human epidermoid carcinoma cell line, were chosen as diseased epithelial cell model line, based on the fact that it has been shown that their collective can be manipulated using EGF, based on their overexpression of EGF receptor (*193*).

Characterization of A431 and MDCK Cell Behavior on CurvChip Substrates with Micro-spherical Segments

Cancerous A431 Cells

Cultivating A431 cells on collagen I-coated PDMS surfaces with different micro-spherical segments shows that cells respond differently to the variation of surface microstructure parameters. Figure 55 shows A431 cells on a substrate with rather small and strongly curved (κ=1/62.7 μm^{-1}) micro-spherical topographies with a structure height of 19.8 µm. For about 95 % of microstructures, it can be observed that, albeit the cells formed a monolayer in the flat area of the substrate, the A431 cells seem to avoid growing onto the convex topography. The nucleus image (Figure 55, top left) indicates that nuclei in the transition zone are denser compared to the flat surrounding.

Additionally, it can be observed that the monolayer in the flat area is also relatively inhomogeneous with varying nucleus densities, as well as differences in f-actin staining, with brighter, more pronounced cortical actin for denser areas. Based on the raw data containing the z-stack sequence (cf. Chapter VIII Appendix, Part VI: Supplementary Materials, Figure 90, p. 232), one can, additionally, observe that cells in the dense areas with more pronounced cortical f-actin are higher in z-direction, compared to the other areas. However, this irregular growth height seems to be normal for A431 cells and not induced by the microstructure substrate, since these different areas could also be observed for A431 growing on flat PDMS (cf. Chapter VIII Appendix, Part VI: Supplementary Materials, Figure 91, p. 233).

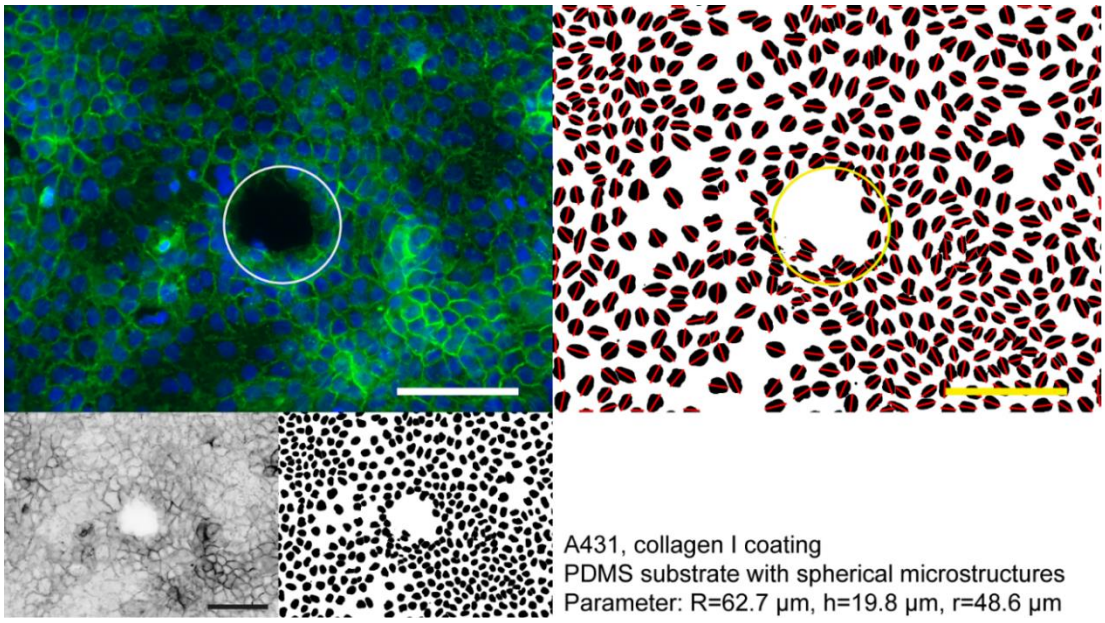

Figure 55 **Fluorescence and processed images of A431 cells on convex CurvChip substrate with R=62.7 µm partial micro-spherical topographies.** (***top left***) shows fluorescence image with nuclei displayed in blue and f-actin in green, circular structure indicates the basis of the topography with r=48.6 µm. (***bottom left and right***) show f-actin channel inverted, and the nucleus channel processed to a binary image, both for better visualization. (***top right***) visualizes the binary nucleus channel with major axis displayed in red and microstructure base, as well as scale bar in yellow. R indicates the radius of curvature; h indicates the structure height. Scale bar 100 µm.

Contrary to cell behavior observed on R=62.7 µm substrates, for A431 cells on micro-spherical topography substrates with larger radius of curvature R=134 µm and a lower height of 6.8 µm, visualized in Figure 56, it can be observed, that these cells grow over the microstructure without any gap formation in 100 % of the observed microstructures that were surrounded by a monolayer without defects. Additionally, the for R=62.7 µm substrates indicated increased cell density in the transition zone of flat PDMS to the convex micro-spherical topography, is not recognizable for the cells growing on R=134 µm microstructures.

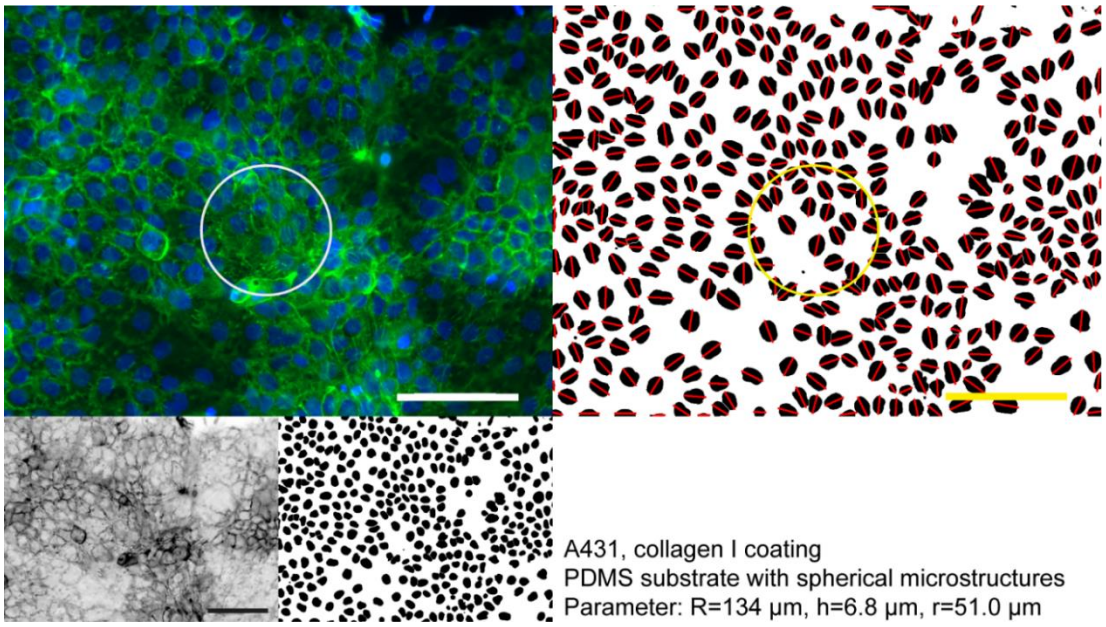

Figure 56 **Fluorescence and processed images of A431 cells on convex CurvChip substrate with R=134 µm partial micro-spherical topographies.** (***top left***) shows fluorescence image with nuclei displayed in blue and f-actin in green, circular structure indicates the basis of the topography with r=51 µm. (***bottom left and right***) show f-actin channel inverted, and the nucleus channel processed to a binary image, both for better visualization. (***top right***) visualizes the binary nucleus channel with major axis displayed in red and microstructure base, as well as scale bar in yellow. R indicates the radius of curvature; h indicates the structure height. Scale bar 100 µm.

Comparing the different substrate parameters (cf. Table 3, p. 41) shows that the topography basis radius r (cf. Figure 11, p. 51) is approximately the same, as well as resulting half arc length $a_{0.5}$, while structure height h, and resulting radius of curvature R vary strongly, with R=134 µm microstructures being less than half the height of R=62.7 µm substrate microstructures. This comparison suggests that one of these parameters (R or h) might be responsible for the difference in cell response.
As described previously, A431 cells seem to have a relatively irregular growth pattern with differences in layer height of about 6.5 µm, also visualized in Figure 91 (Chapter VIII Appendix, Part VI: Supplementary Materials, p. 233). Taking this observation into consideration, the relatively low structure height of 6.8 µm might be the relevant parameter for the observed difference in A431 cell layer gap occurrence.

This hypothesis is in accordance with the observations that can be made for A431 cells on R=193.2 µm substrates, visualized in Figure 57: the previously described gap in the cell layer, occurring on the curved area, is again prominently visible in about 77 % of the investigated microstructures.

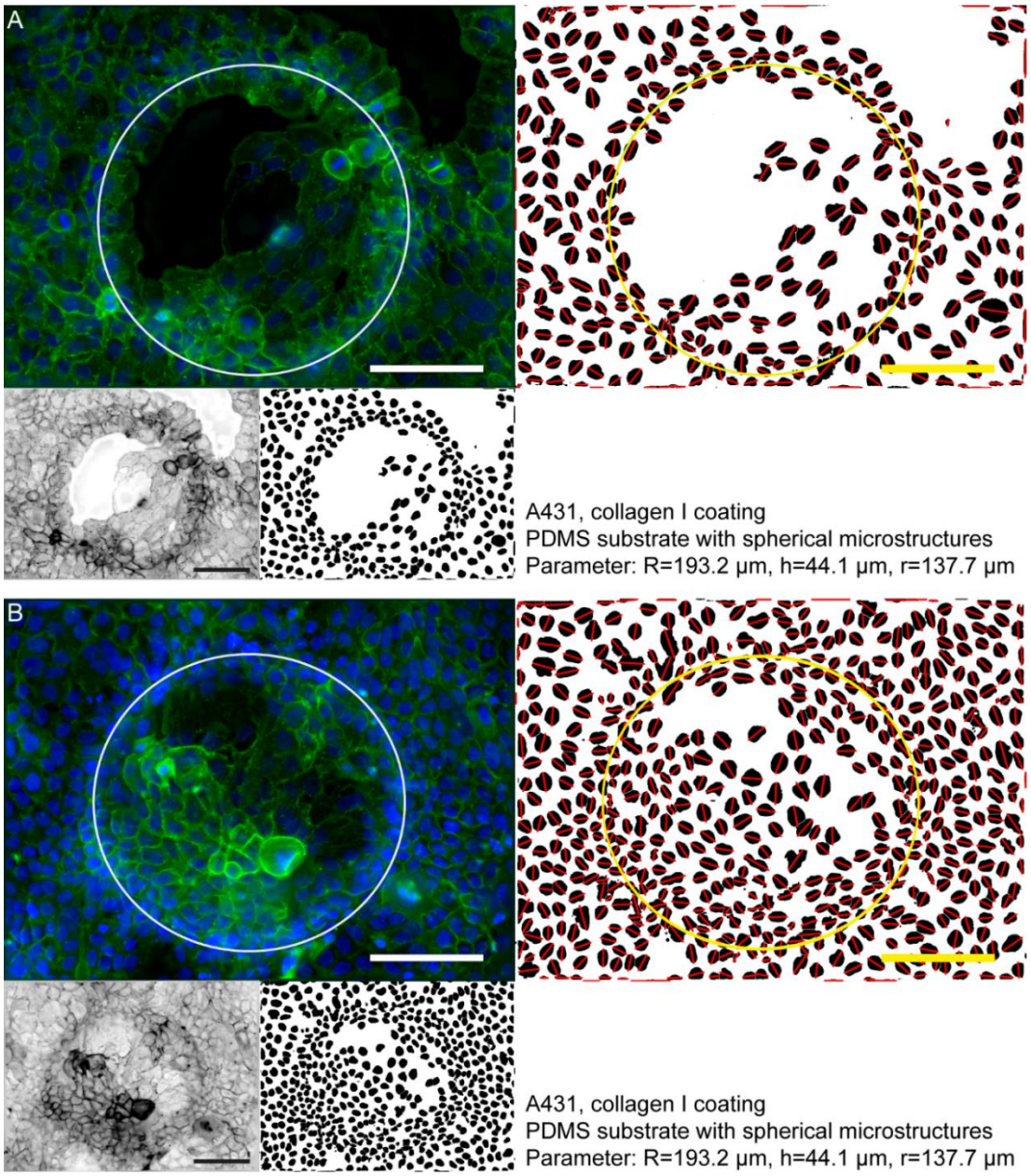

Figure 57 **Fluorescence and processed images of A431 cells on convex CurvChip substrate with R=193.2 µm partial micro-spherical topographies.** **A** and **B** show two conditions that can be observed, **A** where the top curved region is not overgrown and **B** where the whole micro-spherical convex topography is covered with cells. In both cases (***top left***) shows fluorescence image with nuclei displayed in blue and f-actin in green, circular structure indicates the basis of the topography with r=137.7 µm. (***bottom left and right***) show f-actin channel inverted, and the nucleus channel processed to a binary image, both for better visualization. (***top right***) visualizes the binary nucleus channel with major axis displayed in red and microstructure base, as well as scale bar in yellow. R indicates the radius of curvature; h indicates the structure height. Scale bar 100 µm.

However, the other micro-spherical segments that are overgrown by cells still appear to have a lower density on the curved regions compared to the flat surrounding substrate (cf. Figure 57 B).

The topographies of these substrates with R=193.2 µm are approximately 44.1 µm in height with a topography basis radius of about r=137.7 µm. Therefore, compared to substrates with R=134 µm micro-spherical segments, the microstructure curvature (1/R) is lower, but the microspheres are higher, further consolidating that for R=134 µm substrates, the relatively low structure height might be the reason for the complete coverage of the micro-spherical segments by A431 cells.

Additionally to the clearly visible gap and lower nucleus density in the overgrown curved region, an increased cell density in the transition zone of micro-spherical topographies with R=193.2 µm, that was previously described for R=62.7 µm substrates is also prominently visible on the nucleus images (both bottom and top right of Figure 57) as well as f-actin images (bottom left).

For A431 cells on surfaces with micro-spherical segments of further increased radius of curvature R=318.6 µm and increased height h=47.9 µm, the gap formation on the curved regions can still be observed, but the incidence is further decreased to about 61 % of the investigated microstructures. Figure 58 shows exemplary images of both cases.
Interestingly, in either situation an increased nucleus density in the transition zones can be identified in the nucleus images, however the difference in the actin staining is almost not visible, unlike for substrates with R=193.2 µm micro-spherical segments.

Together, the decreasing incidence of A431 cell monolayer gaps on curved regions (cf. Table 21, p. 199), despite the increasing microstructure height indicates that cells do not only respond to structure height, like indicated by cell behavior on substrates with R=62.7 µm and R=134 µm micro-spherical segments. It seems that other parameters like substrate curvature 1/R, microstructure base radius r or half arc length $a_{0.5}$, or a combination of the above also have an influence on the response of A431 cells.
The percentage of microstructures with cell-layer defects decreases for instance with decreasing curvature (increasing radius of curvature R), except for structures below h=19.8 µm, or increasing base structure radius r/half arc length, again with an exception for microstructures with low height. Moreover, it also decreases for increasing ratio of R to r (without an exception). (cf. Chapter VIII Appendix, Part V: Supplementary Materials, Table 26, p.231, for a comparison of topography metrics.) To further elucidate the interdependence of gap occurrence and surface parameter more experiments with different substrates would be necessary.
Furthermore, the qualitative observation indicates that there are varying cell/nucleus densities in the different areas of the substrate, to examine this observation more closely, the density was quantified.

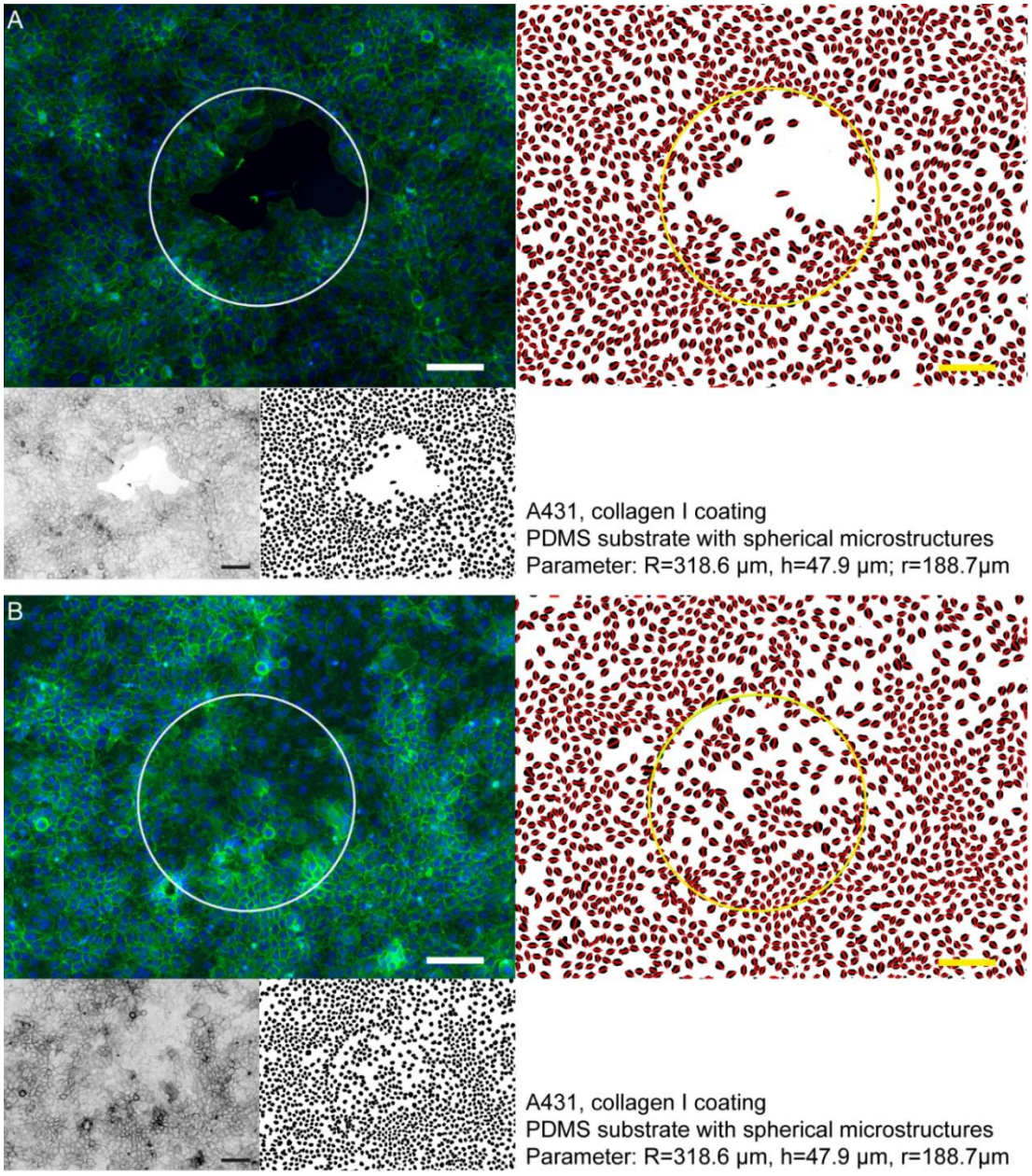

Figure 58 **Fluorescence and processed images of A431 cells on convex CurvChip substrate with R=318.6 µm partial micro-spherical topographies.** **A** and **B** show two conditions that can be observed, **A** where the top curved region is not overgrown and **B** where the whole micro-spherical convex topography is covered with cells. In both cases (***top left***) shows fluorescence image with nuclei displayed in blue and f-actin in green, circular structure indicates the basis of the topography with r=188.7 µm. (***bottom left and right***) show f-actin channel inverted, and the nucleus channel processed to a binary image, both for better visualization. (***top right***) visualizes the binary nucleus channel with major axis displayed in red and microstructure base, as well as scale bar in yellow. R indicates the radius of curvature; h indicates the structure height. Scale bar 100 µm.

Quantification of Cell Density in Different Areas of the Substrates

As visualized in Figure 11 (p. 51), the substrates were divided into three different areas, first, the inner curvature (I), defined by the projected area of the topography basis radius r subtracted by 10 %. The second area is the transition zone (II), comprising the area where the flat structure and the curved micro-spherical topography meet, therefore, it is composed of the curved region remaining after subtraction of the inner curved area, as well as a ring surrounding the microstructure with the radius of the topography basis r plus 20 µm. The remaining area of the image is classified as the third region (III), described as flat PDMS between the microstructures.

Sorted by ascending radius of curvature R (decreasing curvature 1/R), Figure 59 shows box plots of A431 cell density in the different areas of PDMS substrates with spherical convex curvatures and flat PDMS as a comparison.

When comparing the median density on the flat areas of the substrates (flat (III)) with each other and with flat PDMS, one can see that, albeit the difference is not statistically significant, the median density is decreased for substrates with spherical convex microstructures (2606 cells per mm²; 3083 cells per mm²; 2886 cells per mm²; 2413 cells per mm², sorted by increasing R) compared to all flat PDMS (3447 cells per mm²). Suggesting that the presence of microstructures also affects cell growth in non-structured areas of the substrates.

Overall, the median density in only two areas is larger compared to all flat PDMS, inner curvature (I) region of the R=134.0 µm substrate (3876 cells per mm²) and transition zone (II) of the R=193.2 µm substrate (4705 cells per mm²), while the median density of the transition zone (II) of R=134.0 µm (3416 cells per mm²) is about equal to flat PDMS. Furthermore, A431 on R=134 µm substrates show additional particularities, as already indicated by the fluorescence images in Figure 56 and the finding that no cell layer gap on the curvature could be observed on this substrate.

For the other three substrates, the highest median density could always be observed for the transition zone (II) and the lowest for the curved region (I), which could be expected based on the fluorescence images. Compared to this finding, for the substrate with R=134 µm micro-spherical segments, the highest median density was found for the curved region (I) and the lowest for the flat area. However, for the R=318.6 µm substrate the differences between the different areas are negligibly small. This difference could indicate that the curvature is too small to be recognized by the A431 layer.

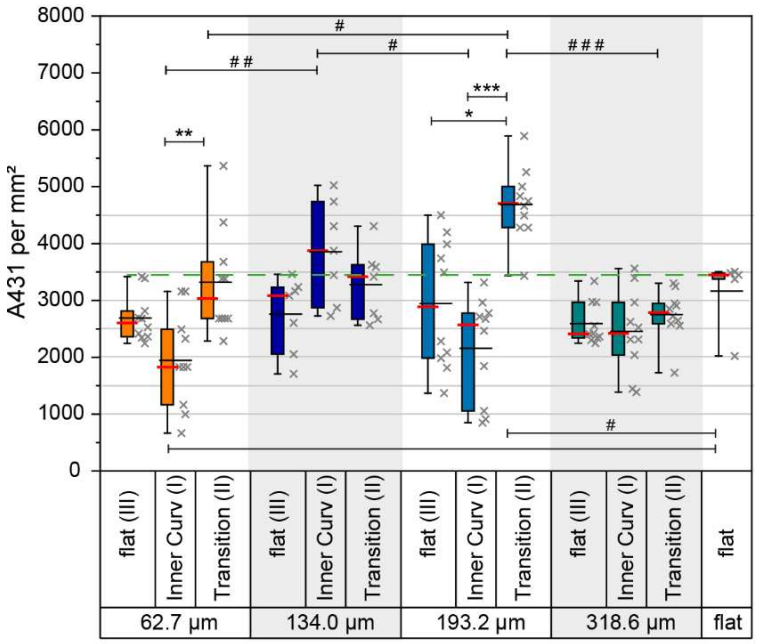

Figure 59 **Density of A431 cells in different regions of convex spherically curved CurvChip substrates sorted by ascending radius of curvature R as indicated**. Box plots (left) with data points (right), box indicates 25th and 75th percentile, whiskers 5th and 95th percentile. Black line shows the mean value, red line the median. The dashed green line indicates the median of A431 cells on flat PDMS (3447 cells per mm²) for comparison. Different regions are flat surrounding (flat (III)), the transition zone (transition (II)) consisting of part of the sphere and directly surrounding flat area, and the curved area (inner curv (I)), all as indicated in Figure 11, p. 51. Statistical significance (Kruskal-Wallis with Dunn's post-hoc) on same substrates is indicated by *, between the substrates by # (*p<0.05; *p<0.005; *p<0.005, or #; # #; # # # respectively).

Since the observations made using fluorescence images suggest the involvement of microstructure height in influencing cell behavior and ultimately leading to the variation between the median densities of the different substrates, the density data of transition zone and inner curvature was sorted by increasing microstructure height and displayed in Figure 60.

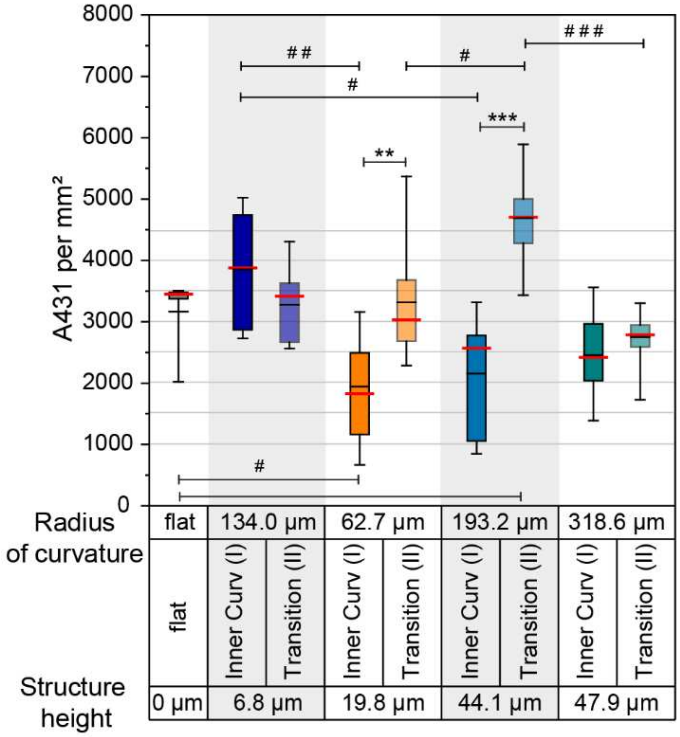

Figure 60 **Density of A431 cells in different regions of convex spherically curved CurvChip substrates sorted by ascending microstructure height.** Box plots, box indicates 25th and 75th percentile, whiskers 5th and 95th percentile. Black line shows the mean value, red line the median. Different regions are the transition zone (transition (II)) consisting of part of the sphere and directly surrounding flat area and indicated by transparent boxes, and the curved area (inner curv (I)), all indicated in Figure 11, p. 51. Statistical significance (Kruskal-Wallis with Dunn's post-hoc) on same substrates is indicated by *, between the substrates by # (*p<0.05; *p<0.005; *p<0.005, or #; # #; # # # respectively).

This sorting further stresses, that the particularities for the R= 134 µm substrate might be a result from very low structure height, of only approximately 6.8 µm. Which, like stated previously, could indicate, that the curved spherical topographies need to be of a certain height to be recognized by the A431 cells. Since the height variations of A431 monolayers on flat PDMS were found to range from 6.5 µm to 9.8 µm, it is most likely that the height would need to be larger than about 10 µm. For higher structures (h>19.8 µm) with low and intermediate radii of curvature (R=62.7 µm and R=193.2 µm, equal to high and intermediate curvature), the median density of A431 in the transition zone is significantly higher compared to the density on the micro-spherical topographies, and the difference even increases with increasing structure height (also with radius of curvature). This observed influence of structure height indicates either some kind of hindrance for the cells to grow onto the curvatures, causing cells to "pile-up", or a preference of quasi-concave area over convex curvature, comparable to what was previously described in the present work for mesenchymal cells on cylindrical

topographies (cf. Chapter V Mesenchymal Cells on Uniaxial, Cylindrical Curvatures) and by Pieuchot et al. (*120*) on hill and valley sinusoidal topographies.

Pieuchot et al. (*120*) also investigated epithelial cells and found that the preference of concave over convex is reduced with increasing density of cell clusters and lost in the colony center of growing epithelium compared to the colony edge. Which is an interesting finding since the presented density data includes, next to completely overgrown micro-spherical topographies, structures with growth defects. And these growth defects are the same as colony edges.

Taking a closer look on the density data displayed in Figure 59, also shows that for inner curvature the interquartile range (IQR) seems to be the widest compared to flat and transition zone. Additionally, especially for R=193.2 µm nicely visible, the data points seem to be distributed bimodally, further suggesting the existence of two different populations within the dataset, which are most likely “with” and “without” growth defect.

Interestingly, A431 growing on the structure with the lowest curvature (κ=1/318.6 μm^{-1}), which is simultaneously the structure with the highest micro-spherical topographies, still show comparably low differences (max. Δ median cell density of 374 cells per mm^2) between the different surface areas. This observation indicates that neither height nor curvature alone seem to be responsible for the density differences observed in the different areas and on the different substrates. To better visualize the effect of height and radius on density 3-D surface graphs were generated from the median density values, shown in the Appendix Figure 97 (Part VI: Supplementary Materials, p. 240).

Healthy MDCK Cells

As a comparison MDCK cells were used. They were cultivated on the same collagen I-coated CurvChip topographies with three-dimensional, micro-spherical segments that were used for A431 cells. Additional to the convex microstructures, for MDCK cells also concave PDMS imprints were used.

Convex Micro-spherical segments of the CurvChip

Figure 61 shows MDCK cells on substrates with R=62.7 µm convex microstructures. The cells fully cover the microstructures in 65% of the cases, and, neither the nucleus, nor the f-actin channel shows any particularity indicating cytoskeletal or orientational adaptions of the cells in presence of microstructures.

Yet, Figure 61 B shows the occurrence of a dome to the left of the microstructure, indicated by the red arrow. Domes are epithelial sheets covering a pressurized liquid filled cavity, MDCK cells are known to frequently form, especially on impermeable substrates like PDMS.

This phenomenon is based on the cells ability to actively transport fluids form their apical to basal site that is maintained in vitro, which then causes a pressure buildup between the impermeable substrate and cell layer (tight junctions) and subsequently delamination of the cell sheet and the formation of a fluid filled dome. (*252, 253*)

Based on the z-stack sequence shown in Figure 92 (Chapter VIII Appendix, Part VI: Supplementary Materials; p.234), the dome is about the same height as the micro-spherical topography, and unlike for the microstructure, cell sheet adaptions associated with the dome can be seen in both, the nucleus channel, showing an increased density on the base of the dome, as well as the f-actin channel, also showing indications for a more prominent staining. The latter needs to be interpreted with caution, since it could also be a result of the projection bias caused by depicting a 3-D structure in a 2-D image.

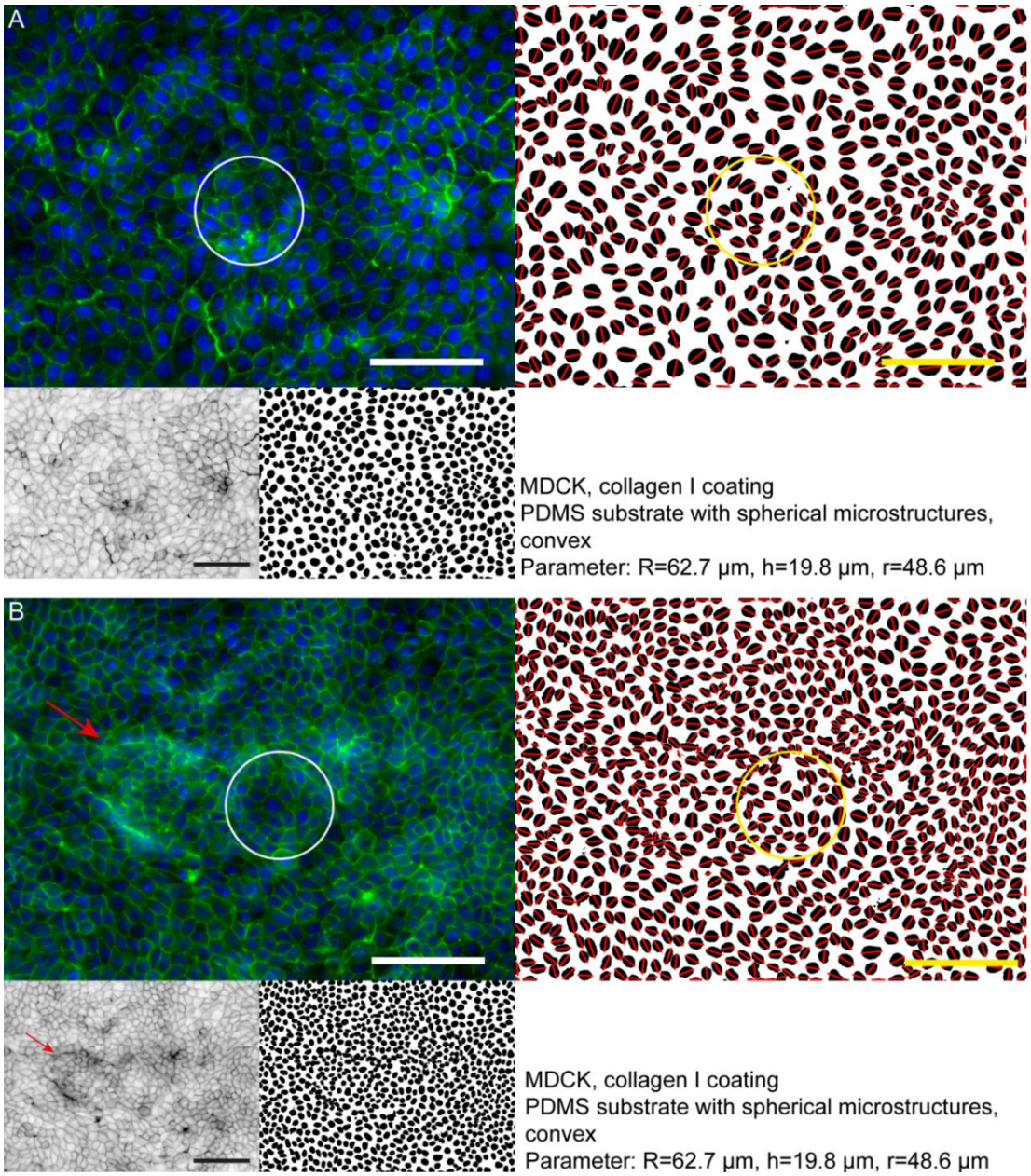

Figure 61 **Fluorescence and processed images of MDCK cells on convex CurvChip substrate with R=62.7 µm partial micro-spherical topographies**. ***A*** and ***B*** show two conditions that can be observed, ***A*** where the top curved region is overgrown and ***B*** the formation of dome-like structures indicated by the red arrow. In both cases (***top left***) shows fluorescence image with nuclei displayed in blue and f-actin in green, circular structure indicates the basis of the topography with r=48.6 µm. (***bottom left and right***) show f-actin channel inverted, and the nucleus channel processed to a binary image, both for better visualization. (***top right***) visualizes the binary nucleus channel with major axis displayed in red and microstructure base, as well as scale bar in yellow. R indicates the radius of curvature; h indicates the structure height. Scale bar 100 µm.

Like also described for A431 cells, the occurrence of cell layer defects of MDCK cells on microstructures with convex, R=134 µm (h=6.8 µm) micro-spherical segments is strongly

decreased to only 20% (0% for A431 cells) . The presence of the microstructure does not seem to affect nucleus density and f-actin, as visualized in the exemplary image in Figure 62.

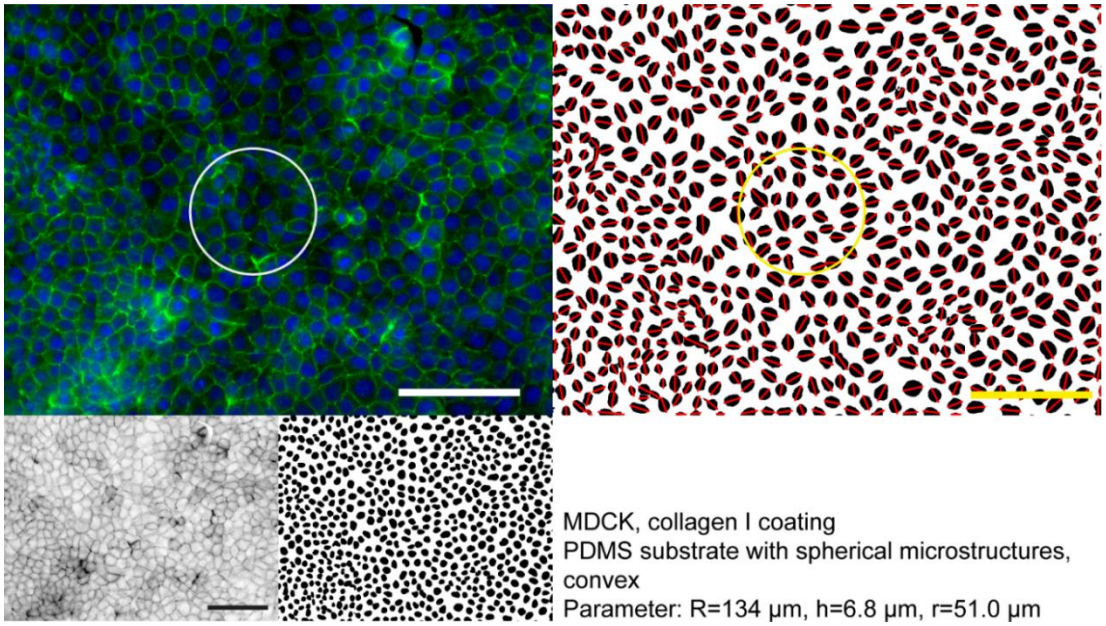

Figure 62 **Fluorescence and processed images of MDCK cells on convex CurvChip substrate with R=134 µm partial micro-spherical topographies**. (***top left***) shows fluorescence image with nuclei displayed in blue and f-actin in green, circular structure indicates the basis of the topography with r=51.0 µm. (***bottom left and right***) show f-actin channel inverted, and the nucleus channel processed to a binary image, both for better visualization. (***top right***) visualizes the binary nucleus channel with major axis displayed in red and microstructure base, as well as scale bar in yellow. R indicates the radius of curvature; h indicates the structure height. Scale bar 100 µm.

For substrates with R=193.2 µm and h=44.1 µm microstructures, the percentage of micro-spherical segments with cell layer defects increases to 39 %, compared to the substrates with shallow R=134 µm topographies (20 %), and decreases compared to substrates R=62.7 µm/h=19.8 µm microstructures (65 %).

The presence of the microstructure also seems to increase the density of the nuclei around the topography basis, especially for substrates with cell layer defects, like shown in Figure 63 B.

Particularly remarkable, is not only the more elongated cell shape of MDCK cells on the microstructure (Figure 63 A and B) and partly also in the close vicinity (Figure 63 A) but also the presence and clear perceptibility of central f-actin fibers, that cannot be observed for other substrates. For better visualization a part of the f-actin channel image of Figure 63 A was enlarged, as indicated by the red box, and additionally, a slice of the underlying z-stack was also extracted and is provided in Part VI: Supplementary Materials section of Chapter VIII Appendix (p. 235, Figure 93).

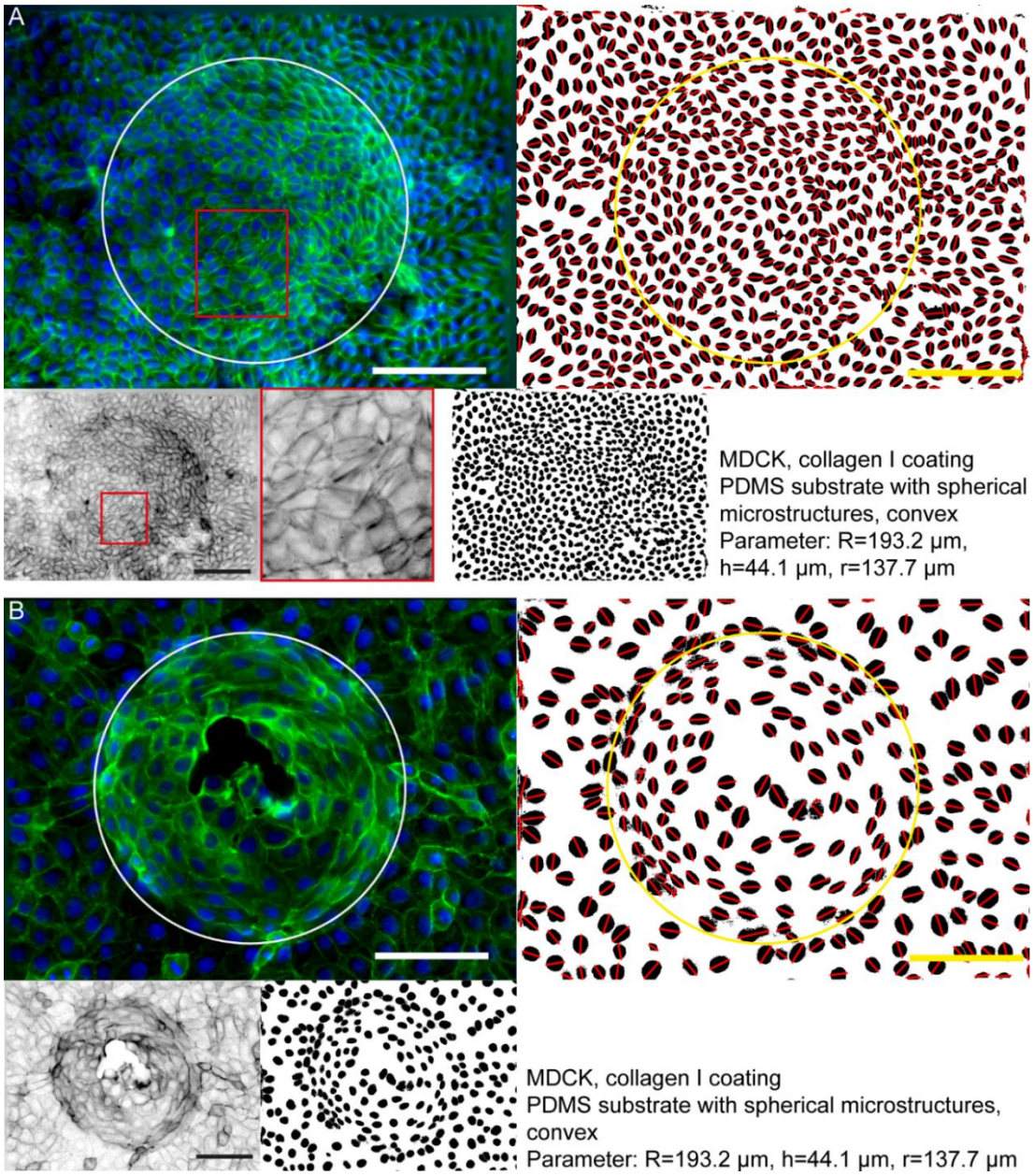

Figure 63 **Fluorescence and processed images of MDCK cells on convex CurvChip substrate with R=193.2 partial micro-spherical topographies.** ***A*** and ***B*** show two conditions that can be observed, ***A*** where the whole micro-spherical convex topography is covered with cells and ***B*** where the top curved region is not overgrown. In both cases (***top left***) shows fluorescence image with nuclei displayed in blue and f-actin in green, circular structure indicates the basis of the topography with r=137.7 µm. (***bottom left and right***) show f-actin channel inverted, and the nucleus channel processed to a binary image, both for better visualization. ***A*** also includes an enlarged section of the f-actin channel placed between the f-actin and nucleus image, framed red. (***top right***) visualizes the binary nucleus channel with major axis displayed in red and microstructure base, as well as scale bar in yellow. R indicates the radius of curvature; h indicates the structure height. Scale bar 100 µm.

Moreover, on Figure 63 B cells seem to form a swirling pattern on the convex structure with almost all nuclei being oriented with their long axis parallel to the base structure outline, while

a growth front to close the cell layer defect in the center of the micro-spherical segment seems to be missing.

For substrates with the highest (h=47.9 µm) micro-spherical segments and the highest radius of curvature of R=318.6 µm, these particularities cannot be observed that explicitly. However, less prominent central f-actin cables can also be observed Figure 64 A and B, like also indicated by the overall more greyish f-actin image.
The occurrence of layer defects, like exemplarily shown in Figure 64 B, on the microstructures is with about 52 % of the investigated structures, lower than for R=62.7 µm/h=19.8 µm (65 %) substrates but higher compared to substrates with R=134 µm/h=6.8 µm (20 %) and R=193.2 µm/h=44.1 µm (39 %) microstructures. In other words, a direct relationship between cell layer defects occurrence and the increasing radius of curvature or microstructure height could not be observed for MDCK cells.
Unlike for A431, also no direct correlation could be found for MDCK on increasing ratio of R to r, nor for R to h (an approximation of the curvature of the transition zone). Comparing the two substrates with the lowest percentage of cell layer gaps shows that the only similarity the two substrates have, is a comparable radius of curvature with only a difference of 58.8 µm. This observation could indicate that there might be an optimal curvature for the cells in this region or simply a threshold affecting cell cytoskeleton and behavior in a way of where convex substrate curvature is better tolerated.
The latter is also in accordance with the observed f-actin particularities on R=193.2 µm, where more prominent central f-actin fibers could be observed (cf. Figure 63 A, p. 176 and Figure 93, p. 235). To further investigate on what parameters these changes depend, more detailed studies would be needed.

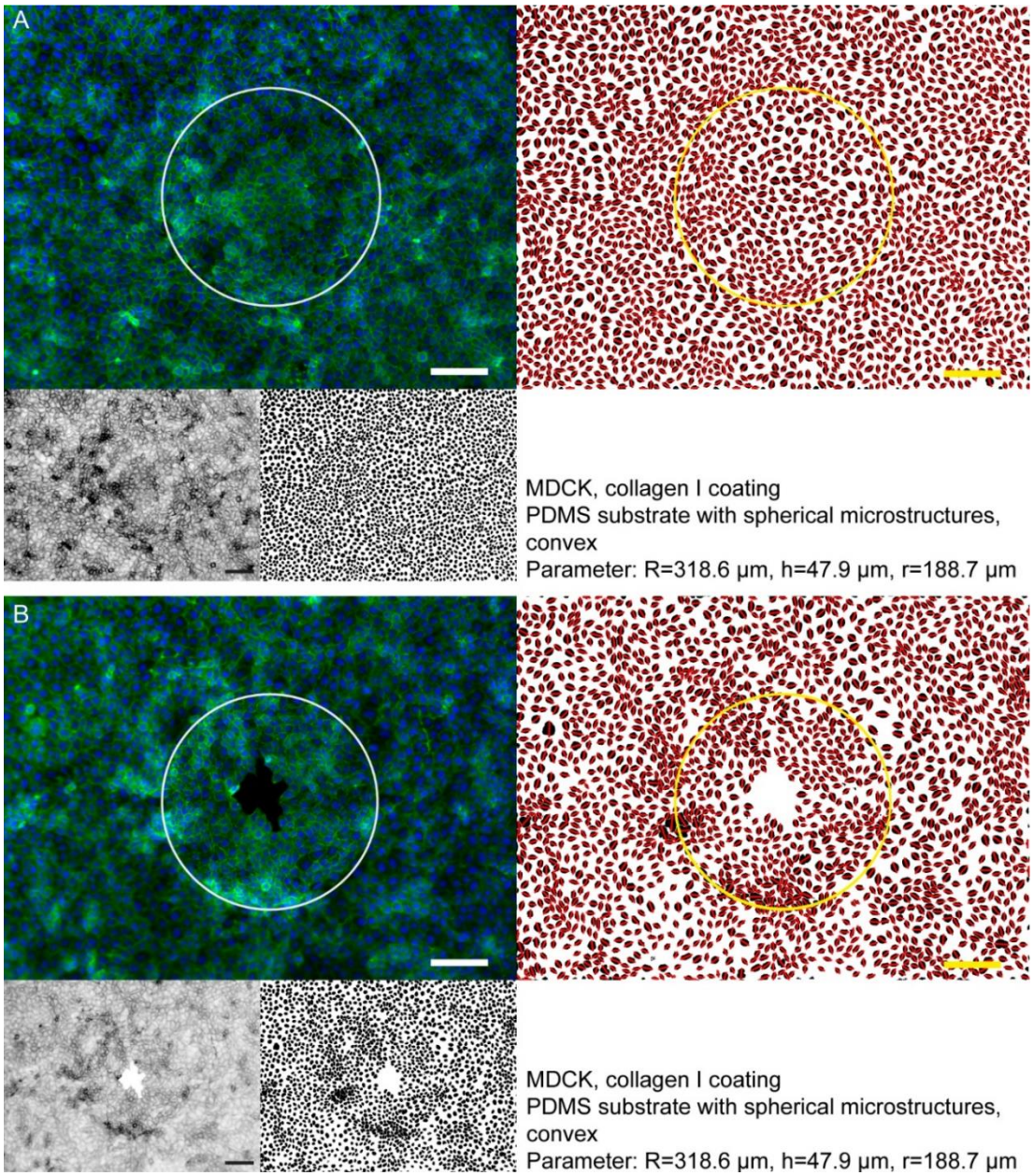

Figure 64 **Fluorescence and processed images of MDCK cells on convex CurvChip substrate with R=318.6 µm partial micro-spherical topographies.** ***A*** and ***B*** show two conditions that can be observed, ***A*** where the whole micro-spherical convex topography is covered with cells and ***B*** where the top curved region is not overgrown. In both cases (***top left***) shows fluorescence image with nuclei displayed in blue and f-actin in green, circular structure indicates the basis of the topography with r=188.7 µm. (***bottom left and right***) show f-actin channel inverted, and the nucleus channel processed to a binary image, both for better visualization. (***top right***) visualizes the binary nucleus channel with major axis displayed in red and microstructure base, as well as scale bar in yellow. R indicates the radius of curvature; h indicates the structure height. Scale bar 100 µm.

For a more profound identification of the influencing parameter on cells and a better comparability, also to A431 cells, the densities in the different areas of the varying substrates, was quantified as displayed in Figure 65.

Quantification of MDCK Cell Density in Different Areas of the Convex Substrates

Figure 65 shows the density of MDCK epithelial cells on different areas of PDMS substrates with varying convex partial-sphere topographies of increasing radius of curvature and all flat PDMS for comparison purposes.

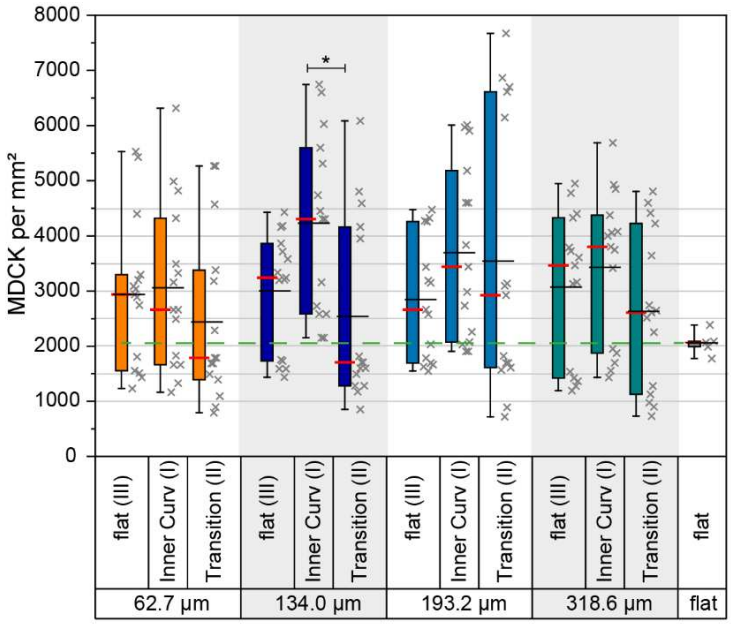

Figure 65 **Density of MDCK cells in different regions of convex spherically curved CurvChip substrates sorted by ascending radius of curvature R as indicated**. Box plots (***left***) with data points (***right***), box indicates 25th and 75th percentile, whiskers 5th and 95th percentile. Black line shows the mean value, red line the median. The dashed green line indicates the median of MDCK (2067 cells per mm²) on flat PDMS for comparison. Different regions are flat surrounding (flat (III)), the transition zone (transition (II)) consisting of part of the sphere and directly surrounding flat area, and the curved area (inner curv (I)), all as indicated in Figure 11, p. 51. Statistical significance (Kruskal-Wallis with Dunn's post-hoc) on same substrates is indicated by *, between the substrates by # (*p<0.05; *p<0.005; *p<0.005, or #; # #; # # # respectively).

Comparing the density on flat areas between the curvatures (III) of different substrates and flat PDMS shows, that the median density on substrates with micro-spherical, convex topographies (2938 cells per mm²; 3241 cells per mm²; 2663 cells per mm²; 3467 cells per mm²) is increased compared to all flat PDMS (2067 cells per mm²), but this difference is in all cases not statistically significant, which was expected based on the wide IQR for substrates with microstructures.

The overall highest median density can be observed for the inner curvature region (I) of the R=134 µm substrate with 4306 cells per mm², while the lowest median density is found in the transition zone (II) of R=134 µm substrates (1708 cells per mm²), directly followed by R=62.7 µm substrates (1789 cells per mm²).

Generally, except for substrates with R=62.7 µm (h=19.8 µm) micro-spherical topographies, the highest median density on a substrate can be observed for the inner curved region, while for R=62.7 µm the median density on the flat areas between the curvatures (III) is highest (2938 cells per mm²), followed by the median density in the curved region (2659 cells per mm²).

The lowest median density of a substrate is generally observed for the transition zones (II) of the different substrates. However, the only statistically significant difference could be found for the median density of the inner curvature and the transition zone of R=134 µm substrates.

Altogether, these findings are in accordance with the observations based on the exemplary fluorescence images of MDCK cells in Figure 61 to Figure 64, where, unlike for A431 cells:In most cases (except for R=193.2 µm) no increased density in the transition zone was observed. And in accordance with this observation, R=193.2 µm is the only substrate where the median cell density in the transition zone (II) is higher than the median density on flat (not significant $p>0.05$).

To further characterize the substrate parameter influencing the variation in cell density, the density data of inner curvature region (I) and transition zone (II) were sorted by microsphere increasing height, like previously done for A431 cell density data (cf. Figure 60).
Interestingly, for MDCK cells, the microstructure with the lowest structure height (R=134 µm h=6.8 µm) evoked the only significant difference between the two substrate regions ((I) and (II)). Additionally, also the substrate with the lowest curvature ($\kappa=1/318.6\ \mu m^{-1}$) shows a clear difference in median density for the curved region and transition zone, unlike for A431 cells.

These observations might indicate, that MDCK cells, compared to A431 cells, could be more sensitive concerning microstructure height and curvature, since MDCK cells seem to respond even to weak curvature. Interestingly, for higher structures (R=62.7 µm; R=193.2 µm and R=318 µm with h=19.8 µm, 44.1 µm and 47.9 µm, respectively) the median density on the curved region (I) seems to be increasing constantly with height. While for transition zone (II) median density seems to peak on R=193.2 µm with 44.1 µm height, although the difference in structure height between R=193.2 µm and R=318.6 µm substrates is negligibly small (3.8 µm), indicating that the radius of curvature might be the major influencing factor of the observable difference.

These finding stresses that, like previously described for A431 cells, here also neither structure height, nor microsphere curvature alone seem to be the responsible factors for the observable differences in median density. Again, as done for A431 cells, to better visualize the effect of height and radius on density 3-D surface graphs were generated from the median density values, shown in Figure 98 (Chapter VIII Appendix, Part VI: Supplementary Materials, p. 241).

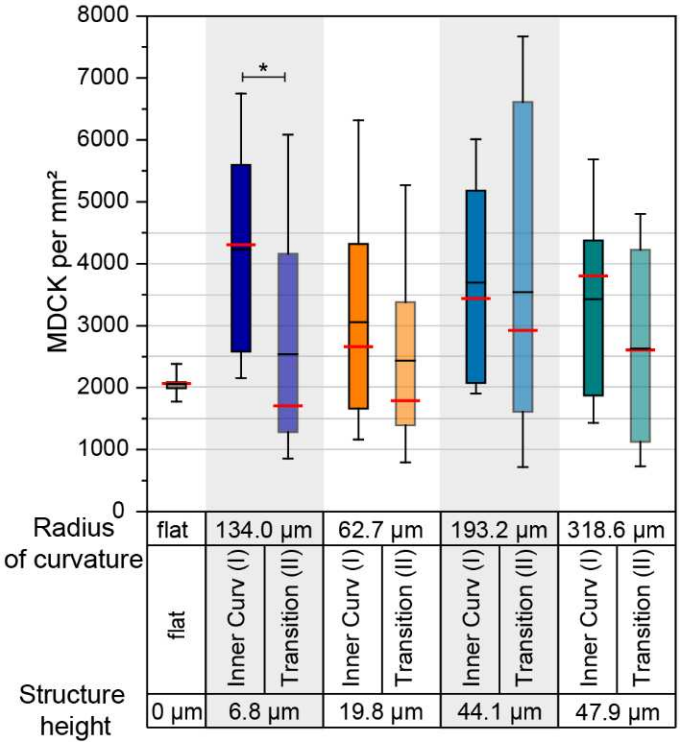

Figure 66 **Density of MDCK cells in different regions of convex spherically curved CurvChip substrates sorted by ascending microstructure height**. Box plots, box indicates 25th and 75th percentile, whiskers 5th and 95th percentile. Black line shows the mean value, red line the median. Different regions are the transition zone (transition (II)) consisting of part of the sphere and directly surrounding flat area and indicated by transparent boxes, and the curved area (inner curv (I)), all indicated in Figure 11, p. 51. Statistical significance (Kruskal-Wallis with Dunn's post-hoc) on same substrates is indicated by *, between the substrates by # (*p<0.05; *p<0.005; *p<0.005, or #; # #; # # # respectively).

Concave Micro-spherical segments of the CurvChip

Figure 67 to Figure 70 show MDCK on PDMS substrates with concave micro-spherical segment indentations of varying radius of curvature R, depth h and base circle radius r, as indicated. On all substrates the MDCK cells were able to fully cover the negative curvature without (large) gaps in the cell monolayer.

For substrates with R=62.7 µm (Figure 67) the cells seem to show an increased density in the concave area and occasionally cells seem to detach from the convex surface, like it can be seen in Figure 67 B, and more closely in the z-stack sequence and xz-/yz-projections in Figure 94 in Chapter VIII Appendix, Part VI: Supplementary Materials (p. 236).

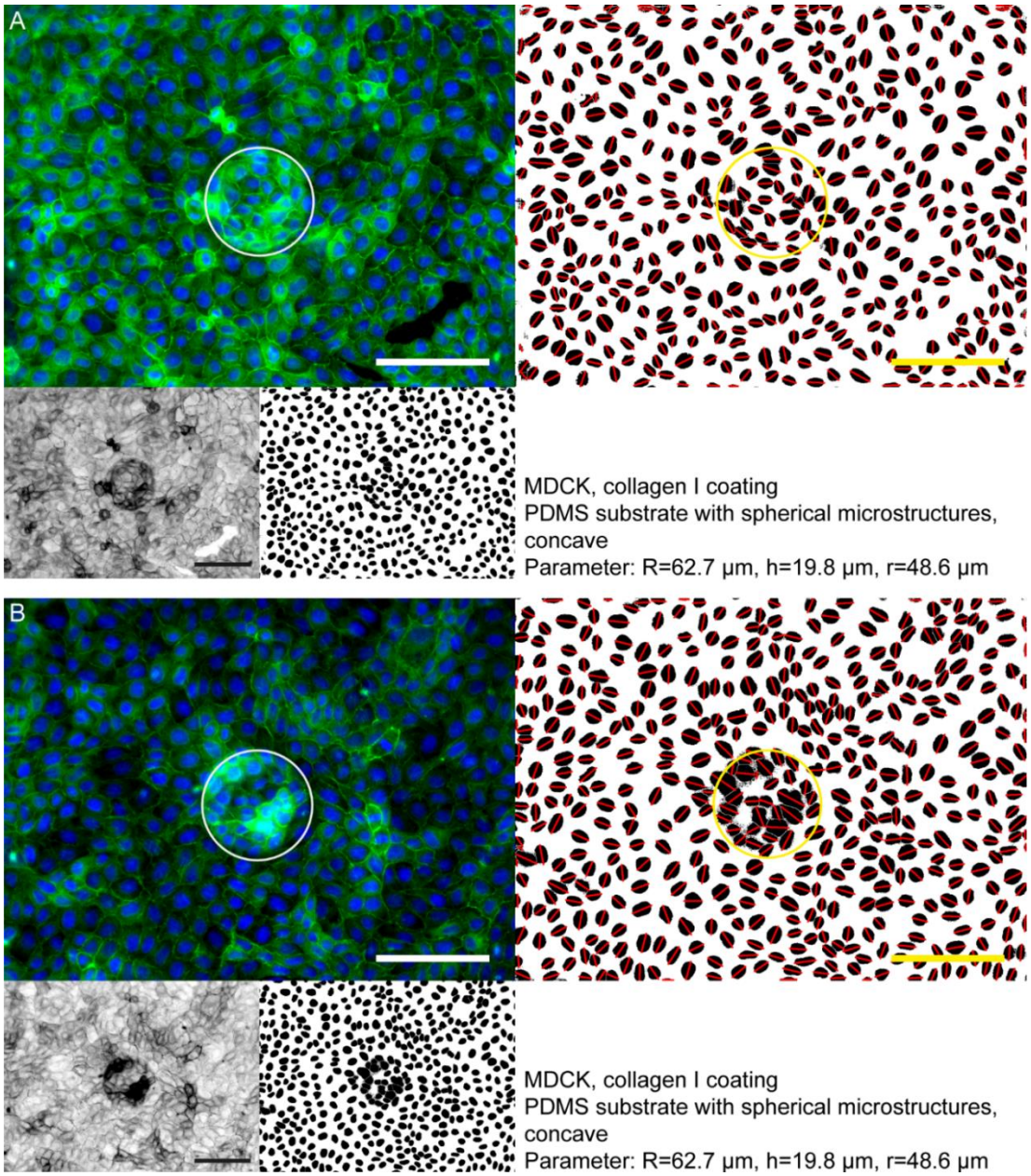

Figure 67 **Fluorescence and processed images of MDCK cells on concave CurvChip substrate with R=62.7 µm partial micro-spherical topographies.** ***A*** and ***B*** show two conditions that can be observed, ***A*** where the cells are attached to the surface of the concave cavity ***B*** where some cells detached from the concave surface. In both cases (***top left***) shows fluorescence image with nuclei displayed in blue and f-actin in green, circular structure indicates the basis of the topography with r=48.6 µm. (***bottom left and right***) show f-actin channel inverted, and the nucleus channel processed to a binary image, both for better visualization. (***top right***) visualizes the binary nucleus channel with major axis displayed in red and microstructure base, as well as scale bar in yellow. R indicates the radius of curvature; h indicates the structure height/depth. Scale bar 100 µm.

However, a clear interdependence between the concave surface and the delamination of the cell layer could not be observed and is considered to be part of the, for MDCK cells, normal dome formation.

In indentations without cell layer lamination cells occasionally arrange in swirling patterns with the major axis of the nuclei mostly oriented parallel to the topography basisoutline, like shown in Figure 67 A. This behavior, however, could not be observed for all investigated indentations of the same substrate. It can be assumed that this swirling pattern is also accompanied by the presence of prominent central actin fibers, like also observed for comparable patterns on convex substrates (cf. Figure 63). Yet, due to the relatively steep structure and using conventional, non-confocal fluorescence microscopy the fibers are not visualizable. Furthermore, the apparent increased f-actin staining in the concave indentation might also be partly caused by the lense-effect of the microstructure. Based on these circumstances, interpretation is not easy.

MDCK cells on substrates with shallow, R=134 µm micro-spherical indentations (Figure 68) also seem to show an increased nucleus density in the concave area of the substrate, like previously described for R=62.7 µm substrates. Unlike in R=62.7 µm indentations, a favored nucleus orientation in the indentation or close to the edge of the microstructure could not be observed.

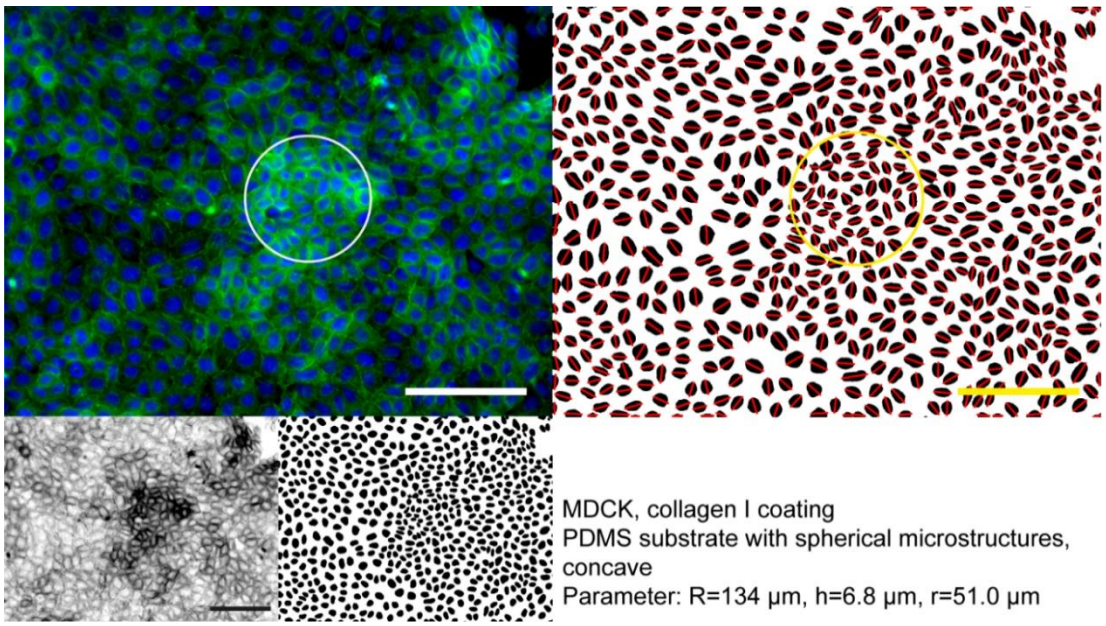

Figure 68 **Fluorescence and processed images of MDCK cells on concave CurvChip substrate with R=134 µm partial micro-spherical topographies**. (***top left***) shows fluorescence image with nuclei displayed in blue and f-actin in green, circular structure indicates the basis of the topography with r=51.0 µm. (***bottom left and right***) show f-actin channel inverted, and the nucleus channel processed to a binary image, both for better visualization. (***top right***) visualizes the binary nucleus channel with

major axis displayed in red and microstructure base, as well as scale bar in yellow. R indicates the radius of curvature; h indicates the structure height/depth. Scale bar 100 µm.

For MDCK cells on R=193.2 µm, on the contrary, a possible change in nucleus density in the different substrate areas cannot be observed qualitatively, but nuclei in the micro-spherical dents, seem to prefer an orientation where their nucleus major axis is parallel to the closest edge of the micro-spherical base circle.
Moreover, nuclei seem to be excluded from the quasi-convex edge resulting in an almost blank "belt" on the nuclei images (cf. Figure 69). Furthermore, noteworthy is that the rim of the microstructure is also visible in the actin image, where the fluorescence of the f-actin is decreased compared to the flat and concave area suggesting the absence or exclusion of f-actin from this area.

Closer examination of this quasi-convex rim (cf. Figure 96, in Chapter VIII Appendix, Part VI: Supplementary Materials, p. 238) shows that f-actin can and does traverse this area in some cases, however in most cases it still seems like f-actin is excluded from this area. Although, an imaging artefact cannot be ruled out completely, it seems to be unlikely to be responsible for the whole phenomenon, since some actin filaments can be observed crossing the rim. Moreover, the observation that most cells additionally avoid placing their nuclei in this region consolidates the theory that the rim of the substrate with R=193. µm indentations affects MDCK intracellular organization.

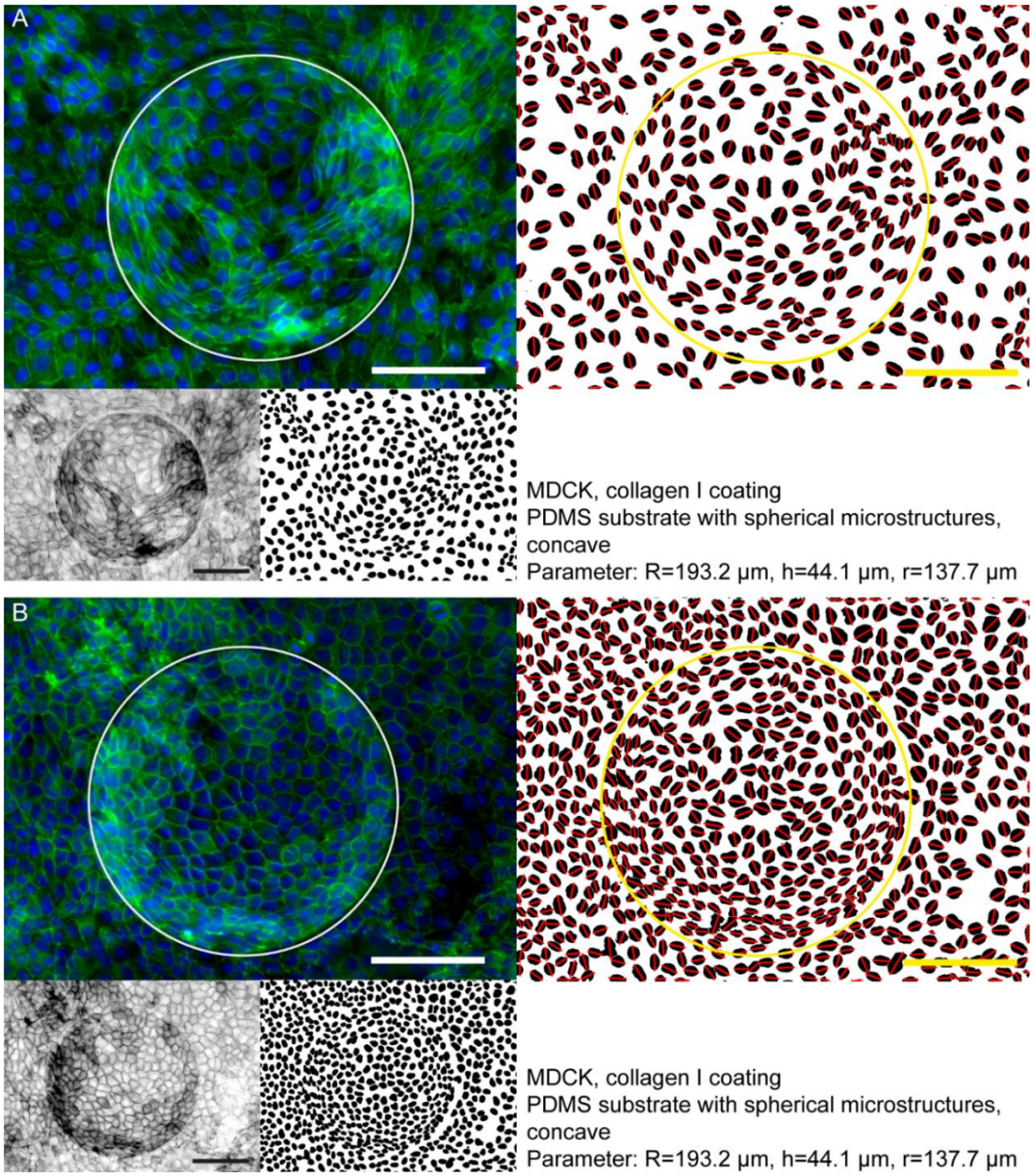

Figure 69 **Fluorescence and processed images of MDCK cells on concave CurvChip substrate with R=62.7 µm partial micro-spherical topographies.** ***A*** and ***B*** show two conditions that can be observed, ***A*** where the cells seem elongated and show strong central actin fibers B where cells in the concave cavity show normal, not elongated polygonal morphology. (***top left***) shows fluorescence image with nuclei displayed in blue and f-actin in green, circular structure indicates the basis of the topography with r=137.7 µm. (***bottom left and right***) show f-actin channel inverted, and the nucleus channel processed to a binary image, both for better visualization. (***top right***) visualizes the binary nucleus channel with major axis displayed in red and microstructure base, as well as scale bar in yellow. R indicates the radius of curvature; h indicates the structure height/depth. Scale bar 100 µm.

This artefact is also visible for MDCK cells on substrates with R=318.6 µm, while nuclei on the contrary do not seem to be excluded from the rim, like observed for R=193.2 µm substrates shown in Figure 70.

Additionally, the nucleus orientation response, with major axis alignment to the closest basic outline, seems to be less prominent but is still observable for most cells up to 3 or 4 cell width away from the outline (approximately r-20%). Furthermore, MDCK cells in the whole imaging area show pronounced stress fibers occurring simultaneously with a more elongated morphology.

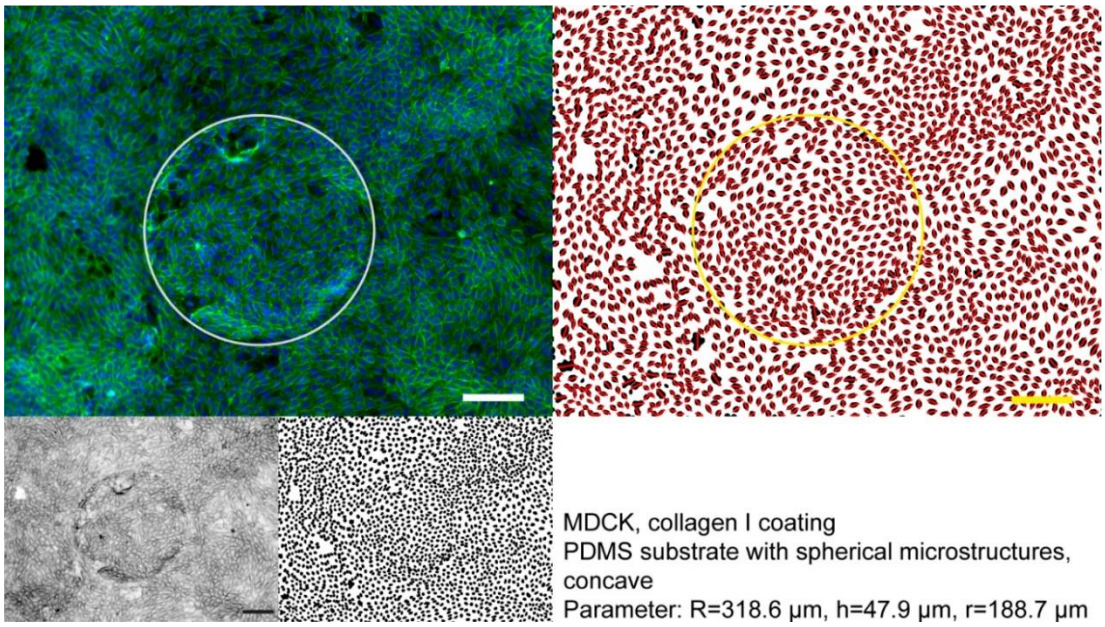

Figure 70 **Fluorescence and processed images of MDCK cells on concave CurvChip substrate with R=134 µm partial micro-spherical topographies**. (***top left***) shows fluorescence image with nuclei displayed in blue and f-actin in green, circular structure indicates the basis of the topography with r=188.7 µm. (***bottom left and right***) show f-actin channel inverted, and the nucleus channel processed to a binary image, both for better visualization. (***top right***) visualizes the binary nucleus channel with major axis displayed in red and microstructure base, as well as scale bar in yellow. R indicates the radius of curvature; h indicates the structure height/depth. Scale bar 100 µm.

All in all, unlike described by Broaders et al. (*204*) for MDCK cells (and other epithelial cells) on cylindrically concave curved PDMS substrates, MDCK cells grow on the concave spherical substrate shape, without lifting up and spanning over the indentation or complete clearance of the curved area. Dome formations are not considered. The MDCK cell growth is visualized in. Figure 94, for areas without dome formation and Figure 95 for larger radii of curvature (Chapter VIII Appendix, Part VI: Supplementary Materials, p. 236 and p. 237 , respectively).
Admittedly, Broaders et al. (*204*), do not specify the radius of curvature of the cylindrical channels nor the channel depth, or if the phenomenon exists independently of the radius of curvature, structure depth, or other parameters of the substrate, except for the spacing between the channels. Interestingly, when taking a closer look on the fluorescence images

presented by Broaders et al. (*204*) one can also observe the decreased fluorescence intensity at the quasi-convex rim of the indentations, although they are not addressed in the publication.

Rougerie et al. (*147*), on the contrary, even measure f-actin density on different cell-scale, ridge and groove geometries “with a progressive smoothing of the junction between the ridge and the adjacent groove”. Which means that the transition rim is ranging from a sharp edge between the flat surface and curved groove (almost angular, highest convex curvature), which comparable to what is also found in the present work, to a sinusoidal wavy pattern (lowest convex curvature).
They found that f-actin distribution is affected differently based on the different convex transition rims, with the most prominent effect observable on most curved topographies, where the f-actin density is low on flat area between the grooves with a further drop at the transition junction (esp. for high curvature) and an f-actin accumulation in the vicinity of the rim of the concave groove. With decreasing convexity of the transition rim the drop diminishes as well as the accumulation in its vicinity, finally yielding a relatively smooth distribution but still with a lower f-actin intensity in the convex compared to the concave areas of the sinusoidal topography. According to these results, the f-actin decrease should be observable in substrates R=62.7 µm concave indentations of the present work, which is the substrate with the highest rim curvature.

For a better investigation and comparison of the effect of the change in rim curvature in the present work, Figure 71 shows inverted f-actin images of MDCK cells on concave substrates sorted by decreasing rim curvature (decreasing R to h ratio).

Interestingly, for substrates with R=62.7 µm indentations, presenting the highest rim curvature (R/h=3.2) the effect is much less prominent compared to R=193.2 µm substrates, which have a lower rim curvature (R/h=4.4) but seems to have the most prominent effect on f-actin distribution. For substrates with R=318.6 µm, presenting lower rim curvature (R/h=6.7 µm), it seems the effect is decreased compared to R=193.2 µm, while for the shallowest topographies (R=134 µm, R/h=19.8 µm) the f-actin drop is not discernible at all.
The observation that the highest effect is visible for substrates with R=193.2 µm (R/h=4.4) is also in line with the exclusion of nuclei from the rim area, with is only observable for this substrate. This finding could be an indication that other parameters, like base structure radius r or structure depth in relation to cell layer

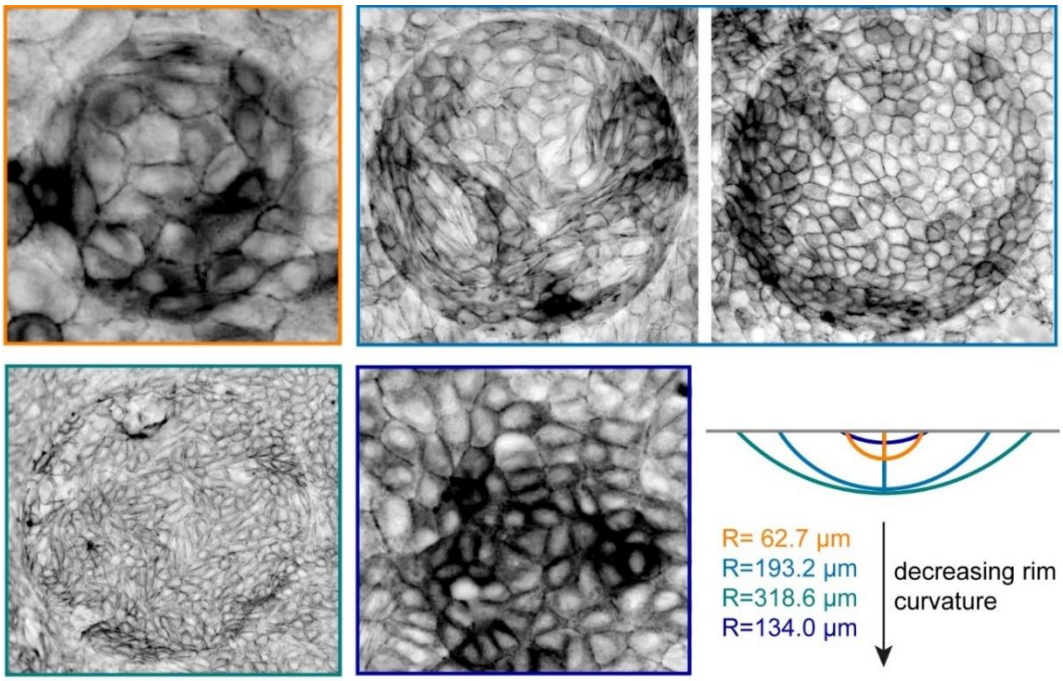

Figure 71 **Inverted fluorescence images of f-actin stained in MDCK cells on substrates with concave spherical indentations of varying radius of curvature R and structure height/depth h, resulting in different rim curvatures.** The rim curvatures are representable by the radius of curvature R to structure height h (R/h) ratio. The color of the fluorescence image frame indicates the topography type. The schematic drawing (in scale) reflects and illustrates the resulting rim curvature from radius of curvature R and indention height h. R/h ratio: R=62.7 µm: 3.2; R= 193.2 µm: 4.4; R=318.6 µm: 6.7; R=134 µm: 19.7.

height might also have an effect on the f-actin distribution across the quasi-convex rim.

Rougerie et al. (*147*), furthermore, argue that the only model representing their explanation is the model of Biton and Safran (*171*), suggesting the orientation of stress fibers to be a result form balancing bending energy cost and cell contractility, (cf. Chapter II, Objectives, Cell Studies Curvature). Rougerie et al. (*147*) suggest that for high convex curvature substrates (radii < 10 µm) the energetic cost of actin bending becomes too high causing the cell reorientation along the groove axis. However, they could not rule out a possible effect by the concave curvature itself. This finding could also explain the nucleus reorientation of MDCK in the here presented concave spherical segments, predominantly observed close to the rim.

Quantification of MDCK Cell Density in Different Areas of the Concave Substrates

To further analyze the potential differences in cell density, that were previously indicated, MDCK cell density was quantified on different areas of substrates with concave micro-spherical indentions. Figure 72 displays the density of MDCK epithelial cells on these different areas of

PDMS topographies of increasing radius of curvature and all flat PDMS for comparison purposes.

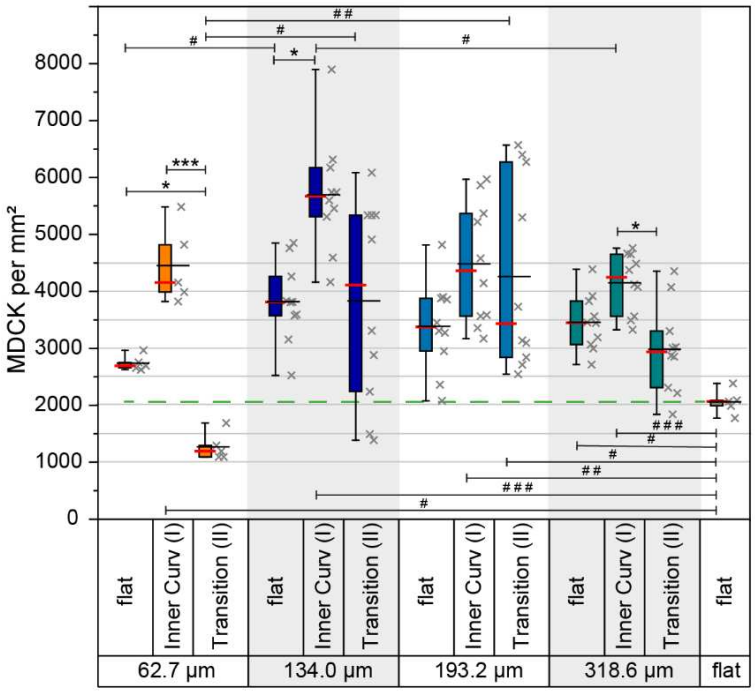

Figure 72 **Density of MDCK cells in different regions of concave spherically curved CurvChip substrates sorted by ascending radius of curvature R as indicated.** Box plots (***left***) with data points (***right***), box indicates 25th and 75th percentile, whiskers 5th and 95th percentile. Black line shows the mean value, red line the median. The dashed green line indicates the median of MDCK (2067 cells per mm²) on flat PDMS for comparison. Different regions are flat surrounding (flat), the transition zone (transition (II)) consisting of part of the sphere and directly surrounding flat area, and the curved area (inner curv (I)), all as indicated in Figure 11, p. 51. Statistical significance (Kruskal-Wallis with Dunn's post-hoc) on same substrates is indicated by *, between the substrates by # (*p<0.05; *p<0.005; *p<0.005, or #; # #; # # # respectively).

Generally, all median densities of all substrates are larger compared to the density on all flat PDMS substrates, except for the density in the transition zone of R=62.7 µm substrates where the median density is smaller (1193 cells per mm²; not statistically significant) compared to the density on flat PDMS (2067 cells per mm²). The median density of the R=62.7 µm transition zone is simultaneously the overall lowest median density value (significant decreased compared to R=134 µm and 193.2 µm), while the highest median density (5670 cells per mm²) was found on the inner curved region of the R=134.0 µm substrate, which equals about 2.7 times the median density on flat PDMS.

On all substrates, the highest median density, relative to the other areas of the same substrate, can be found in the micro-spherical in indentations, while the lowest density can be found for

the transition zones between flat and curved area, except for R=134 µm. Here flat PDMS (3811 cells per mm²) is slightly less densely overgrown compared to the transition zone (4110 cells per mm²).

Overall, this finding corresponds to what Baptista et al. (*149*) describe for different epithelial cells on membranes with concave, spherical structures and what was suggested by in the exemplary images given in Figure 67 to Figure 70. However interesting is, that only for the substrates with the two extreme curvatures, R=62.7 µm (strongest curvature) and R=318.6 µm (weakest curvature), the differences between the inner curvature region and the transition zone is statistically significant. This significance, and the observation that the lowest density can be found in the transition-zone of R=62.7 µm is somehow surprising, since the nuclei images of MDCK cells on substrates R=193.2 µm indentations suggest that the lowest density would be found in the transition zone of these concave microstructures.
However, the transition zone extends the area of the rim ranging from r-10 % to r+20 µm, as visualized in Figure 11 (p. 51). Keeping this definition of the transition zone in mind and taking another look at Figure 69 B, it shows that, in some cases, cells seem to accumulate close to the rim, which is included in the transition zone and thus increases the density and, therefore, possibly causing this discrepancy.

Furthermore, noteworthy is that the nucleus density on the substrate with the strongest quasi-convex rim curvature (R=62.7 µm; R/h=3.2) is the lowest, although the difference could not be observed without quantification. Moreover, a relationship between rim curvature and median cell density is not continued for increasing R/h (decreasing curvature), which would be R=62.7 µm (3.2), R=193.2 µm (4.4); R=318.6 µm (6.7) and R=134 µm (19.7). Which is due to the fact that the density in the transition zone of R=193.2 µm substrates is slightly higher compared to the median value for R=318.6 µm.

Considering that not only the radius of curvature varies between the different substrates, but also the microcavity depth Figure 73 shows the density data sorted by ascending depth. Interestingly, R=134 µm substrates exhibit the shallowest micro-spherical intentions (h=6.8 µm) but are showing higher density median values compared to the same regions of substrates with deeper structures, although this difference is not statistically significant. For deeper structures (R=62.7 µm; R=193.2 µm and R=318 µm with h=19.8 µm, 44.1 µm and 47.9 µm, respectively) the median density on the curved region (I) seem to stay constant.

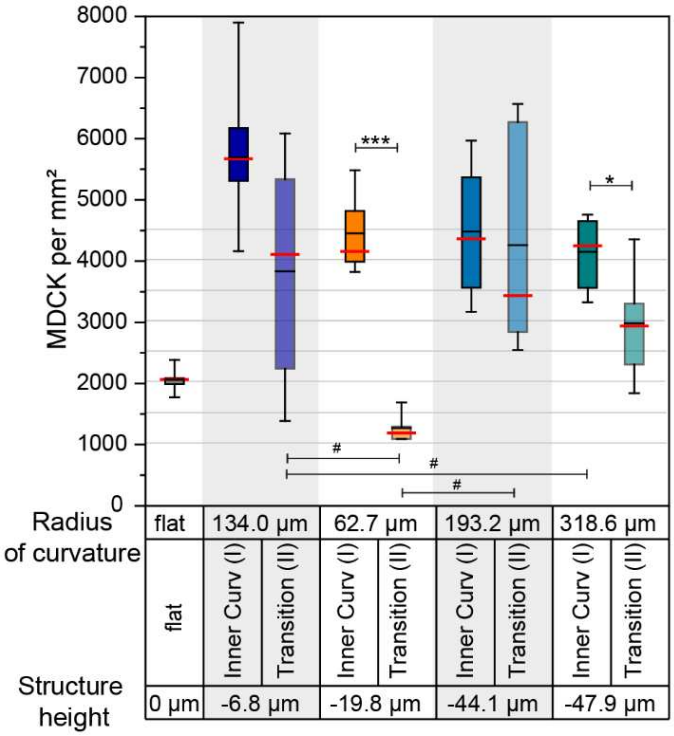

Figure 73 **Density of MDCK cells in different regions of concave spherically curved CurvChip substrates sorted by ascending microstructure depth.** Box plots, box indicates 25th and 75th percentile, whiskers 5th and 95th percentile. Black line shows the mean value, red line the median. Different regions are the transition zone (transition (II)) consisting of part of the sphere and directly surrounding flat area and indicated by transparent boxes, and the curved area (inner curv (I)), all indicated in Figure 11, p. 51. Statistical significance (Kruskal-Wallis with Dunn's post-hoc) on same substrates is indicated by *, between the substrates by # (*p<0.05; *p<0.005; *p<0.005, or #; # #; # # # respectively).

Generally, again no clear tendencies can be found that either the radius of curvature or the indention depth have a clear influence on density, moreover it seems like a combination of both influence cell density. Like done previously for A431 and MDCK on substrates with convex micro-spherical topographies, the interdependency of height hand radius of curvature R on the median density in the different regions is visualized in more detail in the Figure 99 in Chapter VIII Appendix, Part VI: Supplementary Materials, p 242, showing 3-D areas with height dependent color scaling.

Comparison of MDCK Cells Growing on Convex and Concave Micro-spherical Segments

When comparing MDCK cell behavior on substrates with convex and concave micro-spherical segments, the major difference manifests in the occurrence of cell layer defects on the curved regions. They only occur for convex topographies, while all concave indentations were fully

overgrown by MDCK cells (cf. Table 21, p.199). This is comparable to what van Gaal et al. (*248*) observed for human renal epithelial cells on semi-cylindrical microstructures of varying radius: cells avoided growing onto the cylinder summit, but prolonged cultivation and increased seeding density decreased gap size.

Together these results indicate the existence of some kind of hindrance or avoidance behavior of epithelial cells to fully cover the convex curvature.

Which is consistent with what Pieuchot et al. (*120*) describe for leading edges of epithelial monolayers. On their sinusoidal hill and valley substrates, MDCK cells of the leading edge were described to respond to underlying topography and, therefore, preferring concave areas over convex hills, just like mesenchymal cells and small clusters of epithelial cells. MDCK cells in mature epithelial sheets, on the contrary, did not show a preferred positioning. Pieuchot et al. (*120*) conclude that progressive embedding into the epithelium modifies the cell response to the topographies and propose that the degree of freedom might be the explanation for this observation. Based on this observation they suggest, that “cell-cell interactions might impose cell positioning” (*120* (p. 2)) independent from the underlying topography.

The here presented results on the gap occurrence, as well as the findings presented by van Gaal et al. (*248*), additionally, indicate that the cell avoidance of convex substrate areas by leading front of an epithelium might not be the same for all investigated topographies. And, although van Gaal et al. (*248*) claim that relative gap size decreases with decreasing curvature of uniaxially curved surfaces, data shows that this claim is only valid for R>50 µm. Although, the investigated radius range was 25- 250 µm, with the maximum gap size at 50 µm, while for smaller radii (25 µm and 35 µm) interestingly gap size decreased again.

On the contrary, the gap incidence on (convex) spherical segments of the CurvChip, where cells are exposed to curvature in all directions, did not show a direct relationship with increasing structure height or radius of curvature R, nor the approximated curvature of the transition zone (ratio of R to h) or with the ratio of R to base structure radius r (cf. Chapter VIII Appendix, Part V: Supplementary Materials, Table 26, p.231, for a comparison of topography metrics.).

Though, MDCK cells are reported to have a correlation length of about 100 to 150 µm (*86*), which means that they can coordinate their movement and transfer intercellular stresses over a length scale of multiples of their cell diameter (*89*). This correlation length was previously described to be involved in the occurrence of coordinated swirling patterns in (confined) cell monolayers (*89, 90*), similar to the one observed on R=193.2 µm curvature in Figure 63 B on p. 176.

In line with this finding, one could speculate, that topography basis radius r, or here more accurately the corresponding half arc length $a_{0.5}$ of the micro-spherical segment, in relation to the correlation length might have an impact on the here observed incidence of cell layer defects

on convex micro-spherical segments. In this context, the here deployed substrates can be divided in three categories: starting with small structures, with r≈50 µm and $a_{0.5}$≤56 µm smaller than the cellular correlation length including substrates with R=62.7 µm und R=134 µm microstructures. The second type of substrate meets the correlation length by exhibiting micro-spherical segments with circles of 160 µm>r>130 µm as base structures and $a_{0.5}$≈150 µm. This group is represented by the here deployed substrate with R=193.2 µm microstructures. And the last substrate category with r>160 µm and $a_{0.5}$>200 µm displaying a larger topography basis radius and surface of the microsphere segment compared to the reported MDCK cell correlation length, namely the substrate with R=318.6 µm micro-spherical segments.
Disregarding the shallowest substrate (R=134 µm, h=6.8 µm, MDCK cell height approximately 7°µm (*254*)), interestingly, the lowest gap occurrence was actually observed for the substrate where the corresponding half arc length $a_{0.5}$ (and base structure radius) of the micro-spherical segments is in the range of the correlation length (R=193.2 µm; r≈140 µm, $a_{0.5}$≈150 µm). Moreover, when the absolute difference of structure radius r or half arc length $a_{0.5}$ and correlation length is increasing, the gap incidence increases simultaneously.

These observations indicate that it seems to be most favorable for the leading cells to close the gap on convex substrates, when the distance between the cell(s) in the center of the microstructure to the microstructure rim is in the same size range compared to the correlation length. Which in turn suggests some sort of intercellular stress balancing or distribution between MDCK cells on the curvature and indicates that for other substrate topographies this stress balancing seems to be impaired.
This suggested stress distribution is in line with what is described by Ingber (*255*) in his tensegrity model of cellular mechanotransduction, where cells are described as prestressed structural tensegrity elements at equilibrium and tissues as interconnected (by the cytoskeleton) prestressed structural elements at equilibrium. Upon (external) mechanical forces or other stresses, here for instance the deformation from the curved substratum, the stresses are distributed over the interconnected elements resulting in a global reaction, like reorientation or formation of new cytoskeletal elements among others.
In this relationship additionally noteworthy is, that for MDCK cells on substrates with R=193.2 µm topographies prominent central f-actin stress fibers can be observed when growing on the curvature (cf. Figure 63, p. 176 and Figure 93, p. 235), which, to this extent, could not be observed for the MDCK cells growing other substrates. This observation further consolidates the theory that on the microstructure with R=193.2 µm force transmission between the cells seems vary from force transmission on the other substrates.
To balance the potential curvature induced stress on curvatures with smaller $a_{0.5}$ than correlation length, for instance the force transmission would need to cross the quasi-concave

curved rim which could be hindered in two closely related ways or a combination of both. The first possibility concerns the necessity of actomyosin to bend across the rim, which might be unfavorable for stress fibers and force transmission in general, as suggested by Dunn and Heath (*166*) and also indicated by the actin exclusion from quasi-convex structure rim observed by Rougerie et al. (*147*) as well as in the present work for concave micro-spherical segments (cf. Figure 71, p. 188). This suggestion was also included in the model of Biton and Safran (*171*), describing that cell orientation on curve surfaces results from the competition between the bending energy cost and cell contractility, leading to the second possibility: Force transmission across the rim might be impaired because the coupling of the cytoskeletons of the neighboring cells is affected, since cells close to the rim are elongated and orient themselves, and their actomyosin cytoskeleton and their effective force transmission along the rim. Hereby, the cell orientation can either be affected by the competition between contractility and bending energy (*171*) or based on the reduction of nuclear stress by placing the nucleus in the quasi-concave transition zone, as suggested by Pieuchot et al. (*120*).
Keeping these possibilities in mind while comparing the f-actin images of MDCK on concave and convex substrates, results indicate that f-actin does not seem to be excluded from the quasi-concave rim of convex microspheres, unlike observed for the quasi-convex rim of the concave substrates (cf. Figure 69, p. 185 and Figure 96, in Chapter VIII Appendix, Part VI: Supplementary Materials, p. 238). This observation indicates that force transmission across should be possible. However, nucleus images confirm nucleus, and, therefore, central stress fiber orientation preferentially along the rim and not across, suggesting the effective force transmission length of cells on the curvature seems to be limited to cells on the curvature.

Regarding the cell layer gap incidence on the shallowest microstructure with R=134 µm and h=6.8 µm ($a_{0.5}$≈52 µm) is also noteworthy. Although the structure is only about the same height compared to the reported MDCK cell height (approximately 7°µm (*254*)), still 20% of microstructures show gaps on the peak of the microstructure. Compared to R=62.7 µm microstructures, which have a comparable $a_{0.5}$ of approximately 56 µm, this is a reduction of 45%. However, it is still remarkable that cells are able to perceive this low structure and even seem to avoid growing onto it. Furthermore, it also indicates that not only the arc length in relation to the cells' correlation length was shown to have an effect on cell growth on to the structures, moreover, structure height seems to have an influence too, especially low microstructure height. In line with this observation and the previously presented hypothesis, no preferred nucleus orientation along the weakly curved rim can be observed which might increase force transmission across the rim stabilizing MDCK cell growth over the micro-spherical segment and thus decreasing the gap incidence.

For larger and higher micro-spherical segments (R=318.6 µm r≈190 µm $a_{0.5}$≈200 µm), the balancing of curvature induced stress should also not be impaired by the rim or rim induced nucleus orientation. But on the contrary the gap incidence is increased by 13 % compared to microstructures with R=193.2 µm, having a half arc length within the range of reported correlation length. The most plausible explanation might be that for larger structures the stress transmission, as also reported for the coordination of cell movement in larger 2-D confinements, on the substrate is different compared to microstructure in the size range of the cell correlation length. Conceivable would be, for instance, that locally occurring orientation patterns (e.g. reported swirls) could locally disturb transmission between neighboring cells which could be unfavorable, due to local decreased stress balancing. And this circumstance, in turn, seems to affect gap closure on the top of the microstructure. As stated previously this theory is in line with what was observed for 2-D confinements, where cell layers did not show fully coordinated movements but local swirls and vortices (*89, 90*). However, more experiments are needed to generate a more detailed understanding of how the different coordination of cell movement affects gap closure.

Attempts to stain E-cadherin in MDCK cells, in order to get a more detailed information on force transmission between the cells, however showed a high unspecific background signal on PDMS substrates independent of the sign of the curvature. Therefore, only few to none clearly stained adherence junctions were visible, although the staining was optimized by antibody titration for MDCK cells in chambered glass slides (cf. Chapter VIII Appendix, Part VI: Supplementary Materials Figure 100, p. 244). Moreover, on substrates with concave micro-spherical segments some cells in the curved region of the substrate did not show any E-cadherin staining, not even unspecific staining, while f-actin and nucleus staining was unaffected. An exemplary image showing the greatest of the observed e-cadherin staining “defects” is displayed in Figure 101 (Chapter VIII Appendix, Part VI: Supplementary Materials, p. 245) for MDCK cells growing on R=193.2 µm.
Generally, Jung et al. (*202*) show, that it is possible that the negative curvature and resulting change in tension between the neighboring cells growing on the micro-spherical segment affects e-cadherin expression. They observed a decrease in e-cadherin level for MDCK cells treated with Y-27632 and Blebbistatin, both affecting cell contractility, compared to untreated cells. Nevertheless, this phenomenon of absent e-cadherin staining on the CurvChip substrates was only observed randomly, therefore, a closer investigation is necessary to exclude that it is not an unspecific staining artefact and to improve the overall outcome of the e-cadherin staining.

Additional to the gap incidence quantification, qualitative description of the differences in stress fiber and nucleus distribution, and their probable partial exclusion from convex rims of concave

micro-spherical topographies, the density of the MDCK cells in different areas of the substrates was quantified. Comparing the general course of densities on the different substrate areas shows, as illustrated in Figure 74, that generally the median values of substrates with concave topographies are higher compared to the corresponding values of substrates with convex microstructures.

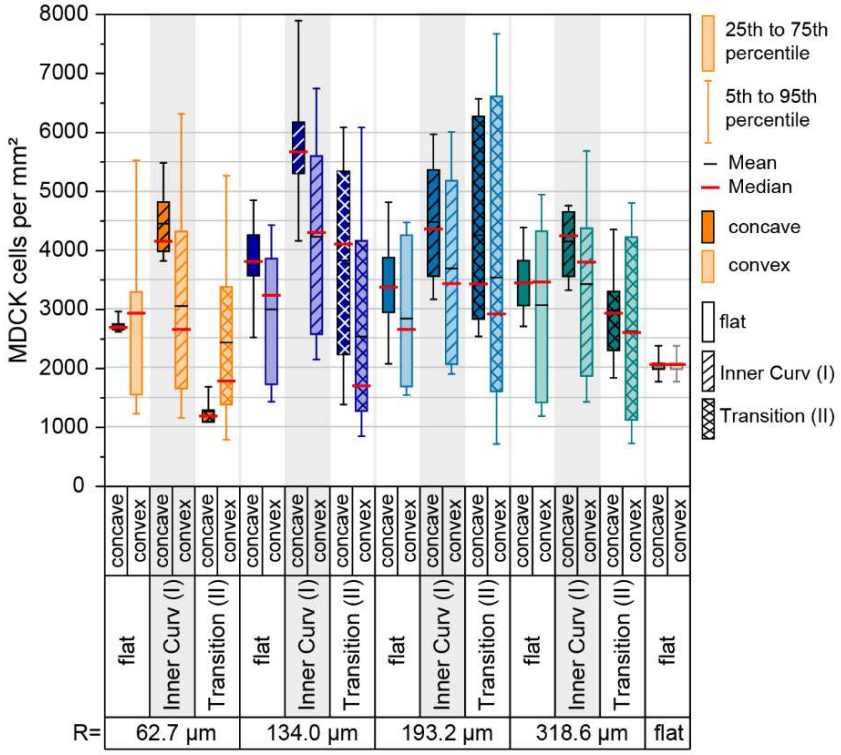

Figure 74 **MDCK cell density on different areas of PDMS substrates with concave and convex micro-spherical topographies of varying structure radius of curvature R and structure height/depth h as well as base structure radius r.** Graph shows Box plots with characteristics as indicated by the graph legend on the right side of the figure. No statistically significant differences between the values for concave and convex of the same substrate areas are detectable. Different regions are flat surrounding (flat), the transition zone (transition (II)) consisting of part of the sphere and directly surrounding flat area, and the curved area (inner curv (I)), all as indicated in Figure 11, p. 51.

With the only exception for R=62.7 µm where in the flat area as well as in the transition zone (II) the median density for convex microstructure substrates is larger, also shown by the ratio of concave to convex in Table 20.

The ratio of concave to convex, additionally stresses that the difference between the density values of transition zones of R=134 µm substrates is particularly high. Since this is the shallowest substrate, the high ratio of concave to convex might indicate a difference in the influence of structure height for the different types of curvature.

Furthermore, the IQR is smaller for substrates with concave indentions compared to convex topographies, indicating a more homogeneous random sample. At least partially, this

difference between IQR of concave and convex topographies might be due to the fact that the convex sample includes both structures with and without MDCK cell layer gaps on the curvature, while layer gaps did not occur on substrates with concave micro-spherical segments.

Generally, in both cases, convex and concave micro-spherical segments, the lowest median density on every substrate is occurring in the transition zone (II) between flat and curved region, while the highest median density values are found for the curved regions. For an easier comparison of the difference between the median density on curved areas (I) and transition zones (II), their ratio was calculated and displayed in Table 20.

Table 20 **Ratio of median density of concave to convex on curved region (I) and transition zone (II), as well as ratio of median density on curved region (I) to median density of transition zone (II) for MDCK cells on substrates with convex and concave micro-spherical topographies.** Median densities are as visualized in Figure 74.

Substrate radius of curvature R	Concave to convex (I)	Concave to convex (II)	Convex (I) to (II)	Concave (I) to (II)
62.7 µm	1.56	0.67	1.49	3.48
134 µm	1.32	2.41	2.52	1.38
193.2 µm	1.27	1.17	1.18	1.27
318.6 µm	1.12	1.13	1.46	1.45

Interestingly the ratios for R=318.6 µm and 193.2 µm substrates is almost the same for concave and convex surfaces, while the values for R=134 µm and R=62.7 µm vary distinctly. While for convex microstructure with R=134 µm (h=6.8) the ratio of curved region (I) to transition zone (II) is larger, representing a larger difference between (I) and (II), the ratio for the substrates with concave microstructures is comparable to the previously compared substrates (R=193.2 µm and R=318.6 µm). This obsevation consolidates what was previously discussed about the observation that a low structure height decreases gap incidence and, therefore, seems to facilitate MDCK cell migration onto the convex curvature and further indicates that for concave curvature structure height is a neglectable surface parameter. This variation in (I) to (II) ratio is the result of an increased median value for the curved area compared to the other substrates with convex micro-spherical segments accompanied by a decreased median value for the transition zone (II) in relation to the substrates with larger radii of curvature (R=193.2 µm and R=318.6 µm).

For R=62.7 µm micro-spherical topographies on the contrary the ratio of curved (I) to transition zone (II) indicates a strong difference for concave microstructures, while the ratio convex is in the same range as for R=193.2 µm and R=318.6 µm. Recalling the observation that nuclei and

f-actin seemed to be excluded from the quasi-convex rim of the concave microstructures (best observed for R=193.2 µm, cf. Figure 71) might explain this difference, since substrates with R=62.7 µm indentations have the strongest quasi-convex curvature in the rim and the main reason for the here described difference seems to be the low median density value for the transition zone.

Comparison of Cancerous A431 and healthy MDCK Cell Behavior

When comparing the behavior of A431 cells and MDCK cells on topographies with convex micro-spherical segments one needs to consider the origin of the cells. A431 cells are human squamous cells from a skin epidermoid carcinoma, while MDCK cells are canine cells derived from cocker spaniel kidneys. Unfortunately, their isolation does not seem to be published (*192*), but they are commonly used as a model for healthy epithelial cells.

Literature indicates different cell responses to topographies between cancerous and healthy cells (*256–259*), but also between cancerous cells of different malignancies (*260*). Many studies focus on nucleus deformation (*258–260*) while some focus on a more phenomenological observation of cell orientation or migration (*256, 257*), describing that cancerous cells seem to be less sensitive to topographical cues.

Cell Growth Characteristics and Incidence of Growth Defects on Convex Micro-spherical Segments

Starting the comparison of results with the gap incidence of the two different cell lines on convex spherical topographies, as listed in Table 21, shows that gap occurrence is higher in A431 cells for all substrates, except for the substrate with shallow micro-spherical segments of only 6.8 µm height (R=134 µm). Like described previously, the most likely reason for this difference with shallow micro-spherical segments is that the flat A431 monolayers already show a high variability in layer height (cf. Chapter VIII Appendix, Part VI: Supplementary Materials, Figure 91, p. 233), that is within the height of the shallow substrate. This comparability of structure height and layer height is thought to reduce the microstructure recognition of this substrate by A431, causing the lack of monolayer gap. While no direct relationship between gap incidence and substrate parameters could be observed for MDCK cells, A431 cells show a decreasing incidence with increasing radius of curvature R, segment height h and base structure radius r or rather half arc length $a_{0.5,}$ as well as ratio of R/h (approximation of how concave the rim is) with an exception for the lowest structure.

However, taking a closer look at the substrates with R=193.2 µm and R=318.6 µm, which are approximately the same height (Δh=3.8 µm) but still show an incidence reduction of 16 %, for A431 cells, indicates that radius of curvature R might play an important role.

Furthermore, gap occurrence is decreasing with increasing ratio of the curvature imposed by the base structure of the segment 1/r to spherical curvature 1/R, or short R to r, without exclusion of the shallowest structures with R=134 µm. However, to finally identify which parameters are the pivotal ones, more experiments with additional substrates are necessary.

Table 21 **Incidence of cell layer defects on micro-spherical segments of indicated radius of curvature R and segment height h for cancerous A431 cell line and healthy MDCK cell line.**

Substrates	Gap incidence		
	A431 (convex)	MDCK (convex)	MDCK (concave)
R=62.7 µm, h=19.8 µm	95 %	65 %	0 %
R=134 µm, h=6.8 µm	0 %	20 %	0 %
R=193.2 µm, h=44.1 µm	77 %	39 %	0 %
R=318.6 µm, h=47.9 µm	61 %	52 %	0 %

More generally the results on gap incidence on microstructures indicate that A431 cells are more sensitive concerning convex micro-spherical surface topographies causing an increased avoidance of growing onto the structures compared to MDCK cells.

This observed increased avoidance of convex regions by A431 could have different reasons. According to the results published by Peuchot et al. (*120*) the increased stress on the nucleus when cells are situated on convex surfaces and the decreased stress when they are positioned over concave areas is involved in the cells mechanism of perceiving curvature and respond to it, which results in the so called “curvotaxis”. In line with this theory of “curvotaxis” cancerous cells are frequently reported to have an altered composition of the nuclear envelope (*261*), which is often associated with altered nuclear mechanics, and could imply an explanation for the difference between A431 cells’ and MDCK cells’ response to the here investigated convex micro-spherical segments. Ratios of Lamin A to Lamin B, for instance, are associated with tissue elasticity, and moreover high Lamin A to B ratios are reported to correspond to stiffer, less deformable nuclei (*85*).

Interestingly, for cancerous cells, both increased Lamin A to B ratios as well as decreased ratios are reported (*261*, Table 1), which is thought to have a relation to cancer invasiveness. In addition to these findings, Luciano et al. (*144*) recently reported varying Lamin A to B ratios for epithelial cells in different regions of a wavy substrate. While cells in concave areas have a nucleus with a higher Lamin A to B ratio, nuclei in convex regions exhibit a low Lamin A to B ratio. These findings suggest that cells on convex curvatures need to be more deformable, compared to cells on concave substrate areas, or in other words, stiffer nuclei, with higher Lamin A to B ratio, are less deformable and this resistance against deformation might cause the avoidance of the curvature.

In turn this hypothesis would imply that A431 cell nuclei might have an increased Lamin A to B ratio compared to MDCK cell nuclei. Unfortunately, there is no published value for Lamin A to B ratio for A431 cells or MDCK cells on flat substrate. However, the hypothesis is in line with the reported values for cell stiffness for both cell lines, measured with AFM. MDCK are reported to have an E-modulus between 5 and 7 kPa (*249*), while A431 cells have a reported average cell stiffness of about 11 kPa (*262*). (cell stiffness related to nuclear stiffness).

Nevertheless, alterations in the cytoskeleton of cancerous cells can also not be disregarded. Using micropillar substrates that are known to cause prominent nucleus deformations, cancerous and health, as well as epithelial to mesenchymal cells were compared. Generally, studies showed that cancerous cells (mostly osteosarcoma cells and invasive tumor cells) showed an extensive nucleus deformation, while healthy cells showed minor to no deformation of the nucleus (*258, 259*). Based on these findings, it was suggested that the often-reported decrease in Lamin A might be the reason for the differences described. However, Liu et al. (*263*) found a more pronounced difference between epithelial and mesenchymal cells compared to healthy and cancerous cells. And furthermore, most recently, Tusamda Wakhloo et al. (*224*) found, that on micropillar topographies, actomyosin, vimentin and their coupling to the nucleus via the LINC complex plays a role in nucleus deformation but not the extent of Lamin A expression.
Additionally, they found that pulling forces are predominantly responsible for the nucleus deformation. Comparing the results of osteosarcoma cells to MSCs, which have a comparable Lamin A level, moreover, showed that nuclei of MSC do not deform. On the basis of this difference between osteosarcoma and MSCs, they hypothesize that healthy cells might have a mechanism to prevent nucleus deformation and that this might include different coupling between the nucleus and adhesion complexes and adherence junctions.

As mentioned previously for MDCK cells, staining E-cadherin on cells growing on the PDMS substrates with microstructure, to further analyze the differences between MDCK cells and A431 cells was not successful, although antibody titration was performed (cf. Chapter VIII Appendix, Part VI: Supplementary Materials, Figure 100, p. 244 and Figure 101, p. 245).

Additionally, some exemplary time-lapse movies were recorded from MDCK and A431 cells after seeding (cf. Chapter VIII Appendix, Part VI: Supplementary Materials, Figure 102 to Figure 104, pp. 246-250) on substrates with R=193.2 µm topographies as well as after wound generation on substrates with R=318.6 µm micro-spherical segments (wound-healing or scratch assay; Figure 105 and Figure 106, pp. 251-252).
For a detailed statement, more videos would be needed but generally, time-lapse microscopy directly after cell seeding shows, that A431 cells grow about three times slower compared to

MDCK cells and tend to from clusters with layer defects in between and low cell motility. On the contrary, MDCK cells rapidly form a monolayer, closing the existing defects, and show high motility. In accordance with that, in exemplary time-lapse sequences, defects on topographies are closed rapidly by MDCK cells, partly even before defect closure on flat areas, whereas A431 fist close gaps in flat areas, while topographies remain mostly clear from cells.
Taking the difference in growth rate into account, the seeding density for the wound healing assay was adjusted, but results were as expected: rapid wound closure by MDCK cells, where topographies were almost irrelevant, while the wound healing of A431 cells took much longer with faster growth on flat compared to convex areas.
Interestingly, these preliminary observations seem to conflict with the previously described gap occurrence of MDCK cells on curved substrates. A closer examination of the time-lapse sequence images, however, reveals a particularity for MDCK cells, which could pose an answer to this discrepancy. During coverage of the convex micro-spherical segment a new defect occurred on the curvature after what looks like a cell division. This gap initially increased in area and persisted for almost 5 hours (cf. Figure 107, p. 254). While increased cell division induced by stretching is a known phenomenon (*264*), the emergence of gaps is highly untypical for epithelial cells. This unusual nature becomes especially clear for MDCK cells, since they are known for their strong cell-cell contact and barrier function that is able to withstand increasing fluid pressure during dome formation. But as mentioned previously, these are only exemplary and to further investigate the discrepancy between gap occurrence in fluorescence images of MDCK cells on convex micro-spherical segments and the shown time-lapse images as well as to closer examine the indicated gap occurrence more experiments are necessary.

Cell density in different areas of micro-spherical segments

To contrast further characteristics of cell growth on different convex micro-spherical topographies, the cell density in different areas was compared between A431 and MDCK cell lines, as visualized in Figure 108 (Chapter VIII Appendix, Part VI: Supplementary Materials, p. 255. Generally, the median value range is comparable between the two cell types, for A431 cells the median densities range from about 1900 to 4600 cells per mm², while for MDCK cells the range is from 1700 to 4400 cells per mm². The interquartile range, on the contrary varies strongly from maximal about 2000 for A431 cells to about 5000 for MDCK cells, suggesting that A431 cells might show a more homogeneous response to substrate topographies compared to MDCK cells, also indicated by the lack of statistically significant differences for MDCK cells as well as the reduced gap incidence.

For A431 the median density values on substrates with microstructures are lower compared to the median density on all flat PDMS (3447 cells per mm²), with only two exemptions: The

median density in the inner curved region of R=134 µm is not significantly higher than flat, and the median density in the transition zone of substrates with R=193.2 µm microstructures are significantly ($p<0.05$) higher compared to all flat PDMS. Additionally, there is only one other significant difference to of A431 cells on flat PDMS: inner curved region of R=62.7 µm with 1828 cells per mm² is significantly ($p<0.05$) lower than the median density on flat PDMS. All other differences are not statistically significant.
In contrast, for MDCK cells densities on substrates with micro-spherical segments tend to be higher compared to all flat PDMS (2067 cells per mm²), again with only two exceptions: the values for the transition zones of microstructures with R=62.7 µm and R=134 µm are lower compared to all flat PDMS. For MDCK cells, however, all differences to flat PDMS are not statistically significant. As also indicated by the comparability of the general median value ranges, this difference is mainly caused by the difference in the density values for cells on all flat PDMS, which is higher for A431 cells and lower for MDCK cells.

Comparing the values on the different substrates more closely, reveals that for A431 cells in most cases the lowest median density value can be found in the curved region of the microstructure, and the highest value in the corresponding transition zone, also represented by values lower that one in Table 22, comparing ratios of density values of curved region to transition zone. The only outlier is the substrate with R=134 µm microstructures, here the density on the curvature is higher compared to the transition zone. This observation is in line with what could be observed for the cell layer gap incidence, since for R=134 µm A431 cells fully cover all investigated microstructures. As displayed in Table 22, for MDCK cells the median density on the curved region is generally higher than the median density in the transition zone, while the difference is especially high for R=134 µm microstructures and relatively low for R=193.2 µm. Moreover, in most cases the median density in curved regions is the overall highest value on the substrate, only for R=62.7 µm the median density in the flat areas is even higher.

All in all, most of the differences observed for the median densities between A431 cells and MDCK cells can be explained as a result of the differences in gap incidence. Therefore, a more differentiated assessment of the density regarding gap incidence and maybe even gap area should be made, and sample size needs to be increased to generate more statistically meaningful results. These measures should also answer the question if A431 cells are still able to perceive the curvature $\kappa=1/318.6\ \mu m^{-1}$.

Table 22 **Ratio of median density of curved region (I) to transition zone (II) for cancerous A431 cells and healthy MDCK cells on substrates with convex micro-spherical topographies of varying parameters.** Median values as shown in Figure 59(A431 cells) and Figure 65 (MDCK cells).

Substrate radius of curvature R	A431cells ratio of (I) to (II)	MDCK cells ratio of (I) to (II)
62.7 µm	0.60	1.49
134 µm	1.13	2.52
193.2 µm	0.55	1.18
318.6 µm	0.87	1.46

Moreover, the fact that general characteristics differ from findings in literature, where Kushiro et al. (*257*) showes that cancerous cells climbed walls of sharp edged micro-grooves, while healthy cells did not, stresses the importance of studying more in vivo-like curved topographies to further elucidate the difference between cancer cells and healthy cells and maybe even different malignancies of cancer in more native surroundings.

Summary and Conclusion of Findings Obtained from Studies Using Epithelial Cells on Spherical CurvChip Topographies.

All in all, results indicate that cancerous A431 cells seem to be more sensitive in regard to convex substrate curvature 1/R and other substrate metrics as structure height h, compared to MDCK, where the half arc length $a_{0.5}$ of the micro-spherical segment in comparison to the cellular correlation length seems to be responsible for cell behavior. Literature (*85, 120, 144, 224, 261*) suggest a difference in nuclear envelope and mechanics to be involved in this difference, however more studies are necessary to draw a conclusion.
Findings from wound-healing assays consolidate this finding, showing that MDCK cells grow over micro-spherical segments within the wound, while A431 seem to close the wound in the flat area before closing the wound on the convex topographies.

Moreover, the absence of cell defects of MDCK growing on concave substrates and observed nucleus and partial f-actin exclusion from the quasi-convex rim is in line with findings from literature (*120, 147*) suggesting a cellular avoidance of convex areas with high curvature.

Regarding cell density, substrate topographies increase density of MDCK cells (independent from type of micro-spherical segment, including concave and convex curvature) compared to all flat PDMS, while for A431 topographies decrease the density compared to all flat PDMS.
Generally, more experiments including new topographies with varying metrics as well as differentiated assessments and higher sample size are necessary for a better insight.

However, this preliminary study shows that the CurvChip topographies can be used to investigate the difference between cancerous and healthy cells and offer the possibility for more systematic studies.

VII. Conclusion and Outlook

The CurvChip platform is a highly defined, versatile model system with various kinds of convex and concave 2.5-D curvatures, allowing a systematic variation of different surface parameters, including base structure, curvature and spacing between the curvatures, and, therefore, the systematic study of cell response to those variations.
Even though, the use of cylindrical or spherical segment arrays with flat areas between the curvatures might be more artificial compared to the situation in vivo, or the use of sinusoidal patterns, the benefit is that curvatures can be described by one curvature, which enables researchers to link cellular behavior more directly to the curvature of the underlying substratum. Moreover, the very smooth surface roughness generated by the reflow process allows the exclusion of interference of guidance cues on the nanometer-scale.
Combination of the CurvChip platform with a protein micropatterning method, like described by van der Putten et al. (*134*) would further allow to limit cell adhesion to the curved topography or other 2-D micropatterns allowing to add an additional dimension and enabling to extent previous studies.

The use of low-cost photolithography, which does not need a mask-aligner, or a clean room is another advantage of the CurvChip-System over others, since it enables a broad range of scientist to use the technique and subsequently work on systematically studying these cell behaviors, without any post-processing necessary. (*3*)
This broad range of scientists includes those of the fields of basic research, aiming to elucidate cell functions and processes behind cell behavior, but also research of biomaterials and development of organ-on-a-chip-systems (*126–128*) or disease models (*10, 129*), where the introduction of 2.5-D curved surfaces might help to find more realistic test systems, and allow cultivation of cells that do not survive in 2-D (cf. Poon et al. (*150*) and Gouveia et al. (*153*)). In this context further developments of the CurvChip platform could be used to study things like the effect of curvature on endothelialization or to investigate if cells of diseased patents (e.g. hypertension patients, progeria) might respond differently to curvature compared to healthy cells, or if the age of the donor, or duration of cultivation (senescence (*265*)) affects the response to curvature.

In the present work the CurvChip platform was used to investigate the effect of varying cell origins, cell density, protein coatings, manipulation of cytoskeleton as well as varying array parameters (i.e. spacing between curvatures).

Using uniaxial, cylindrical CurvChip topographies with radii of curvature R ranging from R=20.9 µm to 312 µm (or curvature κ=1/20.9 µm^{-1} to 1/312 µm^{-1}) and mesenchymal cells the

present work could systematically characterize cell behavior on the substrates and draw conclusions regarding a possible mechanism of cellular curvature perception.

Results show that mesenchymal cells use two distinct ways of avoiding substrate curvature, either by growing in the (narrow) areas between the cylindrical curvatures or by orienting the cellular axis of elongation along the cylinder axis, representing an effective curvature of zero.

Using mesenchymal cells from human dermis (hdF, different donors) and adipose tissue (ASC), the present work shows that the general cell behavior of mesenchymal cells is independent from cell origin (tissue and donor) and cell density as well as underlying protein coating, although the extent of the orientation with the axis of minimal curvature on cylinders seems vary between donors/cell types and tends to be stronger for cells growing in denser layers and on coatings with higher ligand densities, especially for integrin ligands known to be involved in mechanotransduction.

Moreover, for the general curvature avoidance by positioning in the areas between the cylindrical topographies, a clear dependence on the width of the spacings was observed. However, for narrow spaces no correlation with curvature was found, rather structure height seems to be the influencing factor.

Regarding the second way of curvature avoidance, cell orientation on the cylindrical topographies, results show that single cells do not perfectly align with the cylinder axis and the median angle of orientation increase correlates with the increase in radius of curvature R (decreasing curvature κ). Furthermore, the mesenchymal cells seem to orient in a way to meet an internal setpoint that can be described as a perceived curvature k of about k=1/1671 μm^{-1} to k=1/2307 μm^{-1}. Together with findings from literature (*134*), the results indicate that the setpoint might be the limit of curvature perception, which moreover stresses the necessity of a highly sensitive detection mechanism.

Pharmacological manipulation of the cytoskeleton of hdF indicates that an exclusive involvement of the stress fiber system in the curvature perception mechanism, like it was proposed in literature (*166, 171*), is improbable (cf. Table 22).

Based on these finding, and in line with literature findings (*54, 119, 120, 166*), a mechanism is proposed comprising the nucleus as a central organelle in curvature perception of mesenchymal cells, as well as the cytoskeletal components, including actin filaments, microtubule and intermediate filaments, acting in a way to reduce unfavorable stress on the nucleus.

The involvement of all cytoskeletal components in this mechanism might explain the here found robustness against pharmacological manipulation of single components. Which can further be explained by the interdependency of the cytoskeletal components, their mutual regulation (e.g.

based on RhoA/ROCK pathway (*215*)) and the fact that some deficiencies can possibly be compensated for by the remaining components (*225*).

Further studies would help to consolidate (or refute) the presented theories, for instance in order to distinguish between the role of intermediate filaments and microtubule in nucleus stress shielding studies depolymerized intermediate filaments and cells treated with Nocodazole and a Rho inhibitor (e.g. Y27632) simultaneously, would be helpful.

Moreover, additional studies using for instance full cylinders in the same range of radius, would allow to elucidate the reason why the cell orientation response along the cylinder axis in mesenchymal cells growing in denser layers seems to be increased, and to exclude a “boundary effect” (*91*) from the transition zone of the topography. Additionally, studies using epithelial cells in varying densities would answer the question if the cell type and their density has an effect on curvature perception of uniaxial curvatures.

Results using healthy and cancerous epithelial cells on micro-spherical segments of the CurvChip, moreover, indicate that cancerous A431 cells seem to be more sensitive in regard to convex substrate curvature 1/R and other substrate metrics as structure height h compared to healthy MDCK cells, where the half arc length $a_{0.5}$ of the micro-spherical segment in comparison to the cellular correlation length seems to be responsible for cell behavior.

Further studies would help to elucidate if the by literature (*85, 120, 144, 224, 261*) suggested difference in nuclear envelope and mechanics are involved in this difference. Moreover, comparing their behavior on uniaxial curvatures would further help to broaden the knowledge on cellular curvature perception mechanism. In this context, it would also be interesting to manipulate different cytoskeletal elements like done in Chapter V or via EGF stimulation of A431 to investigate their involvement.

Results could help to understand the invasiveness and metastasis behavior of different cancer types leading to a better understanding and ultimately maybe even better therapy of different cancer types.

All in all the present work systematically characterizes the behavior of mesenchymal cells on cylindrically curved topographies and shows, that the mechanism of cell perception and resulting reorientation on uniaxial curved topographies is highly robust and highly sensitive, allowing cells to perceive radii of curvatures that are about 20 to 29 times the average hdF cell length (*189*). Moreover, results indicate that both the nucleus and all cytoskeletal components are involved in the reorientation and, therefore, the mechanism of perception.

However, further developments of the CurvChip and results from systematic cell studies with the CurvChip will help to better understand the cell-material interaction leading to better understanding in the fields of biomaterials and implant design but also tissue engineering and organ-on-a-chip systems, or disease models.

VIII. Appendix

Part III: Supplementary Materials

Spin-parameter of ma-P1275 HV Photoresist

The standard operation procedure (SOP) was established by Markus Schneider during his Master thesis at Reutlingen University submitted in 2017, based on the manufacturer's data of the photoresist and acquired experience using the same set-up used in the present work.
The following is a verbatim quote of the SOP, personal changes based on own experiences are added in [brackets], and elisions are indicated by ellipsis […].

General information	The photoresist should be stored at room temperature and be protected from light! The optimum processing conditions are a temperature of 20 to 25 °C with a relative humidity in the range of 40 to 60 %.
Cleaning the silicon wafer	To clean the wafer from simple soiling, it can be placed in acetone for a few minutes and afterwards rinsed with isopropanol. In order to remove more persistent residues, [*a combination of the solvents with an ultrasonic bath can be used. For even more persistent residues*] an oxygen or ozone plasma cleaning is recommended. In order to remove adsorbed air humidity [before applying HMDS], it is recommended to heat the wafer up to 200 ° C for about 30 minutes. After the heating the wafer should be cooled down to room temperature immediately before the coating process.
Spin coating of the HMDS primer	To improve the adhesion of the photoresist to the substrate surface, a thin layer of the HMDS (hexamethyldisilazane) adhesion promoter should be applied to the surface. Suitable spin parameters for this purpose are listed below.

Cycles	Spin speed [rps]	Acceleration [s]	Holding time [s]
Cycle 1	8	3	30
Cycle 2	66	3	7

Spin coating of the photoresist	In order to apply the photoresist to the wafer without bubbles, it should be carefully poured from the container directly onto the wafer. When using a pipette, small air pockets are formed which remain on the surface even after the spin coating cycles. The quantity to be applied depends on the desired layer thickness [*and*

size of the silicon wafer], in the case of 30 µm [on a 2-inch wafer] it is about 3 to 4 mL.

The photoresist layer can be applied with the following spin parameters for the different layer thicknesses:

approximately 10 µm

Cycles	Spin speed [rps]	Acceleration [s]	Holding time [s]
Cycle 1	54	3	30
Cycle 2	54	3	15

approximately 20 µm

Cycles	Spin speed [rps]	Acceleration [s]	Holding time [s]
Cycle 1	21	3	30
Cycle 2	21	3	15

approximately 30 µm

Cycles	Spin speed [rps]	Acceleration [s]	Holding time [s]
Cycle 1	12	3	30
Cycle 2	12	3	15

approximately 40 µm

Cycles	Spin speed [rps]	Acceleration [s]	Holding time [s]
Cycle 1	8	3	30
Cycle 2	8	3	15

approximately 50 µm

Cycles	Spin speed [rps]	Acceleration [s]	Holding time [s]
Cycle 1	6	3	30
Cycle 2	6	3	15

[The Calibration curve for determining the needed spin-speed for a desired layer-thickness can be found in Figure 75. The curve can be described by the following equation:

$$y = 181\ x^{-0.723}$$

With y for layer-thickness and x for spin-speed.]

Soft bake of the photoresist layer

In order to avoid the adhesion of the […] [photomask] during the sub-sequent exposure process, the photoresist layer can be dried at 120 °C.

!! Higher temperatures have to be avoided in order to be able to exclude temperature activation of the UV-sensitive group of the photoresist. Suitable soft-bake times are listed below for the respective layer thicknesses.

Resist thickness [µm]	10	20	30	40	50
Time [min]	2	4	5	7	9

[Edge bead removal]

[To improve the contact between the wafer and the photomask the removal of the edge bead might be necessary, as it increases in size with layer thickness of the photoresist. Mechanical removal can be achieved by slowly spinning the wafer with the dried photoresist on the spincoater and scraping the edge bead off by bringing a razor blade in contact with the wafer/photoresist. Resulting resist dust can be removed using a soft paintbrush, without using any pressure and nitrogen gas/ clean pressurized air flow.]

Relaxation [and re-adsorption] of water

Before the photoresist layer can be exposed, it must be allowed to adsorb water molecules from room air [, as water is part of the photoresist's chemical reaction]. The times required for relaxation with optimal air humidity are listed below. These times may need to be adjusted when the humidity is low.

[Alternatively, also storing conditions can be changed by storing the wafer in a humidified environment. Storing the wafer e.g. in a drawer with wet paper towels or an oven heated to approx. 30°C and added beaker with water improved the results.]

Resist thickness [µm]	10	20	30	40	50
Time [min]	10	20	40	60	90

Exposure of the photoresist layer

The required exposure dose depends on the substrate material and the layer thickness of the photoresist. The following parameters are suitable exposure times for the use of the LED exposure unit of the BIOMAT laboratory. The times are valid for the exposure of the

photoresist at maximal distance to the lamp. Shorter exposures are necessary for shorter distances.

Resist thickness [µm]	10	20	30	40	50
Exposure dose [mJ/cm²]	300	1000	2000	3500	4000
Time [s]	120	375	750	1320	1500

! The high exposure dose during development can lead to the formation of bubbles due to the release of nitrogen and lead to a peeling off of the photoresist layer [especially when using a large photomask covering the whole wafer]. However, the formation of bubbles can be avoided by exposure with applied pauses. In the case of the 30 µm layer thickness, for example, an exposure with 3 times 250 seconds and a 250 second break between the exposures can be carried out.

Development with ma-D 331

For development, the exposed wafer is placed in a petri dish. The petri dish is filled with developer until the wafer is surrounded completely. For better detachment of the exposed areas, the petri dish can be slightly swiveled.

The development times for the individual layer thicknesses are listed below. These values are only indications, depending on the structure, the development can proceed much faster or slower. [Therefore, steady control is necessary.]

Resist thickness [µm]	10	20	30	40	50
Time [min]	4	6	8	12	15

Follow-up treatment

In order to stop the development and to clean the structures, the wafer should be thoroughly rinsed with demineralized water. Cleaning with solvents should be avoided since the photoresist is […] [not] solvent resistant.

Afterwards, the wafer is dried [using nitrogen or clean pressurized air flow and stored] at room temperature.

Reflow of the structures

A reflow (rounding off the edges) of the structure can be achieved after drying, by tempering the wafer on a laboratory heating plate. The temperature is raised slowly from 100 °C to 140 °C within 5 minutes and then held at 140 °C for a further 5 minutes. After this

	step, the wafer is cooled slowly to room temperature. [Too fast cooling can cause crack formation in the resist layer.]
Removing of developed photoresist layers	Developed and undeveloped photoresist layers can be removed by placing the wafer in the remover (mr-Rem 700) solution. Alternatively, the photoresist residues can also be removed relatively well […] [using] acetone.
Disposal of photoresist residues, Developer and Remover	All liquid wastes can be added to the halogen-free organic solvent wastes. Solid photoresist residues as well as contaminated consumables can be disposed of via the laboratory waste for contaminated consumables.

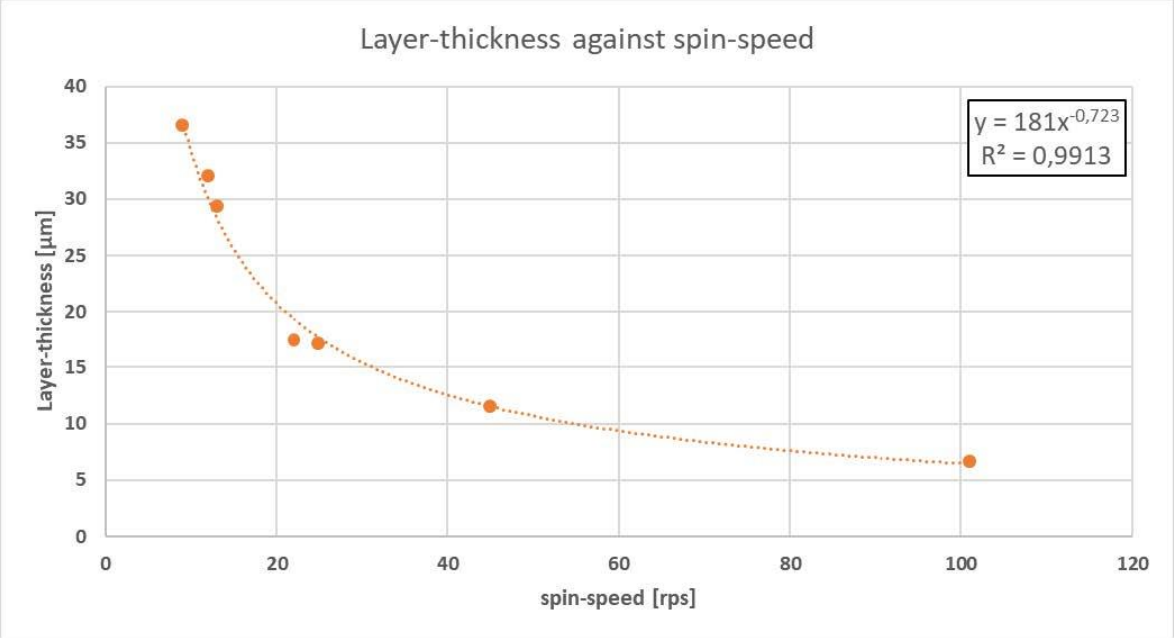

Figure 75 **Calibration curve of ma-P 1275 hv layer-thickness in dependency to spin-speed**.

Origin Note of Adipose-derived Stem Cells (ASCs)

The Cells were isolated from human tissue samples obtained from patients undergoing plastic surgery (Dr. Zieler; Klinik Charlottenhaus, Stuttgart, Germany).

The research was carried out following the rules for the investigation of human subjects as defined in the Declaration of Helsinki. All Patients provided written agreement in compliance with the Landesärztekammer Baden-Württemberg (F-2012- 078, for normal skin from elective surgeries).

Pseudo Code of ImageJ Plugin for the Correction of Microscopy Projection Bias

Pseusocode (by Michael Brunner, Curio Group, School for informatics, Reutlingen Universtiy) for projecting points from cylinder to plane (see Figure 10 A.):

for each *point* **in** *cell's outline ROI* **do**:

$s \leftarrow$ get distance from cylinder middle line/axis

intersection $\leftarrow$ get intersection of line through point with cylinder middle line

$\alpha \leftarrow$ degrees (arcsin (s / R))

$b \leftarrow (R \times \pi \times \alpha) / 180$

projected point $\leftarrow$ ((*point* – *intersection*) / $s \times b$) + *intersection*

The Adapted Code of ImageJ Plugin Called "DrawParticleEllipseAxis.txt"

```
run("Set Measurements...", " area mean centroid fit ");
 run("Analyze Particles...", "size=100 circularity=0 show=Nothing")
 run("RGB Color");
 for(i=0; i<nResults; i++) {
    x=getResult('X',i);
    y=getResult('Y',i);
    d=getResult('Major',i);
    a = getResult('Angle',i)*PI/180;
    setColor("red");
    drawLine(x+(d/2)*cos(a),y-(d/2)*sin(a),x-(d/2)*cos(a),y+(d/2)*sin(a));
 }
```

Part IV: Supplementary Material

Manufacturing and Roughness Testing of 3-D Printed Microlenses

The following paragraphs were part of the Master Thesis "Investigation of optical resonators made of different microlenses for application as a compact refractive index sensor" (original German title "Untersuchung von optischen Resonatoren aus verschiedenen Mikrolinsen für die Anwendung als kompakter Brechungsindexsensor") submitted by Janina Drews, in 2019 at the University of Tübingen, supervised by Prof. Dr. Marc Brecht and Achim Juninger. Parts of this thesis are currently in preparation for publication.
As indicated by the quotation marks, the description of the printing procedure, was directly translated into English by the author of the present work.

"Using the Photonic Professional GT (Nanoscribe GmbH) and the Software DeScribe and NanoWrite was used to generate microlenses. For high resolution Structures the photoresist IP-Dip was used in combination with a 63x objective (NA 1.4), which has a working range of 140 x 140 µm². Structures with a base area of 130 x 130 µm² were constructed using AutoCAD 2019 (Autodesk). The resulting document was processed using the DeScribe software applying the standard parameter for the Resist-Objective combination and only adjusting the slicing mode from fixed to adaptive, since this mode was developed especially for curved contours because id adapts the slicing distance to the slope (here ranging from 0.3 to 0.1 µm). The corresponding Hatching Distance was 0.2 µm, and for printing the structure all in one piece, the splitting mode was set to none. The Galvo-Modus (MBFS) was used as a writing mode.
Using the Nano-3-D-Printer, both convex and concave structures were printed: 3 µm high partial cylinders and spheres (radius 4 mm) were printed using the Fill Mode Solid due to the small size of the printed object. The concave partial spheres (radius 120 µm and 300 µm) were printed in16 µm high cuboids, leaving a distance of 5 µm from the lowest point of the partial sphere to the substrate. This low distance was realized using the Shell & Scaffold parameter as Fill Mode.
DeScribe processes the imported document in a layer-by-layer printing process, reducing the precision of printing curved surfaces. Therefore, the sphere or cylinder surface is post-processed after printing using the piezo printing mode (FBMS). […]
The print itself is conducted in Dip-in laser lithography (DiLL)-writing mode. ScanSpeed was set to 10 000 µm s^{-1}, laser power was 40% for convex spherical segments and 30% for concave partial spheres. "
Surface characterization using a multi-mode AFM was conducted as described in the Materials and Methods section of the present work. The determined RMS was 7.5 nm, the peak to valley

roughness value was 32.7 nm. Figure 76 shows an exemplary topography scan of the microlense, where the “routes of the laser focus of the 3-D printing process are clearly visible. The exemplary roughness profile also shows the concatenated voxels of the print.”

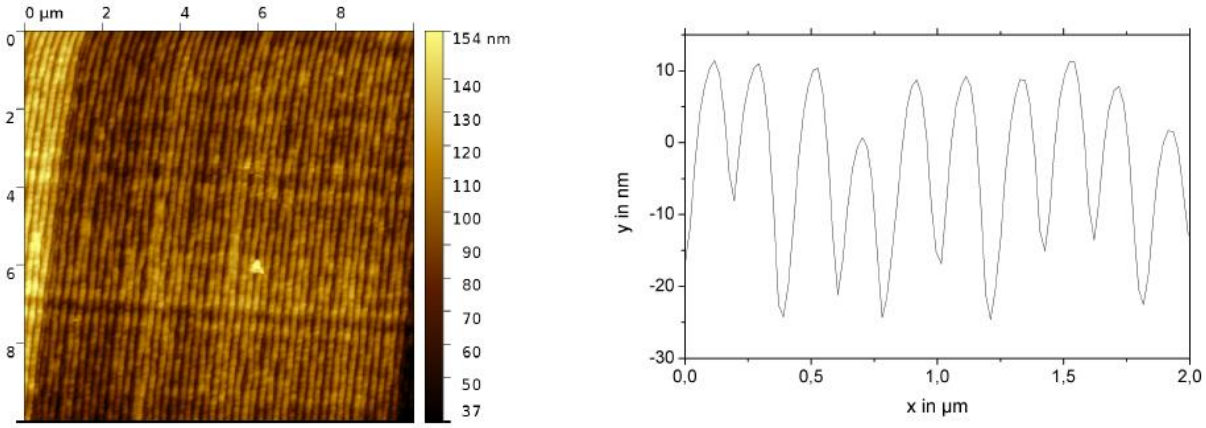

Figure 76 **AFM topography scan (left) and roughness profile (right) of a 3-D-printed microlense (radius= 4 mm)**

Part V: Supplementary Materials

List of Median Angles of Orientation of hdF1

Table 23 **Median angle of orientation ψ_{Med} of hdF1 cultivated in sparse cell densities on convex cylindrical topographies coated with FCS and with radii of curvature R as indicated.**

Radius of curvature R [µm]	**Cell Median Angle of Orientation ψ_{Med}** [°]
20.9	6.3
59.3	6.8
76	10.7
110.2	19.4
118	9.0
129.4	14.2
142.5	15.8
154.2	16.1
160	18.0
213.2	15.4
255	23.6
312	29.0
flat	47.5

Correlation of Cell and Nucleus Orientation without Pharmacological Manipulation

The heatmaps illustrate the correlation of cell and nucleus orientation of hdF without pharmacological manipulation (Pearson correlation coefficients Table 24) by plotting the corresponding angle of orientation. Taking a further look at the heatmap of R= 59.3 µm, it indicates why the Pearson correlation coefficient in this case seems to be so low, nuclei and cells are aligned but the distribution of the orientation angles cluster in the area of 0° to 25°.

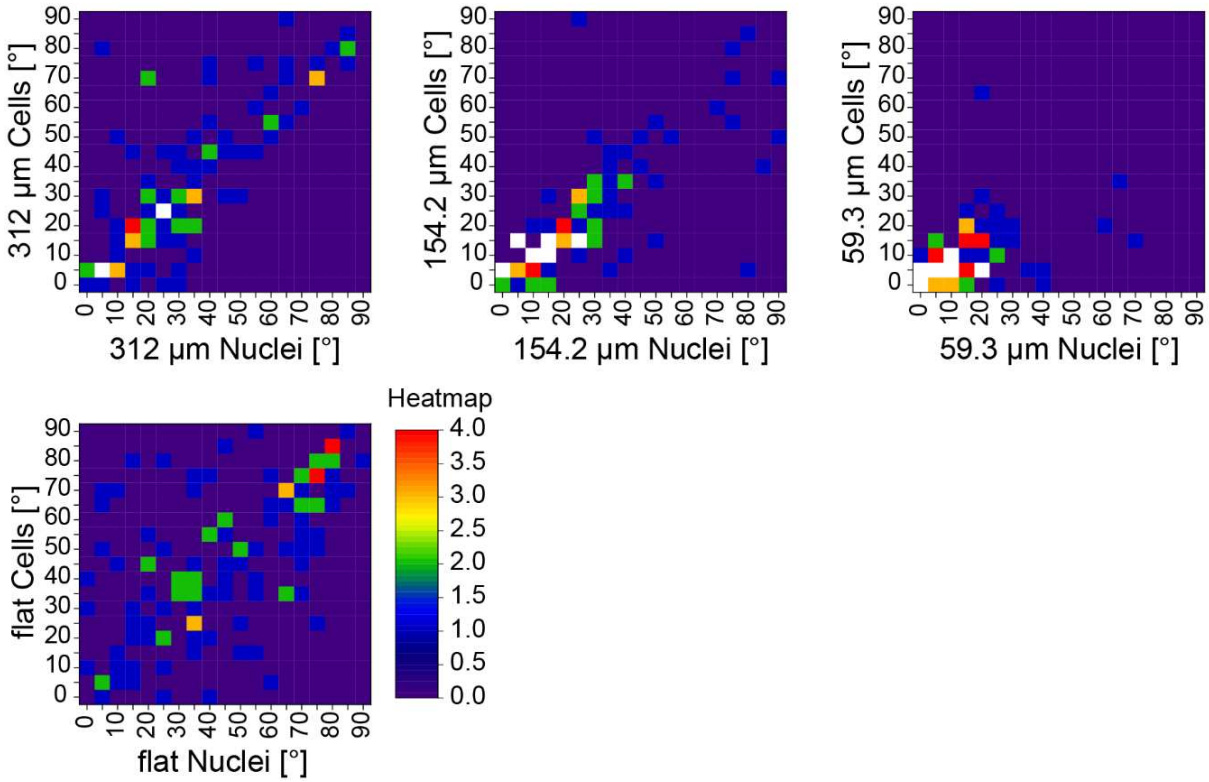

Figure 77 **Correlation of cell and nucleus orientation displayed as heatmaps.** The heatmap indicates the quantity, with red 4 counts, higher counts marked in white, and dark purple indicating 0 counts, group size is 5°. Pearson correlation coefficients as follows: flat: 0.60142; R= 312 µm: 0.78924; R= 154.2 µm: 0.76028; R= 59.3 µm: 0.4115. Note: Angle of orientation for cells on flat PDMS is measured in relation to an imaginary axis. *Adapted from (1)*

Table 24 **Pearson correlation coefficients of correlation of cell and nucleus orientation on cylindrically curved substrates with varying radius of curvature.** Adapted from (*1*)

Radius of curvature R [µm]	**Pearson correlation coefficient**
59.3	0.41155
154.2	0.76028
312	0.78924
flat	0.60142

Larger fluorescence images of pharmacologically manipulated hdF1 (cf. Figure 25, p.87)

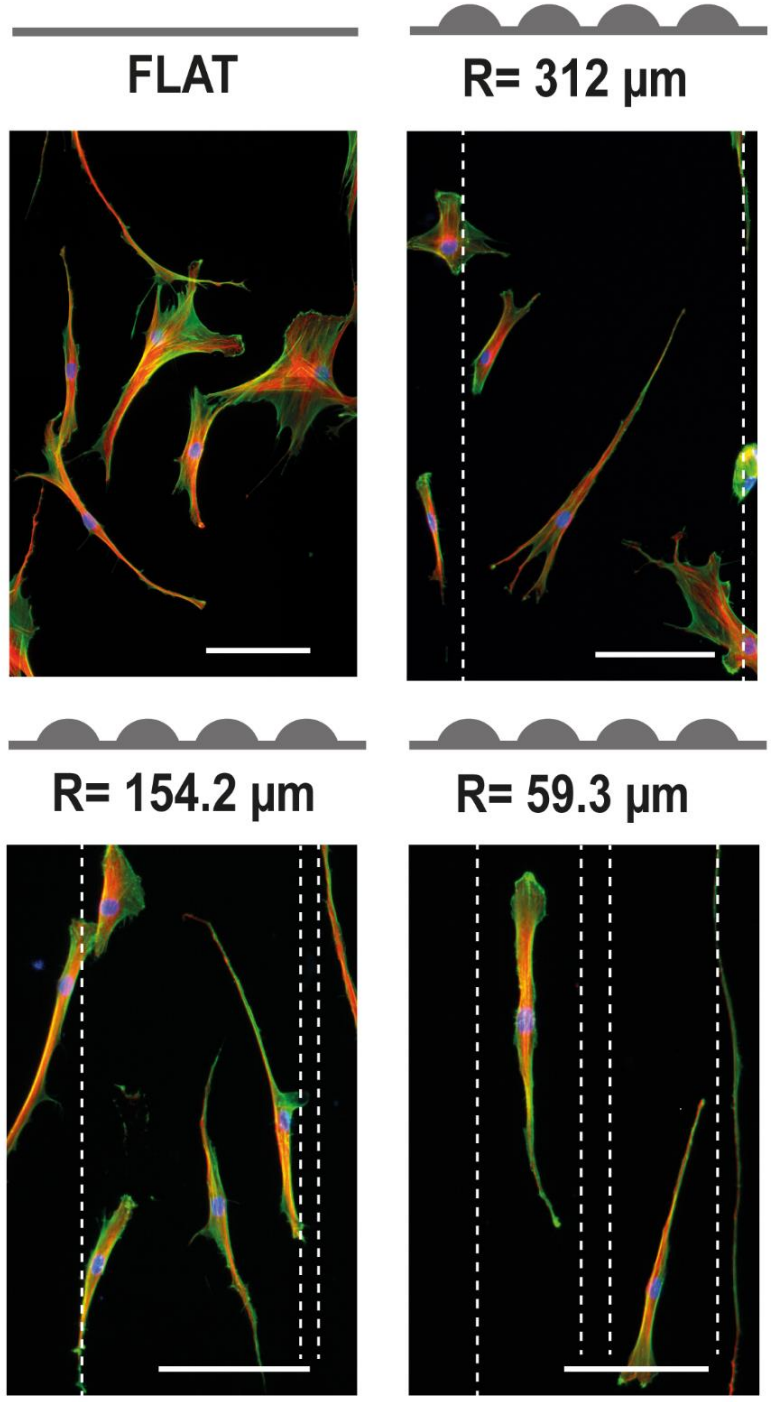

Figure 78 **Fluorescence images of hdF1 on different CurvChip substrates with cylindrical topographies and flat PDMS, all coated with FCS without pharmacological manipulation.** F-actin in green, nuclei blue and microtubule in red. The dashed lines indicate topography boundaries. Scale bars 100 µm

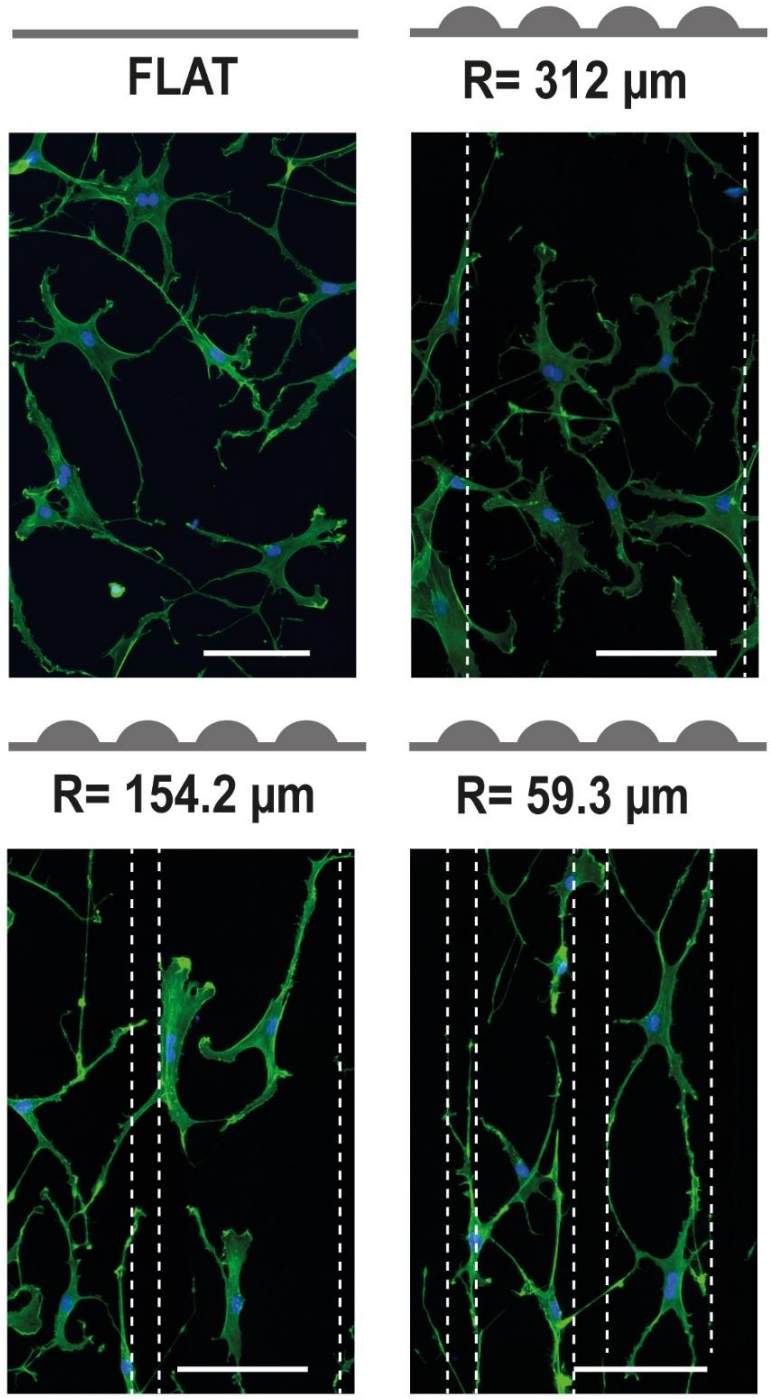

Figure 79 **Fluorescence images of Blebbistatin-treated hdF1 on different CurvChip substrates with cylindrical topographies and flat PDMS, all coated with FCS.** F-actin in green, nuclei blue. The dashed lines indicate topography boundaries. Scale bars 100 µm

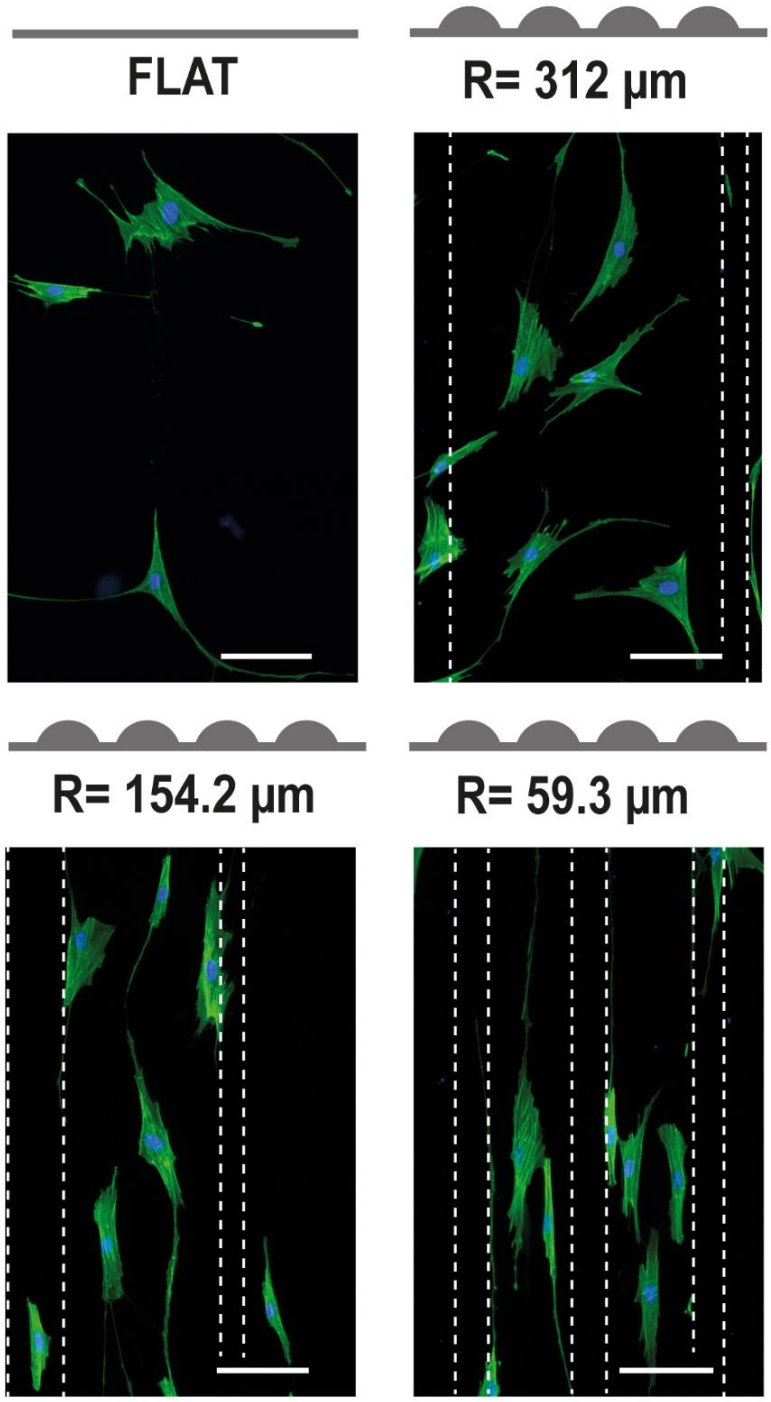

Figure 80 **Fluorescence images of CN03-treated hdF1 on different CurvChip substrates with cylindrical topographies and flat PDMS, all coated with FCS. FCS.** F-actin in green, nuclei blue. The dashed lines indicate topography boundaries. Scale bars 100 µm

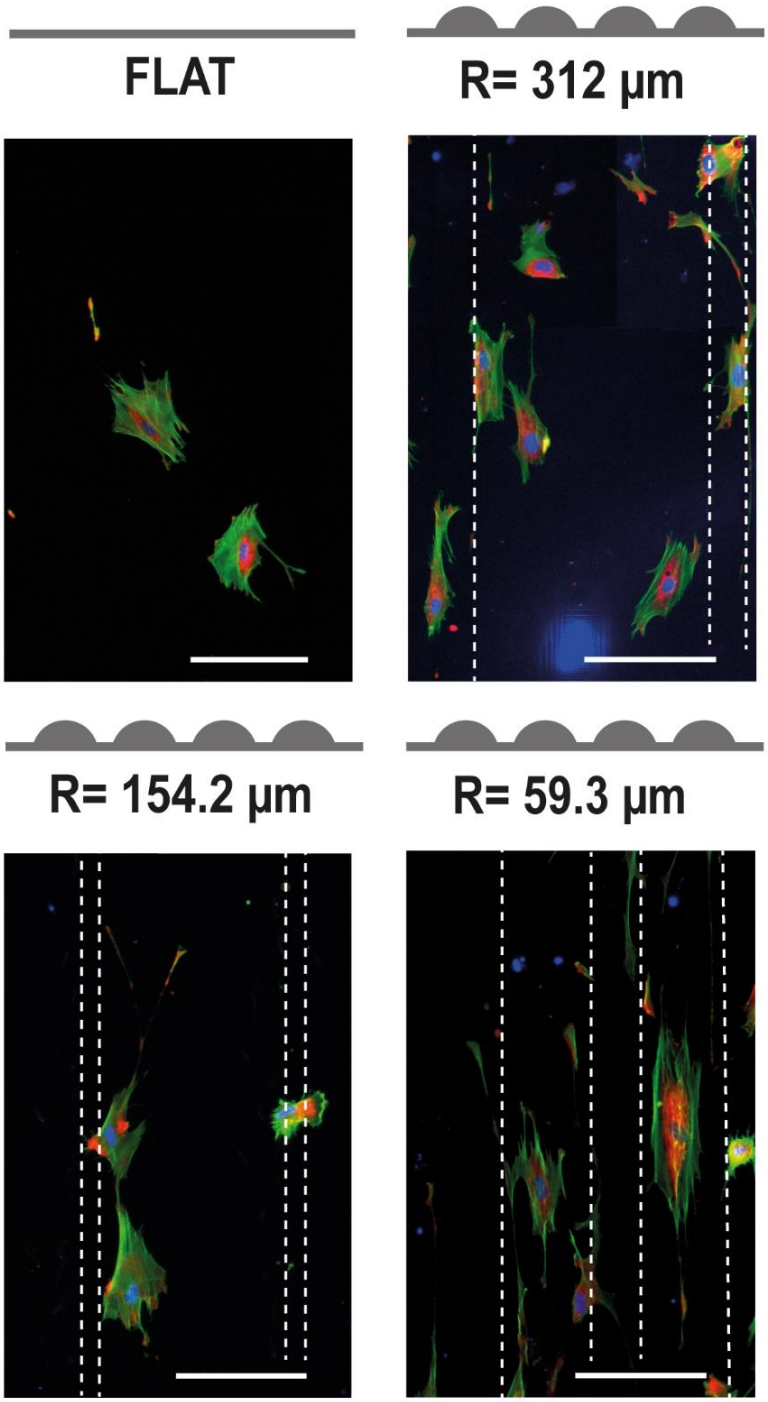

Figure 81 **Fluorescence images of Nocodazole-treated hdF1 on different CurvChip substrates with cylindrical topographies and flat PDMS, all coated with FCS.** F-actin in green, nuclei blue and microtubule in red. The dashed lines indicate topography boundaries. Scale bars 100 µm

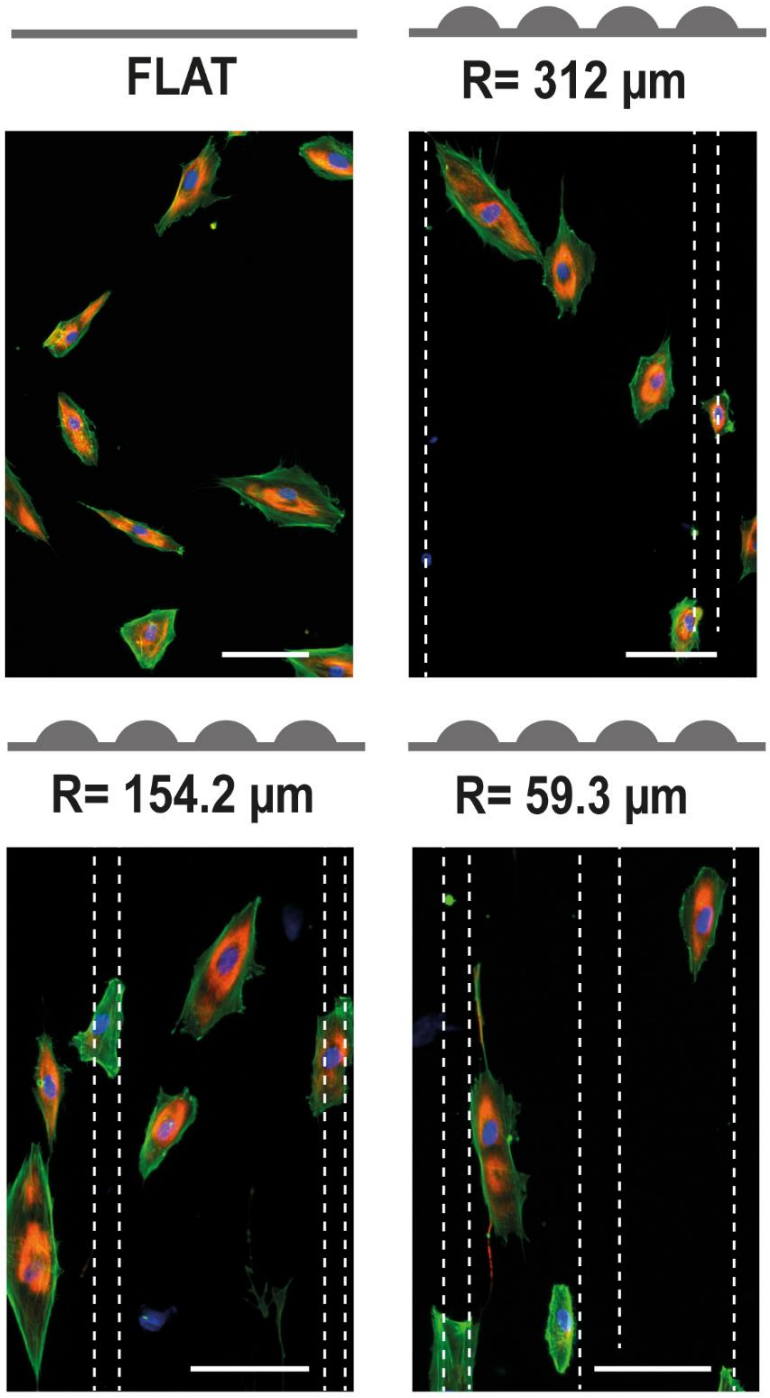

Figure 82 **Fluorescence images of Taxol-treated hdF1 on different CurvChip substrates with cylindrical topographies and flat PDMS, all coated with FCS.** F-actin in green, nuclei blue and microtubule in red. The dashed lines indicate topography boundaries. Scale bars 100 µm

Dose Response Relationship for Curvature κ

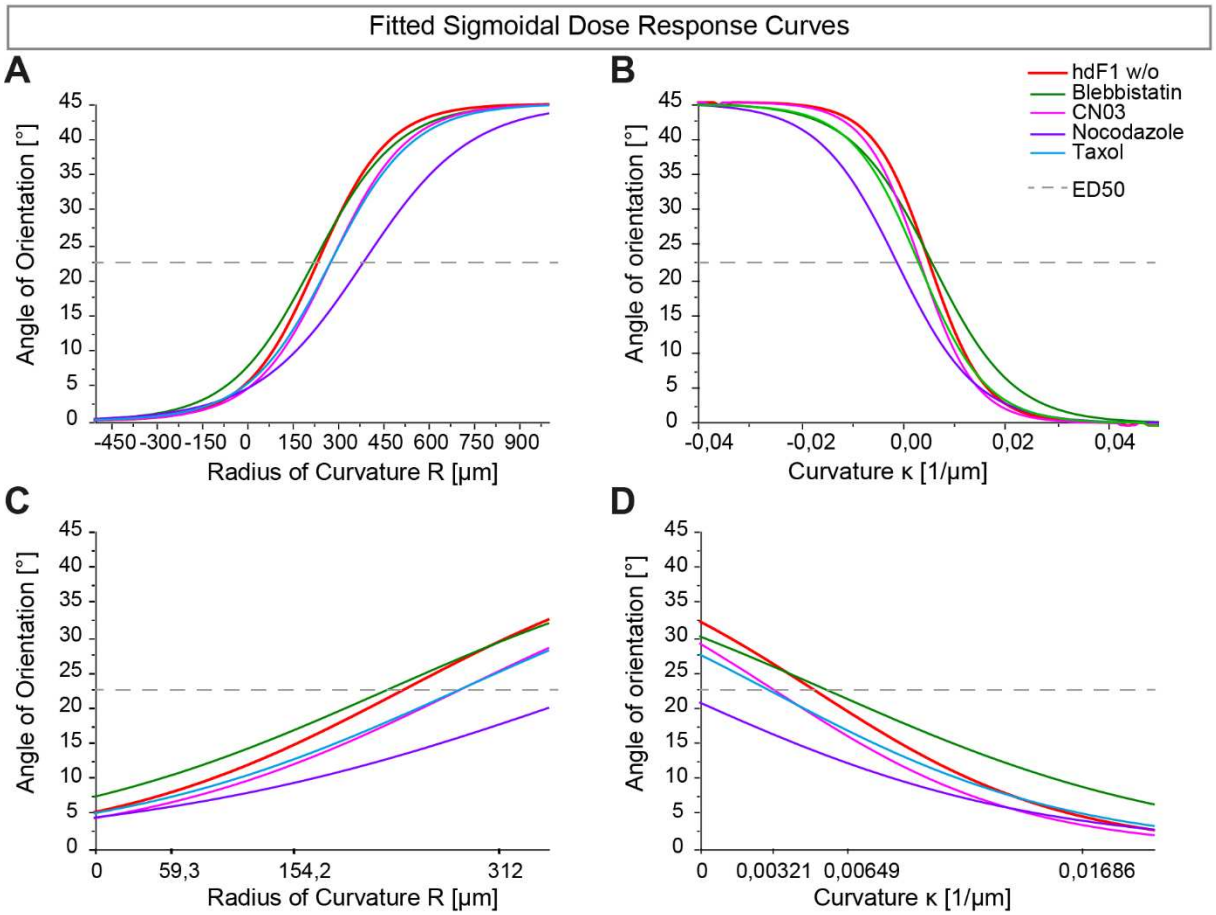

Figure 83 **Cell response to curved surfaces with increasing radii of curvature and with and without pharmacological manipulation displayed as dose response relationships in dependence on either the radius of curvature R (A and C) or curvature κ (B and D) of the underlying substrate with cylindrical topographies.** ***A-D*** Sigmoidal Dose Response fits to median Angles of orientation, with upper boundary set to 45° (random orientation) and lower boundary 0° (perfect alignment). ***A*** and ***B*** show the whole curves, ***C*** and ***D*** show relevant sections. Colors represent different conditions as indicated in upper right corner. Intersection with 22.5° dotted line represents half maximal effective dose ED50. Please note, for purposes of better visualization the data points of ψ_{Med} and k_{Med} are not included in the fitted graphs.

Table 25 **Goodness of fit for dose response relationships (Curvature-Orientation-Relationship) with varying presentation of the dose**.

Condition	adjusted R^2		
	Linear Fit Ψ/Radius of curvature	**Sigmoidal Fit** Ψ/Radius of curvature	**Sigmoidal fit** Ψ/Curvature
hdF1^{all}	0.78521	0.77582	0.60377
hdF1 w/o	0.99375	0.97199	0.80717
Blebbistatin	0.99461	0.99999	0.62809
CN03	0.99465	0.99393	0.72885
Nocodazole	0.97769	0.93256	0.87903
Taxol	0.99293	0.99939	0.65929

Comparison of Results for Varying Protein coatings with Pharmacological Manipulation

1. Cell and Nucleus Angle of Orientation on Cylindrical Convex Substrates

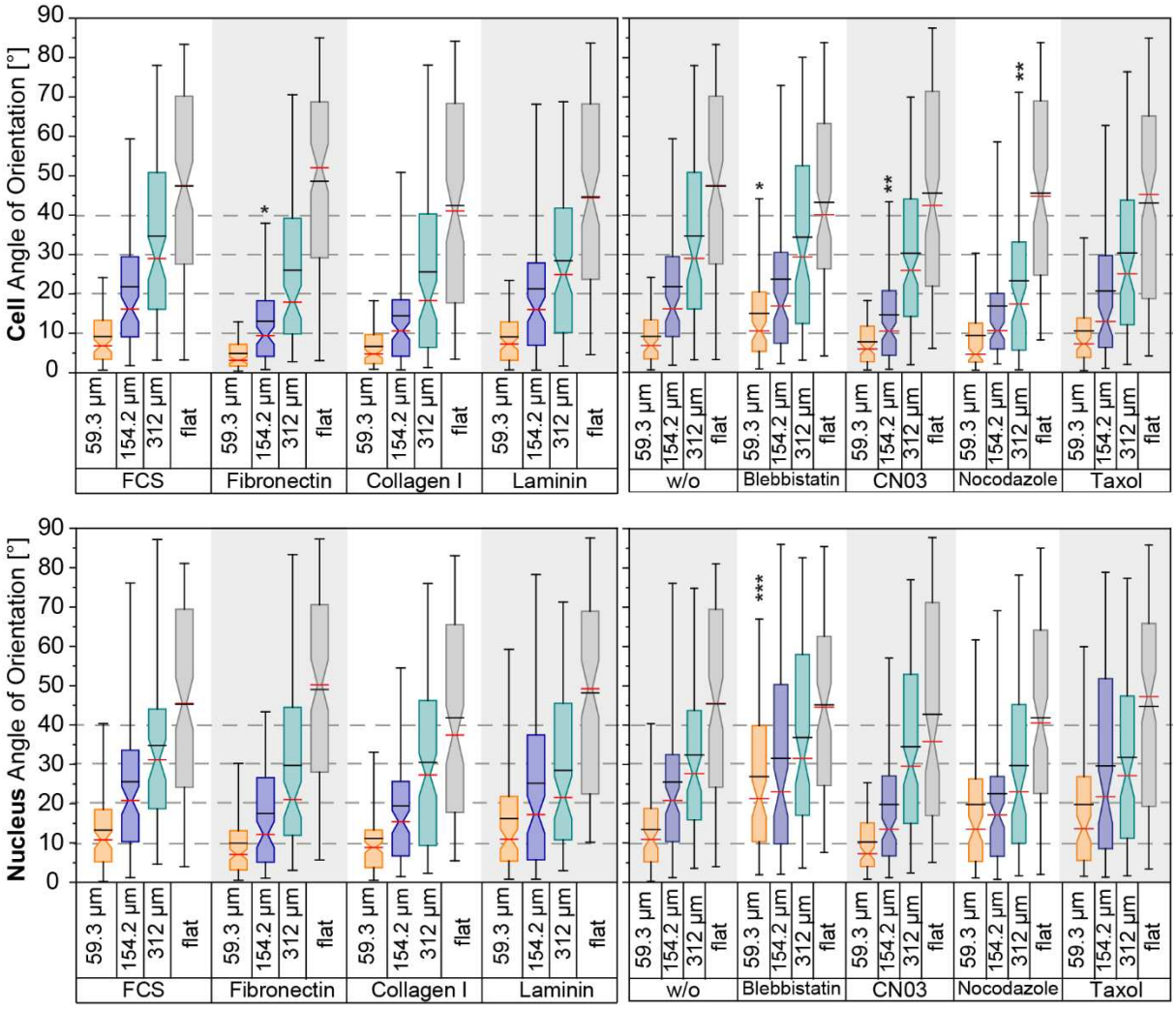

Figure 84 **Comparison of cell and nucleus angle of orientation on cylindrical substrates with varying curvatures and different protein coatings and pharmacological manipulation.** Notched box plots Boxes showing the 25th and 75th percentiles, the red lines indicate the median and the black lines display the mean, whisker show the 5th and 95th percentile range. Sample size cell/nucleus n_{FCS}= 100-118/95-117; $n_{Fibronectin}$=104-129 /104-129; $n_{Collagen\ i}$= 110-131/106-116; $n_{Laminin}$=100-111/100-111; sample size for pharmacological manipulation (always FCS-coating): $n_{w/o}$= 100-118/95-117; $n_{Blebbistatin}$= 99-110/98-110; n_{CN03}= 115-171/115-171; $n_{Nocodazole}$= 101-104/98-101; n_{Taxol}= 100-131/100-131; Note: FCS and w/o is the same dataset. Dashed lines are added to simplify comparison and are displayed at 10°, 20°, 30° and 40°. * Significant ($p< 0.05$), ** highly significant ($p<0.005$), *** most significant ($p<0.001$) to w/o or as indicated; ns not significant ($p> 0.05$) as indicated; Kruskal-Wallis with Dunn's post-hoc test.

2. Morphological Adaptions

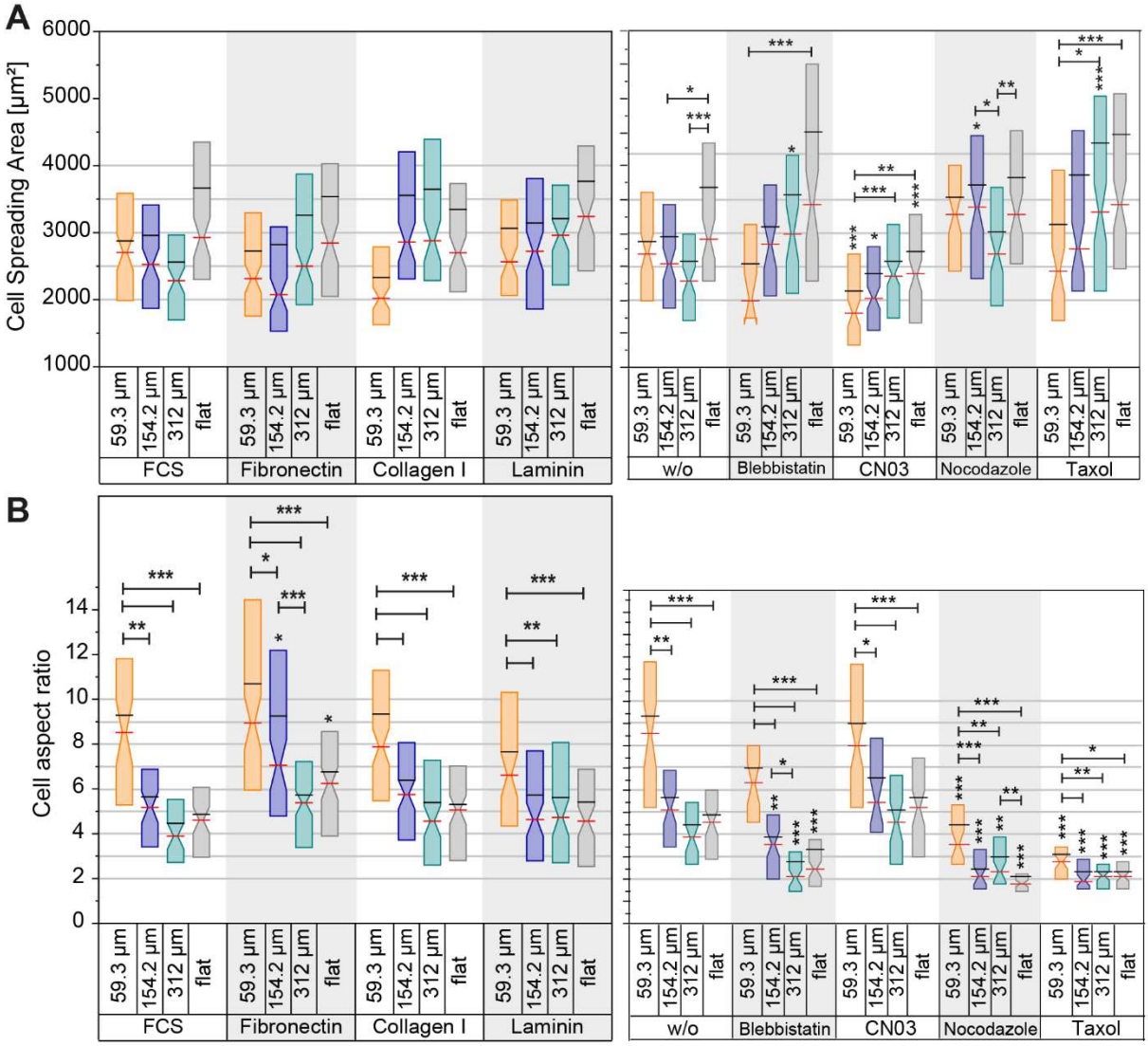

Figure 85 **Adaption of cell morphology, comparison between the effects of substratum coatings and pharmacological manipulation of the cytoskeleton**. ***A*** Cell spreading area (A_{CELL}) corrected for projection bias and ***B*** Cell Aspect ratio (AR), corrected for projection bias. Aspect ratio= Major axis/Minor axis. w/o indicates hdF1 without pharmacological treatment on FCS-coating. Boxes display 25th and 75th percentiles, the red lines the medians, and the black line the mean. * ($p<0.05$) significant, ** ($p<0.005$) highly significant, *** ($p<0.001$) most significant to w/o; * significant ($p<0.05$), ** ($p<0,005$) highly significant, *** ($p<0.001$) most significant as indicated; ns not significant ($p>0.05$) as indicated; Kruskal-Wallis with Dunn's post-hoc test. Sample size: n_{FCS}= 88-118; $n_{Fibronectin}$=102-129; $n_{Collagen\ i}$= 106-130; $n_{Laminin}$=91-111; Sample size for pharmacological manipulation (always FCS-coating): $n_{w/o}$= 84-118; $n_{Blebbistatin}$=33-99; n_{CN03}=114-171; $n_{Nocodazole}$=77-104; n_{Taxol}=100-131; Sample size aspect ratio: $n_{w/o}$= 49-69; $n_{Blebbistatin}$= 34-82; n_{CN03}= 45-88; $n_{Nocodazole}$= 45-68; n_{Taxol}= 54-81

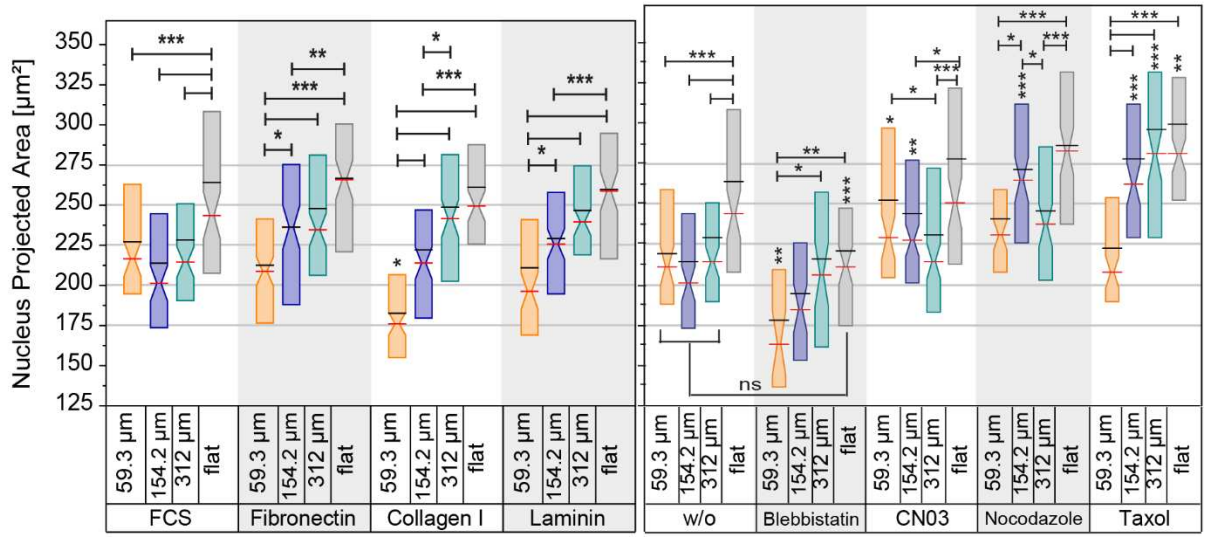

Figure 86 **Nucleus Projected Area comparison between the effects of substratum coatings and pharmacological manipulation of the cytoskeleton**. Notched Box plots of Nuclei Area (A_{NUC}), corrected for projection bias. w/o indicates hdF1 without pharmacological treatment. Boxes display 25th and 75th percentiles, the red lines the medians, and the black line the mean. * ($p<0.05$) significant, ** ($p<0.005$) highly significant, *** ($p<0.001$) most significant to w/o; * significant ($p<0.05$), ** ($p<0,005$) highly significant, *** ($p<0.001$) most significant as indicated; ns not significant ($p>0.05$) as indicated; Kruskal-Wallis with Dunn's post-hoc test. Sample size range n_{FCS}= 88-118; $n_{Fibronectin}$=102-129; $n_{Collagen\ i}$= 106-130; $n_{Laminin}$=91-111; Sample size range for pharmacological manipulation (always FCS-coating): $n_{w/o}$= 84-118; $n_{Blebbistatin}$=33-99; n_{CN03}=114-171; $n_{Nocodazole}$=77-104; n_{Taxol}=100-131;

Nucleus Projected Area: Donor and Density Variation

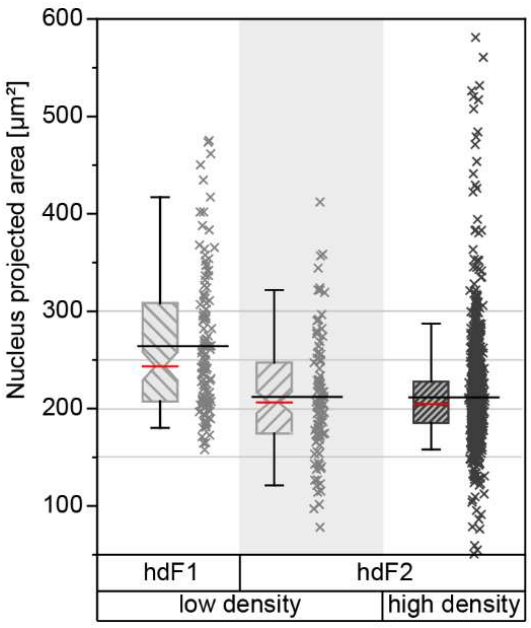

Figure 87 **Comparison of nucleus projected area on flat PDMS of varying donor, cultivation density and protein coating**. Median/IQR: hdF1 (243.5 µm²/100.8 µm²) and hdF2 (206.3 µm²/72.8 µm²) in low density on FCS, hdF2 (204.6 µm²/42.4 µm²) in high density on fibronectin.

Notched Box plots with datapoints. Boxes display 25th and 75th percentiles, the red lines the medians, and the black line the mean. Sample sizes hdF1: n=118; hdF2: n_{LD}=106; n_{HD}=467.

Nucleus Density on flat PDMS with Varying Coatings

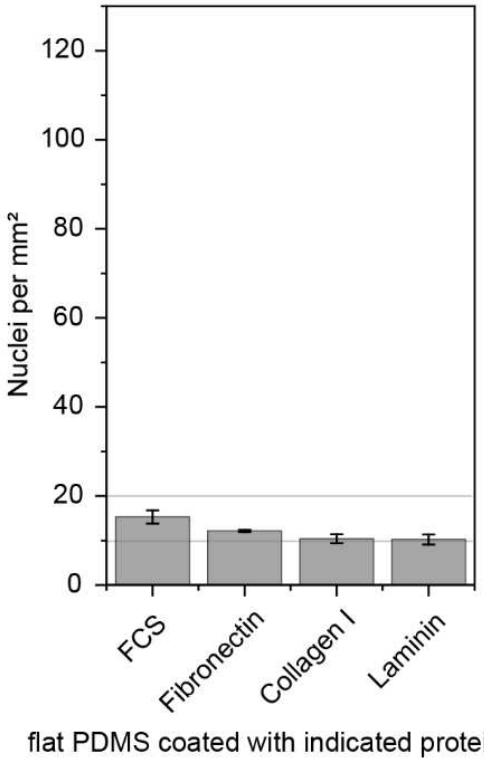

Figure 88 **Nucleus density of sparsely growing hdF1 on flat PDMS coated with different proteins.** Mean ±SE. Sample size n_{FCS}=174; n_{FN}=234; n_{COL}=199; n_{LAM}=197. All not significantly different from each other ($p>0.05$, ANOVA with Dunn-Sidak post-hoc test).

Percentage of Nuclei on Different Areas of Cylindrical Substrates with Varying Radius of Curvature and Coating

Pieuchot et al. (*120*) present their data normalized to total nucleus number (% of nuclei), which is feasible, since the substrate areas are comparable in size for their sinusoidal topographies, and a higher percentage of cells in an area can be considered equal to a higher density. However, for the cylindrical CurvChip surfaces with narrow spacing the difference between the curved regions and flat regions between the cylinders is high, which was considered and, therefore, data is displayed as nucleus density in the present work. For reasons of completeness the results of the present work, displayed as a percentage of total nucleus number, are given in Figure 89 shows, disregarding the differences in surface area between the curved substrate areas “curv” and the narrow (25 µm wide) areas between the cylinders “btw”. (curv/btw: R=312 µm: 13, R=154.2 µm: 8, R=59.3 µm: 4).

hdF on FCS-coated surfaces do not seem to prefer narrow areas between the cylinders over curved areas, as described previously. Furthermore, for fibronectin-, collagen I- and laminin-coatings this trend seems to be reversed, which is a direct result of neglecting the difference in surface area. Additionally, structure height only seems to be a limiting factor for fibronectin-coating, all other coatings seem show a clear dependency from radius of curvature.

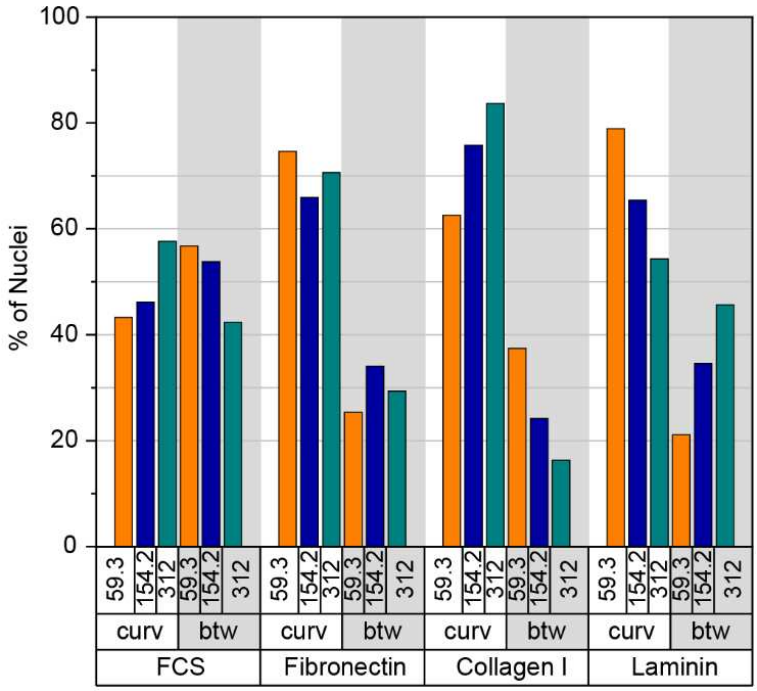

Figure 89 **Positioning of nuclei on different surface areas of cylindrical CurvChip substrates with varying radius of curvature R and protein coating, normalized to nucleus count (% of Nuclei).** R≙h: 59.3 µm≙24.2 µm; 312 µm≙35.3 µm; 154.2 µm≙40.2 µm. Sample sizes FCS: $n_{59.3\,\mu m}$= 443; $n_{154.4\,\mu m}$= 416; $n_{312\,\mu m}$= 390. FN $n_{59.3\,\mu m}$= 402; $n_{154.4\,\mu m}$= 279; $n_{312\,\mu m}$= 276. Col I: $n_{59.3\,\mu m}$= 457; $n_{154.4\,\mu m}$= 153; $n_{312\,\mu m}$= 178, Laminin $n_{59.3\,\mu m}$= 208; $n_{154.4\,\mu m}$= 240; $n_{312\,\mu m}$= 199.

Part VI: Supplementary Materials

Topography metrics

Table 26 **Metrics of spherical topographies of the CurvChip.** R: radius of curvature, h: structure height or depth, r: radius of base structure, $a_{0.5}$: half arc length, R:h: measure of rim curvature, R:r: ratio of R to r

R	**h**	**r**	**$a_{0.5}$**	**R : h**	**R : r**
318.6	47.9	188,7	202.0	6.7	1.7
193.2	44.1	137.7	153.3	4.4	1.4
134.0	6.8	51.0	51.3	19.7	2.6
62.7	19.8	48.6	55.6	3.2	1.3

Z-stack Sequences and Projection-Images

A431 cells

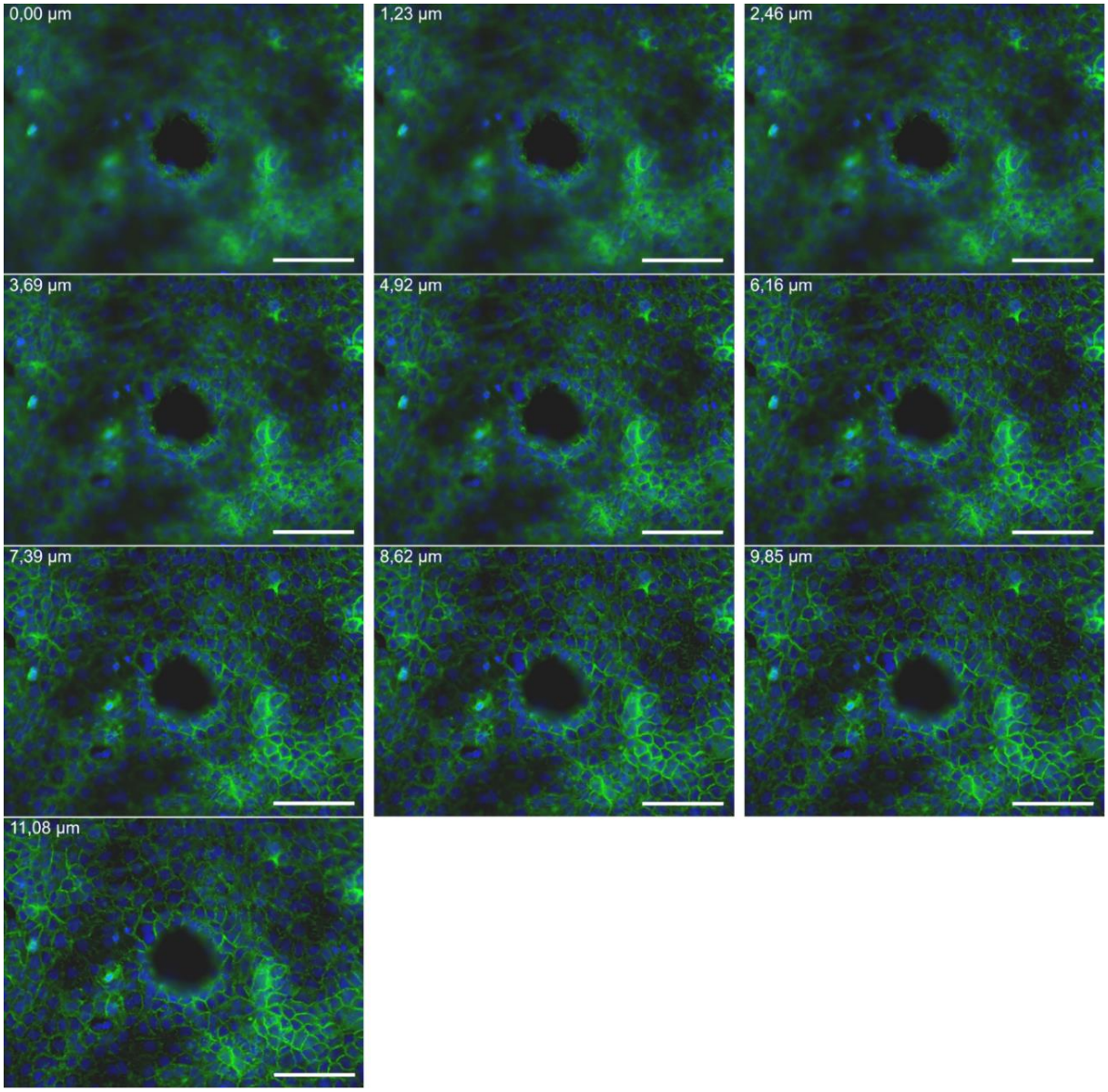

Figure 90 **Section from z-stack sequence of A431 on R=62.7 µm spherical topography.** Nuclei are displayed in blue, f-actin in green. Numbers in upper left corner of each image indicate the relative z-position. Scale bar 100 µm

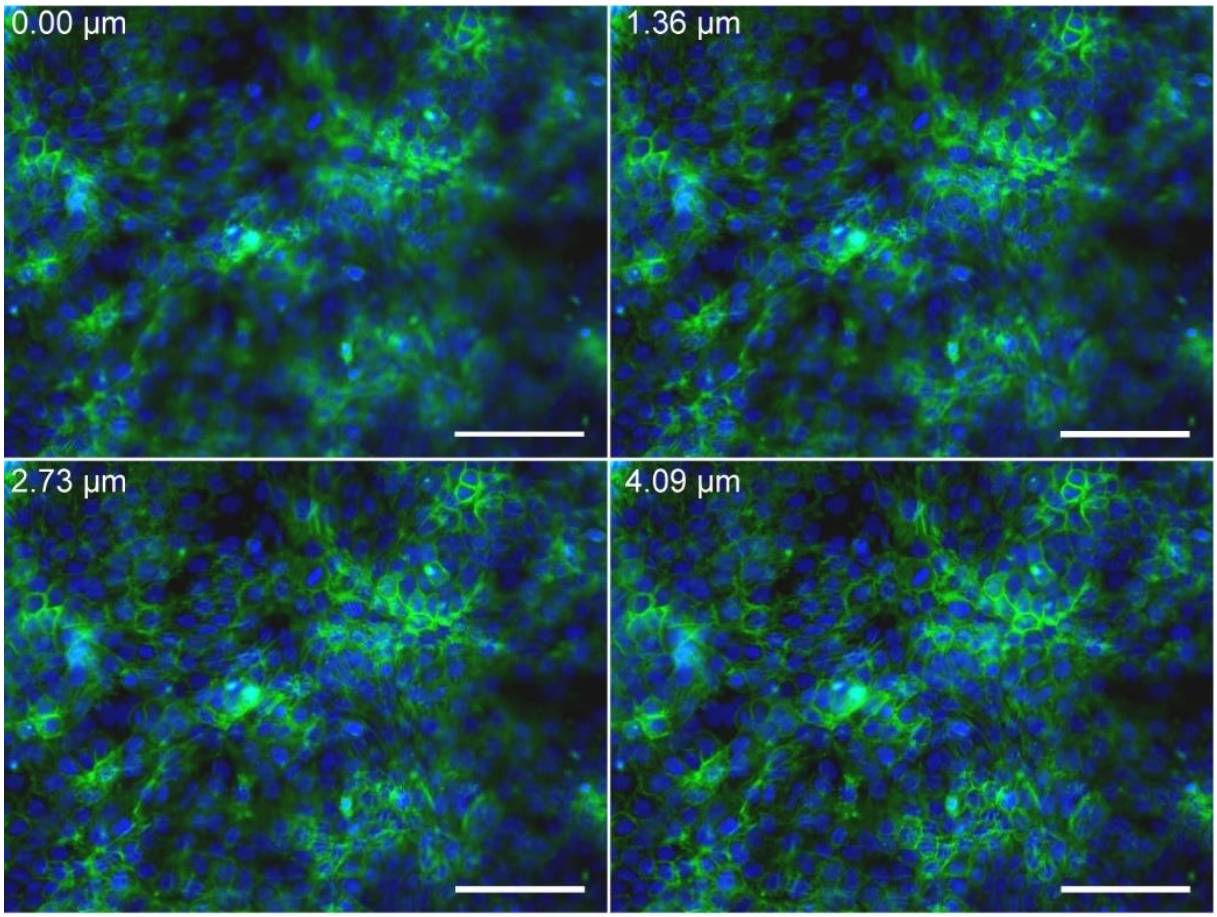

Figure 91 **Sequence from z-stack sequence of A431 on flat PDMS.** Nuclei are displayed in blue, f-actin in green. Numbers in upper left corner of each image indicate the relative z-position of the image, while the whole z-stack covered a depth of 6.5 µm over a total of 20 images. Scale bar 100 µm

MDCK Cells

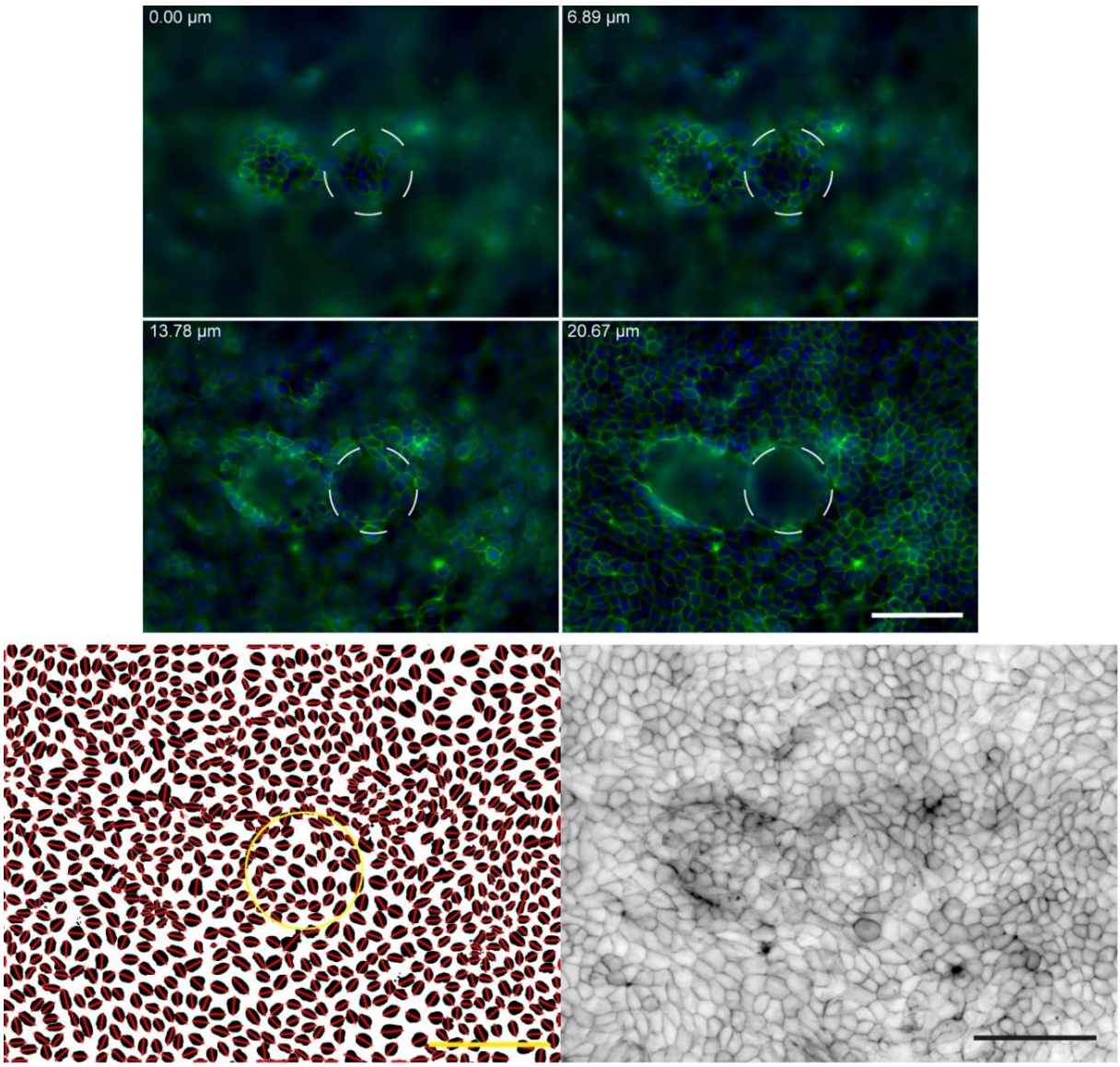

Figure 92 **Section from z-stack sequence of MDCK on R=62.7 µm spherical topography and corresponding nucleus image with indicated major axis.** In multi-channel images nuclei are displayed in blue, f-actin in green. Numbers in upper left corner of each image indicate the relative z-position. Scale bar 100 µm

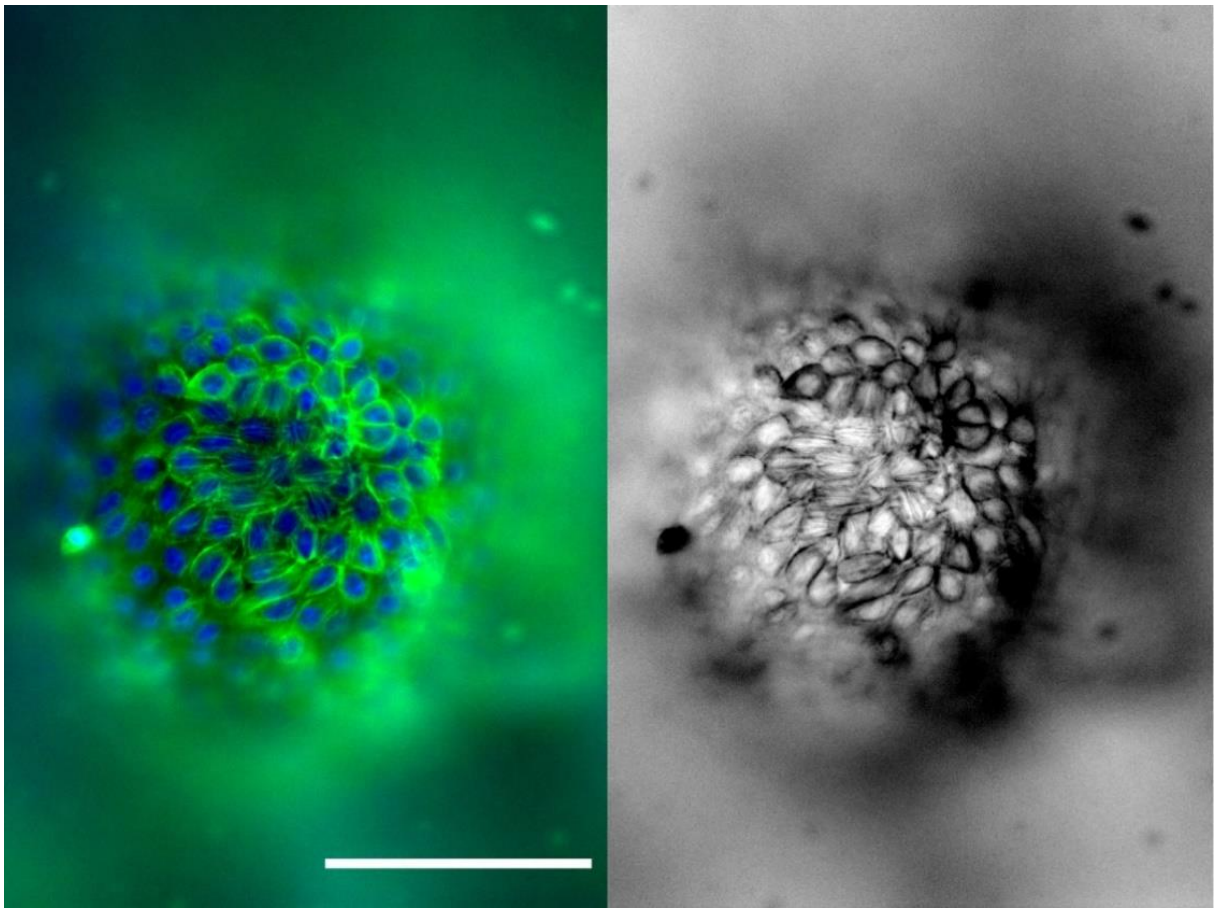

Figure 93 **Single z-slice of MDCK cells on substrate with R=194.2 µm micro-spherical segments.** (left) nuclei in blue, f-actin in green; (right) for better visualization f-actin channel inverted; Both images nicely show prominent central stress fibers additional to always visible cortical f-actin ring in cell periphery. Scale bar 100 µm

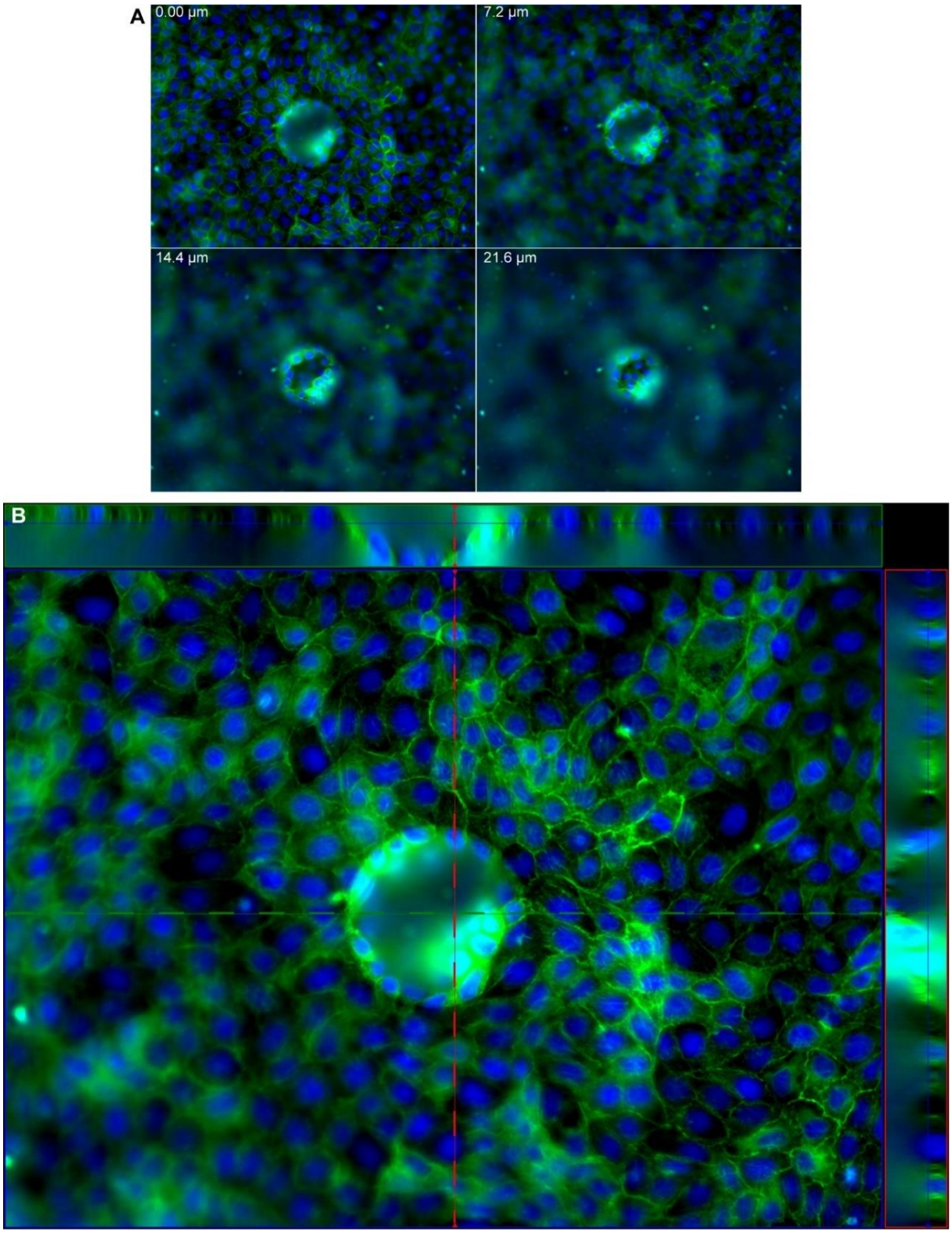

Figure 94 **Fluorescence z-stack sequence** *(A)* **and xy-/xz-/yz-projections** *(B)* **of MDCK on concave micro-spherical segment.** Nuclei are displayed in blue, f-actin in green. Corresponding processed image (extended depth of focus) shown in Figure 67 (p. 182) ***A*** z-stack sequence, numbers in upper left corner of each image indicate the relative z-position. ***B*** dashed green line indicates position of xz-projection shown in top row in green box, red, dashed line indicates position of yz-projection visualized

on right side in red box. Central image is xy-projection of approximately the same z-height like picture one (0.00 µm) in (A). Position is indicated by blue lines in xz- and yz-projections.

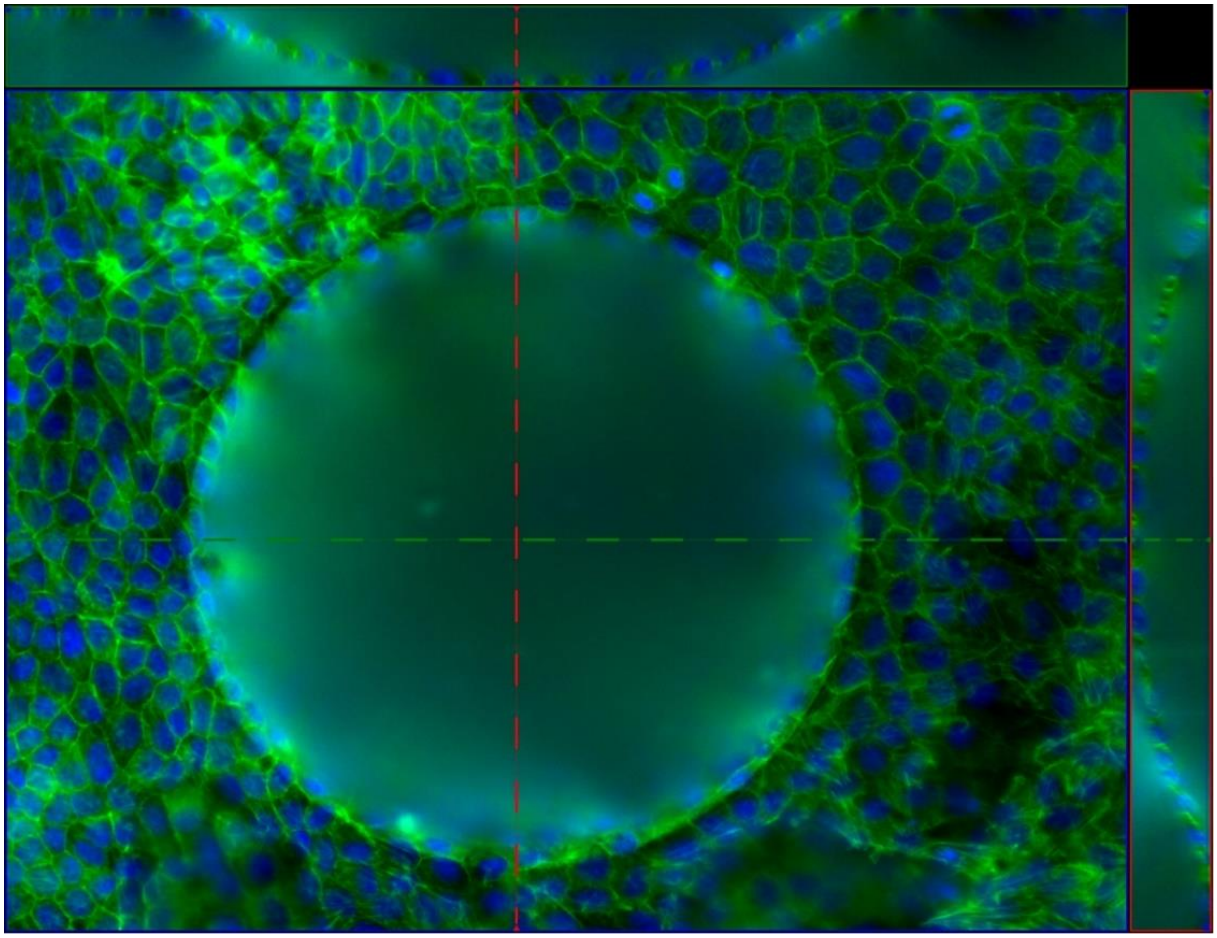

Figure 95 **xy-/xz-/yz-projections (B) of MDCK on concave micro-spherical segment with R=193.2 µm.** Nuclei are displayed in blue, f-actin in green. Corresponding processed image (extended depth of focus) shown in Figure 69 B (p. 185). Dashed green line indicates position of xz-projection shown in top row in green box, red, dashed line indicates position of yz-projection visualized on right side in red box.

F-actin Transitioning Quasi Convex Edge of Concave R=193.2 µm Micro-spherical Segment

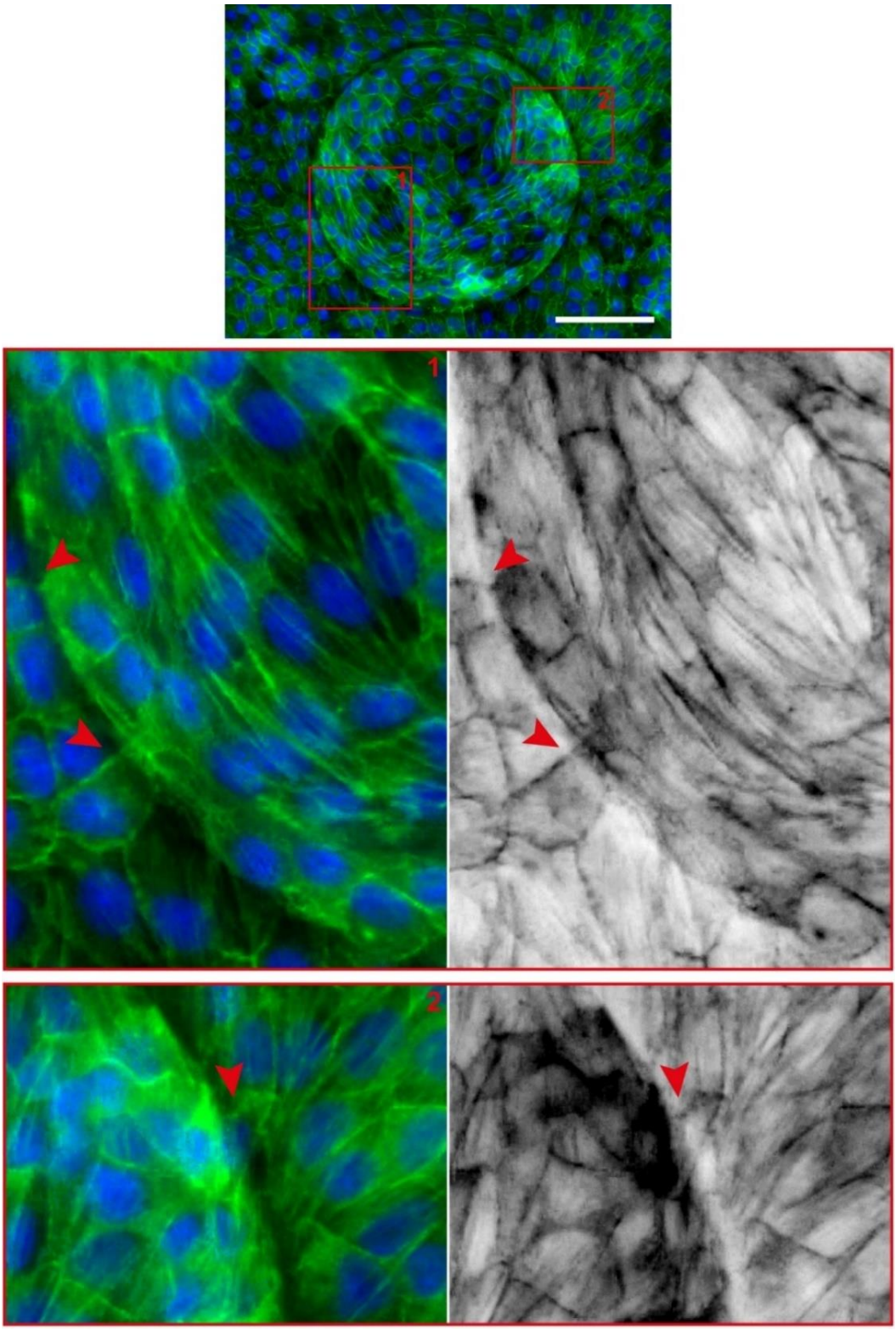

Figure **96 f-actin of MDCK cells spanning the quasi-convex transition zone from flat to concave R=193.2 µm micro-spherical segments.** Fluorescence images in color merged image displaying f-actin in green and nuclei in blue, inverted grey-scale images displaying f-actin. Scale 100 µm

3-D surface Graphs of How Micro-spherical Topography Height and Radius Affect Cell Density

Caution: median color scaling varies between different conditions (convex/concave, A431 cells/MDCK cells).

Surface areas as illustrated in Figure 11, p. 51: the inner curvature (I), defined by the projected area of the topography basis radius r subtracted by 10 %; is the transition zone (II), comprising the area where the flat structure and the curved micro-spherical topography meet, therefore, it is composed of the curved region remaining after subtraction of the inner curved area, as well as a ring surrounding the microstructure with the radius of the topography basis r plus 20 µm; the third region (III), described as flat PDMS between the microstructures.

A431 Cells on Substrates with Convex Micro-spherical Segments

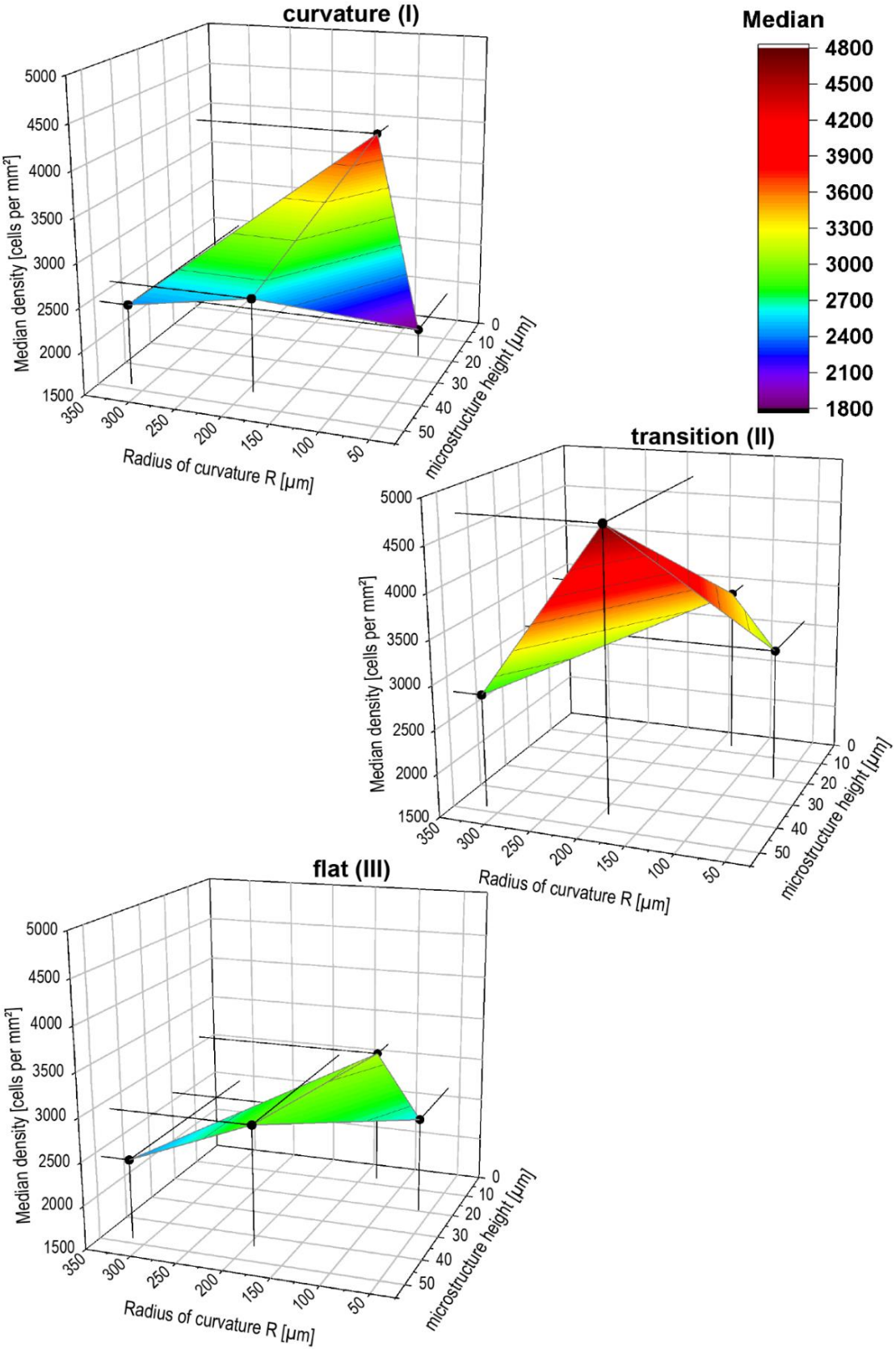

Figure 97 **Median density of A431 cells dependent on microsphere radius of curvature R and structure height h on substrates with convex micro-spherical topographies.** Color code as indicated.

MDCK Cells on Substrates with Convex Micro-spherical Segments

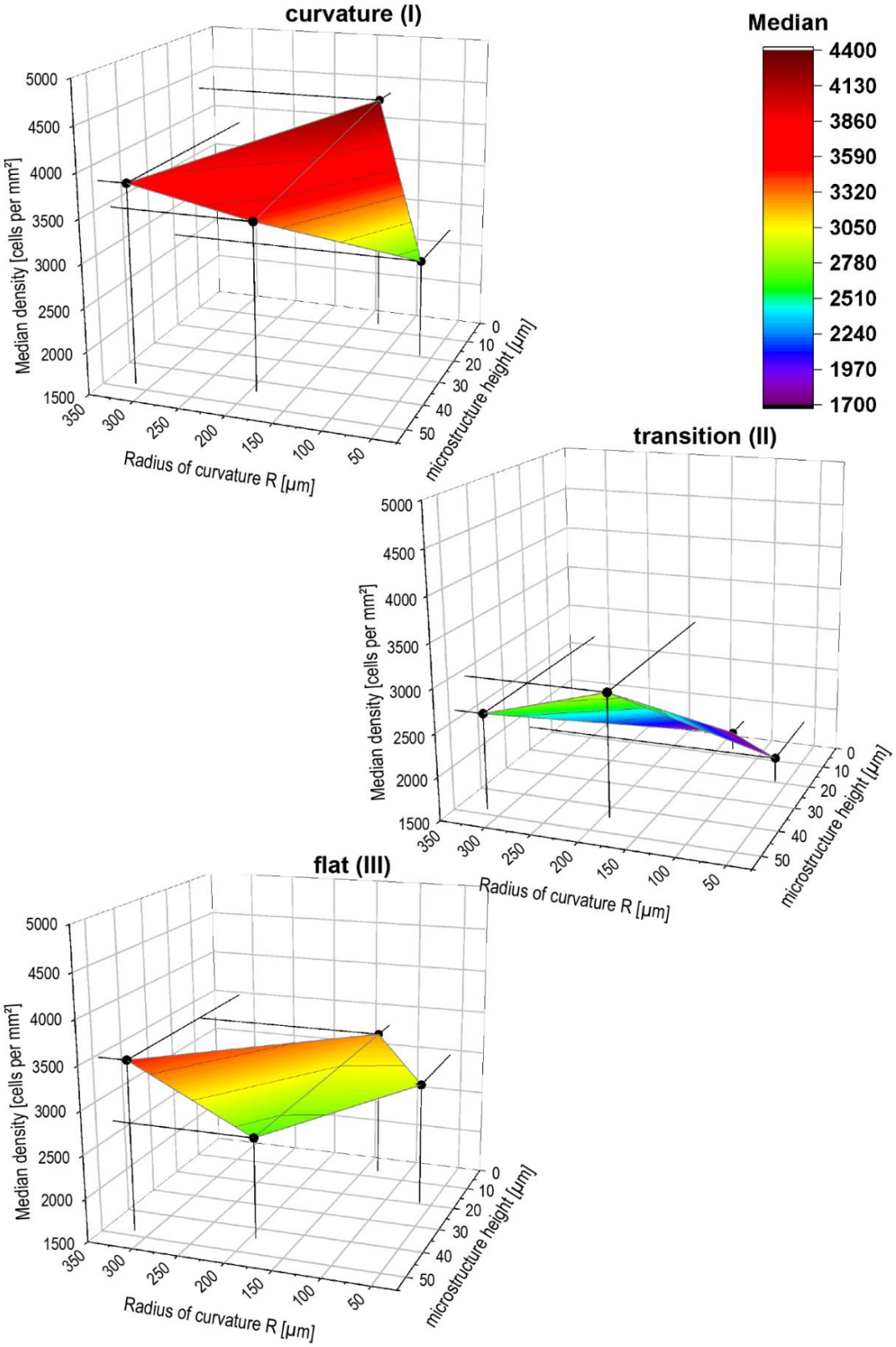

Figure 98 **Median density of MDCK cells dependent on microsphere radius of curvature R and structure height h on substrates with convex micro-spherical topographies**. Color code as indicated.

MDCK Cells on Substrates with Concave Micro-spherical Segments

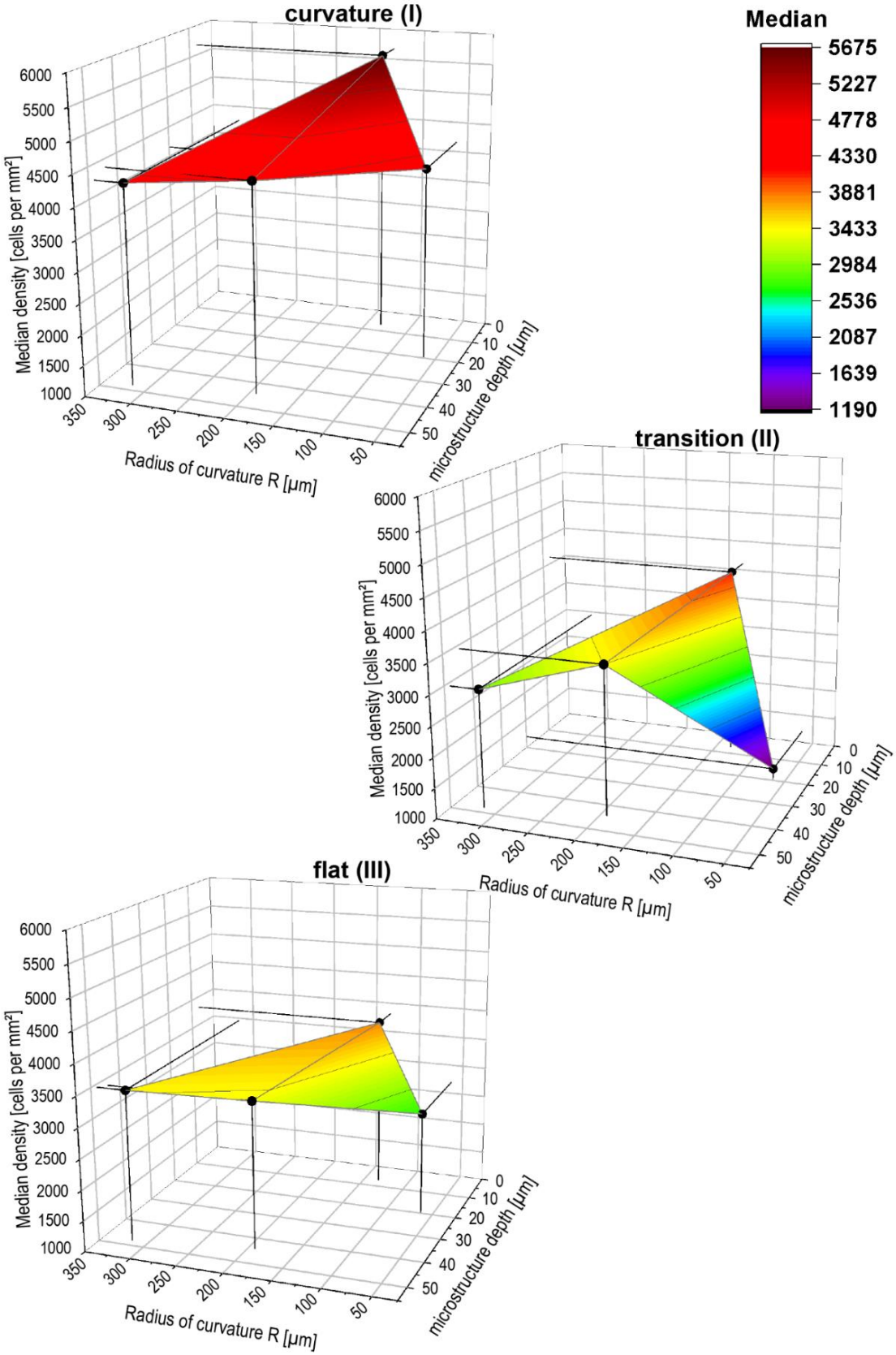

Figure 99 **Median density of MDCK cells dependent on microsphere radius of curvature R and structure height h on substrates with concave micro-spherical topographies.** Color code as indicated.

E-cadherin Staining

Titration of Secondary Antibody

For improving the results of the e-cadherin staining in in MDCK cells, the secondary antibody was varied and tested for the best dilution. Using chambered glass slides cells were cultivated until confluency, fixed and permeabilized as described in the materials end methods part. Primary antibody used was purified mouse anti-e-cadherin from BD Bioscience (cat.: 610182), secondary antibody as indicated in Figure 100, below.

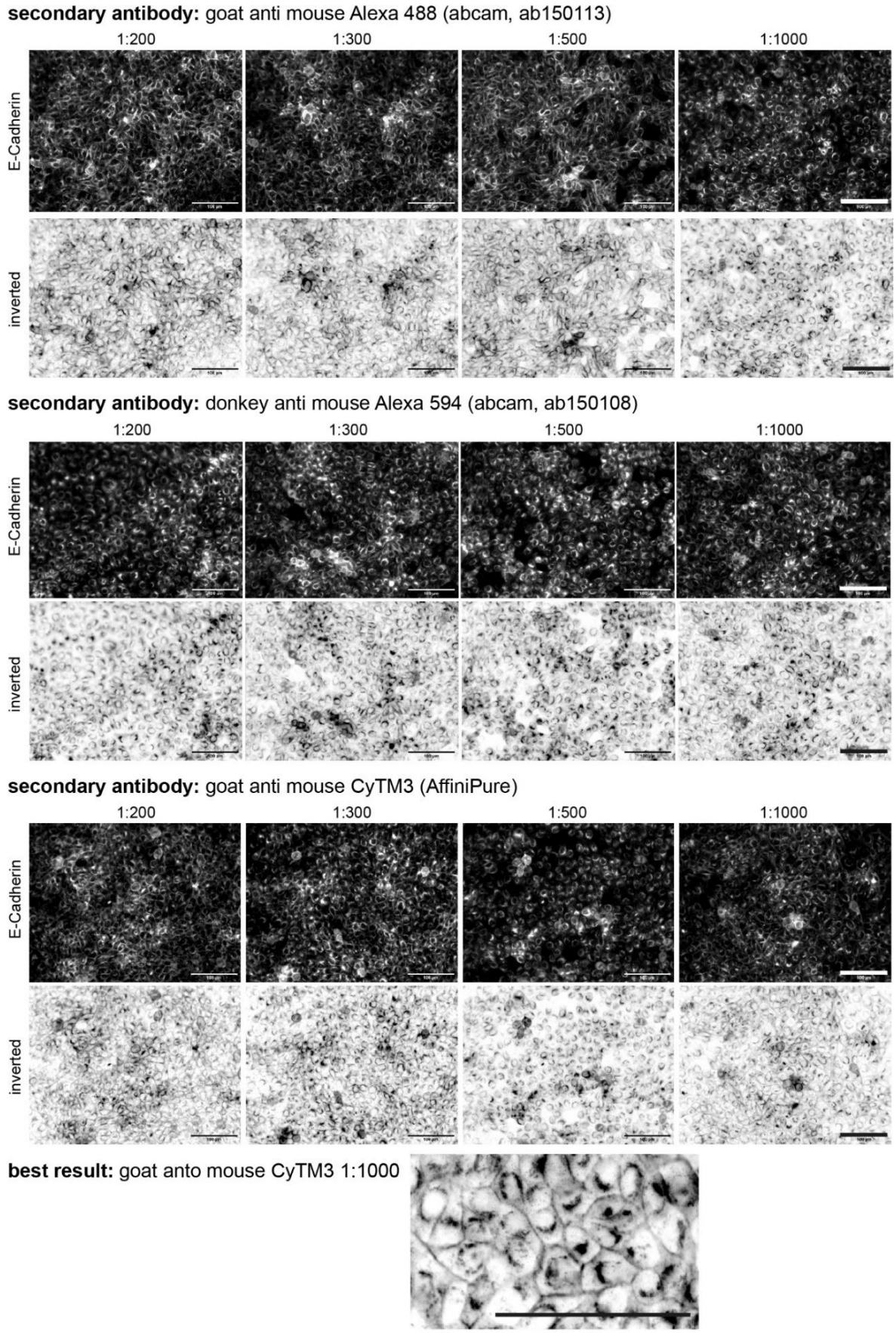

Figure 100 **Fluorescence images and inverted images of secondary antibody titration for e-cadherin staining in MDCK cells.** Cells are growing on glass surfaces, primary antibody was purified

mouse anti-e-cadherin from BD Bioscience, secondary antibody and dilution as indicated. Scale bars 100 µm.

Gap in E-cadherin staining on substrates with R=193.2 µm micro-spherical segments

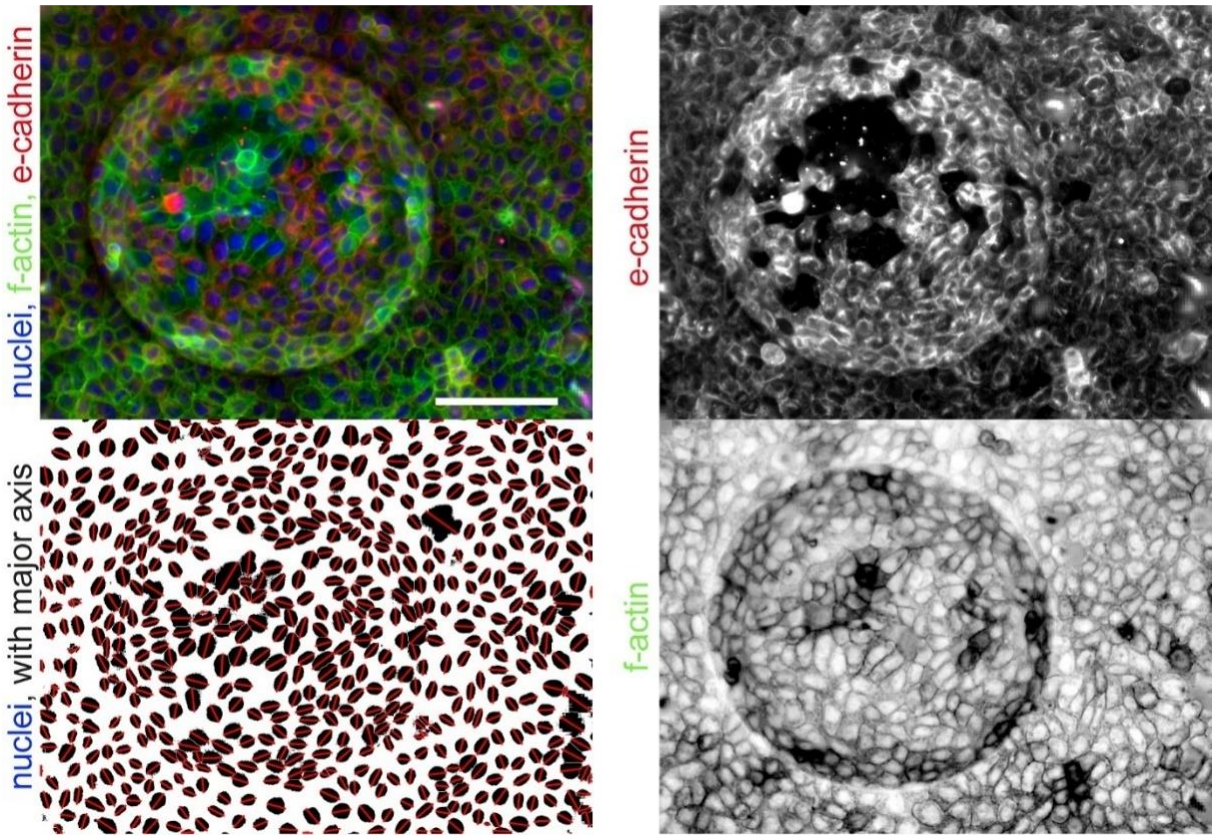

Figure 101 **Fluorescence image or MDCK on substrate with concave micro-spherical segments with a radius of curvature of 193.2 µm.** Recolored, merged image in upper left corner shows nuclei in blue, f-actin in green, and e-cadherin in red. Other images are grey scale (e-cadherin, upper right), black and white (nuclei, lower left) or inverted grey scale (f-actin, lower right) of same sequence. Scale bar 100 µm

Time-lapse Microscopy of Epithelial Cells on CurvChip Substrates with Micro-spherical Topographies

After Seeding on Substrates with R=193.2 µm Topographies

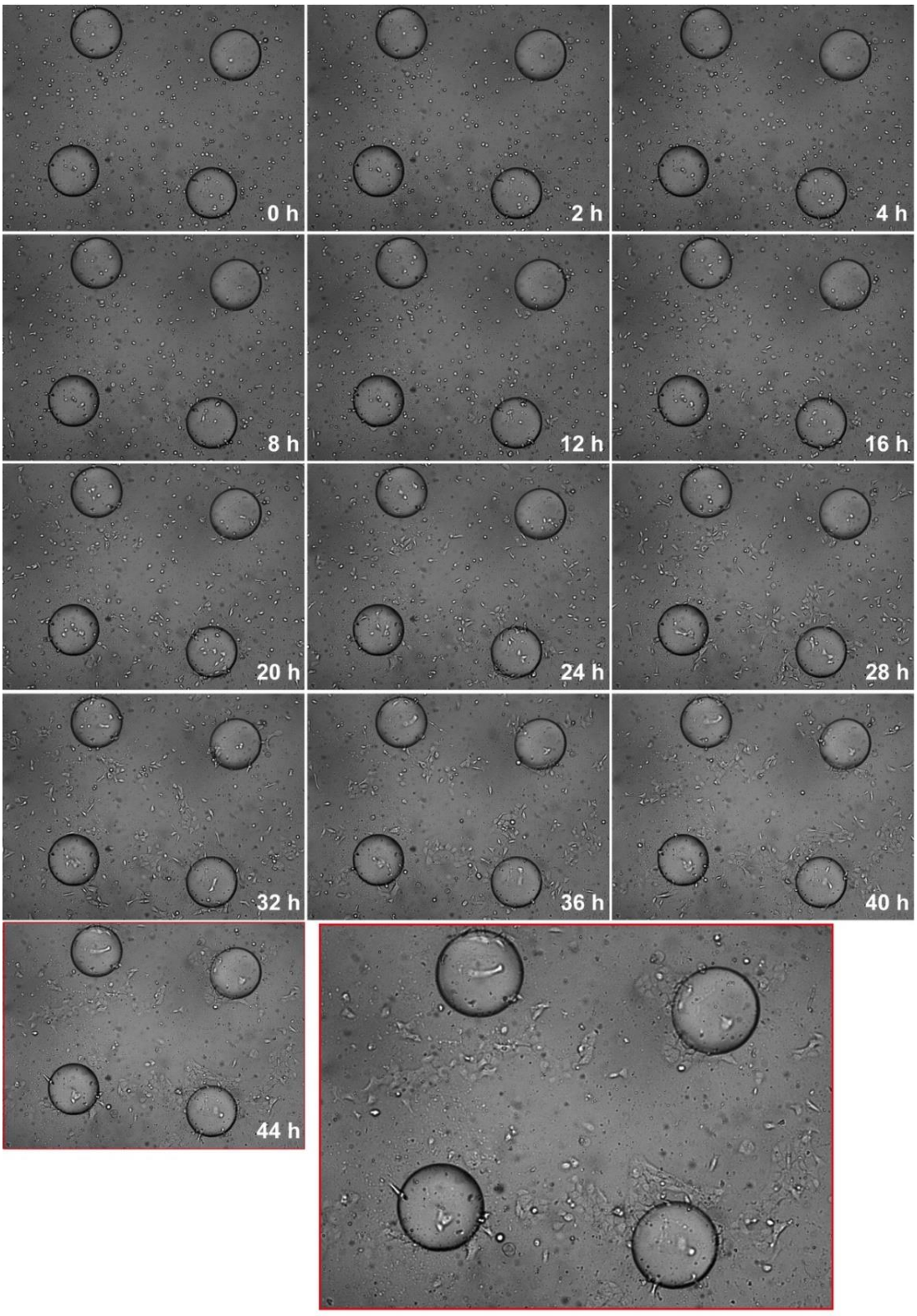

Figure 102 **Time-lapse sequence from A431 cells, recorded 0 hours to 44 hours after seeding (2×10^5 cells per mL) on collagen I-coated substrates with convex R=193.2 µm micro-spherical**

segments. Sequence from time-lapse microscopy using Live Cell Analyzr JuLi™ Br (NanoEnTek Inc.) with 4x magnification. Images show original imaging area, images with red frame display enlarged image for a more detailed examination. Time-stamp states time after seeding in hours (h). Since cell density was so low, medium was exchanged and imaging was continued on same sample but at different region, see Figure 103.

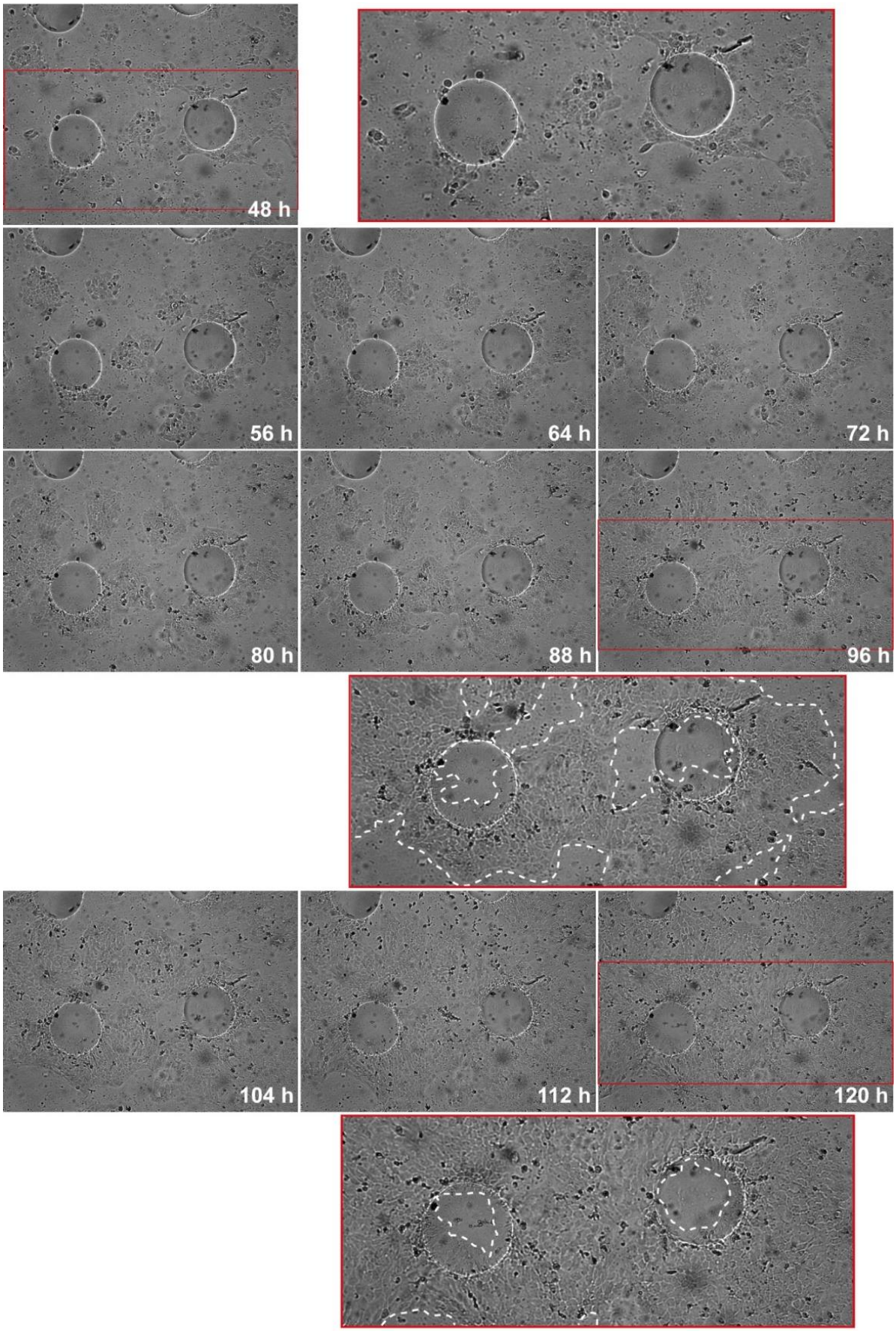

Figure 103 **Time-lapse sequence from A431 cells, recorded 48 hours to 120 hours after seeding (2×10^5 cells per mL) on collagen I-coated substrates with convex R=193.2 µm micro-spherical**

segments. Sequence is the continuation of the sequence shown in Figure 102. Starting time is approximately 48 hours after seeding as indicated by the time stamp and was generated using time-lapse microscopy with the Life Cell Analyzr JuLi™ Br (NanoEnTek Inc.) with 4x magnification. Images show original imaging area, images with red/blue frame display enlarged details with indicated monolayer defects (white dashed lines). Time-stamp states time after seeding in hours (h).

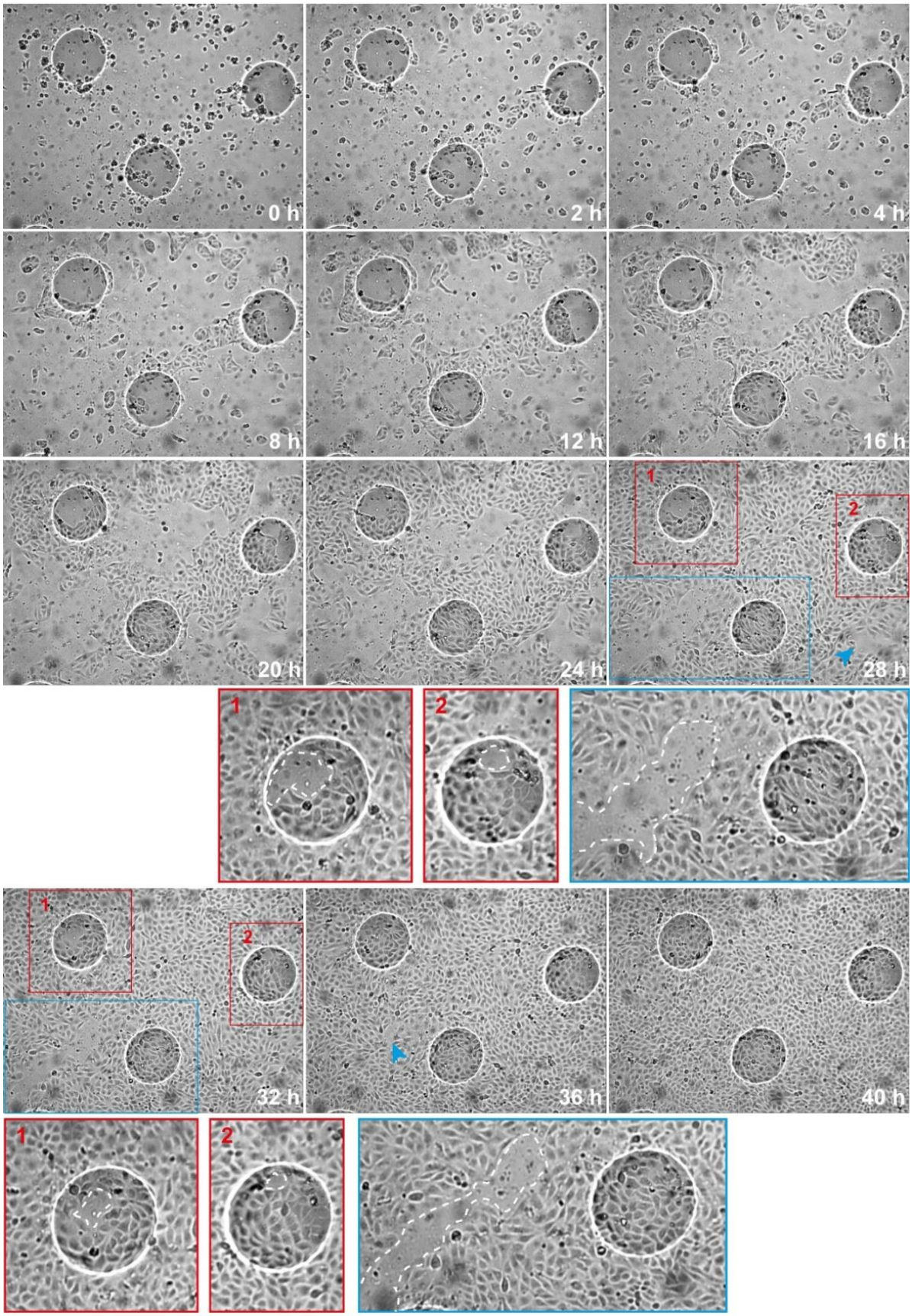

Figure 104 **Time-lapse sequence from MDCK cells, recorded 0 hours to 40 hours after seeding (2×10^5 cells per mL) on collagen I-coated substrates with convex R=193.2 µm micro-spherical segments**. Sequence from time-lapse microscopy using Live Cell Analyzr JuLi™ Br (NanoEnTek Inc.)

with 4x magnification. Images show original imaging area, images with red/blue frame display enlarged details with indicated monolayer defects (white dashed lines), arrowhead indicates layer defects in regions where no detail image is shown. Time-stamp states time after seeding in hours (h).

Wound Healing Assay on Substrates with R=318.6 µm Topographies

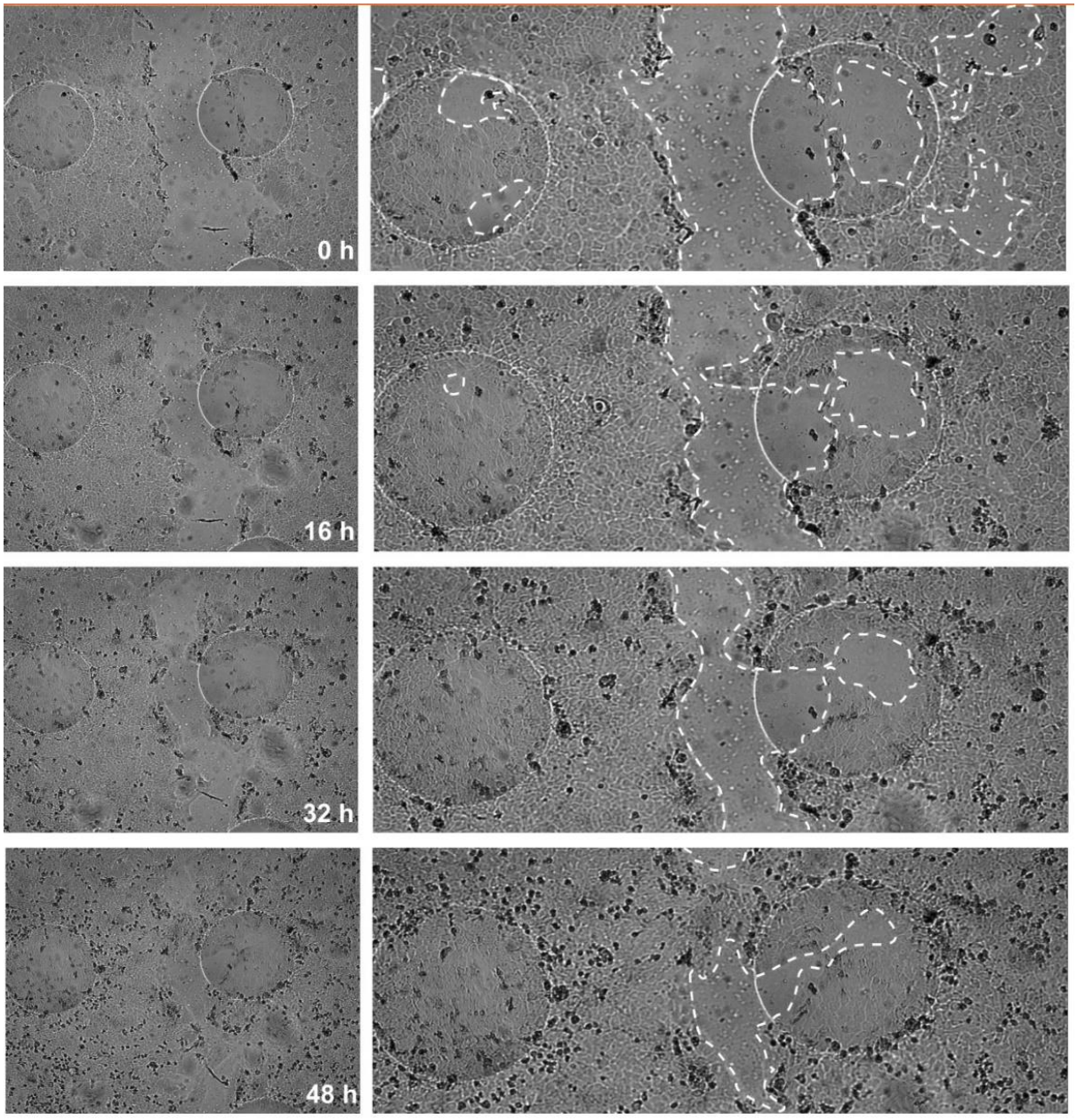

Figure 105 **Wound healing assay of A431 cells growing on a substrate with convex R=318.6 µm micro-spherical segments.** Sequence from time-lapse microscopy using Live Cell Analyzr JuLi™ Br (NanoEnTek Inc.) with 4x magnification. The left image row shows whole images, images in the right row display enlarged details with indicated monolayer defects (white dashed lines). 48 hours cultivation duration after seeding 4×10^5 cells per mL. Timestamp indicates time after wound generation in hours (h).

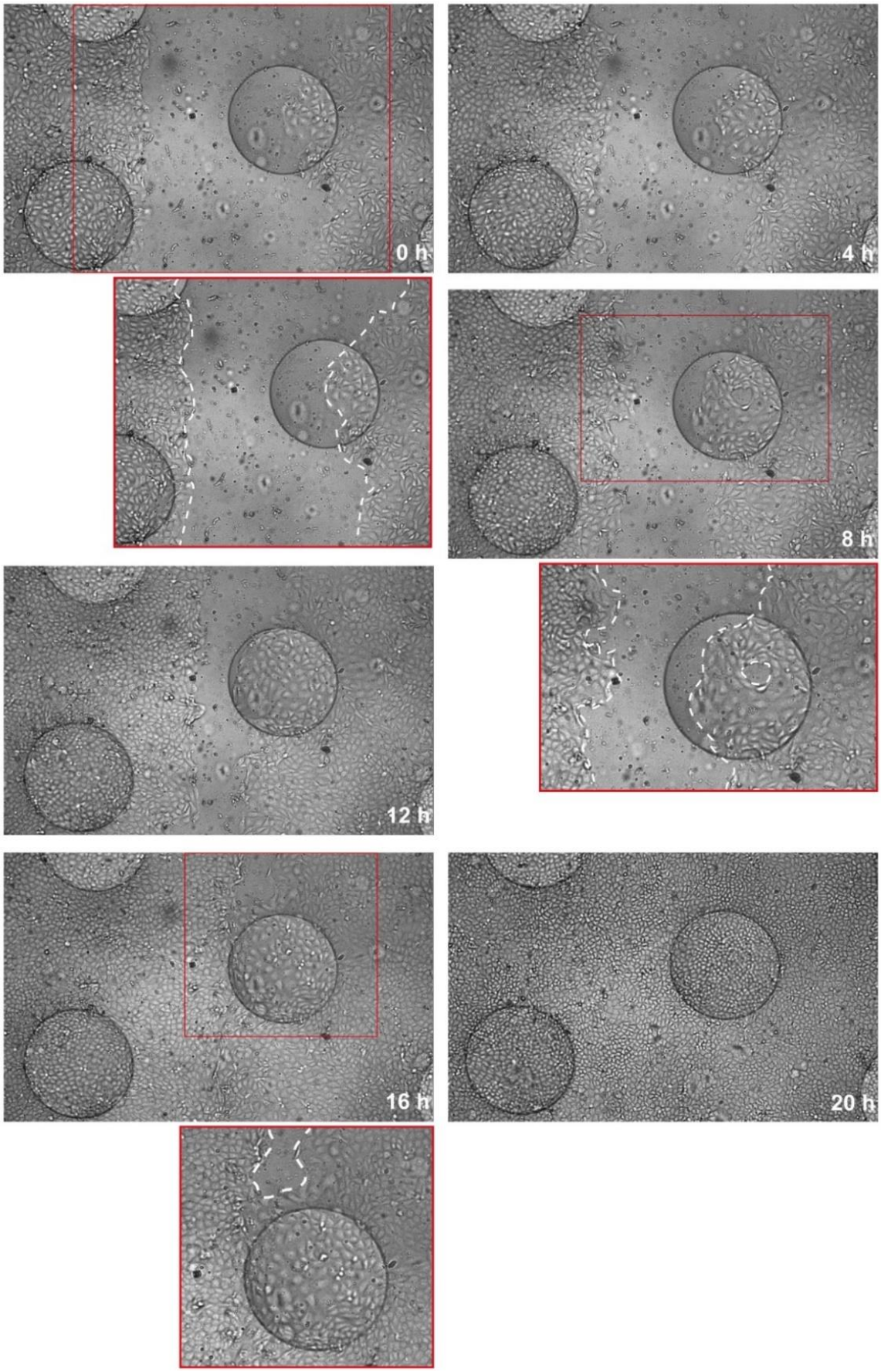

Figure 106 **Wound healing assay of MDCK cells growing on a substrate with convex R=318.6 µm micro-spherical segments.** Sequence from time-lapse microscopy using Live Cell Analyzr JuLi™ Br

(NanoEnTek Inc.) with 4x magnification. Images show region of interest from original imaging area, images with red frame display enlarged details with indicated monolayer defects (white dashed lines). 48 hours cultivation duration after seeding 2×10^5 cells per mL. Timestamp indicates time after wound generation in hours (h).

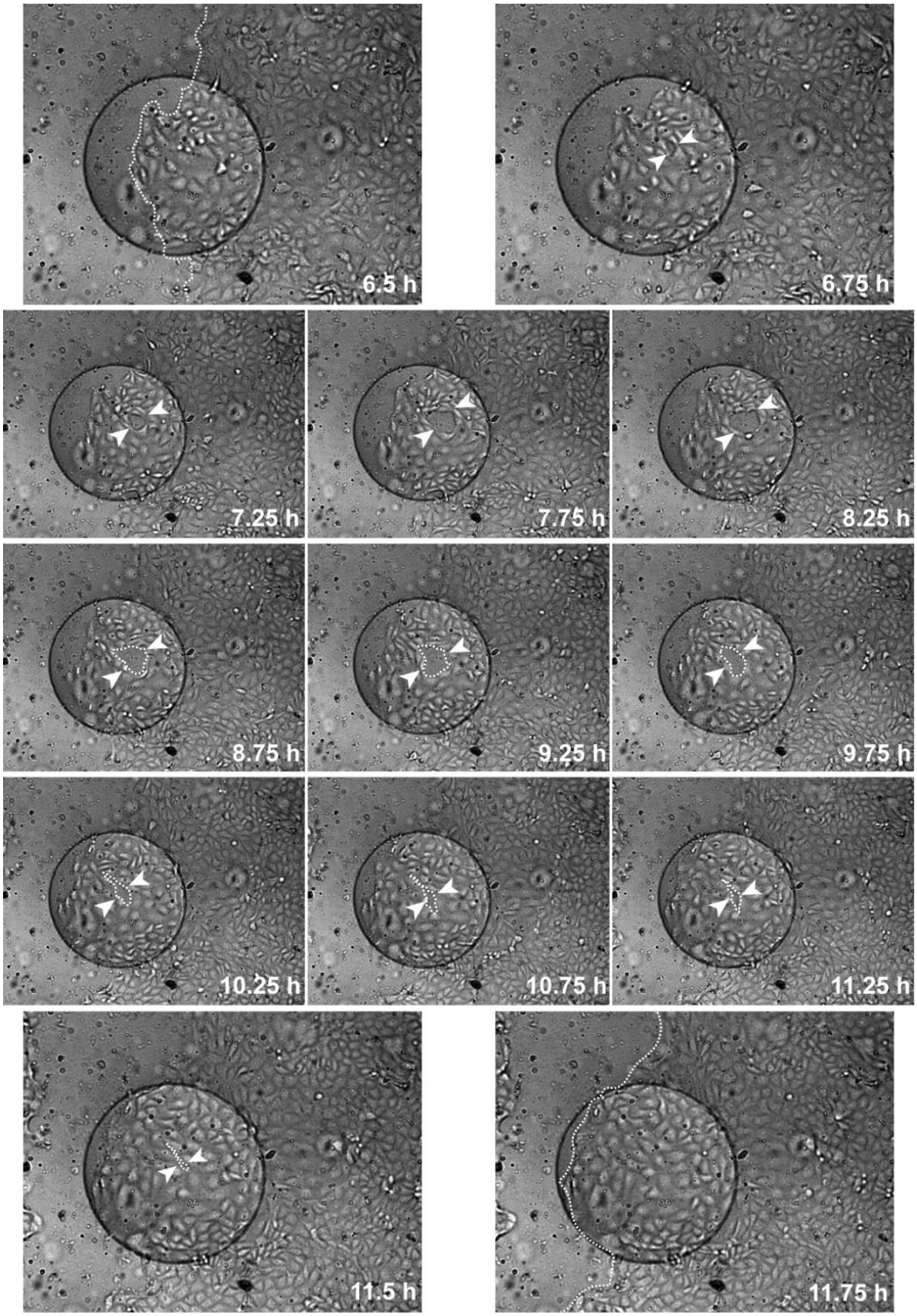

Figure 107 **Monolayer gap occurrence on R=318.6 µm microstructure during wound-healing assay of MDCK cells.** Sequence from time-lapse microscopy using Live Cell Analyzr JuLi™ Br (NanoEnTek Inc.) with 4x magnification. Images show regions of interest from original imaging area,

dashed lines and arrow heads indicate gap and growth front. Timestamp indicates time after wound generation in hours (h). Whole sequence with larger intervals can be seen in Figure 106

Comparison of A431 and MDCK Density on Different Regions of Convex Micro-spherical Segments of the CurvChip

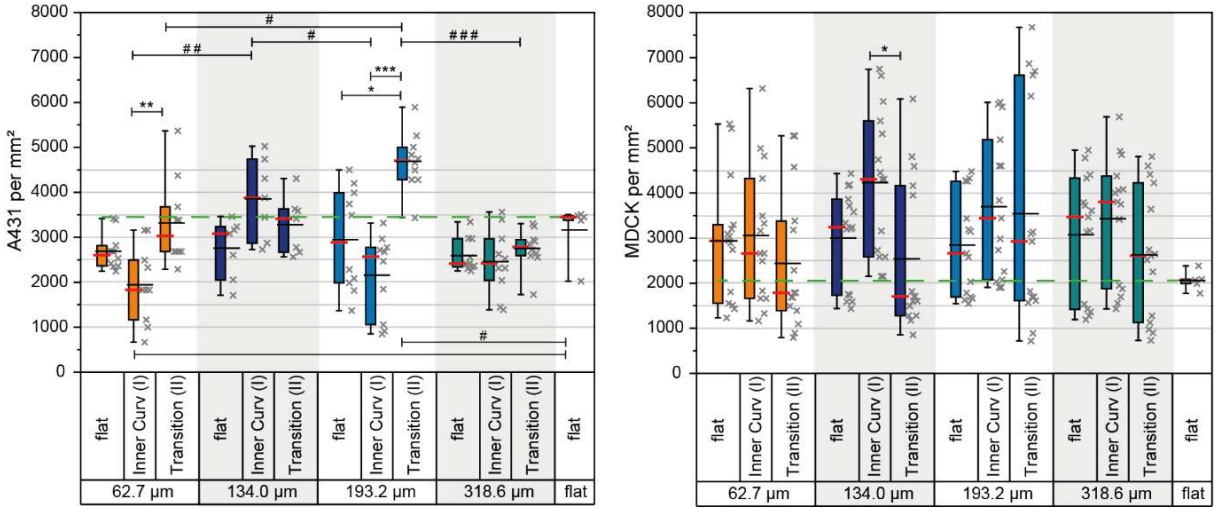

Figure 108 **Density of A431 cells** *(left)* **and MDCK cells** *(right)* **in different regions of convex spherically curved CurvChip substrates sorted by ascending radius of curvature R as indicated.** Box plots ***(left)*** with data points ***(right)***, box indicates 25th and 75th percentile, whiskers 5th and 95th percentile. Black line shows the mean value, red line the median. The dashed green line indicates the median of A431 cells on flat PDMS (3447 cells per mm²) for comparison. Different regions are flat surrounding (flat), the transition zone (transition (II)) consisting of part of the sphere and directly surrounding flat area, and the curved area (inner curv (I)), all as indicated in Figure 11, p. 51. Left graph is identical to Figure 59 (p. 170 , right graph is identical to Figure 65 (p. 179).Statistical significance (Kruskal-Wallis with Dunn's post-hoc) on same substrates is indicated by *, between the substrates by # (*p<0.05; *p<0.005; *p<0.005, or #; # #; # # # respectively).

List of Figures

List of Tables

Acknowledgements

This doctoral thesis was prepared within the framework of the doctoral program Intelligent Process and Material Development in Biomateriomics (Intelligente Prozess- und Materialentwicklung in der Biomateriomics IPMB) between the Eberhard Karls University of Tübingen and University of Applied Sciences in Reutlingen (Reutlingen University). Therefore, the funding by the Ministry of Science, Research and the Arts of the State of Baden-Württemberg within the framework of the state graduate funding program should be acknowledged first.
Secondly, I would like to thank the people within this doctoral program, all professors and fellow doctoral students. But my special thanks and appreciation go to Professor Dr. Günter Gauglitz (University of Tübingen) for the feedback and discussions we had during our meetings and Professor Dr. Ralf Kemkemer (Reutlingen University) for his supervision, trust and input.

I also want to thank the (graduate) students I supervised: Alena Fischer, Hatice Bilgic and Cornelia Kreim. I hope you learned as much as I learned by working with you.
My special thanks go out to my colleagues at Reutlingen University – the Kemkemer-Lab but also the wonderful women I shared an office with. Thank you for everything.

Furthermore, I would like to thank my colleagues at Bentley InnoMed GmbH for their endorsement.

If you are willing to learn and grow – a (doctoral) thesis can give you much more than the skills, you pick up in the lab.

Life is not easy for any of us. But what of that? We must have perseverance and above all confidence in ourselves. We must believe that we are gifted for something and that this thing must be attained.
(Marie Curie)

Finally, I want to express my deep gratitude to my family: without your unconditional support I would not have been able to achieve this. I love you.

IX. References

1. K. Frey, M. Brunner, C. Curio, R. Kemkemer, Curvature Perception of Mesenchymal Cells on Mesoscale Topographies. *Advanced healthcare materials* **14**, e2402865 (2025).
2. K. Frey, A. Fischer, R. Krastev, R. Kemkemer, CurvChip - chip platform for investigating cell responses to curved surface features. *Current Directions in Biomedical Engineering* **4**, 453–456 (2018).
3. B. K. Naggay, K. Frey, M. Schneider, K. Athanasopulu, G. Lorenz, R. Kemkemer, Low-cost photolithography system for cell biology labs. *Current Directions in Biomedical Engineering* **7**, 550–553 (2021).
4. J. Barthes, H. Özçelik, M. Hindié, A. Ndreu-Halili, A. Hasan, N. E. Vrana, Cell microenvironment engineering and monitoring for tissue engineering and regenerative medicine. *BioMed research international* **2014**, 921905 (2014).
5. M. P. Lutolf, J. A. Hubbell, Synthetic biomaterials as instructive extracellular microenvironments for morphogenesis in tissue engineering. *Nature biotechnology* **23**, 47–55 (2005).
6. D. S. Harburger, D. A. Calderwood, Integrin signalling at a glance. *Journal of cell science* **122**, 159–163 (2009).
7. R. Daum, D. Visser, C. Wild, L. Kutuzova, M. Schneider, G. Lorenz, M. Weiss, S. Hinderer, U. A. Stock, M. Seifert, K. Schenke-Layland, Fibronectin Adsorption on Electrospun Synthetic Vascular Grafts Attracts Endothelial Progenitor Cells and Promotes Endothelialization in Dynamic In Vitro Culture. *Cells* **9** (2020).
8. M. I. Gariboldi, S. M. Best, Effect of Ceramic Scaffold Architectural Parameters on Biological Response. *Frontiers in bioengineering and biotechnology* **3**, 151 (2015).
9. L. A. Low, C. Mummery, B. R. Berridge, C. P. Austin, D. A. Tagle, Organs-on-chips: into the next decade. *Nature reviews. Drug discovery* **20**, 345–361 (2021).
10. K. H. Benam, S. Dauth, B. Hassell, A. Herland, A. Jain, K.-J. Jang, K. Karalis, H. J. Kim, L. MacQueen, R. Mahmoodian, S. Musah, Y. Torisawa, A. D. van der Meer, R. Villenave, M. Yadid, K. K. Parker, D. E. Ingber, Engineered in vitro disease models. *Annual review of pathology* **10**, 195–262 (2015).
11. B. Alberts, A. Johnson, J. Lewis, D. Morgan, M. Raff, K. Roberts, P. Walter, J. Wilson, T. Hunt, *Molecular biology of the cell*(Garland Science Taylor and Francis Group, New York, NY, 2015).
12. S. M. Früh, I. Schoen, J. Ries, V. Vogel, Molecular architecture of native fibronectin fibrils. *Nature communications* **6**, 7275 (2015).
13. F. H. Silver, J. W. Freeman, G. P. Seehra, Collagen self-assembly and the development of tendon mechanical properties. *Journal of Biomechanics* **36**, 1529–1553 (2003).

14. M. P. Wiedeman, Dimensions of Blood Vessels from Distributing Artery to Collecting Vein. *Circulation Research* **12**, 375–378 (1963).
15. A. C. Burton, Relation of structure to function of the tissues of the wall of blood vessels. *Physiological reviews* **34**, 619–642 (1954).
16. P. Broulik, J. Kragstrup, L. Mosekilde, F. Melsen, Osteon Cross-sectional Size in the Iliac Crest. *Acta Pathologica Microbiologica Scandinavica Series A :Pathology* **90A**, 339–344 (1982).
17. J. Xu, D. Mosher, in *The extracellular matrix, An overview*, R. P. Mecham, Ed.(Springer Verlag, Berlin, New York, 2011), pp. 41–75.
18. I. Wierzbicka-Patynowski, J. E. Schwarzbauer, The ins and outs of fibronectin matrix assembly. *Journal of cell science* **116**, 3269–3276 (2003).
19. M. M. Martino, J. A. Hubbell, The 12th-14th type III repeats of fibronectin function as a highly promiscuous growth factor-binding domain. *FASEB journal : official publication of the Federation of American Societies for Experimental Biology* **24**, 4711–4721 (2010).
20. R. S. Madhurapantula, J. P. Orgel, in *Accelerator Physics - Radiation Safety and Applications*, M. Malek, I. Ahmad, Eds.(IntechOpen, Erscheinungsort nicht ermittelbar, 2018).
21. M. Nomizu, W. H. Kim, K. Yamamura, A. Utani, S. Y. Song, A. Otaka, P. P. Roller, H. K. Kleinman, Y. Yamada, Identification of cell binding sites in the laminin alpha 1 chain carboxyl-terminal globular domain by systematic screening of synthetic peptides. *The Journal of biological chemistry* **270**, 20583–20590 (1995).
22. MBInfo; Sheetz, Michael P., *What are cell-matrix receptors?* (2017) (available at https://www.mechanobio.info/what-is-mechanosignaling/what-is-the-extracellular-matrix-and-the-basal-lamina/what-are-cell-matrix-receptors/#ITEM-1857-14)(04-10-2017); (last accessed 05-02-2022).
23. Y. Takada, X. Ye, S. Simon, The integrins. *Genome biology* **8**, 215 (2007).
24. S.-T. Sit, E. Manser, Rho GTPases and their role in organizing the actin cytoskeleton. *Journal of cell science* **124**, 679–683 (2011).
25. A. E. Stanton, X. Tong, F. Yang, Extracellular matrix type modulates mechanotransduction of stem cells. *Acta biomaterialia* **96**, 310–320 (2019).
26. J. Guasch, B. Conings, S. Neubauer, F. Rechenmacher, K. Ende, C. G. Rolli, C. Kappel, V. Schaufler, A. Micoulet, H. Kessler, H.-G. Boyen, E. A. Cavalcanti-Adam, J. P. Spatz, Segregation versus colocalization: orthogonally functionalized binary micropatterned substrates regulate the molecular distribution in focal adhesions. *Adv. Mater.* **27**, 3737–3747 (2015).
27. J. D. Humphries, A. Byron, M. J. Humphries, Integrin ligands at a glance. *Journal of cell science* **119**, 3901–3903 (2006).

28. S. Biela, B. Striegl, K. Frey, J. P. Spatz, R. Kemkemer, Distance-dependent adhesion of vascular cells on biofunctionalized nanostructures. *Current Directions in Biomedical Engineering* **3**, 683–686 (2017).
29. K. A. Kilian, M. Mrksich, Directing stem cell fate by controlling the affinity and density of ligand-receptor interactions at the biomaterials interface. *Angewandte Chemie (International ed. in English)* **51**, 4891–4895 (2012).
30. N. Borghi, M. Sorokina, O. G. Shcherbakova, W. I. Weis, B. L. Pruitt, W. J. Nelson, A. R. Dunn, E-cadherin is under constitutive actomyosin-generated tension that is increased at cell-cell contacts upon externally applied stretch. *Proceedings of the National Academy of Sciences of the United States of America* **109**, 12568–12573 (2012).
31. S. Yonemura, M. Itoh, A. Nagafuchi, S. Tsukita, Cell-to-cell adherens junction formation and actin filament organization: similarities and differences between non-polarized fibroblasts and polarized epithelial cells. *Journal of cell science* **108**, 127–142 (1995).
32. S. Yonemura, Actin filament association at adherens junctions. *The journal of medical investigation : JMI* **64**, 14–19 (2017).
33. E. E. Mulkearns-Hubert, O. Reizes, J. D. Lathia, Connexins in Cancer: Jekyll or Hyde? *Biomolecules* **10** (2020).
34. G. S. Karagiannis, D. F. Schaeffer, C.-K. J. Cho, N. Musrap, P. Saraon, I. Batruch, A. Grin, B. Mitrovic, R. Kirsch, R. H. Riddell, E. P. Diamandis, Collective migration of cancer-associated fibroblasts is enhanced by overexpression of tight junction-associated proteins claudin-11 and occludin. *Molecular oncology* **8**, 178–195 (2014).
35. H. P. Ehrlich, B. Sun, G. C. Saggers, F. Kromath, Gap junction communications influence upon fibroblast synthesis of Type I collagen and fibronectin. *Journal of cellular biochemistry* **98**, 735–743 (2006).
36. D. Ribatti, A revisited concept: Contact inhibition of growth. From cell biology to malignancy. *Experimental cell research* **359**, 17–19 (2017).
37. Y. Miyake, N. Inoue, K. Nishimura, N. Kinoshita, H. Hosoya, S. Yonemura, Actomyosin tension is required for correct recruitment of adherens junction components and zonula occludens formation. *Experimental cell research* **312**, 1637–1650 (2006).
38. G. Charras, A. S. Yap, Tensile Forces and Mechanotransduction at Cell-Cell Junctions. *Current biology : CB* **28**, R445-R457 (2018).
39. J. Solon, I. Levental, K. Sengupta, P. C. Georges, P. A. Janmey, Fibroblast adaptation and stiffness matching to soft elastic substrates. *Biophysical journal* **93**, 4453–4461 (2007).
40. S. Huveneers, H. Truong, R. Fässler, A. Sonnenberg, E. H. J. Danen, Binding of soluble fibronectin to integrin alpha5 beta1 - link to focal adhesion redistribution and contractile shape. *Journal of cell science* **121**, 2452–2462 (2008).

41. R. Lutz, T. Sakai, M. Chiquet, Pericellular fibronectin is required for RhoA-dependent responses to cyclic strain in fibroblasts. *Journal of cell science* **123**, 1511–1521 (2010).
42. J. Beyeler, C. Katsaros, M. Chiquet, Impaired Contracture of 3D Collagen Constructs by Fibronectin-Deficient Murine Fibroblasts. *Front. Physiol.* **10**, 166 (2019).
43. J. Foolen, T. Yamashita, P. Kollmannsberger, Shaping tissues by balancing active forces and geometric constraints. *Journal of the Royal Society, Interface* **49**, 53001 (2016).
44. A. Sales, K. Ende, J. Diemer, A. R. Kyvik, J. Veciana, I. Ratera, R. Kemkemer, J. P. Spatz, J. Guasch, Cell Type-Dependent Integrin Distribution in Adhesion and Migration Responses on Protein-Coated Microgrooved Substrates. *ACS Omega* **4**, 1791–1800 (2019).
45. M. Sarkissian, R. Lafyatis, Integrin engagement regulates proliferation and collagenase expression of rheumatoid synovial fibroblasts. *Journal of immunology (Baltimore, Md. : 1950)* **162**, 1772–1779 (1999).
46. A. J. Engler, S. Sen, H. L. Sweeney, D. E. Discher, Matrix elasticity directs stem cell lineage specification. *Cell* **126**, 677–689 (2006).
47. W. J. Hadden, J. L. Young, A. W. Holle, M. L. McFetridge, Y. Du Kim, P. Wijesinghe, H. Taylor-Weiner, J. H. Wen, A. R. Lee, K. Bieback, B.-N. Vo, D. D. Sampson, B. F. Kennedy, J. P. Spatz, A. J. Engler, Y. S. Choi, Stem cell migration and mechanotransduction on linear stiffness gradient hydrogels. *Proceedings of the National Academy of Sciences of the United States of America* **114**, 5647–5652 (2017).
48. S. Cosson, E. A. Otte, H. Hezaveh, J. J. Cooper-White, Concise review: tailoring bioengineered scaffolds for stem cell applications in tissue engineering and regenerative medicine. *Stem cells translational medicine* **4**, 156–164 (2015).
49. B. Cortese, I. E. Palamà, S. D'Amone, G. Gigli, Influence of electrotaxis on cell behaviour. *Integrative Biology* **6**, 817–830 (2014).
50. L. G. Vincent, Y. S. Choi, B. Alonso-Latorre, J. C. Del Álamo, A. J. Engler, Mesenchymal stem cell durotaxis depends on substrate stiffness gradient strength. *Biotechnology journal* **8**, 472–484 (2013).
51. B. K. Brandley, R. L. Schnaar, Tumor cell haptotaxis on covalently immobilized linear and exponential gradients of a cell adhesion peptide. *Developmental Biology* **135**, 74–86 (1989).
52. C. J. Bettinger, R. Langer, J. T. Borenstein, Engineering substrate topography at the micro- and nanoscale to control cell function. *Angewandte Chemie (International ed. in English)* **48**, 5406–5415 (2009).
53. A. S. Curtis, M. Varde, Control of Cell Behavior. *JNCI: Journal of the National Cancer Institute* (1964).

54. M. Werner, N. A. Kurniawan, G. Korus, C. V. C. Bouten, A. Petersen, Mesoscale substrate curvature overrules nanoscale contact guidance to direct bone marrow stromal cell migration. *Journal of the Royal Society, Interface* **15** (2018).
55. C. Tomba, T. Petithory, R. Pedron, A. Airoudj, I. Di Meglio, A. Roux, V. Luchnikov, Laser-Assisted Strain Engineering of Thin Elastomer Films to Form Variable Wavy Substrates for Cell Culture. *Small (Weinheim an der Bergstrasse, Germany)*, e1900162 (2019).
56. J. Petzold, E. Gentleman, Intrinsic Mechanical Cues and Their Impact on Stem Cells and Embryogenesis. *Front. Cell Dev. Biol.* **9**, 761871 (2021).
57. A. Bershadsky, M. Kozlov, B. Geiger, Adhesion-mediated mechanosensitivity: a time to experiment, and a time to theorize. *Current opinion in cell biology* **18**, 472–481 (2006).
58. D. E. Discher, P. Janmey, Y. Wang, Tissue cells feel and respond to the stiffness of their substrate. *Science (New York, N.Y.)* **310**, 1139–1143 (2005).
59. Z. Sun, M. Costell, R. Fässler, Integrin activation by talin, kindlin and mechanical forces. *Nat Cell Biol* **21**, 25–31 (2019).
60. MBInfo; Sheetz, Michael P., *How does the cytoskeleton transmit mechanical forces? | MBInfo* (2017) (available at https://www.mechanobio.info/what-is-mechanobiology/how-does-the-cytoskeleton-transmit-mechanical-forces/)(14-08-2017); (last accessed 12-02-2022).
61. T. Yeung, P. C. Georges, L. A. Flanagan, B. Marg, M. Ortiz, M. Funaki, N. Zahir, W. Ming, V. Weaver, P. A. Janmey, Effects of substrate stiffness on cell morphology, cytoskeletal structure, and adhesion. *Cell motility and the cytoskeleton* **60**, 24–34 (2005).
62. A. Prasad, E. Alizadeh, Cell Form and Function: Interpreting and Controlling the Shape of Adherent Cells. *Trends in Biotechnology* **37**, 347–357 (2019).
63. B. Ladoux, R.-M. Mège, Mechanobiology of collective cell behaviours. *Nature reviews. Molecular cell biology* **18**, 743–757 (2017).
64. K. K. Papachroni, D. N. Karatzas, K. A. Papavassiliou, E. K. Basdra, A. G. Papavassiliou, Mechanotransduction in osteoblast regulation and bone disease. *Trends in Molecular Medicine* **15**, 208–216 (2009).
65. H. B. Schiller, M.-R. Hermann, J. Polleux, T. Vignaud, S. Zanivan, C. C. Friedel, Z. Sun, A. Raducanu, K.-E. Gottschalk, M. Théry, M. Mann, R. Fässler, β1- and αv-class integrins cooperate to regulate myosin II during rigidity sensing of fibronectin-based microenvironments. *Nat Cell Biol* **15**, 625–636 (2013).
66. P. Roca-Cusachs, N. C. Gauthier, A. Del Rio, M. P. Sheetz, Clustering of alpha(5)beta(1) integrins determines adhesion strength whereas alpha(v)beta(3) and talin enable mechanotransduction. *PNAS* **106**, 16245–16250 (2009).
67. C. Guilluy, K. Burridge, Nuclear mechanotransduction: forcing the nucleus to respond. *Nucleus* **6**, 19–22 (2015).

68. F. Donnaloja, E. Jacchetti, M. Soncini, M. T. Raimondi, Mechanosensing at the Nuclear Envelope by Nuclear Pore Complex Stretch Activation and Its Effect in Physiology and Pathology. *Front. Physiol.* **10**, 896 (2019).
69. A. Elosegui-Artola, I. Andreu, A. E. M. Beedle, A. Lezamiz, M. Uroz, A. J. Kosmalska, R. Oria, J. Z. Kechagia, P. Rico-Lastres, A.-L. Le Roux, C. M. Shanahan, X. Trepat, D. Navajas, S. Garcia-Manyes, P. Roca-Cusachs, Force Triggers YAP Nuclear Entry by Regulating Transport across Nuclear Pores. *Cell* **171**, 1397-1410.e14 (2017).
70. F. Haque, D. Mazzeo, J. T. Patel, D. T. Smallwood, J. A. Ellis, C. M. Shanahan, S. Shackleton, Mammalian SUN protein interaction networks at the inner nuclear membrane and their role in laminopathy disease processes. *The Journal of biological chemistry* **285**, 3487–3498 (2010).
71. D. A. Starr, KASH and SUN proteins. *Current biology : CB* **21**, R414-5 (2011).
72. M. Versaevel, J.-B. Braquenier, M. Riaz, T. Grevesse, J. Lantoine, S. Gabriele, Super-resolution microscopy reveals LINC complex recruitment at nuclear indentation sites. *Sci Rep* **4**, 7362 (2014).
73. Y. K. Wu, H. Umeshima, J. Kurisu, M. Kengaku, Nesprins and opposing microtubule motors generate a point force that drives directional nuclear motion in migrating neurons. *Development (Cambridge, England)* **145** (2018).
74. M. Maninová, M. P. Iwanicki, T. Vomastek, Emerging role for nuclear rotation and orientation in cell migration. *Cell adhesion & migration* **8**, 42–48 (2014).
75. M. L. Lombardi, D. E. Jaalouk, C. M. Shanahan, B. Burke, K. J. Roux, J. Lammerding, The interaction between nesprins and sun proteins at the nuclear envelope is critical for force transmission between the nucleus and cytoskeleton. *The Journal of biological chemistry* **286**, 26743–26753 (2011).
76. Q. Li, A. Kumar, E. Makhija, G. V. Shivashankar, The regulation of dynamic mechanical coupling between actin cytoskeleton and nucleus by matrix geometry. *Biomaterials* **35**, 961–969 (2014).
77. Z. Jahed, M. R. Mofrad, The nucleus feels the force, LINCed in or not! *Current opinion in cell biology* **58**, 114–119 (2019).
78. M. Versaevel, T. Grevesse, S. Gabriele, Spatial coordination between cell and nuclear shape within micropatterned endothelial cells. *Nature communications* **3**, 671 (2012).
79. J. T. Philip, K. N. Dahl, Nuclear mechanotransduction: response of the lamina to extracellular stress with implications in aging. *Journal of Biomechanics* **41**, 3164–3170 (2008).
80. K. Damodaran, S. Venkatachalapathy, F. Alisafaei, A. V. Radhakrishnan, D. Sharma Jokhun, V. B. Shenoy, G. V. Shivashankar, Compressive force induces reversible

chromatin condensation and cell geometry-dependent transcriptional response. *Molecular biology of the cell* **29**, 3039–3051 (2018).

81. K. Anselme, N. Tusamda Wakhloo, P. Rougerie, L. Pieuchot, Role of the Nucleus as a Sensor of Cell Environment Topography. *Advanced healthcare materials* **7**, e1701154 (2018).
82. P. Roca-Cusachs, J. Alcaraz, R. Sunyer, J. Samitier, R. Farré, D. Navajas, Micropatterning of single endothelial cell shape reveals a tight coupling between nuclear volume in G1 and proliferation. *Biophysical journal* **94**, 4984–4995 (2008).
83. S.-J. Heo, S. D. Thorpe, T. P. Driscoll, R. L. Duncan, D. A. Lee, R. L. Mauck, Biophysical Regulation of Chromatin Architecture Instills a Mechanical Memory in Mesenchymal Stem Cells. *Sci Rep* **5**, 16895 (2015).
84. A. Buxboim, J. Swift, J. Irianto, K. R. Spinler, P. C. D. P. Dingal, A. Athirasala, Y.-R. C. Kao, S. Cho, T. Harada, J.-W. Shin, D. E. Discher, Matrix elasticity regulates lamin-A,C phosphorylation and turnover with feedback to actomyosin. *Current biology : CB* **24**, 1909–1917 (2014).
85. J. Swift, I. L. Ivanovska, A. Buxboim, T. Harada, P. C. D. P. Dingal, J. Pinter, J. D. Pajerowski, K. R. Spinler, J.-W. Shin, M. Tewari, F. Rehfeldt, D. W. Speicher, D. E. Discher, Nuclear lamin-A scales with tissue stiffness and enhances matrix-directed differentiation. *Science (New York, N.Y.)* **341**, 1240104 (2013).
86. M. Poujade, E. Grasland-Mongrain, A. Hertzog, J. Jouanneau, P. Chavrier, B. Ladoux, A. Buguin, P. Silberzan, Collective migration of an epithelial monolayer in response to a model wound. *Proceedings of the National Academy of Sciences of the United States of America* **104**, 15988–15993 (2007).
87. M. A. Schwartz, D. W. DeSimone, Cell adhesion receptors in mechanotransduction. *Current opinion in cell biology* **20**, 551–556 (2008).
88. S. R. K. Vedula, M. C. Leong, T. L. Lai, P. Hersen, A. J. Kabla, C. T. Lim, B. Ladoux, Emerging modes of collective cell migration induced by geometrical constraints. *PNAS* **109**, 12974–12979 (2012).
89. T. Chen, T. B. Saw, R.-M. Mège, B. Ladoux, Mechanical forces in cell monolayers. *Journal of cell science* **131** (2018).
90. K. Doxzen, S. R. K. Vedula, M. C. Leong, H. Hirata, N. S. Gov, A. J. Kabla, B. Ladoux, C. T. Lim, Guidance of collective cell migration by substrate geometry. *Integrative Biology* **5**, 1026–1035 (2013).
91. G. Duclos, S. Garcia, H. G. Yevick, P. Silberzan, Perfect nematic order in confined monolayers of spindle-shaped cells. *Soft matter* **10**, 2346–2353 (2014).

92. A. E. Stanton, X. Tong, S. Lee, F. Yang, Biochemical Ligand Density Regulates Yes-Associated Protein Translocation in Stem Cells through Cytoskeletal Tension and Integrins. *ACS Appl. Mater. Interfaces* **11**, 8849–8857 (2019).
93. E. A. Cavalcanti-Adam, T. Volberg, A. Micoulet, H. Kessler, B. Geiger, J. P. Spatz, Cell spreading and focal adhesion dynamics are regulated by spacing of integrin ligands. *Biophysical journal* **92**, 2964–2974 (2007).
94. M. Arnold, E. A. Cavalcanti-Adam, R. Glass, J. Blümmel, W. Eck, M. Kantlehner, H. Kessler, J. P. Spatz, Activation of integrin function by nanopatterned adhesive interfaces. *Chemphyschem : a European journal of chemical physics and physical chemistry* **5**, 383–388 (2004).
95. R. McBeath, D. M. Pirone, C. M. Nelson, K. Bhadriraju, C. S. Chen, Cell Shape, Cytoskeletal Tension, and RhoA Regulate Stem Cell Lineage Commitment. *Developmental Cell* **6**, 483–495 (2004).
96. K. A. Kilian, B. Bugarija, B. T. Lahn, M. Mrksich, Geometric cues for directing the differentiation of mesenchymal stem cells. *PNAS* **107**, 4872–4877 (2010).
97. M. Werner, S. B. G. Blanquer, S. P. Haimi, G. Korus, J. W. C. Dunlop, G. N. Duda, D. W. Grijpma, A. Petersen, Surface Curvature Differentially Regulates Stem Cell Migration and Differentiation via Altered Attachment Morphology and Nuclear Deformation. *Adv. Sci.*, 1600347 (2016).
98. C. S. Chen, M. Mrksich, S. Huang, G. M. Whitesides, D. E. Ingber, Geometric control of cell life and death. *Science (New York, N.Y.)* **276**, 1425–1428 (1997).
99. C. M. Bidan, K. P. Kommareddy, M. Rumpler, P. Kollmannsberger, P. Fratzl, J. W. C. Dunlop, Geometry as a factor for tissue growth: towards shape optimization of tissue engineering scaffolds. *Advanced healthcare materials* **2**, 186–194 (2013).
100. M. Rumpler, A. Woesz, J. W. C. Dunlop, J. T. van Dongen, P. Fratzl, The effect of geometry on three-dimensional tissue growth. *Journal of the Royal Society, Interface* **5**, 1173–1180 (2008).
101. P. Weiss, Experiments on cell and axon orientation in vitro. *J. Exp. Zool.* **100**, 353–386 (1945).
102. R. G. Harrison, Regeneration of peripheral nerves. *Anat. Rec.* **1**, 209 (1908).
103. G. A. Dunn, How do cells respond to ultrafine surface contours? *BioEssays : news and reviews in molecular, cellular and developmental biology* **13**, 541–543 (1991).
104. M. Ermis, E. Antmen, V. Hasirci, Micro and Nanofabrication methods to control cell-substrate interactions and cell behavior: A review from the tissue engineering perspective. *Bioactive materials* **3**, 355–369 (2018).
105. C. Leclech, C. Villard, Cellular and Subcellular Contact Guidance on Microfabricated Substrates. *Frontiers in bioengineering and biotechnology* **8**, 551505 (2020).

106. R. Kemkemer, C. Neidlinger-Wilke, L. Claes, H. Gruler, Cell orientation induced by extracellular signals. *Cell biochemistry and biophysics* **30**, 167–192 (1999).

107. A. B. Jaffe, A. Hall, Rho GTPases: biochemistry and biology. *Annual review of cell and developmental biology* **21**, 247–269 (2005).

108. J. Birkenfeld, P. Nalbant, S.-H. Yoon, G. M. Bokoch, *Cellular functions of GEF-H1, a microtubule-regulated Rho-GEF: is altered GEF-H1 activity a crucial determinant of disease pathogenesis?*(2008).

109. H. Goto, H. Kosako, K. Tanabe, M. Yanagida, M. Sakurai, M. Amano, K. Kaibuchi, M. Inagaki, Phosphorylation of vimentin by Rho-associated kinase at a unique amino-terminal site that is specifically phosphorylated during cytokinesis. *The Journal of biological chemistry* **273**, 11728–11736 (1998).

110. M. Schwartz, Rho signalling at a glance. *Journal of cell science* **117**, 5457–5458 (2004).

111. S. Jagannathan, MBInfo; Sheetz, Michael P., *What are Rho GTPases? | MBInfo*, *Mechanosignalling* (2017) (available at https://www.mechanobio.info/what-is-mechanosignaling/what-are-small-gtpases/what-are-rho-gtpases/#cellular-roles-of-rho-gtpases)(28-09-2017); (last accessed 28-05-2022).

112. C. D. Nobes, A. Hall, Rho, Rac, and Cdc42 GTPases regulate the assembly of multimolecular focal complexes associated with actin stress fibers, lamellipodia, and filopodia. *Cell* **81**, 53–62 (1995).

113. K. Bhadriraju, M. Yang, S. Alom Ruiz, D. Pirone, J. Tan, C. S. Chen, Activation of ROCK by RhoA is regulated by cell adhesion, shape, and cytoskeletal tension. *Experimental cell research* **313**, 3616–3623 (2007).

114. S. Seetharaman, S. Etienne-Manneville, Integrin diversity brings specificity in mechanotransduction. *Biol. Cell* **110**, 49–64 (2018).

115. N. Watanabe, T. Kato, A. Fujita, T. Ishizaki, S. Narumiya, Cooperation between mDia1 and ROCK in Rho-induced actin reorganization. *Nat Cell Biol* **1**, 136–143 (1999).

116. S. Narumiya, M. Tanji, T. Ishizaki, Rho signaling, ROCK and mDia1, in transformation, metastasis and invasion. *Cancer metastasis reviews* **28**, 65–76 (2009).

117. C. Garcin, A. Straube, Microtubules in cell migration. *Essays in biochemistry* **63**, 509–520 (2019).

118. A. Bershadsky, A. Chausovsky, E. Becker, A. Lyubimova, B. Geiger, Involvement of microtubules in the control of adhesion-dependent signal transduction. *Current Biology* **6**, 1279–1289 (1996).

119. N. D. Bade, R. D. Kamien, R. K. Assoian, K. J. Stebe, Curvature and Rho activation differentially control the alignment of cells and stress fibers. *Science advances* **3**, e1700150 (2017).

120. L. Pieuchot, J. Marteau, A. Guignandon, T. Dos Santos, I. Brigaud, P.-F. Chauvy, T. Cloatre, A. Ponche, T. Petithory, P. Rougerie, M. Vassaux, J.-L. Milan, N. Tusamda Wakhloo, A. Spangenberg, M. Bigerelle, K. Anselme, Curvotaxis directs cell migration through cell-scale curvature landscapes. *Nature communications* **9**, 3995 (2018).

121. M. Werner, A. Petersen, N. A. Kurniawan, C. V. C. Bouten, Cell-Perceived Substrate Curvature Dynamically Coordinates the Direction, Speed, and Persistence of Stromal Cell Migration. *Adv. Biosys.* **28**, 1900080 (2019).

122. S. J. Lee, S. Yang, Substrate Curvature Restricts Spreading and Induces Differentiation of Human Mesenchymal Stem Cells. *Biotechnology journal* **12** (2017).

123. X. Lin, S. Romanazzo, K. Lin, C. Kelly, J. J. Gooding, I. Roohani, Elliptical supra-cellular topographies regulate stem cells migratory pattern and osteogenic differentiation. *Materialia* **14**, 100870 (2020).

124. C. M. Bidan, K. P. Kommareddy, M. Rumpler, P. Kollmannsberger, Y. J. M. Bréchet, P. Fratzl, J. W. C. Dunlop, How linear tension converts to curvature: geometric control of bone tissue growth. *PloS one* **7**, e36336 (2012).

125. P. Kollmannsberger, C. M. Bidan, J. W. C. Dunlop, P. Fratzl, V. Vogel, Tensile forces drive a reversible fibroblast-to-myofibroblast transition during tissue growth in engineered clefts. *Science advances* **4**, eaao4881 (2018).

126. D. Baptista, L. Moreira Teixeira, D. Barata, Z. Tahmasebi Birgani, J. King, S. van Riet, T. Pasman, A. A. Poot, D. Stamatialis, R. J. Rottier, P. S. Hiemstra, A. Carlier, C. van Blitterswijk, P. Habibović, S. Giselbrecht, R. Truckenmüller, 3D Lung-on-Chip Model Based on Biomimetically Microcurved Culture Membranes. *ACS Biomater. Sci. Eng.* **8**, 2684–2699 (2022).

127. P. Viswanathan, M. Guvendiren, W. Chua, S. B. Telerman, K. Liakath-Ali, J. A. Burdick, F. M. Watt, Mimicking the topography of the epidermal-dermal interface with elastomer substrates. *Integrative biology : quantitative biosciences from nano to macro* **8**, 21–29 (2016).

128. S. H. Kim, M. Chi, B. Yi, S. H. Kim, S. Oh, Y. Kim, S. Park, J. H. Sung, Three-dimensional intestinal villi epithelium enhances protection of human intestinal cells from bacterial infection by inducing mucin expression. *Integrative biology : quantitative biosciences from nano to macro* **6**, 1122–1131 (2014).

129. D. Kaufmann, Y. Su, S. Biela, S. Jungbauer, J. P. Spatz, R. Kemkemer, Soft lithography detects partial mechano-sensoric blindness to micrometre topography in cultured aged and diseased cells. *IJMR* **102**, 896–902 (2011).

130. C. N. Kelly, A. T. Miller, S. J. Hollister, R. E. Guldberg, K. Gall, Design and Structure-Function Characterization of 3D Printed Synthetic Porous Biomaterials for Tissue Engineering. *Advanced healthcare materials* **7**, e1701095 (2018).

131. S. Vermeulen, F. Honig, A. Vasilevich, N. Roumans, M. Romero, A. Dede Eren, U. Tuvshindorj, M. Alexander, A. Carlier, P. Williams, J. Uquillas, J. de Boer, Expanding Biomaterial Surface Topographical Design Space through Natural Surface Reproduction. *Adv. Mater.* **33**, e2102084 (2021).

132. A. A. Zadpoor, Bone tissue regeneration: the role of scaffold geometry. *Biomaterials science* **3**, 231–245 (2015).

133. S. J. P. Callens, R. J. C. Uyttendaele, L. E. Fratila-Apachitei, A. A. Zadpoor, Substrate curvature as a cue to guide spatiotemporal cell and tissue organization. *Biomaterials* **232**, 119739 (2020).

134. C. van der Putten, A. B. C. Buskermolen, M. Werner, H. F. M. Brouwer, P. A. A. Bartels, P. Y. W. Dankers, C. V. C. Bouten, N. A. Kurniawan, Protein Micropatterning in 2.5D: An Approach to Investigate Cellular Responses in Multi-Cue Environments. *ACS applied materials & interfaces* (2021).

135. S. H. Shabbir, M. M. Cleland, R. D. Goldman, M. Mrksich, Geometric control of vimentin intermediate filaments. *Biomaterials* **35**, 1359–1366 (2014).

136. C. J. Bettinger, B. Orrick, A. Misra, R. Langer, J. T. Borenstein, Microfabrication of poly (glycerol-sebacate) for contact guidance applications. *Biomaterials* **27**, 2558–2565 (2006).

137. A. M. Greiner, A. Sales, H. Chen, S. A. Biela, D. Kaufmann, R. Kemkemer, Nano- and microstructured materials for in vitro studies of the physiology of vascular cells. *Beilstein J. Nanotechnol.* **7**, 1620–1641 (2016).

138. A. Sales, A. W. Holle, R. Kemkemer, Initial contact guidance during cell spreading is contractility-independent. *Soft matter* **13**, 5158–5167 (2017).

139. X. Jiang, S. Takayama, X. Qian, E. Ostuni, H. Wu, N. Bowden, P. LeDuc, D. E. Ingber, G. M. Whitesides, Controlling Mammalian Cell Spreading and Cytoskeletal Arrangement with Conveniently Fabricated Continuous Wavy Features on Poly(dimethylsiloxane). *Langmuir* **18**, 3273–3280 (2002).

140. Y. Li, K. A. Kilian, Bridging the Gap: From 2D Cell Culture to 3D Microengineered Extracellular Matrices. *Advanced healthcare materials* **4**, 2780–2796 (2015).

141. J. James, E. D. Goluch, H. Hu, C. Liu, M. Mrksich, Subcellular curvature at the perimeter of micropatterned cells influences lamellipodial distribution and cell polarity. *Cell motility and the cytoskeleton* **65**, 841–852 (2008).

142. J. Lee, A. A. Abdeen, T. H. Huang, K. A. Kilian, Controlling cell geometry on substrates of variable stiffness can tune the degree of osteogenesis in human mesenchymal stem cells. *Journal of the mechanical behavior of biomedical materials* **38**, 209–218 (2014).

143. J. Lee, A. A. Abdeen, A. S. Kim, K. A. Kilian, Influence of Biophysical Parameters on Maintaining the Mesenchymal Stem Cell Phenotype. *ACS Biomater. Sci. Eng.* **1**, 218–226 (2015).

144. M. Luciano, S.-L. Xue, W. H. de Vos, L. Redondo-Morata, M. Surin, F. Lafont, E. Hannezo, S. Gabriele, Cell monolayers sense curvature by exploiting active mechanics and nuclear mechanoadaptation. *Nature Phys* (2021).

145. Q. Zhou, O. Castañeda Ocampo, C. F. Guimarães, P. T. Kühn, T. G. van Kooten, P. van Rijn, Screening Platform for Cell Contact Guidance Based on Inorganic Biomaterial Micro/nanotopographical Gradients. *ACS applied materials & interfaces* **9**, 31433–31445 (2017).

146. K. H. Song, S. J. Park, D. S. Kim, J. Doh, Sinusoidal wavy surfaces for curvature-guided migration of T lymphocytes. *Biomaterials* **51**, 151–160 (2015).

147. P. Rougerie, L. Pieuchot, R. S. Dos Santos, J. Marteau, M. Bigerelle, P.-F. Chauvy, M. Farina, K. Anselme, Topographical curvature is sufficient to control epithelium elongation. *Sci Rep* **10**, 14784 (2020).

148. P. Yang, R. M. Baker, J. H. Henderson, P. T. Mather, In vitro wrinkle formation via shape memory dynamically aligns adherent cells. *Soft matter* **9**, 4705 (2013).

149. D. Baptista, L. M. Teixeira, Z. T. Birgani, S. van Riet, T. Pasman, A. Poot, D. Stamatialis, R. J. Rottier, P. S. Hiemstra, P. Habibović, C. van Blitterswijk, S. Giselbrecht, R. Truckenmüller, 3D alveolar in vitro model based on epithelialized biomimetically curved culture membranes. *Biomaterials* **266**, 120436 (2020).

150. J. C. H. Poon, Z. Liao, T. Suzuki, M. M. Carleton, J. P. Soleas, J. S. Aitchison, G. Karoubi, A. P. McGuigan, T. K. Waddell, Design of biomimetic substrates for long-term maintenance of alveolar epithelial cells. *Biomaterials science* **6**, 292–303 (2018).

151. J. Y. Park, D. H. Lee, E. J. Lee, S.-H. Lee, Study of cellular behaviors on concave and convex microstructures fabricated from elastic PDMS membranes. *Lab on a chip* **9**, 2043–2049 (2009).

152. N. D. Bade, T. Xu, R. D. Kamien, R. K. Assoian, K. J. Stebe, Gaussian Curvature Directs Stress Fiber Orientation and Cell Migration. *Biophysical journal* **114**, 1467–1476 (2018).

153. R. M. Gouveia, E. Koudouna, J. Jester, F. Figueiredo, C. J. Connon, Template Curvature Influences Cell Alignment to Create Improved Human Corneal Tissue Equivalents. *Adv. Biosys.* **1**, e1700135 (2017).

154. C. J. Connon, R. M. Gouveia, Milliscale Substrate Curvature Promotes Myoblast Self-Organization and Differentiation. *Advanced biology* **5**, e2000280 (2021).

155. Y.-J. Choi, S. J. Park, H.-G. Yi, H. Lee, D. S. Kim, D.-W. Cho, Muscle-derived extracellular matrix on sinusoidal wavy surfaces synergistically promotes myogenic differentiation and maturation. *J. Mater. Chem. B* **6**, 5530–5539 (2018).

156. M. Luciano, C. Tomba, A. Roux, S. Gabriele, How multiscale curvature couples forces to cellular functions. *Nat Rev Phys* **6**, 246–268 (2024).

157. X. Cun, L. Hosta-Rigau, Topography: A Biophysical Approach to Direct the Fate of Mesenchymal Stem Cells in Tissue Engineering Applications. *Nanomaterials (Basel, Switzerland)* **10** (2020).

158. S. G. Roy, Y. Nozaki, S. H. Phan, Regulation of α-smooth muscle actin gene expression in myofibroblast differentiation from rat lung fibroblasts. *The International Journal of Biochemistry & Cell Biology* **33**, 723–734 (2001).

159. C. H. Thomas, J. H. Collier, C. S. Sfeir, K. E. Healy, Engineering gene expression and protein synthesis by modulation of nuclear shape. *Proceedings of the National Academy of Sciences of the United States of America* **99**, 1972–1977 (2002).

160. K. Yang, H. Jung, H.-R. Lee, J. S. Lee, S. R. Kim, K. Y. Song, E. Cheong, J. Bang, S. G. Im, S.-W. Cho, Multiscale, hierarchically patterned topography for directing human neural stem cells into functional neurons. *ACS nano* **8**, 7809–7822 (2014).

161. M. J. Dalby, M. O. Riehle, S. J. Yarwood, C. D. Wilkinson, A. S. Curtis, Nucleus alignment and cell signaling in fibroblasts: response to a micro-grooved topography. *Experimental cell research* **284**, 272–280 (2003).

162. C. López-Fagundo, L. L. Livi, T. Ramchal, E. M. Darling, D. Hoffman-Kim, A biomimetic synthetic feeder layer supports the proliferation and self-renewal of mouse embryonic stem cells. *Acta biomaterialia* **39**, 55–64 (2016).

163. S. Mohamed-Ahmed, I. Fristad, S. A. Lie, S. Suliman, K. Mustafa, H. Vindenes, S. B. Idris, Adipose-derived and bone marrow mesenchymal stem cells: a donor-matched comparison. *Stem cell research & therapy* **9**, 168 (2018).

164. S. A. Biela, Dissertation, Heidelberg University Library (2009).

165. R. Kemkemer, S. Jungbauer, D. Kaufmann, H. Gruler, Cell orientation by a microgrooved substrate can be predicted by automatic control theory. *Biophysical journal* **90**, 4701–4711 (2006).

166. G. A. Dunn, J. P. Heath, A new hypothesis of contact guidance in tissue cells. *Experimental cell research* **101**, 1–14 (1976).

167. Y. Rovensky, V. I. Samoilov, Morphogenetic response of cultured normal and transformed fibroblasts, and epitheliocytes, to a cylindrical substratum surface. Possible role for the actin filament bundle pattern. *Journal of cell science* **107 (Pt 5)**, 1255–1263 (1994).

168. T. M. Svitkina, Y. A. Rovensky, A. D. Bershadsky, J. M. Vasiliev, Transverse pattern of microfilament bundles induced in epitheliocytes by cylindrical substrata. *Journal of cell science* **108 (Pt 2)**, 735–745 (1995).

169. E. M. Levina, L. V. Domnina, Y. A. Rovensky, J. M. Vasiliev, Cylindrical substratum induces different patterns of actin microfilament bundles in nontransformed and in ras-transformed epitheliocytes. *Experimental cell research* **229**, 159–165 (1996).

170. Z. Li, W. Wang, X. Xu, K. Kratz, J. Zou, L. Lysyakova, M. Heuchel, A. Kurtz, M. Gossen, N. Ma, A. Lendlein, Integrin β1 activation by micro-scale curvature promotes pro-angiogenic secretion of human mesenchymal stem cells. *Journal of materials chemistry. B* **5**, 7415–7425 (2017).

171. Y. Y. Biton, S. A. Safran, The cellular response to curvature-induced stress. *Physical biology* **6**, 46010 (2009).

172. A. Hamm, N. Krott, I. Breibach, R. Blindt, A. K. Bosserhoff, Efficient transfection method for primary cells. *Tissue engineering* **8**, 235–245 (2002).

173. A. Colosimo, K. K. Goncz, A. R. Holmes, K. Kunzelmann, G. Novelli, R. W. Malone, M. J. Bennett, D. C. Gruenert, Transfer and expression of foreign genes in mammalian cells. *BioTechniques* **29**, 314-8, 320-2, 324 passim (2000).

174. A. Dhaliwal, *Activators and Inhibitors in Cell Biology Research* (2013) (available at https://www.labome.com/method/Activators-and-Inhibitors-in-Cell-Biology-Research.html)(2022-011-06); (last accessed 05-12-2022).

175. A. Á. Rauscher, M. Gyimesi, M. Kovács, A. Málnási-Csizmadia, Targeting Myosin by Blebbistatin Derivatives: Optimization and Pharmacological Potential. *Trends in biochemical sciences* **43**, 700–713 (2018).

176. L. M. Bond, D. A. Tumbarello, J. Kendrick-Jones, F. Buss, Small-molecule inhibitors of myosin proteins. *Future medicinal chemistry* **5**, 41–52 (2013).

177. F. Fleissner, S. Kumar, N. Klein, D. Wirth, R. Dhiman, D. Schneider, M. Bonn, S. H. Parekh, Tension Causes Unfolding of Intracellular Vimentin Intermediate Filaments. *Adv. Biosys.* **4**, e2000111 (2020).

178. A. C. Laly, K. Sliogeryte, O. J. Pundel, R. Ross, M. C. Keeling, D. Avisetti, A. Waseem, N. Gavara, J. T. Connelly, The keratin network of intermediate filaments regulates keratinocyte rigidity sensing and nuclear mechanotransduction. *Science advances* **7**, eabd6187 (2021).

179. Cytoskeleton, Inc.; Cytoskeleton, Inc., *Datasheet Rho Activator II*, *Deamidation of Rho Gln-63 (Cat. #CN03)* (available at https://www.cytoskeleton.com/pdf-storage/datasheets/cn03.pdf); (last accessed 05-12-2022).

180. G. Schmidt, P. Sehr, M. Wilm, J. Selzer, M. Mann, K. Aktories, Gln 63 of Rho is deamidated by Escherichia coli cytotoxic necrotizing factor-1. *Nature* **387**, 725–729 (1997).

181. G. Flatau, E. Lemichez, M. Gauthier, P. Chardin, S. Paris, C. Fiorentini, P. Boquet, Toxin-induced activation of the G protein p21 Rho by deamidation of glutamine. *Nature* **387**, 729–733 (1997).

182. B. A. Weaver, How Taxol/paclitaxel kills cancer cells. *Molecular biology of the cell* **25**, 2677–2681 (2014).

183. C. Dumontet, M. A. Jordan, Microtubule-binding agents: a dynamic field of cancer therapeutics. *Nature reviews. Drug discovery* **9**, 790–803 (2010).

184. K. J. Green, R. D. Goldman, The effects of taxol on cytoskeletal components in cultured fibroblasts and epithelial cells. *Cell motility* **3**, 283–305 (1983).

185. O. J. Pletjushkina, O. J. Ivanova, I. N. Kaverina, J. M. Vasiliev, Taxol-treated fibroblasts acquire an epithelioid shape and a circular pattern of actin bundles. *Experimental cell research* **212**, 201–208 (1994).

186. M. D. Rosenblum, R. R. Shivers, 'Rings' of F-actin form around the nucleus in cultured human MCF7 adenocarcinoma cells upon exposure to both taxol and taxotere. *Comparative Biochemistry and Physiology Part C: Pharmacology, Toxicology and Endocrinology* **125**, 121–131 (2000).

187. T. M. Adams, R. A. Layton, *Introductory MEMS*, *Fabrication and Application*(Springer, New York, 2010).

188. V. N. Goral, Y.-C. Hsieh, O. N. Petzold, R. A. Faris, P. K. Yuen, Hot embossing of plastic microfluidic devices using poly(dimethylsiloxane) molds. *J. Micromech. Microeng.* **21**, 17002 (2011).

189. M. B. Ginzberg, R. Kafri, M. Kirschner, Cell biology. On being the right (cell) size. *Science (New York, N.Y.)* **348**, 1245075 (2015).

190. L. Tang, P. Thevenot, W. Hu, Surface Chemistry Influences Implant Biocompatibility. *CTMC* **8**, 270–280 (2008).

191. M. Singh, K. McKenzie, X. Ma, Effect of dimethyl sulfoxide on in vitro proliferation of skin fibroblast cells. *Journal of Biotech Research* **2017**, 78–82.

192. J. D. Dukes, P. Whitley, A. D. Chalmers, The MDCK variety pack: choosing the right strain. *BMC Cell Biol* **12**, 43 (2011).

193. C. Zambarda, C. Pérez González, A. Schoenit, N. Veits, C. Schimmer, R. Jung, D. Ollech, J. Christian, P. Roca-Cusachs, X. Trepat, E. A. Cavalcanti-Adam, Epithelial cell cluster size affects force distribution in response to EGF-induced collective contractility. *European journal of cell biology* **101**, 151274 (2022).

194. Life Technolgies; Invitrogen, *Click-iT® Plus EdU Imaging Kits*, Pub. no. MAN0009885 MP10637 (6.01.2014) (available at https://www.thermofisher.com/document-connect/document-connect.html?url=https://assets.thermofisher.com/TFS-Assets%2FLSG%2Fmanuals%2Fmp10637.pdf)(06-01-2014); (last accessed 30.10.021).

195. Nationl Instutes of Health of the Federal Government US; , *DrawParticlaEllipseAxis.txt*, *Macro* (2010-07-29 14:18) (available at https://imagej.nih.gov/ij/macros/examples/DrawParticleEllipseAxis.txt;)(29-07-2010); (last accessed 08-11-2021).

196. Microresist technology GmbH; Microresist technology GmbH, *Herstellung von Mikrolinsen-Arrays mittels Reflow und UV-Abformung* (available at https://

www.microresist.de/tech-blogs-micro/herstellung-von-mikrolinsen-arrays-mittels-reflow-und-uv-abformung/); (last accessed 24-06-2021).

197. L. Yang, Z. Zhang, K. Athanasopulu, K. Frey, Z. Cui, H. Su, L. Luo, R. Kemkemer, Surface modification of Polydimethylsiloxane by hydrogels for microfluidic applications. *Current Directions in Biomedical Engineering* **5**, 93–96 (2019).

198. W. S. Choi, Y. K. Joung, Y. Lee, J. W. Bae, H. K. Park, Y. H. Park, J.-C. Park, K. D. Park, Enhanced Patency and Endothelialization of Small-Caliber Vascular Grafts Fabricated by Coimmobilization of Heparin and Cell-Adhesive Peptides. *ACS applied materials & interfaces* **8**, 4336–4346 (2016).

199. M. Nikkhah, J. S. Strobl, B. Peddi, M. Agah, Cytoskeletal role in differential adhesion patterns of normal fibroblasts and breast cancer cells inside silicon microenvironments. *Biomedical microdevices* **11**, 585–595 (2009).

200. B. Sun, K. Xie, T.-H. Chen, R. H. W. Lam, Preferred cell alignment along concave microgrooves. *RSC Adv* **7**, 6788–6794 (2017).

201. Yong Hou, Wenyan Xie, Leixiao Yu, Luis Cuellar Camacho, Chuanxiong Nie, Man Zhang, Rainer Haag, Qiang Wei, Surface Roughness Gradients Reveal Topography-Specific Mechanosensitive Responses in Human Mesenchymal Stem Cells. *Small* **16** (2020).

202. W.-H. Jung, K. Elawad, S. H. Kang, Y. Chen, Cell-Cell Adhesion and Myosin Activity Regulate Cortical Actin Assembly in Mammary Gland Epithelium on Concaved Surface. *Cells* **8** (2019).

203. C. M. Hwang, Y. Park, J. Y. Park, K. Lee, K. Sun, A. Khademhosseini, S. H. Lee, Controlled cellular orientation on PLGA microfibers with defined diameters. *Biomedical microdevices* **11**, 739–746 (2009).

204. K. E. Broaders, A. E. Cerchiari, Z. J. Gartner, Coupling between apical tension and basal adhesion allow epithelia to collectively sense and respond to substrate topography over long distances. *Integrative biology : quantitative biosciences from nano to macro* **7**, 1611–1621 (2015).

205. C. Liu, J. Xu, S. He, W. Zhang, H. Li, B. Huo, B. Ji, Collective cell polarization and alignment on curved surfaces. *Journal of the mechanical behavior of biomedical materials* **88**, 330–339 (2018).

206. H. G. Yevick, G. Duclos, I. Bonnet, P. Silberzan, Architecture and migration of an epithelium on a cylindrical wire. *Proceedings of the National Academy of Sciences of the United States of America* **112**, 5944–5949 (2015).

207. M. Ye, H. M. Sanchez, M. Hultz, Z. Yang, M. Bogorad, A. D. Wong, P. C. Searson, Brain microvascular endothelial cells resist elongation due to curvature and shear stress. *Scientific reports* **4**, 4681 (2014).

208. R. Kemkemer, D. Kling, D. Kaufmann, H. Gruler, Elastic properties of nematoid arrangements formed by amoeboid cells. *Eur. Phys. J. E* **1**, 215 (2000).

209. T. R. Elsdale, Parallel orientation of fibroblasts in vitro. *Experimental cell research* **51**, 439–450 (1968).

210. D. J. G. Pearce, Defect order in active nematics on a curved surface. *New J. Phys.* **22**, 63051 (2020).

211. M. Werner, C. V. C. Bouten, N. A. Kurniawan, *Substrate curvature as a regulator of cellular orientation and migration*(Technische Universiteit Eindhoven, Eindhoven, 2019).

212. A. Fruleux, R. J. Hawkins, Physical role for the nucleus in cell migration. *Journal of physics. Condensed matter : an Institute of Physics journal* **28**, 363002 (2016).

213. T. Omelchenko, J. M. Vasiliev, I. M. Gelfand, H. H. Feder, E. M. Bonder, Mechanisms of polarization of the shape of fibroblasts and epitheliocytes: Separation of the roles of microtubules and Rho-dependent actin-myosin contractility. *Proceedings of the National Academy of Sciences of the United States of America* **99**, 10452–10457 (2002).

214. W. G. Lim, B. J. Tan, Y. Zhu, S. Zhou, J. S. Armstrong, Q. T. Li, Q. Dong, E. Chan, D. Smith, C. Verma, S.-L. Tan, W. Duan, The very C-terminus of PRK1/PKN is essential for its activation by RhoA and downstream signaling. *Cellular signalling* **18**, 1473–1481 (2006).

215. A. Schmandke, A. Schmandke, S. M. Strittmatter, ROCK and Rho: biochemistry and neuronal functions of Rho-associated protein kinases. *The Neuroscientist : a review journal bringing neurobiology, neurology and psychiatry* **13**, 454–469 (2007).

216. A. D. Bershadsky, E. A. Vaisberg, J. M. Vasiliev, Pseudopodial activity at the active edge of migrating fibroblast is decreased after drug-induced microtubule depolymerization. *Cell motility and the cytoskeleton* **19**, 152–158 (1991).

217. P. J. Hollenbeck, A. D. Bershadsky, O. Y. Pletjushkina, I. S. Tint, J. M. Vasiliev, Intermediate filament collapse is an ATP-dependent and actin-dependent process. *Journal of cell science* **92 (Pt 4)**, 621–631 (1989).

218. J. Li, Y. Zou, Z. Li, Y. Jiu, Joining actions: crosstalk between intermediate filaments and actin orchestrates cellular physical dynamics and signaling. *Science China. Life sciences* **62**, 1368–1374 (2019).

219. A. E. Patteson, A. Vahabikashi, K. Pogoda, S. A. Adam, K. Mandal, M. Kittisopikul, S. Sivagurunathan, A. Goldman, R. D. Goldman, P. A. Janmey, Vimentin protects cells against nuclear rupture and DNA damage during migration. *The Journal of cell biology* **218**, 4079–4092 (2019).

220. A. E. Patteson, K. Pogoda, F. J. Byfield, K. Mandal, Z. Ostrowska-Podhorodecka, E. E. Charrier, P. A. Galie, P. Deptuła, R. Bucki, C. A. McCulloch, P. A. Janmey, Loss of Vimentin Enhances Cell Motility through Small Confining Spaces. *Small (Weinheim an der Bergstrasse, Germany)* **15**, e1903180 (2019).

221. S. Neelam, T. J. Chancellor, Y. Li, J. A. Nickerson, K. J. Roux, R. B. Dickinson, T. P. Lele, Direct force probe reveals the mechanics of nuclear homeostasis in the mammalian cell. *PNAS* **112**, 5720–5725 (2015).

222. A. W. Holle, M. Kalafat, A. S. Ramos, T. Seufferlein, R. Kemkemer, J. P. Spatz, Intermediate filament reorganization dynamically influences cancer cell alignment and migration. *Sci Rep* **7**, 45152 (2017).

223. L. Hanson, W. Zhao, H.-Y. Lou, Z. C. Lin, S. W. Lee, P. Chowdary, Y. Cui, B. Cui, Vertical nanopillars for in situ probing of nuclear mechanics in adherent cells. *Nature Nanotech* **10**, 554–562 (2015).

224. N. T. Tusamda Wakhloo, S. Anders, F. Badique, M. Eichhorn, I. Brigaud, T. Petithory, M. Vassaux, J.-L. Milan, J.-N. Freund, J. Rühe, P. M. Davidson, L. Pieuchot, K. Anselme, Actomyosin, vimentin and LINC complex pull on osteosarcoma nuclei to deform on micropillar topography. *Biomaterials* **234**, 119746 (2020).

225. P. Sharma, Z. T. Bolten, D. R. Wagner, A. H. Hsieh, Deformability of Human Mesenchymal Stem Cells Is Dependent on Vimentin Intermediate Filaments. *Annals of Biomedical Engineering* **45**, 1365–1374 (2017).

226. S. Rhee, H. Jiang, C.-H. Ho, F. Grinnell, Microtubule function in fibroblast spreading is modulated according to the tension state of cell-matrix interactions. *Proceedings of the National Academy of Sciences of the United States of America* **104**, 5425–5430 (2007).

227. R. A. Brown, G. Talas, R. A. Porter, D. A. McGrouther, M. Eastwood, Balanced mechanical forces and microtubule contribution to fibroblast contraction. *J. Cell. Physiol.* **169**, 439–447 (1996).

228. K. A. DeMali, K. Burridge, Coupling membrane protrusion and cell adhesion. *Journal of cell science* **116**, 2389–2397 (2003).

229. M. Delcommenne, C. H. Streuli, Control of integrin expression by extracellular matrix. *Journal of Biological Chemistry* **270**, 26794–26801 (1995).

230. H.-D. Haubeck, in *Lexikon der Medizinischen Laboratoriumsdiagnostik*, A. M. Gressner, T. Arndt, Eds.(Springer Berlin Heidelberg, Berlin, Heidelberg, 2019), p. 2481.

231. H.-D. Haubeck, in *Lexikon der Medizinischen Laboratoriumsdiagnostik*, A. M. Gressner, T. Arndt, Eds.(Springer Berlin Heidelberg, Berlin, Heidelberg, 2019), pp. 868–869.

232. P. A. Underwood, F. A. Bennett, A comparison of the biological activities of the cell-adhesive proteins vitronectin and fibronectin. *Journal of cell science* **93**, 641–649 (1989).

233. J. G. Steele, G. Johnson, P. A. Underwood, Role of serum vitronectin and fibronectin in adhesion of fibroblasts following seeding onto tissue culture polystyrene. *J. Biomed. Mater. Res.* **26**, 861–884 (1992).

234. C. D. McFarland, C. H. Thomas, C. DeFilippis, J. G. Steele, K. E. Healy, Protein adsorption and cell attachment to patterned surfaces. *J. Biomed. Mater. Res.* **49**, 200–210 (2000).

235. M. D'Urso, N. A. Kurniawan, Mechanical and Physical Regulation of Fibroblast-Myofibroblast Transition: From Cellular Mechanoresponse to Tissue Pathology. *Frontiers in bioengineering and biotechnology* **8**, 609653 (2020).

236. J. Lu, A. D. Doyle, Y. Shinsato, S. Wang, M. A. Bodendorfer, M. Zheng, K. M. Yamada, Basement Membrane Regulates Fibronectin Organization Using Sliding Focal Adhesions Driven by a Contractile Winch. *Developmental Cell* **52**, 631-646.e4 (2020).

237. H. P. Ehrlich, O. Cremona, G. Gabbiani, The expression of α2β1 integrin and α smooth muscle actin in fibroblasts grown on collagen. *Cell Biochem. Funct.* **16**, 129–137 (1998).

238. H. P. Ehrlich, G. M. Allison, M. Leggett, The myofibroblast, cadherin, alpha smooth muscle actin and the collagen effect. *Cell biochemistry and function* **24**, 63–70 (2006).

239. C. Jones, H. P. Ehrlich, Fibroblast expression of α-smooth muscle actin, α2β1 integrin and αvβ3 integrin. *Experimental and molecular pathology* **91**, 394–399 (2011).

240. H. Sondermann, D. Dogic, M. Pesch, M. Aumailley, Targeting of cytoskeletal linker proteins to focal adhesion complexes is reduced in fibroblasts adhering to laminin-1 when compared to fibronectin. *Cell adhesion and communication* **7**, 43–56 (1999).

241. E. H. Danen, S. Aota, A. A. van Kraats, K. M. Yamada, D. J. Ruiter, G. N. van Muijen, Requirement for the synergy site for cell adhesion to fibronectin depends on the activation state of integrin alpha 5 beta 1. *Journal of Biological Chemistry* **270**, 21612–21618 (1995).

242. J. R. Couchman, M. Höök, D. A. Rees, R. Timpl, Adhesion, growth, and matrix production by fibroblasts on laminin substrates. *The Journal of cell biology* **96**, 177–183 (1983).

243. M. S. Liberio, M. C. Sadowski, C. Soekmadji, R. A. Davis, C. C. Nelson, Differential effects of tissue culture coating substrates on prostate cancer cell adherence, morphology and behavior. *PloS one* **9**, e112122 (2014).

244. G. Song, Y. Ju, X. Shen, Q. Luo, Y. Shi, J. Qin, Mechanical stretch promotes proliferation of rat bone marrow mesenchymal stem cells. *Colloids and surfaces. B, Biointerfaces* **58**, 271–277 (2007).

245. S. J. Streichan, C. R. Hoerner, T. Schneidt, D. Holzer, L. Hufnagel, Spatial constraints control cell proliferation in tissues. *PNAS* **111**, 5586–5591 (2014).

246. M. Deibler, J. P. Spatz, R. Kemkemer, Actin fusion proteins alter the dynamics of mechanically induced cytoskeleton rearrangement. *PloS one* **6**, e22941 (2011).

247. D. V. Krysko, L. Leybaert, P. Vandenabeele, K. D'Herde, Gap junctions and the propagation of cell survival and cell death signals. *Apoptosis* **10**, 459–469 (2005).

248. R. C. Gaal, R. P. R. S. Miltenburg, N. A. Kurniawan, C. V. C. Bouten, P. Y. W. Dankers, Renal Epithelial Cell Responses to Supramolecular Thermoplastic Elastomeric Concave and Convex Structures. *Adv. Mater. Interfaces* **8**, 2001490 (2021).

249. S.-M. Yu, J. M. Oh, J. Lee, W. Lee-Kwon, W. Jung, F. Amblard, S. Granick, Y.-K. Cho, Substrate curvature affects the shape, orientation, and polarization of renal epithelial cells. *Acta biomaterialia* **77**, 311–321 (2018).

250. M. Cereijido, J. Ehrenfeld, I. Meza, A. Martínez-Palomo, Structural and functional membrane polarity in cultured monolayers of MDCK cells. *The Journal of membrane biology* **52**, 147–159 (1980).

251. N. Elia, J. Lippincott-Schwartz, Culturing MDCK cells in three dimensions for analyzing intracellular dynamics. *Current protocols in cell biology* **Chapter 4**, Unit 4.22 (2009).

252. J. Leighton, Z. Brada, L. W. Estes, G. Justh, Secretory activity and oncogenicity of a cell line (MDCK) derived from canine kidney. *Science (New York, N.Y.)* **163**, 472–473 (1969).

253. C. Tanner, D. A. Frambach, D. S. Misfeldt, Transepithelial transport in cell culture. A theoretical and experimental analysis of the biophysical properties of domes. *Biophysical journal* **43**, 183–190 (1983).

254. S. M. Zehnder, M. Suaris, M. M. Bellaire, T. E. Angelini, Cell Volume Fluctuations in MDCK Monolayers. *Biophysical journal* **108**, 247–250 (2015).

255. D. E. Ingber, Tensegrity: the architectural basis of cellular mechanotransduction. *Annual review of physiology* **59**, 575–599 (1997).

256. P. M. Davidson, M. Bigerelle, G. Reiter, K. Anselme, Different surface sensing of the cell body and nucleus in healthy primary cells and in a cancerous cell line on nanogrooves. *Biointerphases* **10**, 31004 (2015).

257. K. Kushiro, T. Yaginuma, A. Ryo, M. Takai, Differences in Three-Dimensional Geometric Recognition by Non-Cancerous and Cancerous Epithelial Cells on Microgroove-Based Topography. *Sci Rep* **7**, 4244 (2017).

258. P. M. Davidson, O. Fromigué, P. J. Marie, V. Hasirci, G. Reiter, K. Anselme, Topographically induced self-deformation of the nuclei of cells: dependence on cell type and proposed mechanisms. *Journal of materials science. Materials in medicine* **21**, 939–946 (2010).

259. M. Ermis, D. Akkaynak, P. Chen, U. Demirci, V. Hasirci, A high throughput approach for analysis of cell nuclear deformability at single cell level. *Sci Rep* **6**, 36917 (2016).

260. M. B. Alvarez-Elizondo, C. W. Li, A. Marom, Y.-T. Tung, G. Drillich, Y. Horesh, S. C. Lin, G.-J. Wang, D. Weihs, Micropatterned topographies reveal measurable differences between cancer and benign cells. *Medical engineering & physics* **75**, 5–12 (2020).

261. C. Denais, J. Lammerding, Nuclear mechanics in cancer. *Advances in experimental medicine and biology* **773**, 435–470 (2014).

262. J. A. Broussard, R. Yang, C. Huang, S. S. P. Nathamgari, A. M. Beese, L. M. Godsel, M. H. Hegazy, S. Lee, F. Zhou, N. J. Sniadecki, K. J. Green, H. D. Espinosa, The desmoplakin-intermediate filament linkage regulates cell mechanics. *Molecular biology of the cell* **28**, 3156–3164 (2017).

263. R. Liu, Q. Liu, Z. Pan, X. Liu, J. Ding, Cell Type and Nuclear Size Dependence of the Nuclear Deformation of Cells on a Micropillar Array. *Langmuir : the ACS journal of surfaces and colloids* **35**, 7469–7477 (2019).

264. C.-P. Heisenberg, Cell biology: Stretched divisions. *Nature* **543**, 43–44 (2017).

265. E. Brauer, T. Lange, D. Keller, S. Görlitz, S. Cho, J. Keye, M. Gossen, A. Petersen, U. Kornak, Dissecting the influence of cellular senescence on cell mechanics and extracellular matrix formation in vitro. *Aging cell*, e13744 (2022).